INAUGURAL - DISSERTATION

Zur

Erlangung der Doktorwürde

der

Naturwissenschaftlich-Mathematischen Gesamtfakultät

der

Ruprecht-Karls-Universität Heidelberg

vorgelegt von

Jabadurai Jayapaul MSc

aus Melur (Indien)

Tag der mündlichen Prüfung:

Fluorescent Iron Oxide Nanoparticles for Molecular MR and Optical Imaging

Gutachter: Prof. Dr. Peter Comba

Prof. Dr. Fabian Kiessling

This work was performed at the department of experimental molecular imaging (ExMI), University clinics, RWTH Aachen University in co-operation with Helmholtz Institute for Applied Medical Engineering, Aachen and German Cancer Research Center (DKFZ), Heidelberg

To my parents, brothers and sisters

List of abbreviations:

acac	acetylacetonate
AEP	2-aminoethylphosphonic acid
AFM	Atomic force microscopy
ANDS	7-amino-1, 3-naphthalene disulfonic acid
APTMS	3-aminopropyl trimethyl silane
DAPI	4`,6-diamidino-2-phenylindole
DEAD	Diethyl azodicarboxylate
DIPEA	N,N-diisopropylethylamine
DLS	Dynamic light scattering
EDC	1-ethyl-3-(3-dimethylamino propyl) carbodiimide
EDTA	Ethylene diamine tetraacetic acid
EDX	Energy dispersive X-ray
EPR	Enhanced permeation and retention
ESI-MS	Electron spray ionization mass spectrometry
FACS	Fluorescence assisted cell sorting (Flow cytometry)
FAD USPIO	Flavin adenine dinucleotide coated Ultrasmall
FAD	Flavin adenine dinucleotide
FBS	Fetal bovine serum
FLUSPIO	Fluorescent Ultrasmall Super Paramagnetic Iron Oxides
FMN	Flavin mononucleotide
FMT	Fluorescence mediated tomography
FRET	Fluorescence resonance energy transfer
FT-IR	Fourier transform infrared spectrometry
H-acid	4-amino-5-hydroxy-2,7-naphthalene disulfonic acid
HOBt	1-hydroxybenzotriazole
ICP-MS	Inductively coupled plasma mass spectrometry
ICP-OES	Inductively coupled optical emission spectrometry
JCPDS	Joint committee on powder diffraction standards
LDH	Lactate dehydrogenase
Ln-USPIO	Lanthanide doped Ultrasmall SuperParamagnetic Iron Oxides
MALDI-MS	Matrix assisted laser desorption ionization mass spectrometry
MRI	Magnetic resonance imaging
MTT	3-(4,5-dimethylthiazol-2-yl)-2,5-diphenyltetrazolium bromide
NMR	Nuclear magnetic resonance
NUSPIO	Naphthalene coated Ultrasmall SuperParamagnetic Iron Oxides
PBS	Phosphate buffered saline
PDI	Polydispersity index
Pen/Strep	Penicillin/Streptomycin
PET	Positron emission tomography
r	Relaxivity
R2, R1	Relaxation rates
RCP	Riboflavin carrier protein
RET	Resonance energy transfer
RF	Radiofrequency
Rf	Riboflavin
RPMI medium	Roswell Park Memorial Institute medium
SEM	Scanning electron microscopy
SPECT	Single photon emission computed tomography
SQUID	Superconducting quantum interface device
	Super Paramagnetic Iron Oxides
T_1	spin-lattice relaxation (longitudinal relaxation)
T_2	spin-spin relaxation (transverse relaxation)

TE	Echo time
TEM	Transmission electron microscopy
TEOS	Tetraethyl orthosilicate
TGA	Thermogravimetric analysis
TLC	Thin layer chromatography
TOF-SIMS	Time of flight secondary ion mass spectrometry
TR	Repetition time
TUNEL	Terminal deoxynucleotidyl transferase dUTP nick end labeling
US	Ultrasound
USPIO	Ultrasmall Super Paramagnetic Iron Oxides
XRD	X-ray diffraction

Acknowledgement:

I would like to extend my sincere gratitude and heartfelt thanks to my supervisor and friendly guide Prof. Fabian Kiessling, Department of Experimental imaging (ExMI), University Clinics, RWTH Aachen University. I am grateful to him, for providing me an excellent research facility and for introducing me to the fascinating field of MRI and molecular imaging. I thank him for his belief in me during hard times in research and for his timely encouragement towards achieving my research goals. I learned a lot about molecular imaging from his lectures.

I would also like to thank my supervisor Prof. Peter Comba, Institute of Inorganic Chemistry, Heidelberg University for his excellent guidance and support. I thank him for his innovative suggestions and helpful solutions for solving research problems during hard times. He is easily approachable, kind, induces new ideas and has a great concern towards his students. I really enjoyed my association as graduate student under his guidance. I remember him saying that "try to learn new things in research and focus on finding a permanent position as soon as possible" which intensely increased my appetite for research.

I would like to thank and appreciate the excellent guidance of Dr. Jessica Gaetjens, ExMI department, University Clinics, RWTH Aachen University during the past two years. Thank you for listening to my ideas and for improvising them with your timely and helpful suggestions/comments. I would like to specifically thank you for your immense patience in correcting my papers and thesis. I learned from you in terms of writing a scientific paper and how to bring out a complete story so that it is interesting for the scientific audience. Thanks for your belief in my hardwork. I would like to thank you for your continuous support and encouragement that you have extended during my research stay in Aachen.

I extend my heartfelt thanks to Dr. Michael Hodenius, for introducing me to the new techniques in nanoparticle synthesis. I thank him for teaching me more material chemistry aspects and for the fruitful discussions which we had in Helmholtz Institute during the late working hours. I would like to thank Dr. Wiltrud Lederle for her help, suggestions and support regarding the *in vitro* and *in vivo* experiments. Further, I would like to thank her for correcting my manuscript. I thank Dr. Twan Lammers for his help in organizing the measurements with Molecular Profiles, UK and for his comments towards my manuscript.

I would like to thank my sister Susanne Arns for helping and supporting me in most of the cell and animal experiments which I have performed in University clinics Aachen. I thank her for teaching me cell culture, histology, animal handling, excising the animal, intravenous injection etc. I thank her for the fruitful discussions and ideas which we had towards different experiments. I thank for her patience in explaining facts and for allowing me to do experiments myself.

I thank Mrs. Natascha Mertens for her extended help during different experiments. I would like to thank her specially for teaching me MRI and for allowing me to work individually. Further, I thank her for suggestions, comments towards my experiments. I also thank Ms. Anne Rix for her help in different experiments and for the discussions and suggestions.

I would like to specially thank Mrs. Birgit Tiemann for her help in organizing my research stay in Aachen. I thank her for the patience, support and friendship. Further, I would like to thank other PhD students from the ExMI department of University Clinics Aachen for their support, suggestions, and comments during my research stay in Aachen. I thank Mr. Lotfi for his help in western blot; Mr. Dennis for his immense help with the computers and programmes during my thesis writing; Mr. Stanley for his friendship, fruitful discussions and for teaching FACS. I thank Mr. Sijumon Kunjachan for his support, friendship and comments and help in research.

I would like to sincerely extend my thanks to the patience and guidance provided by Dr. Jochen Huppert, DKFZ Heidelberg, Heidelberg University, during the initial two years of my PhD thesis work. He was a big source of teaching, suggestion, experimenting things along with me. I thank him for introducing me to Prof. Peter Comba as a supervisor for my PhD thesis from the Institute of Inorganic Chemistry, Heidelberg University. He used to insist me that "I should try to do independent research and if nothing works in the lab, just go and relax on the

banks of river Neckar". I greatly admired his patience in handling research difficulties. I miss the fruitful interaction, the fun in research which we had together in DKFZ Heidelberg.

I thank Prof. Semmler for providing me support during my initial PhD thesis work in DKFZ Heidelberg. I learned a lot about imaging from his lectures. I thank him for his kind heart, cheerfulness and helping tendency. I am grateful to Dr. Tobias Bäulere for his constant support and help during my research work in DKFZ. Further, I thank Dr. Manfred Jugold for his friendship, valuable discussions, suggestions, and comments and for the fun we had together in research. He is a man of ideas and tries to help a lot by providing inputs. I thank him for introducing me to the biological concepts and perspectives. I would like to thank Dr. Bartling for introducing me to CT imaging and for his friendship.

I would like to thank Dr. Stefan Zwick for his excellent friendship, guidance, helpfulness, and for teaching many aspects about physics of MRI. Specially, I would like to thank him for his guidance and help during my hard times in research. He was a big motivation for me, in terms of doing research in a systematic way. I miss the fun which we had together in research and his good friendship.

I extend my deep sense of gratitude to Mrs. Renate Bangert, for introducing me to the basic cell experiments and for performing various *in vitro* studies for me. I thank Dr. Ute for her guidance during the synthesis of organic compounds. I thank Dr. Dörte Oltmanns, radiopharmaceutics department, DKFZ for her constant support and help with different measurements.

I thank Dr. Christina Haaf, Dr. Christoph Busche and Mr. Maik Jacob from the group of Prof. Peter Comba for extending their help in performing various measurements and for their availability to discuss problems related to the measurements. I would like to thank Mrs. Marlies Schilli and Mrs. Karin Stelzer for their administration help.

I would like to thank the following persons for helping me with various measurements: Dr. Ute Resch (Quantum yield and fluorescence lifetime, BAM, Berlin), Mr. Christian Würth (Quantum yield and fluorescence lifetime, BAM, Berlin), Dr. Paul Müller (powder XRD, Inorganic chemistry department, RWTH Aachen); Dr. Christina Graf (TEM, FU Berlin), Mr. Manfred Spieldrich (SQUID, Inorganic chemistry department, RWTH Aachen); Ms. Ioana Slabu (phosphate estimation, AME, Helmholtz Institute Aachen); Dr. Matt Bunker (DLS, powder XRD, SIMS, XPS, Molecular Profiles, UK); Dr. Chunfu Zhang (TEM, China); Dr. Hanswalter Zentgraf (TEM, DKFZ Heidelberg); Dr. Jochen Huppert (TEM, DLS, ICP-OES, INM Saarbruken); Dr. Jörg Bornemann (TEM, University clinics, RWTH Aachen); Mr. Manfred Bovi (SEM/EDX, University clinics, RWTH Aachen); Mr. Sörnen (ICPMS, University clinics, RWTH Aachen); Mr. Sebastian Schwarz (FACS, University clinics, RWTH Aachen); Mr. Stefan Weinandy (Fluorescence microscope, University clinics, RWTH Aachen); Ms. Eva Siepert Maria (western blot, AME, Helmholtz Institute Aachen); Ms. Claudia Rösgen (plate reader, AME, Helmholtz Institute Aachen); Dr. John Wong (DLS, DWI Aachen); Ms. Andreea (DLS, DWI Aachen)

The financial supports provided by the DFG grant KI 1072/1-3 "Dual mode contrast agents for MRI and optical imaging techniques" and by the InnoMeT grant z0909im008a "Entwicklung und Bildgebung patientenoptimierter Implantate" for carrying out this thesis work are greatly acknowledged.

I would like to thank my sisters Suguna and Sivaasankari for their support, care, guidance, patience. I would like to also thank my brothers Jebaraj, Viji and Alwin for their support and care. I would like to thank my parents for believing in me, for their emotional, financial and physical support under all circumstances. I miss you all.

Finally I would like to thank the Lord Almighty for being with me in all circumstances and for His guidance and for His eternal love.

List of Publications:

1. **Jabadurai Jayapaul**, Michael Hodenius, Susanne Arns, Wiltrud Lederle, Twan Lammers, Peter Comba, Fabian Kiessling, Jessica Gaetjens. "FMN-coated fluorescent iron oxide nanoparticles for RCP-mediated targeting and labeling of metabolically active cancer and endothelial cells". *Biomaterials*, 2011, 32(25), 5863-5871.
2. Kiessling F., Huppert J., Zhang C., **Jayapaul J**., Zwick S., Woenne E.C., Mueller M.M., Zentgraf H., Eisenhut M., Addadi Y., Neeman M., Semmler W. "RGD-labeled USPIO inhibit adhesion and endocytotic activity of $\alpha_v\beta_3$ integrin expressing glioma cells and only accumulate in the vascular tumor compartment" *Radiology*, 2009, 253, 462 – 469.
3. Michael Hodenius*, Christian Würth*, **Jabadurai Jayapaul**, John Wong, Twan Lammers, Jessica Gätjens, Susanne Arns, Natascha Mertens, Ioana Slabu, Gergana Ivanova, Jörg Bornemann, Marcel De Cuyper, Ute Resch-Genger, Fabian Kiessling. "Fluorescent magnetoliposomes as a platform technology for functional and molecular MR and optical imaging" *Contrast Media and Molecular Imaging* (accepted).
4. Sijumon Kunjachan, **Jabadurai Jayapaul**, Marianne E. Mertens, Gert Storm, Fabian Kiessling, Twan Lammers. "Theranostic systems and strategies for monitoring nanomedicine-mediated drug targeting". *Current Pharmaceutical Biotechnology* 2011 (Revew article in press)

The original research articles (1-3) can be found after the Appendix section at the end of the thesis.

Abstracts:

1. **Jayapaul, J.;** Hodenius, M.; Buhl, A.; Comba, P.; Kiessling, F.; Gaetjens, J.;
   "Novel non-polymeric fluorescent bimodal contrast agent for magnetic resonance and optical imaging"
   6. Coordination chemistry meeting 2010, Mainz, Germany.
2. **Jabadurai Jayapaul**, Michael Hodenius, Alexandra Buhl, Peter Comba, Fabian Kiessling, Jessica Gaetjens
   "Dual modal contrast agent with novel non-polymeric fluorescent coating (FLUSPIO)"
   World Molecular Imaging Congress, 2009, Montreal, Canada.
3. Jochen Huppert, Chunfu Zhang, **Jabadurai Jayapaul**, Stefan Zwick, Eva C. Woenne, Margartea M. Mueller, Hanswalter Zentgraf, Michael Eisenhut, Yoseph Addadi, Michael Neeman, Wolfhard Semmler, Fabian Kiessling
   "Opposing effects of RGD-labeled USPIO on glioma and endothelial cells"
   World Molecular Imaging Congress, 2008, Nice, France.

Table of contents

Abstract

The thesis focuses on design and development of iron oxide nanoparticle-based dual modal contrast agent for magnetic resonance (MR) and optical imaging (OI). Iron oxide cores of size 5-6 nm with low polydispersity index were generated by co-precipitation under aqueous reaction conditions. Firstly, we tested lanthanide-doped iron oxide nanoparticles (Ln-USPIO), which seemed to exhibit no florescence due to lower levels of lanthanide incorporated into the iron crystal structure, which can be explained by the size-based difference between lanthanide and iron cations, thus, limiting doping efficiency considerably. Secondly, we attempted fluorescence coating of the nanoparticles using naphthalene disulfonic acids and it´s modified analogues, which also proved unsuccessful (although stable) due to quenching (accounted to the prominent electron transfer between aromatic ring of naphthalene sulfonates and iron oxide particles). Thereafter, we explored coating (ligand) molecules, which are essentially non-quenching and relatively stable. To this end, we researched on flavin analogues (flavin mononucleotide (FMN) and flavin adenine dinucleotide (FAD))- relatively simple structured molecules, which are endogenous and internalized by highly over-expressed riboflavin carrier protein (RCP) in cancer/metabolically active cells.

Based on the advantages exhibited by flavin analogues, biocompatible, fluorescent and non-polymeric FMN- and FAD-decorated USPIO (FLUSPIO and FAD USPIO) were developed as versatile MR contrast agents. Stable flavin adsorbed nanoparticles were generated by sonicating USPIO with FMN/FAD. It was then coated with GMP (guanosine monophosphate) under aqueous conditions. The core diameter, surface morphology and surface coverage of FLUSPIO and FAD USPIO were evaluated using TEM, DLS, SEM, AFM, powder XRD, EDX, and TGA. The magnetic properties of FLUSPIO and FAD USPIO were studied using MRI and SQUID. The fluorescence properties of FLUSPIO and FAD USPIO were analyzed using fluorescence- spectroscopy, microscopy and imaging. Cell viability/biocompatibility of FLUSPIO and FAD USPIO was evaluated using Trypan blue and 7-AAD staining, and TUNEL assay. *In vitro* evaluation of FLUSPIO/FAD USPIO labeling efficiency and their specificity towards RCP was studied using MRI and fluorescence microscopy. The pharmacokinetic behavior of FAD USPIO was analyzed in CD1 nude mice after its intravenous injection by fluorescence spectroscopy. The *in vivo* uptake of FAD USPIO nanoparticles was assessed using MRI in CD1 male nude mice bearing subcutaneous prostate tumors (LnCap) and duly compared with Resovist and further tested using Prussian blue staining and immunohistochemistry.

The high relaxivities (r2 and r1) and super paramagnetic behavior of FLUSPIO\FAD USPIO was confirmed by MRI and SQUID. The biocompatibility of FLUSPIO and FAD USPIO was proven via different cell viability assays and staining. FLUSPIO/FAD USPIO high efficiency in labeling cancer (PC-3, DU-145, LnCap) and activated endothelial (HUVEC) cells and their specificity for RCP was confirmed by MRI, ICP-MS and fluorescence microscopy. The *in vivo* uptake of FAD USPIO by experimental prostate carcinomas was significantly higher than the uptake of the commercial SPIO contrast agent Resovist.

In summary, of our different attempts to generate magnetoflourescent iron oxide nanoparticles for optical and MR imaging, those with FAD/FMN-adsorptive coating were most promising. These particles showed a strong RCP-mediated uptake by cancer- and activated endothelial cells and also strongly accumulated in tumors after intravenous injection. Thus, RCP-targeting may be a new and promising way to transport nanoparticles and drugs into metabolically active cells.

Kurzfassung

Der Fokus dieser Arbeit liegt im Design und der Herstellung von Eisenoxyd-Nanopartikeln zur Verwendung als Kontrastmittel für die Magnetresonanztomographie (MRT) sowie die optische Bildgebung (OI). Eisenoxyd Kerne der Größe 5-6 nm, mit niedrigem Polydispersitäts-Index wurden durch Kopräzipitations-Strategien unter wässrigen Reaktionsbedingungen hergestellt. Zunächst wurden lanthanid-dotierte Nanopartikel (Ln-USPIO) getestet, welche scheinbar aufgrund von zu geringen Mengen von, in das Eisenkristallgitter inkorporierten, Lanthaniden nicht fluoreszent waren. Dies lässt sich durch die größenbasierenden Unterschiede zwischen Lanthaniden und Eisenkationen erklären, welche die Dotierungseffizienz entscheidend verringern. Als zweites haben wir eine Fluoreszenzummantelung der Nanopartikel durch Naphthalin-Sulfonsäure und deren modifizierter Analoge verwendet, was allerdings (trotz vorhandener Stabilität) ebenfalls erfolglos blieb, da die Partikel nicht fluoreszent waren. Grund war das Quenchings der Fluoreszenz aufgrund von Elektronenübertragung zwischen den aromatischen Naphthalin-Sulfatringen und den Eisenoxyd-Partikeln. Danach erforschten wir adsoptive Coatingsubstanzen, welche nicht quenchen und relativ stabil sind. Erfolgversprechend erwiesen sich Flavinanaloga (Flavinmononukleotid (FMN) und Flavin Adenin Dinukleotid (FAD)). Dies sind relativ simpel strukturierte, endogene Moleküle, die von Krebs- oder metabolisch aktiven Zellen, über den Flavin Rezeptor (RCP) internalisiert werden. Biokompatible, fluoreszierende und nicht-polymere FMN-und FAD-beschichtete USPIO (FLUSPIO und FAD USPIO) konnten als vielseitiges MR-Kontrastmittel entwickelt. Herstellung stabiler flavin adsorbierter Nanopartikel durch Beschallung der USPIO mit FMN/FAD mit anschließender GMP-Beschichtung unter wässrigen Bedingungen.

Der Kerndurchmesser, die Oberflächenmorphologie und die Oberflächenbedeckung der FMN- und FAD-ummantelten USPIO (FLUSPIO; FAD USPIO) wurden mittels TEM, DLS, SEM, AFM, Power XRD, EDX und TGA ermittelt. Die magnetischen Eigenschaften der FLUSPIO und FAD USPIO wurden mit Hilfe von MRT und SQUID untersucht. Die Analyse der Fluoreszenzeigenschaften von FLUSPIO and FAD USPIO erfolgte durch Fluoreszenz -Spektroskopie, Mikroskopie und Bildgebung. Zellvitalität und Biokompatibilität der FLUSPIO und FAD-USPIO wurden durch Trypanblau-, 7-AAD- und TUNEL-Färbung ermittelt. Die in vitro-Evaluierung der Labelingeffizienz sowie der Spezifität bezüglich RCP wurde mittels MRT und Fluoreszenzmikroskopie untersucht. Das pharmakokinetische Verhalten von FAD USPIO wurde in CD1 Nacktmäusen nach intravenöser Injektion durch Fluoreszenzspektroskopie gezeigt. Die in vivo Aufnahme der

FAD USPIO Nanopartikel wurde in männlichen, subkutane Prostatakarzinome tragenden CD1 Nacktmäusen ermittelt. Die Aufnahme wurde mit der des klinisch verwendeten SPIO-Kontrastmittels Resovist verglichen und weiterhin getestet durch Berliner Blau- sowie immunhistologische Färbungen an Tumorschnitten.

Die hohe Relaxivität (r2 und r1), sowie das superparamagnetische Verhalten der FLUSPIO / FAD USPIO wurden mittels MRT und SQUID validiert. Die Biokompatibilität der FLUSPIO und FAD USPIO wurde durch verschiedene Zellvitalitätsassays und Färbungen nachgewiesen. Die hohe Effizienz der FLUSPIO / FAD USPIO in Bezug auf die Markierung von Krebszellen (PC-3, DU-145, LnCaP) sowie aktivierter Endothelzellen (HUVEC) und ihre Spezifität für RCP wurde durch MRT, ICP-MS und Fluoreszenzmikroskopie bestätigt. Die in vivo-Aufnahme der FAD USPIO durch experimentell erzeugte Prostatakarzinome war signifikant höher als die Aufnahme des kommerziellen SPIO-Kontrastmittels Resovist.

Zusammenfassend lässt sich sagen, dass sich in unseren Ansätzen magnetisch-fluoreszente Eisenoxyd-Nanopartikel mit FAD/FMN Beschichtung als am aussichtsreichsten erwiesen. Diese Partikel zeigten eine starke RCP-vermittelte Aufnahme durch Krebs – und aktivierte Endothel-Zellen sowie eine starke Akkumulation innerhalb der Tumoren, nach intravenöser Injektion. Die Möglichkeit des RCP-Targeting könnte demnach ein neuer vielversprechender Weg sein, um Nanopartikel und Arzneimittel in metabolisch aktive Krebszellen einzuschleusen.

Chapter 1.

Introduction and Background

Introduction

Imaging has become an indispensable tool in cancer research, clinical trials and medical practice. Biomedical imaging can be sub-divided into anatomical, functional and molecular imaging. Anatomical imaging deals with the visualization of organs or tissues, in general, with a resolution of centimetres to millimetres. Functional imaging conveys information related to physiological processes such as tissue perfusion and vessel permeability. In contrast, molecular imaging deals with the visualization of physiological processes at the cellular and molecular level[1]. Molecular imaging enables the determination of both, temporal and the spatial distribution of biological and patho-physiological processes [2].

Imaging systems can be grouped by the energy used to derive visual information (X-rays, positrons, photons or sound waves), the spatial resolution that is attained (macroscopic, mesoscopic or microscopic) or the type of information that is obtained (anatomical, physiological, cellular or molecular) respectively[3]. Macroscopic imaging systems such as magnetic resonance imaging (MRI), computed tomography (CT) and ultrasound (US) are widely used in (pre-)clinics to provide anatomical and physiological information. The increased metabolic activities of tumors can be imaged via positron emission tomography (PET) by specific accumulation of radiolabeled tracers (fluorodeoxyglucose (FDG))[4]. Quantitative kinetic data of an imaged site (tumor) can be acquired repeatedly using PET[5]. In mice and humans, rapid screening for pathologies (e.g., bladder tumors), blood flow measurement[6-8] and developing embryos examination[9] was also performed using US imaging. Angiogenesis, inflammatory response and release of therapeutic compounds rely on US detection of microbubbles that contain gas[10;11]. Bone metastasis is often imaged using CT, owing to their high spatial resolution and fast imaging time. Additionally, CT promotes hybrid anatomical imaging in combination with other imaging modalities, e.g., in PET-CT and SPECT-CT.

Characterising vascularisation, cell tracking and functional brain imaging are domains of MRI. MR spectroscopy can detect individual molecules (metabolites) in tumors without using magnetically labelled affinity molecules. When MRS is used in combination with MRI, concurrent anatomical and biochemical information are generated. Intra-operative cell labeling, mammography, diagnosis and staging in arthritis in future may be guided by optical imaging. In line with this, fluorescence mediated tomography (FMT) is useful in pre-clinical research, as it helps to quantify protein expression or localization *in vivo* without radioactive labeling.

All these imaging modalities have strengths and limitations (Table 1.1). PET is a highly sensitive, minimally-invasive technology that is ideally suited for pre-clinical and clinical imaging of cancer biology. PET is ideally suited for monitoring molecular events early in the course of a disease, as well as during pharmacological or radiation therapy and further used to acquire prognostic information and to image disease recurrences[12;13]. However, the spatial resolution of PET is comparably poor. It yields no anatomical information and is limited by radioactive isotopes with short half-lifetimes. US display high spatial and temporal resolution and provide detailed anatomical information. Additionally, US imaging is economical, and allows real-time imaging. The limitations of US imaging are user-dependency, inability to promote whole-body imaging and the restriction of targeted imaging to the vascular compartment. CT displays high spatial resolution, which is needed to visualize fine anatomical details. The radiation dose of CT, however, is not negligible and this limits repeated imaging in human studies due to health risks[14].

MR tomography serves as an exquisite tool for anatomic and functional imaging with high penetration depth and excellent spatial resolution but lacks high sensitivity for contrast agents. The two main advantages of MRI are its excellent soft tissue contrast and lack of ionizing radiation[15]. However, sensitivity of MR to contrast agents is still poor although it has been improved by recent developments in MR radiofrequency/coil technology, pulse sequences, by increasing the field strength of the scanners and by new MR contrast agents[16-22]. Optical imaging applied in microscopy, endoscopy or whole-body small-animal imaging, has a high sensitivity and spatial resolution but suffers from a low penetration depth and high background signals due to photon scattering[23-27]. Additionally, optical imaging is versatile, cost-effective, easy to handle, helps in rapid screening of molecular events and allows performing multichannel imaging via multiple probes, respectively.

Table 1.1 summarizes the spatial resolution, depth penetration, imaging time and cost of available imaging systems[28]

Technique	Resolution	Depth	Acquisition Time	Quantitative	Imaging agents	Target	Clinical use
MRI	10-100 µm	No limit	Minutes to hours	Yes	Paramagnetic chelates, magnetic nanoparticles	Anatomical, physiological, molecular	Yes
CT	50 µm	No limit	Minutes	Yes	Iodinated molecules	Anatomical, physiological	Yes
Ultrasound	50 µm	cm	Seconds to minutes	Yes	Microbubbles	Anatomical, physiological	Yes
PET	1-2 mm	No limit	Minutes to hours	Yes	^{18}F-, ^{64}Cu, ^{11}C-labelled compounds	Physiological, molecular	Yes
FMT	1mm	<10 cm	Minutes to hours	Yes	Near-infrared fluorochromes	Physiological, molecular	In development

The combination of imaging systems significantly helps in data quantification and validation, and brings together information about morphology, tissue function and molecular target expression. Platforms that combine different imaging technologies are emerging and these multimodality platforms allow for meaningful interpretation of the images in terms of its sensitivity and resolution. The true strength of a hybrid system is that high-resolution structural images that can be annotated with molecular information derived from an inherently registered data set. For example PET-MRI, MRI-CT, and MRI-FMT are widely used currently to extract relevant information pertaining to diseases such as tumor or arthritis etc.

Based on the afore-mentioned advantages of combining imaging systems, the combination of MR and fluorescence imaging constitutes an attractive concept for preclinical research. In line with this, MRI is favourably suited for whole body imaging, e.g., tumor staging, while optical imaging has its strengths in characterizing superficial tissues or for diagnosis during surgery (endoscopy, laparoscopy and histological validation). Therefore, combining optical imaging with MRI provides an accurate anatomical reference for fluorescence imaging data and thereby enables the correlation of molecular with high quality structural/functional information[29]. However, progress in the multi-modality imaging systems can be extensively made if there is a parallel effort to synthesize and develop multimodal contrast agents. Development of dual/tri-modal contrast agents can considerably improve the utility of multimodality imaging *per se* and can end up in further advancement in

this area. To this end, the development of dual probes valid for MRI and optical (bi-modal) imaging is an attractive task that might help to improve the sensitivity and spatial resolution of the images obtained from both modalities and consequently help in the co-validation of results gained from different image data sets respectively.

1.1. Multimodal contrast agents

Multimodal contrast agents were synthesized using inorganic nanoparticles, polymers, liposomes, and rare earth metals (lanthanide chelates) as the backbone. Their physico-chemical properties can be tuned to impart more specific moieties (e.g., fluorescent dyes (optical imaging), radioactive tracers (PET, SPECT imaging) which may facilitate multimodal imaging. The functional units which are commonly used to generate (molecular) multimodal contrast agents comprise of different endogenous coating molecules, antibodies and peptides (Figure 1.1.1).

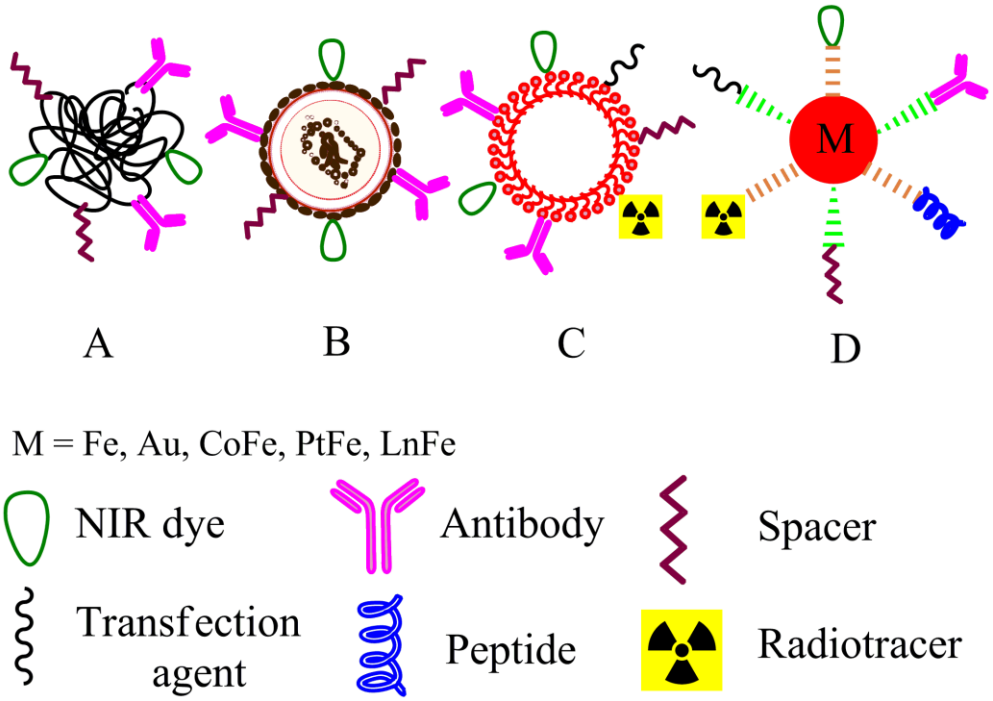

Figure 1.1.1. Schematic diagram shows different types of platform used for designing and generating multimodal imaging probes. Polymers (A), viral vectors (B), liposomes (C) and inorganic nanoparticles (D) serve as a basic platform to generate multifunctional probes by functionalization with NIR dye, antibody, peptides, spacers, transfection agent and radiotracer which makes them suitable for multimodal imaging respectively.

Nanoparticles generated using organic materials like liposomes, micelles and polymers have been explored in addition to inorganic nanoparticles as contrast agents for molecular imaging purposes[30;31]. Most of the generated organic materials were used as a carrier for metallic nanoparticles by means of encapsulation and as a platform for conjugation of fluorescent dyes, and as coordination compounds. Most organic materials that can be easily and conveniently processed as nanoparticles lack relevant imaging qualities like paramagnetism and fluorescence with few exceptions such as dye-based contrast agents used for optical imaging. Some of the organic nanomaterials such as conjugated polymers display tunable fluorescence properties suitable for optical imaging. However, there could be problems arising due to synthesis and purification of polymer-based materials and further, elimination of organic materials from the body might be slow. Therefore, the inorganic nanoparticles have gained much more momentum as versatile contrast agents for molecular imaging (different modalities) due to their inherent properties (magnetism: (Ultrasmall) Super Paramagnetic Iron Oxides ((U)SPIO)), fluorescence (quantum dots (QD)) compared to organic nanomaterials. However, the toxicity of inorganic nanoparticles is a crucial issue that could hinder their application in biomedical imaging e.g., QDs might become cytotoxic due to the oxidative and/or photolytic destruction of their surface coatings[32]. Further, it is important to use a minimal dose of inorganic nanoparticles for imaging in order to avoid possible *in vivo* toxicity.

1.1.1. Contrast agents in MRI

There are two different types of MR contrast agents which are widely being used in clinics based on their contrast enhancement properties in tissues. They are the Gd-based paramagnetic species used for generating positive T_1 contrast enhancement and the iron oxide nanoparticle-based superparamagnetic species for negative T_2 contrast enhancement (cuts down the signal enhancement), respectively. Gd(III) complexes are used as versatile T_1 contrast agent in clinics and they are thermodynamically stable, water-soluble and highly paramagnetic and display high relaxivity (r1). However, these Gd-based systems suffer from relatively short pharmacokinetic profile (short accumulation time) in the vascular system, thereby reducing considerably the MR imaging time. Therefore, nanoparticles-based contrast agents can be efficiently employed for MR imaging as they internalize into the cells in large amounts when conjugated with specific ligands and thereby increase the MR imaging time. In order to modulate the pharmacokinetic properties of Gd-based systems, several attempts were made to tag the paramagnetic species (Gd(III)) to polymers, dendrimers, polypeptides,

polysaccharides, liposomes and further, chelated Gd(III) ions were also anchored onto the surface of nanoparticles).

Iron oxide nanoparticles with intrinsic superparamagnetic properties exhibit a negative MR contrast enhancement, and are used as versatile T_2 contrast agents in clinics e.g., Ferridex and Combidex (iron oxide nanoparticles coated with polysaccharides). However, clinical applications of these T_2 contrast agents are limited as they suffer from negative contrast effect and magnetic susceptibility effects respectively[33].

1.2. Magnetic Resonance Imaging (MRI)

The superparamagnetic behavior exhibited by magnetic nanoparticles (at critical size) is exploited for MR imaging in biomedical applications. Resonance is an energy coupling that causes the individual nuclei, when placed in a strong external magnetic field, to selectively absorb, and later release, energy unique to those nuclei and their surrounding environment. The magnetic field gradients are used to localize the NMR signal and to generate images that display magnetic properties of the proton, reflecting clinically relevant information.

1.2.1 Relaxation

Relaxation of the protons under the influence of the external magnetic field occurs after the application of RF pulse, by releasing the absorbed energy and return to their original equilibrium state. There are two major processes contributing to their return to the equilibrium state: T_1 and T_2 relaxation times[34].

T_1 relaxation

T_1 termed as "longitudinal" relaxation time, is a measure of how long a substance needs to regain its longitudinal magnetization following an RF pulse. T_1 relaxation time represents the correlation between the frequency of molecular motions and the Larmor frequency. The frequencies of small molecules (e.g., water) and large molecules (e.g., proteins) are significantly different from Larmor frequency and thereby have long T_1. Contrarily, cholesterol (a medium-sized molecule), has natural frequencies similar to those employed in MRI, thereby it has a short T_1. The T_1 relaxation time of the MR contrast agents

can decrease due to the interaction between the unpaired electrons in the paramagnetic iron (or Gd ions) and the protons in water.

T_2 relaxation

T_2 termed as "transverse" relaxation time, is a measure of how long the resonating protons of a substance can be coherent or rotated after a 90° RF pulse. Depending on alignment of protons in response to the external magnetic field (align with/against), the local regions of increased /decreased magnetic fields can be created by the fluctuating magnetic fields of the substance. Subsequently, after the 90° RF pulse the protons can lose their coherence and transverse magnetization resulting in T_2 relaxation of the protons.

T_2* relaxation

T_2* relaxation is the loss of signal seen with dephasing of individual magnetizations. It is characterized macroscopically by loss of transverse magnetization at a rate greater than T_2. It is caused by magnetic field inhomogeneity and occurs in all magnets.

1.2.2. Pulse sequences

MR relies on three major pulse sequences: spin echo, inversion recovery, and gradient recalled echo. When these are used in conjugation with localization methods (i.e. the ability to spatially encode the signal to produce an image), "contrast-weighted" images are obtained. Spin echo (SE) sequences generally produce the best quality images but they take a relatively long time. Inversion recovery (IR) sequences can produce excellent T_1-weighted images of tissues with relatively long TR (Repetition times) by selectively suppresing the T_1 contributions from fluid or fat. Gradient echo (GE) sequences can produce images with shorter TR`s than SE sequences, so they have shorter scan times. However they are highly depending on the quality of the main magnetic field as well as on timing parameters[35].

T_1-weighted images

T_1-weighted images can be produced using either the SE or the GE sequence. A "T_1-weighted" spin echo sequence is designed to produce contrast based on the T_1 characteristics of tissues by de-emphasizing T_2 contributions. This is achieved with the use of a relatively **short TR** to maximize the differences in longitudinal magnetization during the

return to equilibrium, and a **short TE** (Echo time) to minimize T_2 dependency during signal acquisition.

T_2-weighted images

T_2-weighted contrast can be produced by using SE sequences. SE T_2 images require **long TR** and **long TE**, so they take longer to acquire than T_1-weighted images (scan time depends on TR).

T_2* weighted images

GE sequences are used to generate T_2* weighted images based on the effects which originates from imperfect magnetic field: a perfectly uniform magnetic field can't be produced, as even the patient would make it imperfect due to *susceptibility* effects. Air pockets (sinuses or intestines), dense bone (skull base), and iron-rich blood breakdown products (met-haemoglobin or haemosiderin) all change the main magnetic field in their immediate vicinity, so tissues around such inhomogeneities will experience different magnetic fields. In a GE sequence, the combined effect of T_2 and magnetic field inhomogeneities is observed. This relaxation is called the 'apparent' relaxation time and in short called T_2*.

1.2.3. Advantages of MRI

The advantage of using MRI is that it produces sectional images of equivalent resolution in any projection across multiple planes without moving the patient. Therefore, MRI is considered as a versatile diagnostic tool for planning surgical treatments. Additionally, a number of advanced contrast imparting agents and techniques have emerged that render MRI a highly versatile imaging tool in clinics[36;37]. Novel contrast agents that modulate T_1 and T_2 relaxivities, combined with molecular targeting strategies provided by advances in nanotechnology, have yielded a significant progress in developing MRI as a platform for visualizing cellular and subcellular events[38;39].

1.3. Inorganic Nanoparticles as contrast agents

Inorganic nanoparticles including iron oxide, rare earth metal-doped, rare earth metal and gold nanoparticles along with semiconductor quantum dots are usually desired for generating contrast agents for different imaging modalities as they explicitly display electronic, optical, scattering, x-ray attenuation and magnetic properties compared to the non-metallic nanoparticles (traditional counterparts) e.g., Si-based nanoparticles. Inorganic nanoparticles could be tailored and tuned by controlling the composition, geometry and structure of the nanoparticles. Table 1.2 summarizes inorganic nanoparticles which are explored as contrast agents for (pre-)clinical molecular imaging purposes.

Table 1.2. Inorganic nanoparticles-based contrast agents for molecular imaging (adapted from Eun Chul Cho et.al, Trends in Molecular medicine, 2010)[40].

Nanoparticle type	Imaging modality
Semiconductor quantum dots	Fluorescence imaging
Magnetic nanoparticles	MR imaging
Gold colloids	Photoacoustic tomography
	Surface enhanced Raman spectroscopy
	Multiphoton luminescence imaging
	X-ray (Computed tomography)
Rare-earth doped nanoparticles	Luminescence imaging
	MR and near-infrared imaging

The inorganic nanoparticles provide opportunity for developing new imaging agents (multimodal) based on surface engineering of their composition, crystal structure, size, and shape, respectively. The surface of the inorganic nanoparticles were covered with coating molecules like silica, (bio-)polymers, non-polymeric molecules, to increase their stability under physiological conditions and to provide a platform for further functionalization with components that will generate multimodal imaging agents (Figure 1.1.2). The surface modification should be performed to preserve the imaging properties (like fluorescence, magnetism). The cellular uptake of inorganic nanoparticles could be enhanced by conjugating them to transfection agents such as protamine sulphate, poly-lysine, poly-arginine and HIV-tat, thereby facilitating their high accumulation in the cancer cells and tumors. The specificity of the probes for receptors expressed (*in vitro* and *in vivo*) could be modulated by attaching target specific antibodies, peptides. During conjugation, the structure and conformation of

macromolecules (proteins and antibodies) should be preserved from denaturation[41-43]. Polyethylene glycol (PEG) spacers with different molecular weights are coupled to inorganic nanoparticles to prolong their circulation time in blood thus facilitating imaging for a longer period of time. The interaction between a targeting ligand and the receptor on the cell surface is sensitive and influenced by their chemical and molecular structures[44;45].

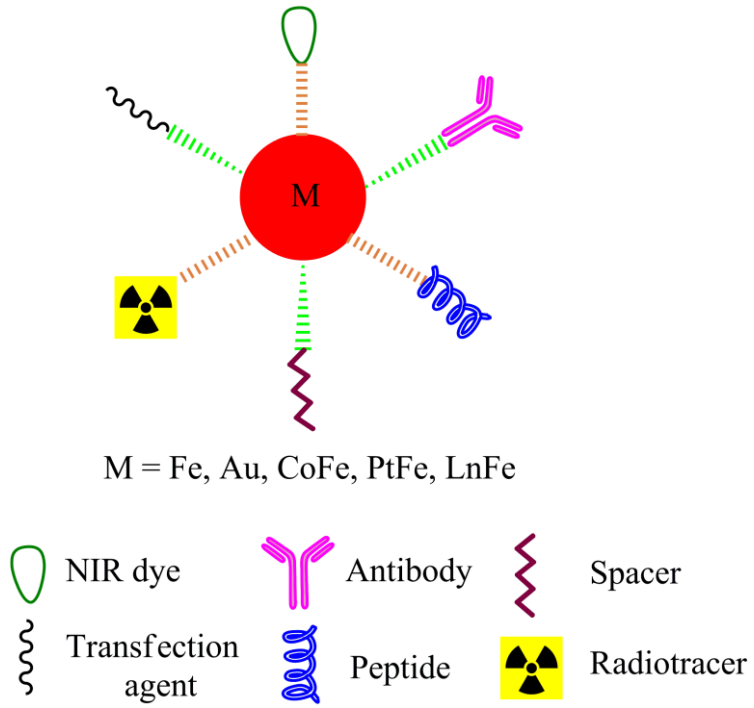

Figure 1.1.2. Schematic diagram of a multimodal contrast agent. Metallic nanoparticles (Fe, Au, CoFe, PtFe and LnFe) can be used as platform for generating multimodal contrast agents due to their useful physico-chemical properties. Radiotracer incorporation helps in SPECT, PET imaging. Optical imaging is facilitated by conjugation with NIR dyes. Specific targeting is achieved by functionalization using target specific antibodies and peptides. Cellular uptake of the multimodal contrast agents is enhanced by adding a transfection agent. The *in vivo* pharmacokinetics of nanoparticles can be tuned by introducing spacers like polyethylene glycol with different molecular weights respectively.

1.3.1. Iron oxide nanoparticles

Iron oxide nanoparticles find application in different fields such as magnetic data storage, bio-sensing, (bio-)medical applications (targeted drug delivery), and as contrast agents in MRI. The MR imaging applications require the nanoparticles to exhibit high magnetization values, a size smaller than 100 nm with a narrow particle size distribution. Iron oxide nanoparticles, such as ultrasmall superparamagnetic iron oxides (USPIO, 50 nm (hydrodynamic diameter)) and superparamagnetic iron oxides (SPIO, 50-500 nm (hydrodynamic diameter)), are used as agents that cause negative contrast effects (decreased MRI signal) on T_2 and T_2*-weighted MR images[46]. The major challenges in developing iron

oxide nanoparticle-based versatile MR contrast agents are coating, surface functionalization with specific ligands (for tumor accumulation) and long circulation of the iron oxide-based nanoparticles in the blood.

1.3.2. Biomedical applications of magnetic nanoparticles

Iron oxide nanoparticles are intensely used in MR-cellular labeling and cell tracking studies. The contrast enhancement achieved in MR depends on the size of the nanoparticles used and the molecular imaging is facilitated by using target specific ligands conjugated nanoparticles.

1.3.2.1. Cellular labeling (MRI)

The ability to load iron oxide nanoparticles (μM Fe) in cells via cell-permeable peptide or transfection agents, in combination with negative surface charged magnetic nanoparticles is used to label and track cells *in vivo* by MRI[47;48]. The first cellular imaging studies were performed with unfunctionalized iron oxide nanoparticles for labeling leukocytes, lymphocytes, etc.[49-52]. Cells loaded with nanoparticles can be tracked using MRI with a resolution equal to size of a single cell[53]. To increase the cellular uptake of magnetic iron oxide nanoparticles, they are conjugated with peptides, vitamins e.g., folic acid-coated magnetic particles for targeting folate receptors[54;55]. Bulte has used MRI to provide information on the location and migration of cells after transplantation or transfusion which requires magnetic prelabeling of the cells[56].

1.3.2.2. Molecular Imaging

Herschman defined molecular imaging as "non-invasive, quantitative and repetitive imaging of targeted macromolecules and biological processes in living organisms"[57]. Wickline stated that molecular imaging can be used "to improve diagnostic accuracy and sensitivity by providing an *in-vivo* analogue in immunocytochemistry or *in situ* hybridization"[58]. Molecular imaging employs contrast agents that are used to identify particular biomarkers or pathways with high sensitivity and selectivity[59]. The contrast agents would ideally accumulate (selectively) at the target site and would interact with the target physically, (bio-)chemically and thereby altering the attained image contrast. Molecular imaging approaches using magnetic nanoparticles was used to detect apoptosis by MRI[60]. The therapeutic response from tumor cells can be studied using MRI based on MR image

contrast that reflects the morphological features of apoptosis, such as cell shrinkage and membrane blebbing[61]. Magnetic nanoparticles accumulate inside the tumors either unspecifically through the enhanced permeation and retention (EPR) effect (passive targeting) or specifically (active targeting).

1.3.2.3. Passive targeting

The difference in vasculatures between the normal and cancerous tissues plays a crucial role towards the accumulation of the nanoparticles in solid tumors. Endothelial cells in normal tissues are aligned and tightly packed, whereas those of solid tumors are relatively leaky[62-64]. Due to their large sizes, the magnetic nanoparticles circulating in the blood stream are unable to extravasate in normal tissues (endothelial cells). However, they are readily taken up by the solid tumors due to the leaky blood vessels. This type of selective accumulation of the magnetic nanoparticles in solid tumors is due to the EPR effect or passive targeting which is extensively used for systemic delivery of nanoparticles and macromolecular drugs[65-67]. EPR based passive targeting of iron oxide nanoparticles is highly dependent on the sizes and surface modification of the nanoparticles as well as on the pore cutoff size of the endothelial boundary in different tumors. Smaller nanoparticles display relatively longer circulation time in the blood stream compared to larger nanoparticles, which has been applied to study the increase in sensitivity in perfusion imaging e.g., organ perfusion imaging[68;69], functional MRI (fMRI)[70;71]

1.3.2.4. Specific targeting

To increase the accumulation, the efficiency in delivery and to retain the nanoparticles inside the cancer cells, they should adhere to specific receptors over-expressed on the surface of the cancer cells. The highly specific and selective interaction between the targeting ligand and the receptor is termed as active targeting, which in combination with passive targeting leads to the intense accumulation of nanoparticles in cancer cells/tissues[72]. Active targeting of the endothelial inflammatory cells was achieved using E-selectin functionalized magnetic nanoparticles[73]. Similarly, Montent, et al., employed cRGD coupled-CLIO nanoparticles for active targeting of integrins on BT-20 tumor models[74;75].

1.4. In-vivo fluorescence imaging

Three-dimensional fluorescence images of the internal structures of humans or small animals can be generated by *in-vivo* fluorescence imaging techniques. In-vivo imaging based on fluorescence could be traced to the suggestion made by Chance and co-workers who demonstrated that images could be obtained from the diffusive migration of photons in scattering tissues[76-78]. A strong absorption, high scattering and low penetration of photons in the tissues (become translucent) are prevalent at wavelengths below 650 nm (Figure 1.1.3). The translucent tissue properties could be seen upon trans-illumination of a mouse using a red light at 670 nm[79]. When light with long-wavelength (680 – 850 nm) pass through tissues, the light is anticipated to migrate in a diffusive manner similar to molecules in the gas phase. However, the absorbed photons move in a straight line until they are scattered due to tissue specific characteristics. The extent of light scattering in tissues is described by the scattering coefficient μ_s. The light absorbed through the tissue could be expressed as the absorption coefficient μ_a. Different types of tissues and different regions of tissue display different values of μ_s and μ_a, and affect the photon migration (rate and distance) in tissues. The concept of photon migration imaging (PMI) was used to measure spatially dependent transport of photons in tissues. The problems associated with PMI technique are numerous scattering and the limited contrast from different regions of tissues, which can be eliminated by using fluorescent dyes such as indocyanine green[80;81].

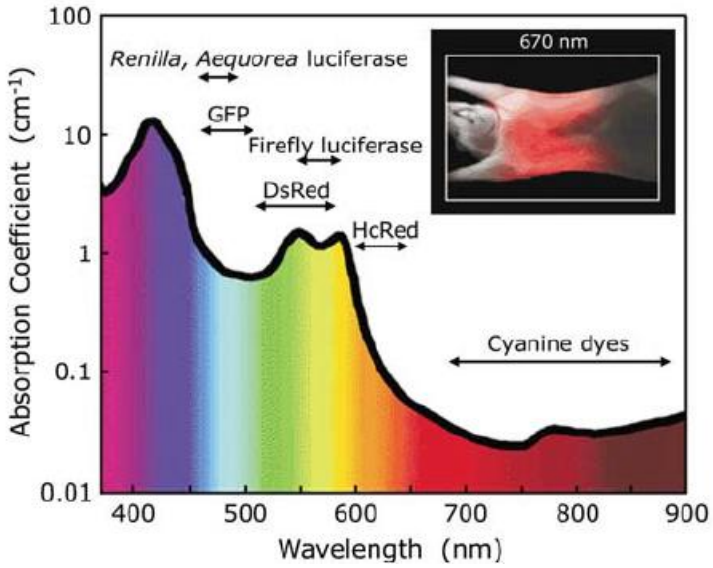

Figure 1.1.3. Absorption coefficient of a typical tissue. The insert shows the trans-illumination of a mouse at 670 nm [adapted from Weissleder, Ntziachristos, Nature Med, 2003].

1.4.1. Optical properties of tissues

The design of fluorescent probes for clinical applications is determined partly by considering the influence of the optical properties of water and tissues on fluorescence emission of a fluorophore. In general, the auto fluorescence emerging from tissues or any biological sample is usually lower for longer excitation wavelengths and further the use of longer wavelengths (>650 nm) also prevent light (photon) absorption by haemoglobin and melanin (Figure 1.1.4).

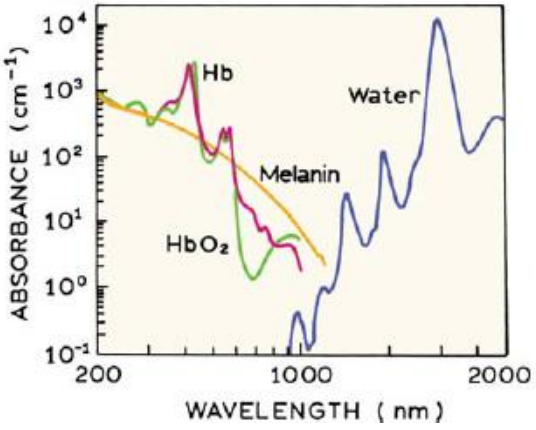

Figure 1.1.4. Optical absorbance of tissues including water, melanin, and haemoglobin[82].

The near-infrared (NIR) spectral window (650 to 900 nm) is suitable for *in vivo* fluorescence imaging investigations as it takes advantage over the low absorbance of tissue chromophores such as oxy- and deoxy-haemoglobin, water, melanin and fat (Figure 1.1.4). At NIR wavelengths, $\mu_s > \mu_a$ compared to lower wavelengths (<650 nm). The current state of the art is that majority of *in vivo* fluorescence imaging approach reported was based on planar detection of fluorescent light emerging out of the tissues. This planar fluorescence imaging approach has shown limitation in deriving quantitative information. The non-linearity problem related to depth at which the fluorescent signal is generated could be avoided by using fluorescence molecular tomography (FMT), with improved signal quantification[83-85].

1.4.2. Advantages of fluorescence imaging

Fluorescence based-imaging techniques are known to possess several attractive characteristics, such as:

i. The ability to concurrently resolve several distinct biological targets by utilizing fluorophores that emit at different spectral bands (wavelengths)

ii. Offers high flexibility in developing and utilizing fluorescent reporters (fluorophores) for diverse cellular processes and molecular pathways

iii. High detection sensitivity reaching limits in the sub-picomole range for common organic fluorochromes (small animal imaging), and even to higher sensitivity for imaging superficial activity (e.g., in endoscopic and intraoperative applications)

iv. Provides high resolution images for imaging events at superficial depths from fluorescence based-microscopy (epifluorescence, confocal, two photon, histopathological correlation etc.) techniques

1.4.3. Fluorescence lifetimes and Quantum yields

The fluorescence of any biological molecule (fluorophore) is characterized by its quantum yield and its lifetime. The fluorescence quantum yield is the ratio of the number of photons emitted to the number absorbed. Substances with the largest quantum yields (approaching unity), such as rhodamines display the brightest emissions. The lifetime determines the time available for the fluorophore to interact with or diffuse in its environment, and hence the information (lifetime) is available from its emission. The emissive rate of the fluorophore (Γ) and its rate of non-radiative decay (k_{nr}) to ground state were determined. The rate constants Γ and k_{nr} both depopulate the excited state of the fluorophores. The fraction of the fluorophores that decay through emission, and hence the quantum yield is given by the following expression

$$Q = \Gamma/\Gamma+k_{nr} \qquad \text{Equation 1}$$

The quantum yield can be close to unity if the radiationless decay rate is much smaller than the rate of radiative decay, that is $k_{nr} < \Gamma$.

The lifetime of the excited state is defined by the average times the molecule spends in the excited state prior to its return to the ground state. Generally, fluorescence lifetimes are around 10 ns. The lifetime of a fluorophore is given by

$$\tau = 1/\Gamma+k_{nr} \qquad \text{Equation 2}$$

Heavy atoms such as iodine typically result in shorter lifetimes and lower quantum yields.

1.5. Fluorophores

Fluorophores are divided into two general classes, namely intrinsic and extrinsic fluorophores. Intrinsic fluorophores are those that occur naturally (fluorescent biomolecules). Extrinsic fluorophores are those which are added to a sample of interest that does not display the desired spectral properties (organic dyes for fluorescent labeling of peptides, antibodies etc.).

1.5.1. Intrinsic fluorophores

Intrinsic fluorophores are the biological molecules which exist in cells (normal and malignant), tissues, organs, animal models and exhibits relatively weak endogenous fluorescence. These endogenous fluorophores include amino acids, structural proteins, enzymes and co-enzymes, vitamins, lipids and porphyrins. The excitation maxima range of these endogenous fluorophores lies between 250 and 450 nm, while their emission maxima range lies between 280 and 700 nm (Table 1.3). Intrinsic fluorescence from protein are known to originate from the aromatic amino acids[86-88] such as tryptophan (trp), tyrosine (tyr), and phenylalanine (phe). The indole groups of the tryptophan residues are the dominant source of UV absorbance and fluorescence emission in different proteins. The weak fluorescence in proteins occurs owing to the native form of the tryptophan amino acid residues and further, its fluorescence could be enhanced on denaturation of the protein. Thus, the change in fluorescence of tryptophan could ideally serve as a valid fluorescence-based technique to study the conformational changes involved in the protein.

Among other known biological molecules present in cells/tissues, one could also observe fluorescence contribution from reduced nicotinamide adenine dinucleotide (NADH) and from oxidized flavins (FAD, flavin adenine dinucleotide, and FMN, flavin mononucleotide) respectively (Figure 1.1.5). The isoalloxazine rings of Rf, FMN, and FAD absorb light in the visible range (450 nm) and display emission around 535 nm. The oxidized forms of flavins are fluorescent, in contrast to the reduced forms of NADH (fluorescent). Typical fluorescence lifetimes for FMN and FAD are 4.7 and 2.3 ns. The quenching of flavin fluorescence in FAD occurs due to the complex formation between the flavin and the adenosine moieties[89]. The latter process is referred to as static quenching. Most of the auto fluorescence observed from different cells are due to the presence of inherent NADH and flavins[90;91].

Table 1.3. Excitation and emission maxima of some of the endogenous fluorophores (adapted from Ramanujam, Neoplasia, 2000)

Endogenous fluorophores	Excitation maxima (nm)	Emission maxima (nm)
Tryptophan	280	350
Tyrosine	275	300
Phenylalanine	260	280
Collagen	325, 360	400, 405
Elastin	290, 325	340, 400
FAD, flavins	450	535
NADH	290, 351	440, 460
Vitamin B12	275	305
Phospholipids	436	540, 560
Porphyrins	400-450	630, 690

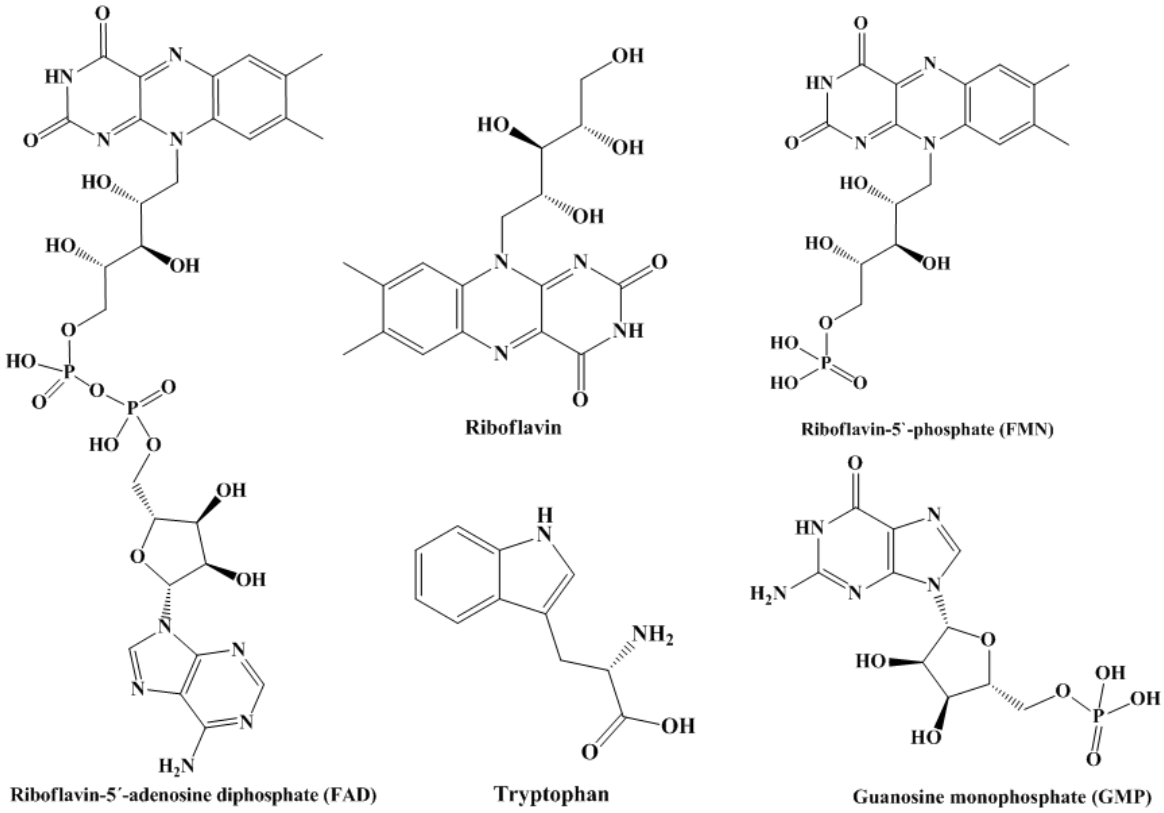

Figure 1.1.5. Schematic diagram of few intrinsic biochemical fluorophores.

The fluorescence lifetime measurements of flavins (FMN, FAD) could be explained in terms of two different configurations (open or stacked configuration) of flavins in solution as shown in Figure 1.1.6. The nature of the flavin quenching by the adenine moiety was studied by fluorescence intensity decay measurements. The fluorescence intensity decay of the flavin alone (FMN) displayed a single exponential with a decay time of 4.89 ns. However, FAD displayed a double-exponential decay with a decay time of 3.38 ns and of 0.12 ns, respectively. The observed short decay component (0.12 ns) of FAD was assigned to the stacked forms, thus facilitating the calculation of different fraction of FAD present in the stacked and open configurations. The long fluorescence lifetime of 3.38 ns might be due to the dynamic quenching of the flavin by the adenine moiety (Figure 1.1.6)

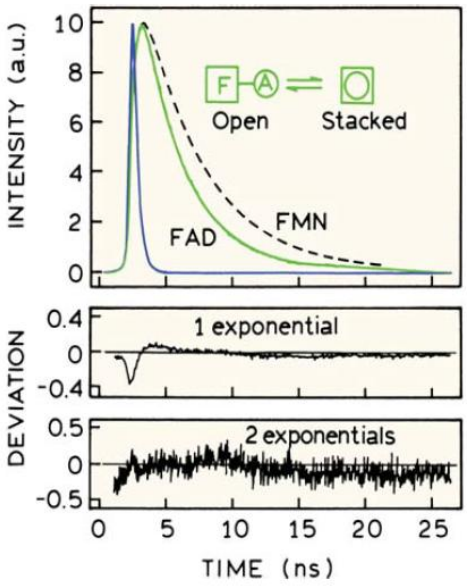

Figure 1.1.6. Intensity decays of FAD and FMN at pH 7.5, 3 ºC. Also shown is the laser pulse profile. The deviations are for fits to the FAD intensity decay (adapted from Visser AJWG, Photochem Photobiol 1984).

Guanosine monophosphate (GMP) is one of the most important nucleotide which is incorporated into DNA and RNA during hybridization in order to increase their stability and to preserve the imparted genetic informations. The aromatic moiety of GMP absorbs light in UV region and displays weak emission around 350 nm. Photo induced electron transfer that occurs (by UV light) in GMP leads to quenching of its fluorescence and result in loss of hybridization in DNA. GMP exists in three different forms like cyclic GMP (cGMP), di- and tri- phosphates (GDP, GTP), respectively. The human guanylate binding proteins (hGBP) which belongs to the family of GTPases enzymes are actively involved in hydrolyzing the different forms of guanosine triphosphate (GTP) into a mixture of GDP and GMP with unequal ratios[92]. The quenching effect exhibited by the guanine moiety in dimer GMP (dGMP) on different fluorophores is used to design molecular beacons for monitoring

different molecular and cellular processes[93] and in addition it was also applied to RNA based structural studies[94]. Further, GMP serves as an efficient template for different nanomaterials synthesis, and enhances the electronic properties of the generated nanomaterials[95]. Furthermore, GMP undergoes self-assembly with different transition metal ions via chelation to form new nanomaterials[96].

1.5.2. Extrinsic fluorophores

Based on their emission wavelength (UV, visible and NIR), the extrinsic fluorophores were selected as fluorescent agents for the detection of various cellular and sub-cellular events. Extrinsic fluorophores are exogenous fluorophores which are widely being used to label a target tissue, protein, and biomolecules, and further, used to assess changes at the molecular level based on fluorescence. The advantage of using exogenous fluorophores is due to their known properties i.e. photophysical and pharmacokinetic properties, used for labeling biomolecules and for delineating the malignant tissues from normal ones [97]. The exogenous fluorophores display fluorescence with high intensity compared to their endogenous counterparts. Some exogenous fluorophores were used as DNA specific labeling agents that facilitate the study of the conformational changes and molecular events that occur in the DNA by fluorescence technique. A wide variety of organic dyes like acridines, ethidium bromide, 4´,6-diamidino-2-phenolindole (DAPI) and other planar cationic species bind spontaneously to DNA which are often used to visualize and identify chromosomes. The macromolecules are fluorescent labeled for different biological application using extrinsic probes such as dansyl chloride DNS-Cl (1-dimethylamino-5-naphthylsulfonyl chloride) and fluorescein isothiocyanate (FITC). The sulfonyl (DNS-Cl) and isothiocyanate (FITC) groups of these probes react with free amino groups of the macromolecules (proteins), and results in proteins that display blue (DNS) or green (FITC) fluorescence (Figure 1.1.7).

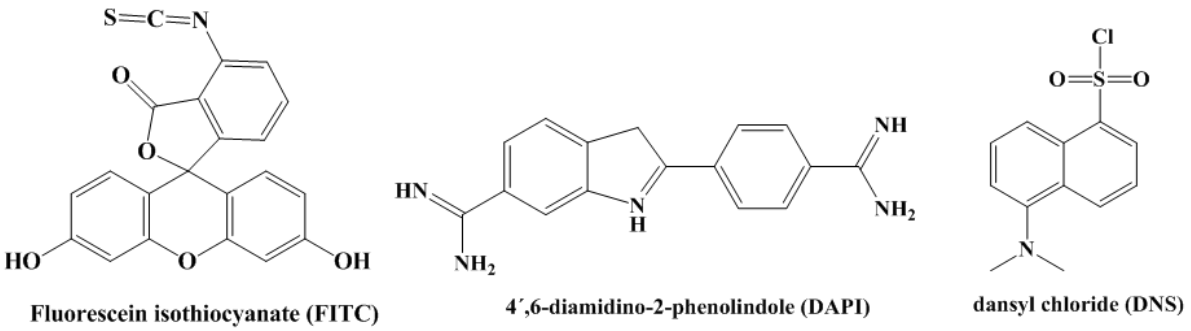

Figure 1.1.7. Fluorophores for covalent labeling of DNA and biomolecules.

To this end, the first type of exogenous dyes that were selected based on emission wavelengths are the ones with UV fluorescence e.g., naphthalene sulfonates. Naphthalene disulfonic acids are highly water soluble due to the inherent sulphonic acid groups and their absorption and emission occur in the UV spectral region (200-400 nm). These naphthalene sulfonates are usually coupled to specific ligands, proteins, dyes, sensors, nanomaterials, in order to make them hydrophilic and further used for sensing the biologically relevant targets and mechanisms using fluorescence. Azo compounds based on amino and hydroxyl naphthalene sulfonates are used as metal chelators (dyes), acid-base indicators and as histological stains[98-101]. H-acid (Figure 1.1.8) is one of the most important dye intermediates and often used in chemical and textile, as well as in the pharmaceutical industries for the direct synthesis of acidic, reactive and azoic dyes[102;103]. Non-symmetric derivaties of cholesterol linked to H-acid acts as a small molecule based selective inhibitors for HIV-1 RT (reverse transcriptase) by facilitating the inhibitory effect on catalytic activity of RNA-dependent DNA polymerases (RDDP)[104]. ANDS (Figure 1.1.8) conjugated oligosaccharides (mono- to hexa- saccharides) are used in fluorimetric assays due to the availability of two fixed negative charges (from sulphonic acids) on the naphthalene moieties and these conjugates are analyzed with high sensitivity using capillary zone electrophoresis[105;106]. ANDS is also employed as a reagent in a colorimetric method in which the proteolytic degradation of feed proteins by rumen microorganisms are determined using ANDS fluorescence[107]. Further, ANDS is used in a facile, accurate and sensitive non-radioactive method for detection and analysis of lipid-linked oligosaccharides (LLO) via fluorophore-assisted electrophoresis of carbohydrates[108]. Furthermore, ANDS is used as a labeling agent for capillary zone electrophoresis for simple and mild determination of fatty acids (with C_1-C_{10}) via the condensation reactions respectively[109].

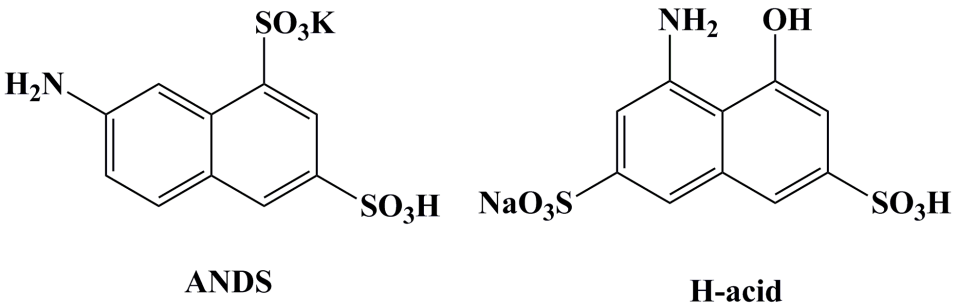

Figure 1.1.8. Schematic diagram shows the structures of 7-amino-1,3-naphthalene disulfonic acid (ANDS) and 4-amino-5-hydroxy-2,7-naphthalene disulfonic acid (H-acid) respectively.

The second type of exogenous dyes that was selected based on emission wavelengths is the one with NIR fluorescence e.g., cyanine dyes. The most commonly used dyes that emit at long-wavelengths are the cyanine dyes i.e. Cy-3, Cy-5 and Cy-7, which is predominantly used for *in vivo* optical imaging techniques. These dyes display absorption and emission wavelengths above 550 nm[110-112]. The cyanine dyes typically display a small Stokes shift, with the absorption maxima (about 30 nm) blue shifted from the emission maxima. Charged side chains are incorporated into these dyes in order to improve their water solubility and to prevent self-association of these dyes, which often results in self-quenching, respectively. The cyanine dyes with reasonable photostability are widely used for optical imaging, histological analysis (in conjugation to the antibodies) and for fluorescence microscopy techniques.

Rare earth metal ions were also employed as exogenous agents to induce fluorescence for various biological applications (e.g., lanthanides). Lanthanides are widely used in high sensitive detection of immunoassays, by utilizating its infra-red fluorescence emission [113;114]. The lanthanides are unique fluorescent metals that display emission in aqueous solution with decay times ranging from 0.5 to 3 ms[115-118]. Emission of the lanthanide ions are known to occur due to transitions that involve 4*f* orbitals, which usually are spin- and parity forbidden. As a result the absorption coefficients of these transitions are very low (<10 $M^{-1}cm^{-1}$), and the emissive rates are slow, thus leading to long fluorescence lifetimes for lanthanides. The lanthanide (metal-)ions behave like independent atoms and display line spectra characteristics specific for the metal atoms. Due to the lanthanides weak photon absorptions, they are usually not excited directly, but rather excited via the chelated organic ligands that contain a fluorophore. The excited fluorophore must transfer the absorped energy through its emission, to match the energy required for the lanthanide excitation. The chelators complexed to the lanthanide increase the quantum yield of the lanthanide by displacing the bound water molecules that act as fluorescence quenchers. Further, the chelator also acts as a versatile platform to bind the lanthanide metal ion to a biomolecule (such as peptides, antibodies), using standard coupling chemistry. Therefore, the excitation spectrum obtained from the lanthanide-chelator complex reflects only the absorption spectrum of the bound ligand (chelator) and not that of lanthanide. The lanthanides suffer from several limitations, the chelator (ligand) with conjugated fluorophores is required for its excitation and the absence of polarized emission prevents it from fluorescence-based anisotropy measurements.

1.5.3. Contrast agents for MR and Optical imaging

Iron oxide nanoparticles are widely explored in order to develop a nanoparticle-based system that is active to both MR and optical imaging techniques. These nanoparticles when reduced to a critical size, the prevalent multiple magnetic domains change into a single domain and cause the spins of the nuclei to flip under an external magnetic field (magnetic moments), thus leading to a superparamagnetic behavior and an active MR signal[119]. The magnetic properties (relaxivities) displayed by the iron oxide nanoparticles are highly dependent on its core size as illustrated in Table 1.4. In MRI, the administration of exogenous imaging agents enhances the quality of the acquired anatomical data and provides additional information on physiological parameters[120]. Iron oxide nanoparticles are relatively non-toxic compared to other inorganic nanoparticles and accumulate intensely in the biological targets[121;122]. The size of these nanoparticles and surface modifications are regulated to display reasonable circulation times and to arrive at the tissue targets by avoiding the organism´s particle filter (i.e. reticulo-endothelial system).

Contrast agents generated for optical imaging are based on NIR fluorescent dyes, which are usually coupled to target-specific ligands and carriers such as antibodies, proteins, peptides, nanoparticles or polymers, and small molecules. However, they suffer from certain limitations (like quenching, unspecific uptake) due to the bulky nature of the dye molecules[123;124]. Combined MRI and optical agents are being explored due to their ability to enhance contrast (complementary information) in both modalities[125] e.g., as they could be used for preoperative imaging and intraoperative tumor delineation,[126;127] on the basis of the key features that occur during *in vivo* nanoparticle metabolism and due to their imaging properties (i.e. optical and magnetic), respectively.

Table 1.4. T_2 relaxivities of magnetic nanoparticles (adapted from Eun Chul Cho et.al, Trends in Molecular medicine, 2010)

Types of magnetic nanoparticles	**Core size (nm)**	**T_2 relaxivities [$mM^{-1}s^{-1}$]**
USPIO, transferrin-coated	5	52.1
Cross-linked iron oxides (CLIO), cyclic RGD (cRGD) modified	28	111
Cross-linked iron oxides (CLIO), scrambled	36	118
Dextran-coated iron oxides	2-4	72
	6-8	95
	10-15	185
	15-20	242
	20-25	320
Fe_3O_4	9	265
	6	208
	12	218
$MnFe_2O_4$	12	358
$CoFe_2O_4$	9	134
	6	109
	12	172
$NiFe_2O_4$	12	152
Gold-coated Co nanoparticles	-	10^7

1.5.4. Magnetofluorescent nanoparticles

Magnetofluorescent nanoparticles serves as a platform for hybrid imaging with the co-registration of MR and fluorescence images acquired under different geometries enabling better visualization[128]. Figure 1.1.9 shows different types of magnetofluorescent nanoparticles designed and developed in this thesis. Iron oxide nanoparticles (USPIO) were generated by adopting the co-precipitation synthesis strategy. Initially, lanthanide-doped iron oxide nanoparticles with anticipated NIR emission were developed and stabilized with a silane coating (Figure 1.1.9 A). Further, naphthalene sulfonates coated iron oxide nanoparticles with anticipated UV emission were synthesized and characterized (Figure 1.1.9 B). Finally, mixed coating of iron oxide nanoparticles with endogenous flavin analogues (anticipated visible emission) in combination with GMP were developed and characterized (Figure 1.1.9 C). The importance and cellular internalization pathways of the endogenous flavin analogues (FMN and FAD) used for coating the iron oxide nanoparticles and its specificity towards the riboflavin carrier protein (RCP) will be discussed in the following sections.

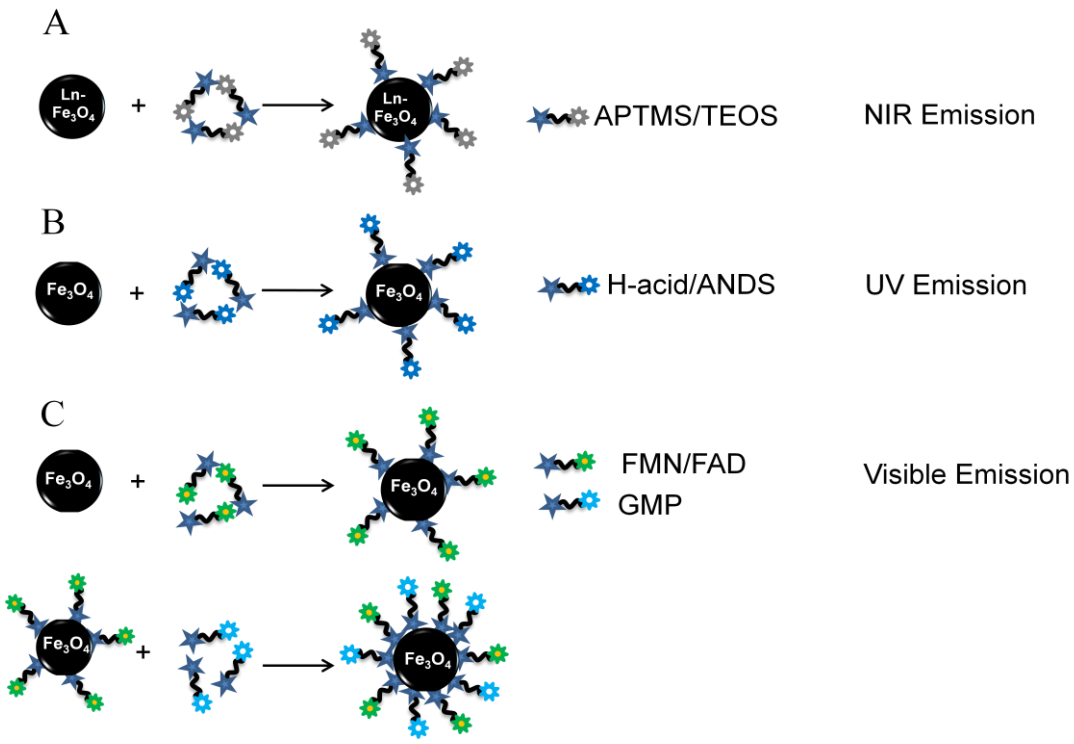

Figure 1.1.9. Schematic diagram displays different attempts made in generating magnetofluorescent nanoparticles. (A) Lanthanide-doped magnetic nanoparticles coated with silane molecules (APTMS/TEOS), (B) H-acid/ANDS coated iron oxide nanoparticles and (C) endogenous FMN/FAD and GMP coated fluorescent iron oxide nanoparticles respectively.

1.6. The Riboflavin carrier protein as a biological target

Riboflavin (Rf), also known as Vitamin B2, is a water-soluble vitamin essential for normal cellular function, growth and development. In its coenzyme forms like FAD and FMN, Rf performs key metabolic functions and acts as an intermediate in the electron transfer in the biological oxidation-reduction (redox) reactions. Rf deficiency leads to variety of clinical abnormalities including growth retardation, anemia, skin lesions and degenerative changes in the nervous system[129]. In order to avoid Rf deficiency in cells, the cellular uptake of Rf is enhanced and mediated by a membrane protein known as the riboflavin carrier protein (RCP), which strongly binds and transports Rf into the cells.

RCP is a growth- and development-specific protein proven to be highly conserved through amphibians, reptiles, and birds[130-132]. Chicken RCP (cRCP) is a 37 kDa phosphoglycoprotein found in chicken egg white, egg yolk and the plasma of egg laying hens. The human RCP has a molecular weight of 38 kDa (confirmed by siRNA inhibition analysis), similar to cRCP and shares physico-chemical characteristics, such as isoelectric point, electrophoretic mobility, and molecular weight (~ 36 kDa) with its chicken analogue.

The crystal structure of cRCP shows the binding mode of Rf with cRCP that occurs in a cleft with the isoalloxazine ring of Rf stacked between the parallel planes of Tyr75 and Trp156 as shown in Figure 1.2.1 respectively. The isoalloxazine ring of flavins is amphiphile since the xylene portion is hydrophobic and the pyrimidine moiety hydrophilic. The major interactions of the isoalloxazine ring with the protein are hydrophobic in nature (Figure 1.2.0 and 1.2.1). A characteristic feature of a ligand interaction to RCP is the fluorescence quenching which is clearly elucidated from the binding of Rf, and its analogs to RCP.

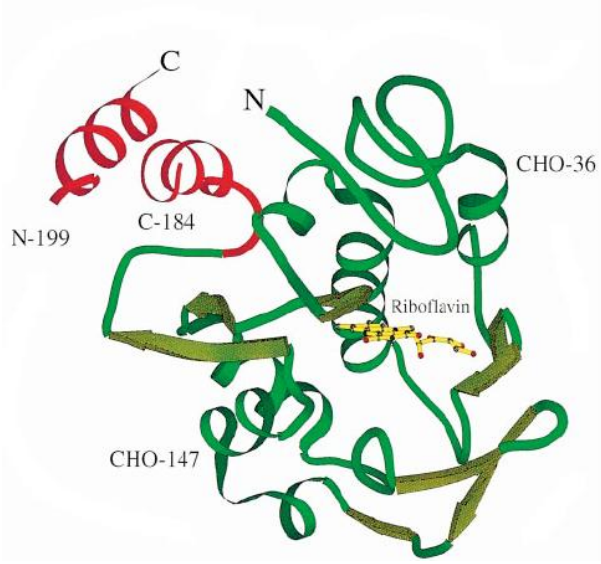

Figure 1.2.0. Ribbon diagram of the Rf-binding protein molecule. The ligand-binding domain is colored in green and the phosphorylated motif in red. The vitamin is represented by the yellow stick drawing. The letters 'N' and 'C' identify the N- and C-termini of the protein, the labels CHO-36 and CHO-147 indicate the positions of the oligosaccharide chains. The gap between the two helices in the red motif is the disordered part of the molecule which corresponds to the phosphorylated region between Leu184 and Glu199. The diagram was produced with the program MOLSCRIPT (Kraulis, 1991) (adapted from Monaco, The EMBO journal, 1997).

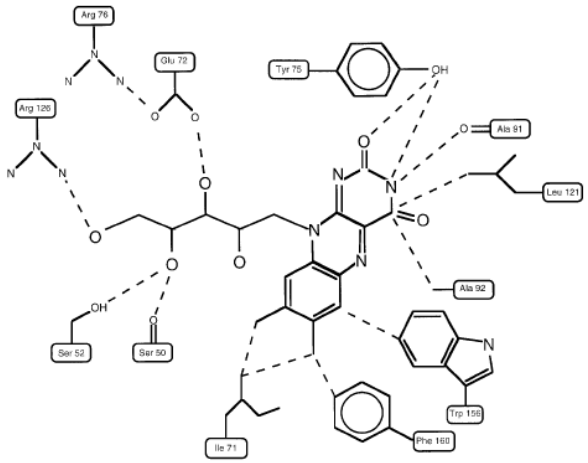

Figure 1.2.1. Schematic representation of the interactions showing the amino acids in the ligand-binding site that are in closest contact with the bound vitamin[133].

1.6.1. Riboflavin cellular internalization pathway

The Rf internalization in cells occurs via non-specific and specific cellular uptake pathways, respectively. Cellular internalization of Rf via non-specific transport is facilitated by albumin (co-transport or binding with Rf) and by Rf binding immunoglobins. It is believed that specific transport for delivering Rf into cells was mediated by carrier proteins

called “riboflavin binding/carrier protein (RCP)”. Though the mechanism of the Rf transport process remains elusive, it is believed that more than one mode of transport process may exist.

Saturable (active) transport (*in vitro*)

The Rf transport velocity and affinity constants for Rf-receptor binding were studied using different cell types expressing active Rf transport. The discrepancies observed in the Rf uptake could be related to the existence of different Rf uptake mechanisms (varied expression in cell lines) or due to highly mutant prone characteristics of cancer cell lines. Despite these observed differences, the Rf uptake mechanism seems to be highly specific and saturable. Competitve analog assays showed that FMN, FAD, lumiflavin, lumichrome, iso-Rf, and 8-[NH_2]-Rf display significant inhibition on cellular Rf uptake[134-138]. The temperature, osmalarity, metabolic inhibitors, ion substitutions, organic anions, anion exchangers, organic ion transport, modulators targeting cAMP, protein tyrosine kinase, protein kinase A, G, C and calmodulin-mediated pathways are also known to display inhibitory action on Rf transport which was elucidated through divergent cell models.

Passive diffusion component in Rf uptake

At Rf concentrations higher than in human plasma (> 12 nM), Huang, et al., reported Rf absorption in intestinal epithelial cells (Caco-2), which displayed predominantly passive diffusion kinetics, whereas, saturation kinetics are observed at Rf concentrations (~ 12 nM).

Receptor-mediated or carrier mediated transport of riboflavin

The criteria used to define the active Rf transport in cells, i.e. energy dependency and saturation transport kinetics; does not pave way to distinguish the carrier-mediated transport from the receptor-mediated endocytosis (RME). Receptor-mediated events (transport) typically involve endocytosis followed by subsequent microtubule driven vesicular sorting to various cellular organelles respectively[139]. To account for the RME pathway, the sub-cellular localization of Rf in BeWo cells was studied[140] using rhodamine-labeled Rf and FITC-labeled transferrin (FITC-Tf) to trace the sub cellular distribution patterns of these compounds upon its cellular uptake. The sub cellular localization investigation was evaluated using fluorescence microscopy, which showed a distinct perinuclear staining pattern for

rhodamine-Rf conjugates, with co-localization of FITC-Tf suggested that Rf transport in BeWo cells involves RME pathway.

The rate and extent of Rf internalization and its sub cellular trafficking were evaluated using breast cancer cell line (MCF-7),[141] and it displayed an alteration in Rf trafficking pathways due to the modifications that originated from the cellular environment, such as changes in temperature, compartmental pH, ligand concentration, and cytoskeletal networks respectively. Some of the limitations of this model: first, the permeation of ligand in and out of vesicles via passive diffusion was ignored; second, the effect on trafficking of enzymatic Rf conversion into its coenzyme forms (FMN and FAD), an efficient mechanism for capturing and storing Rf within the cell referred as "metabolic trapping"[142] has not been determined and may affect or influence the Rf trafficking kinetics.

1.6.2. Role of RCP expression in cancers

The increase in metabolic activity of cancer cells are expected to have a higher demand for Rf. The Rf uptake in cells is facilitated by RCP. Therefore, the increased uptake of Rf by metabolically active (cancer) cells points to an up regulation of RCP expression, respectively. In line with this, the (over-)expression of RCP has been reported in breast adenocarcinoma tumors, which was accompanied by high serum levels, suggesting its potential use as a (bio-)marker for early detection of breast cancer[143;144]. Further, the (over-) expression of RCP is also reported in different cancer tumors like ovarian adenocarcinoma, endometrial adenocarcinoma and hepatocellular carcinoma[145].

The RCP generation in the liver has been shown to be influenced by estrogen, however, its expression was also highly regulated in androgen sensitive LnCap, as well as androgen insensitive (PC-3 and DU-145) prostate cancer cells/tumors. This unique finding indicates that the expression level of RCP is independent of the hormonal regulation in prostate cancers. The internalization of Rf may involve a RME pathway as shown in several adenocarcinomas, including prostate, and placental trophoblast cells[146]. Studies using sera from prostate cancers of various stages will be necessary to evaluate and validate the potential of RCP to serve as a serum marker for early detection of prostate cancer.

1.6.3. RCP targeting

RCP receptors can be targeted by conjugating carriers like nanomaterials, liposomes, polymers, drugs with RCP specific endogenous ligands (Rf, FMN, FAD), respectively. To increase the delivery of macromolecules into cultured cells Rf was conjugated to macromolecules like bovine serum albumin (BSA) via the vitamin´s ribityl side chain. The RCP mediated high uptake of Rf-BSA by KB, A549, SK-LU-1 or SK-OV cells was compared to the unconjugated BSA where the former displayed high internalization (> 10^6 molecules/cell)[147]. Thomas, et al., also showed that the design of Rf conjugatedG5 dendrimer would provide key possibilities required for targeted (drug) delivery based on RME pathway respectively[148].

1.6.4. FMN/FAD coated iron oxide nanoparticles for RCP targeting

The vast majority of (pre-)clinically used MR contrast agents based on iron oxide nanoparticles are functionalized with polymers like dextran, carboxydextran and polyethylene glycol. However, with few exceptions[149], polymeric coated magnetic nanoparticles are known to display relatively large hydrodynamic diameters and therefore display limitations in tissue penetration, diffusion, bio-distribution and metabolic clearance and might even induce side effects. To overcome the afore-mentioned setbacks of polymer coatings, a thin layer of non-polymeric coating using organic biocompatible molecules was introduced in a simple and straightforward synthetic method. Based on the advantages of non-polymeric coatings, we here report fluorescent and non-polymeric FMN and FAD-decorated iron oxide nanoparticles as versatile MR contrast agents. FMN and its precursor Rf mediate various redox reactions that regulate the metabolism of carbohydrates, amino acids and lipids[150]. The cellular uptake of Rf is mediated by RCP, which strongly binds and transports Rf into the cell[142;151]. RCP is up regulated in cells with high metabolic activity like tumor cells[152;153] and activated endothelial cells. The current state of the art is that fluoro-2-deoxy-D-glucose (^{18}F-FDG) used for positron emission tomography (PET) imaging is the only clinically approved diagnostic agent for labeling cells with high metabolic activity[154-156]. On that basis, it was reasoned that besides ^{18}F-FDG-uptake, also the uptake of FMN/FAD-functionalized probes by RCP could serve as an effective metabolic marker for diagnostic (and therapeutic) interventions using non-invasive imaging modalities.

Aim of the thesis

The specific aims of this thesis are the following

1. To develop stable, biocompatible and fluorescent iron oxide nanoparticles (bimodal probes) for MR and optical imaging.
2. To generate the fluorescent USPIO by employing different strategies such as non-polymeric coating, conjugation of nanoparticles to organic dyes and via loading lanthanides into iron crystal lattices.
3. To evaluate the suitability of the generated magnetofluorescent nanoparticles (FLUSPIO/FAD USPIO) for cellular labeling.
4. To evaluate the *in vivo* target specificity of FAD USPIO for RCP using MRI and further to co-validate the MR findings through histology.

The scheme below shows the different synthesis strategies adapted in generating the fluorescent iron oxide nanoparticles as dual modal contrast agents for MRI and optical imaging techniques respectively.

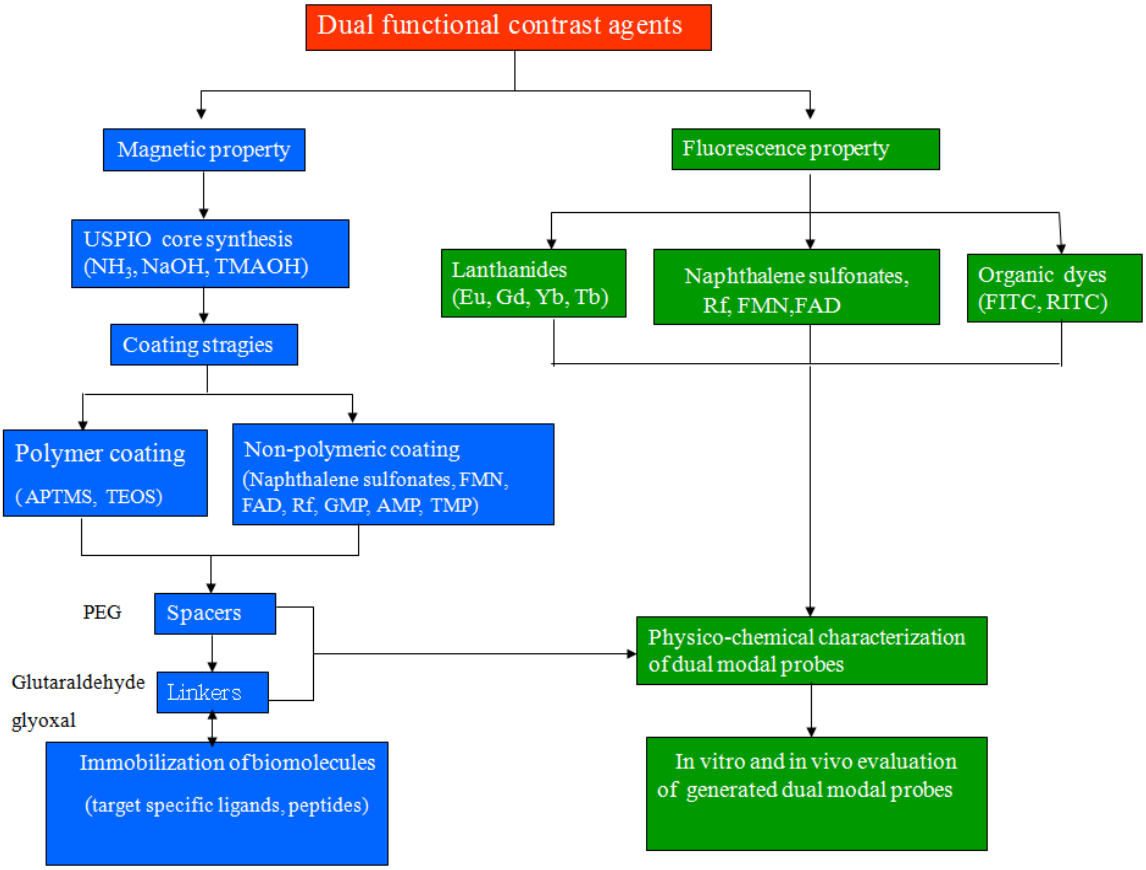

Chapter 2.

Results and Discussion

Dual modal fluorescent and magnetic iron oxide nanoparticles were generated by following different synthesis strategies. The first synthetic strategy was employed to generate iron oxide nanoparticles (USPIO) loaded (doped) with lanthanide metal ions (Ln) into its crystal lattice (Ln-USPIO). Subsequently, after doping surface coating was achieved with a protective layer of silane. However, the incorporation of lanthanides into the iron crystal lattice did not yield fluorescent nanoparticles, likely due to improper loading of lanthanides and due to the discrepancies observed in size between lanthanides and iron metal ions respectively. The second synthetic strategy, which was implemented to generate fluorescent nanoparticles, is by employing a thin layer of non-polymeric coating using fluorescent (UV emission) and biocompatible naphthalene sulfonates. Interestingly, the naphthalene sulfonates modified iron oxide nanoparticles (NUSPIO) displayed reasonable stability with a slight degree of agglomeration (pH 6) observed by visual inspection. However, NUSPIO did not show any fluorescence due to the quenching that occurred via electron transfer, due to the interaction of the aromatic naphthalene sulfonates moiety with the paramagnetic species (iron oxide nanoparticles). Therefore, these Ln-USPIO and NUSPIO could not be used as dual modal contrast agents for MR and optical imaging.

In order to overcome the above mentioned shortcomings from other coating/synthetic strategies used for generating fluorescent iron oxide nanoparticles, we used fluorescent, biocompatible and endogenous ligands (FMN, FAD and GMP) to achieve a thin layer of protective non-polymeric coating for the USPIO. The FMN/FAD based nanoparticles (FLUSPIO and FAD USPIO) displayed a reasonable stability and high intensity fluorescence without showing any agglomeration under physiological conditions. The fluorescent nanoparticles can be excited in a wide wavelength range (250-500 nm), resulting in an intense green emission at 530 nm. Further, the imaging properties (magnetism and fluorescence) of these newly generated nanoparticles were evaluated for their cellular labeling efficiency and for *in vivo* MR imaging.

2.1. Generation of bimodal contrast agents (MR and Optical imaging)

In this section, the synthesis, physico-chemical characterization, *in vitro* and *in vivo* evaluation results of different types of generated iron oxide nanoparticles (i.e. Ln-USPIO, NUSPIO, FLUSPIO, and FAD USPIO) based bi-modal contrast agents will be discussed. In this respect, new non-polymeric fluorescent ligand systems were synthesized and immobilized on the surface of iron oxide nanoparticles. The resulting bimodal probes

(FLUSPIO and FAD USPIO) were evaluated for their suitability for *in vivo* MR imaging and subsequently the MR findings were co-validated using histological analysis respectively.

2.2. Ligand systems used for coating of iron oxide nanoparticles

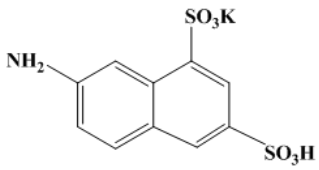

7-amino-1,3-naphthalene disulfonic acid monopotassium salt

Naph 1 (ANDS)

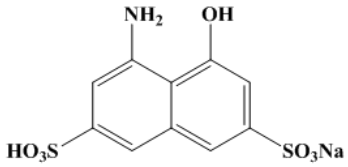

4-amino-5-hydroxy-2,7-naphthalenedisulfonic acid monosodium salt

Naph 2 (H-acid)

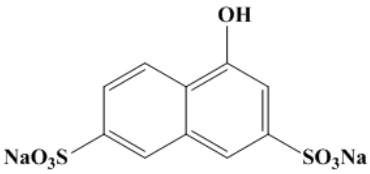

1-hydroxy-3,6-naphthalene disulfonic disodium salt

Naph 4

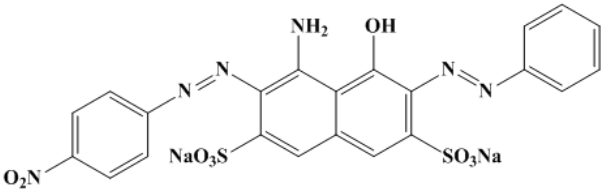

Naphthol blue black

Naph 3

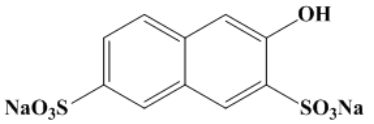

sodium 3-hydroxynaphthalene-2,7-disulfonate

Naph 5

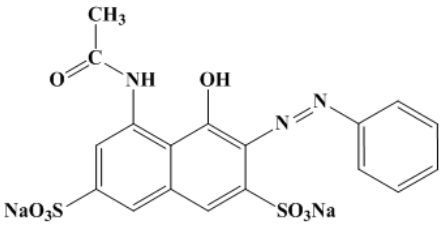

sodium 5-acetamido-4-hydroxy-3-(phenyldiazenyl) naphthalene-2,7-disulfonate

Naph 6

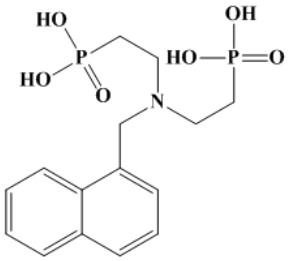

2,2'-(naphthalen-1-ylmethylazanediyl) bis(ethane-2,1-diyl)diphosphonic acid

Naph 7

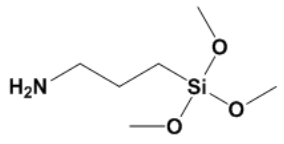

3-aminopropyltrimethoxysilane

APTMS

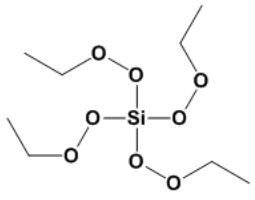

tetraethoxyorthosilicate

TEOS

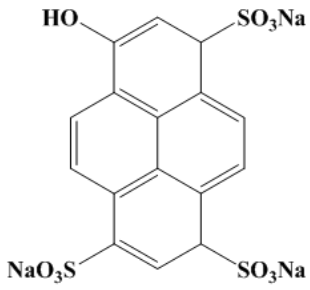

sodium 8-hydroxy-3,6-dihydropyrene-1,3,6-trisulfonate

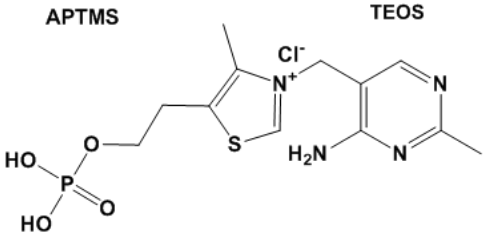

thiamine monophosphonic acid

TMP

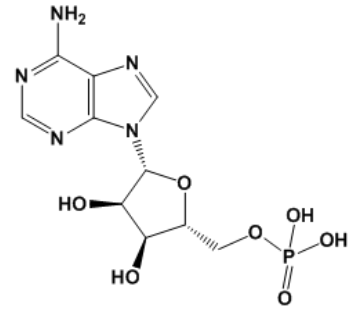

adenosine monophosphate
AMP

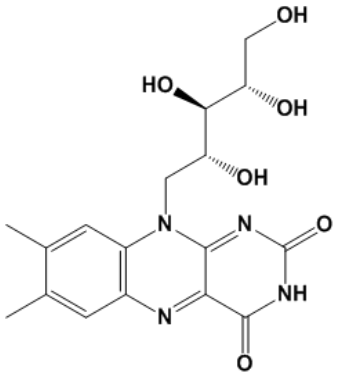

riboflavin
Rf

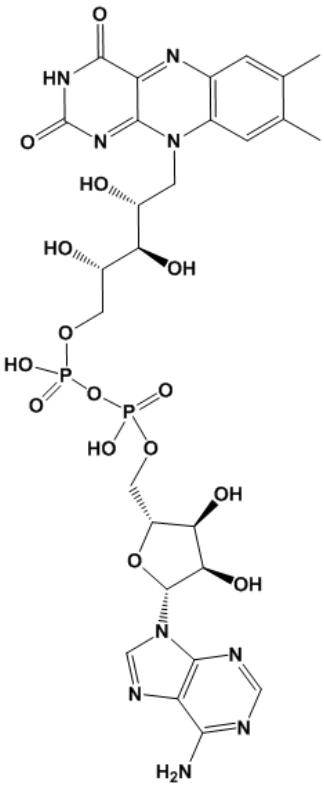

Riboflavin-5´-adenosine diphosphate
FAD

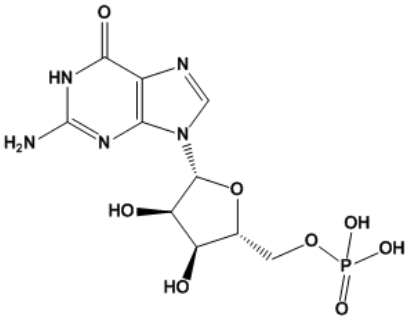

Guanosine monophosphate
GMP

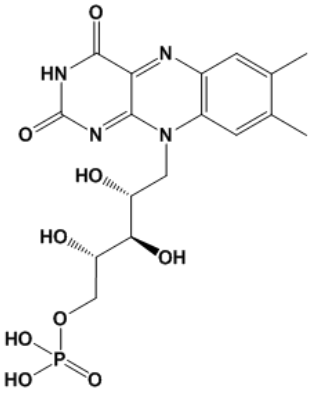

Riboflavin-5`-phosphate
FMN

Most of the simple fluorescent non-polymeric and non-fluorescent polymeric ligand systems were obtained from commercial sources and used directly for coating iron oxide nanoparticles without any further purification. Additionally, new hybrid fluorescent non-polymeric ligand systems were also designed and synthesized by coupling together the surface binding moiety (i.e. sulphonic acid, phosphonic acid) to a fluorescent aromatic moiety. Most of the fluorescent hybrid ligand synthesis was carried out in polar solvents and purified by using re-crystallization technique. The overall reaction yield at the end of the ligand generation was about 50 to 60%. After ligands synthesis, their fluorescence characteristics were checked by fluorescence spectroscopy prior to their coating on iron oxide nanoparticles.

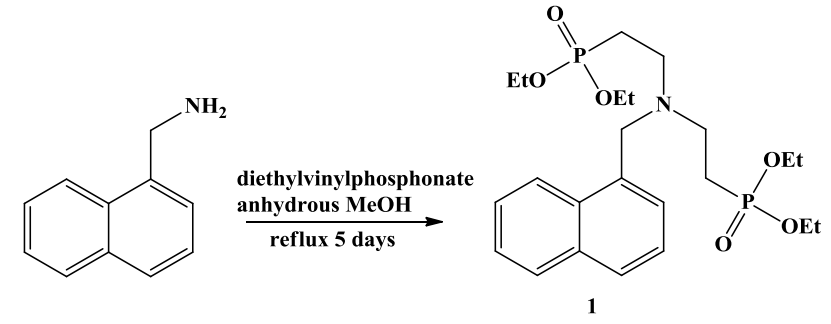

1

aminomethyl naphthalene

2-([2-(diethoxy-phosphoryl)ethyl]-naphthalen-1-ylmethyl-amino)-ethyl)-phosphonic acid diethyl ester

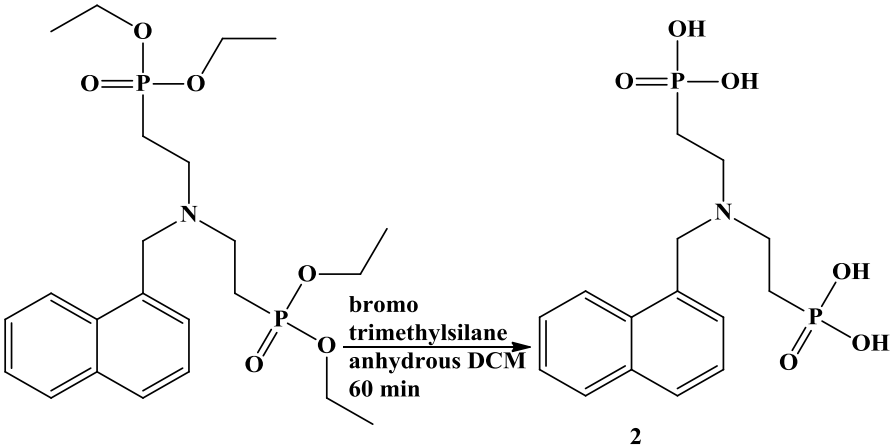

2

2-([2-(diethoxy-phosphoryl)ethyl] naphthalen-1-ylmethyl-amino)-ethyl)-phosphonic acid diethyl ether

[2-naphthalen-1-ylmethyl-(2-phosphono-ethyl)amino]ethyl]-phosphonic acid

Naphthalene bis(phosphonate) (**2**) (abv. Naph 7) was synthesized using a reported procedure[211]. The synthesis was carried out in two steps, where in the first step, aminomethyl naphthalene was treated with diethyl vinylphosphonate to produce the tetra ester (**1**), followed by the second deprotection step using bromomethylsilane. The deprotection step was quite fast but the reaction yield was low. The reaction was carried out under neutral conditions as the presence of acids or bases result in decomposition or incomplete or no reaction. The fluorescence (UV emission) originates from naphthalene moiety and the non-polymeric ligand was adsorbed to the metallic nanoparticles via the bis(phosphonate) groups.

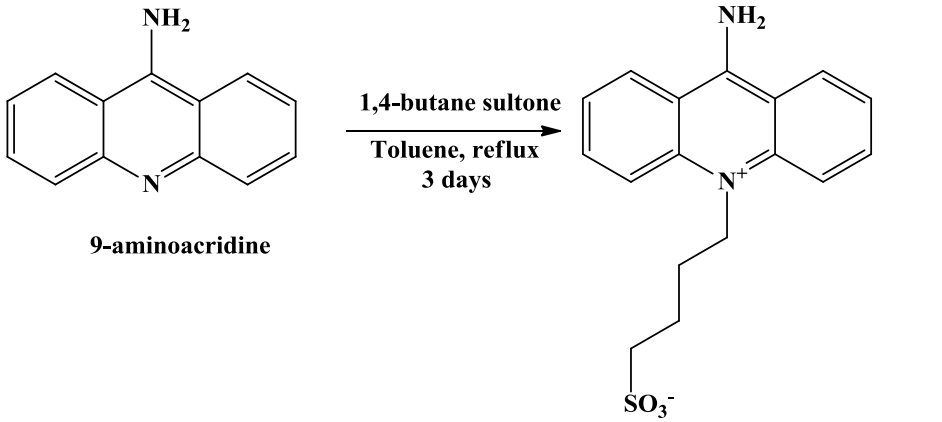

9-aminoacridine

4-(9-aminoacridinium-10-yl)butane-1-sulfonate

3

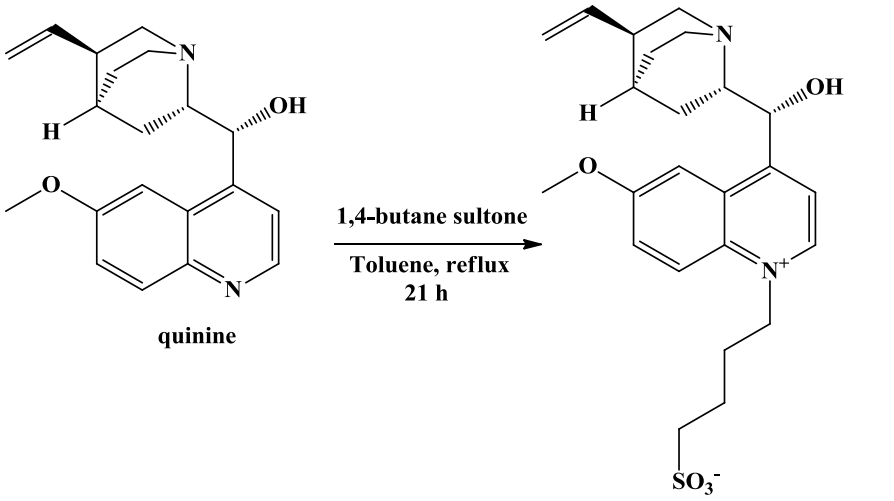

quinine

4-(4-((*R*)-hydroxy((2*S*,4*S*,8*R*)-8-vinylquinuclidin-2-yl)methyl)-6-methoxyquinolinium-1-yl)butane-1-sulfonate

4

Acridine and quinine are treated with 1,4-butane sultone to form quaternary salts having hydrophilic sulphonic acid groups (**3** and **4**) for the respective fluorophores via the quaterization reaction. The quaternary salt formation can be clearly seen from a change in colors during and after completion of the reaction. These salts are highly water soluble due to the presence of sulphonic acid groups. The 1,4-butane sultone introduces four carbons to the tertiary amine of the aromatic moiety and additionally a sulphonic acid group at the terminal carbon. Quaterization reaction carried out with 1,4-butane sultone resulted in better yields and reaction efficiency (i.e. reaction completion) than 1,3-butane sultone which was inefficient due to the reaction carried out at solid state and at elevated temperatures[157]. However, acridine and quinine quaterization reaction using 1,4-butane sultone in toluene

proceed via long reaction time (24 to 48 h)[212]. The pure crystals of the quaterized compounds were obtained by applying re-crystallization techniques.

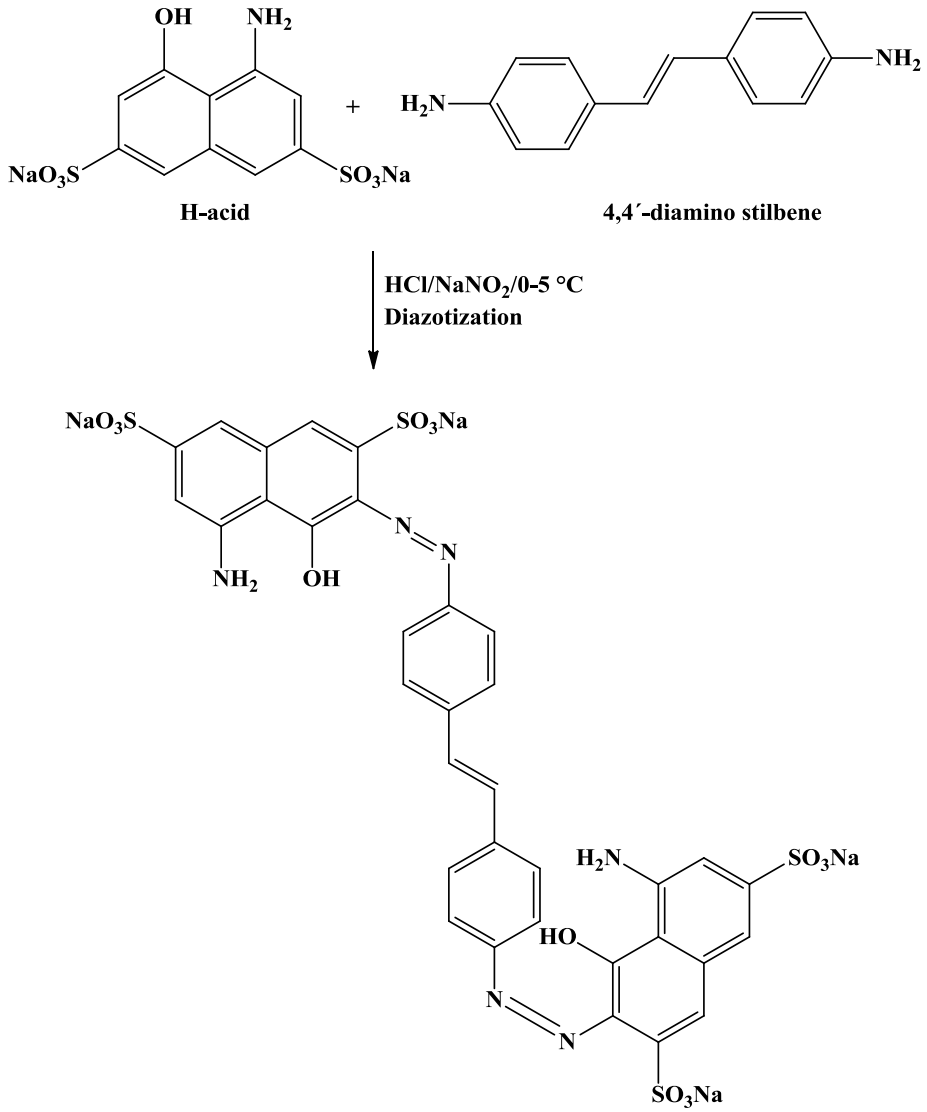

H-acid **4,4´-diamino stilbene**

**sodium 3,3'-(1'*Z*)-(4,4'-((*E*)-ethene-1,2-diyl)bis(4,1-phenylene))
bis(diazene-2,1-diyl)bis(5-amino-4-hydroxynaphthalene-2,7-disulfonate)**

5

The stilbene-based azo dye (**5**) was prepared according to reported literature[213]. The primary amine of the stilbene undergoes nitrosation (diazotization) with nitrous acid (generated *in situ* from sodium nitrite and a strong acid like HCl) at low temperatures. The diazotized stilbene salt was treated with amino naphthalene sulfonates (H-acid) at low temperature and at basic conditions to generate the azo dye. The azo dye was formed due to the electrophilic substitution of the diazotized stilbene salt at the *ortho* position of hydroxyl group of H-acid which renders stilbene-based azo dyes linear and coplanar which occurs due

to the hydrazone formation via intramolecular hydrogen bonds[158]. The stilbene-based azo dye was precipitated from the solution using sodium chloride and purified by crystallization technique. The proton peaks involved in hydrogen bonds are known to appear at much lower field in NMR than the normal proton peak of hydroxyl group[159].

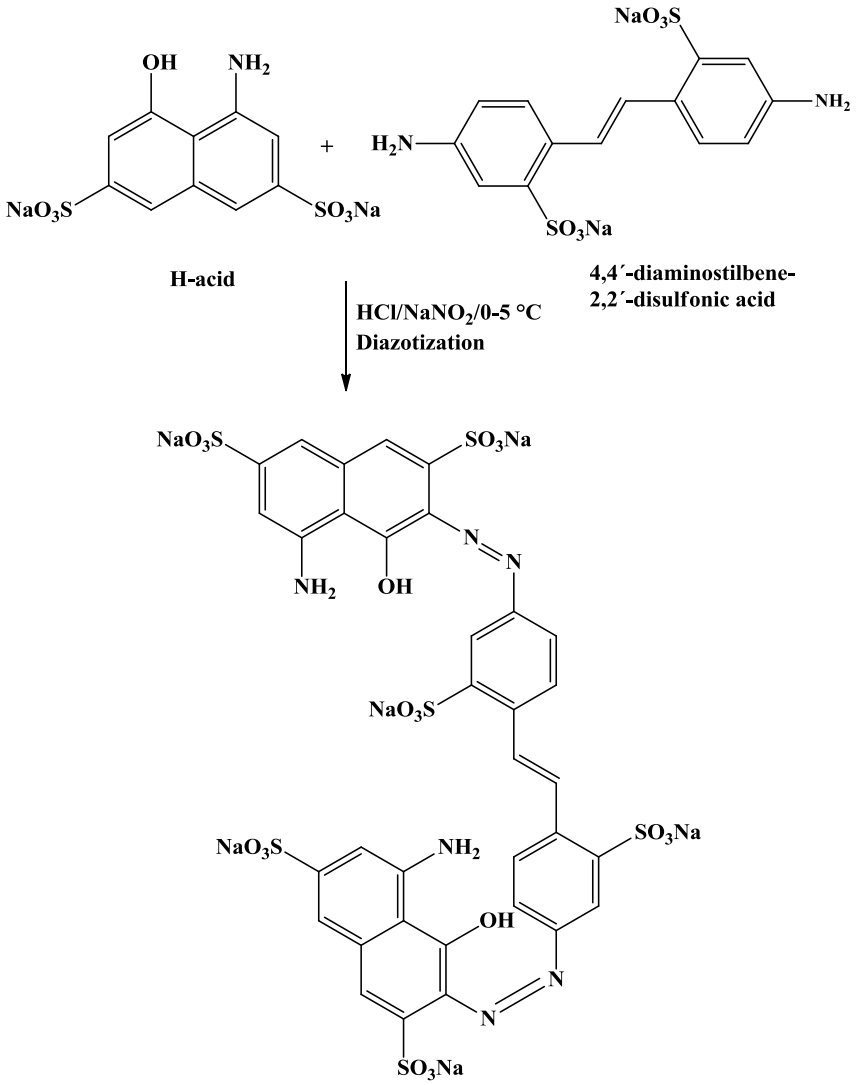

sodium 3,3'-(1'*Z*)-(4,4'-((*E*)-ethene-1,2-diyl)bis(3-sulfonato-4,1-phenylene)) bis(diazene-2,1-diyl)bis(5-amino-4-hydroxynaphthalene-2,7-disulfonate)

6

The stilbene-based azo dye (**6**) was prepared by a slight modification of the reported procedure[214]. In this synthesis, 4,4´-diamino stilbene-2,2´-disulfonic acid was used as the substrate for diazotization which proceeds via electrophilic substitution at the H-acid respectively. The stilbene-azo dye exhibits a linear and coplanar geometry after diazotisation. The resulting azo dye could not be precipitated from the solution by the addition of sodium chloride, which could be attributed to the presence of more hydrophilic sulphonic acid groups

and low ionic strength prevailing at the reaction medium. Hence, the crude product with sodium chloride was recovered from the reaction solution by rotatory evaporation and re-crystallization was performed in water, in order to generate pure crystals of the azo dye. However, the re-crystallization technique did not yield any crystals of the generated azo dye respectively.

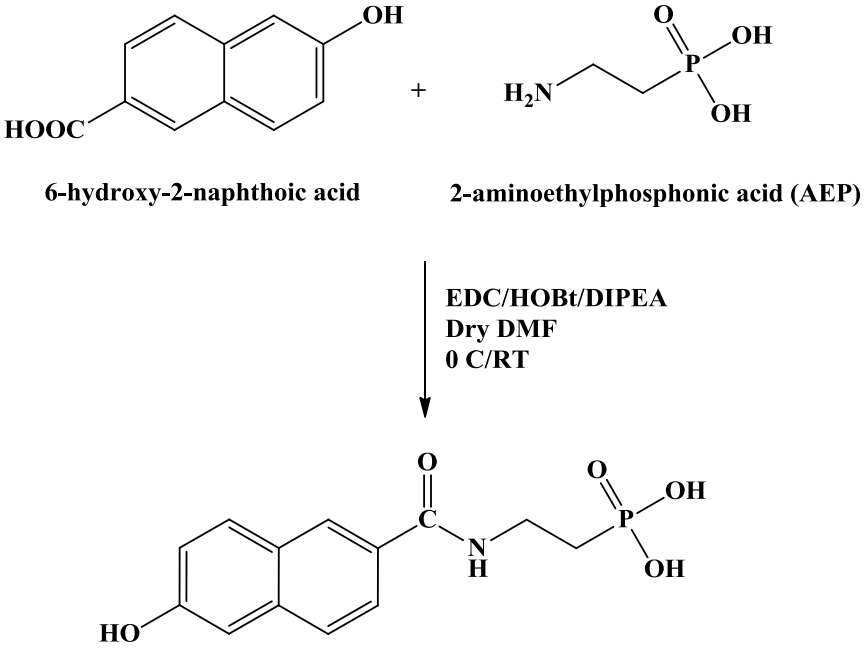

7

The carboxylic acid of the naphthalene substrate was activated by using 1-ethyl-3-(3-dimethylaminopropyl) carbodiimide (EDC) at low temperature. 1-hydroxybenzotriazole (HOBt) serves as a catalytic additive for the efficient conversion of acid and amine to amide[160;161]. The amide bond formation proceeds via the catalytic amounts of HOBt and stoichiometric EDC concentration[215]. N,N-diisopropylethylamine (DIPEA) serves as a base that facilitate the EDC coupling to form amides. The activated carboxylic acid was treated with amine substrate (AEP) at ambient temperature. The TLC showed that the conversion of the carboxylic acid to amide (**7**) was only 50% after overnight reaction. Increasing the reaction time, did not improve the reaction yield and the amine conversion to amide. The side products like urea and unreacted HOBt were removed by washing the final residue with ether. The pure product was recovered by re-crystallization from water.

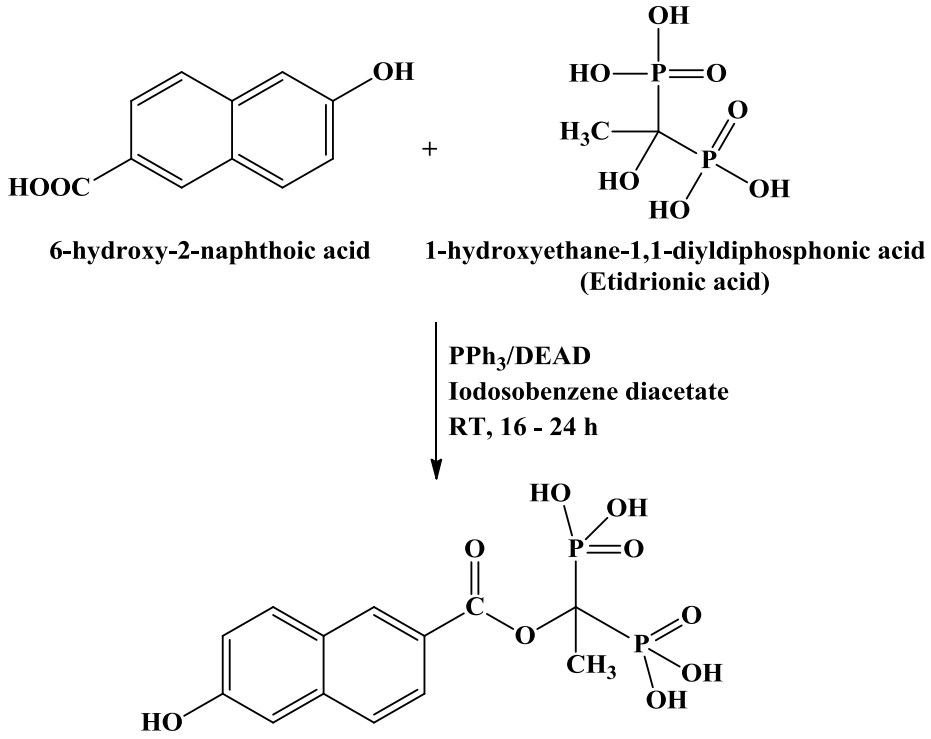

6-hydroxy-2-naphthoic acid **1-hydroxyethane-1,1-diyldiphosphonic acid (Etidrionic acid)**

1-(6-hydroxy-2-naphthoyloxy)ethane-1,1-diyldiphosphonic acid

8

The Mitsunobu reaction was carried out between 6-hydroxy-2-naphthoic acid and 1-hydroxyethane-1,1´-diyldiphosphonic acid (Etidrionic acid) to form ester (**8**). This reaction involves the dehydrative coupling of an alcohol with an acidic component (carboxylic acid) to form esters using a combination of a reducing (phosphine) and an oxidizing (azo) reagent. Iodosobenzene diacetate is known to oxidize 1,2-dicarbethoxyhydrazine to diethyl azodicarboxylate (DEAD), in line with this, it might be possible to use iodosobenzene diacetate as the stoichiometric oxidant and DEAD as a catalyst in Mitsunobu reactions[162]. The Mitsunobu reaction inverts the stereochemistry of the alcohol that was used as the starting material[163]. However, a significant drawback of these reactions is the requirement of four reagents and starting materials (an alcohol, an acid/pro-nucleophile, a phosphine, and an azo reagent), which leads to difficulty in the separation of the desired product from the excess starting materials/reagents and by-products[216]. The mitsunobu reaction completion was monitored using TLC and the residue obtained after evaporation was soluble in water under sonication. The final product in aqueous solution was re-crystallized with a moderate reaction yield.

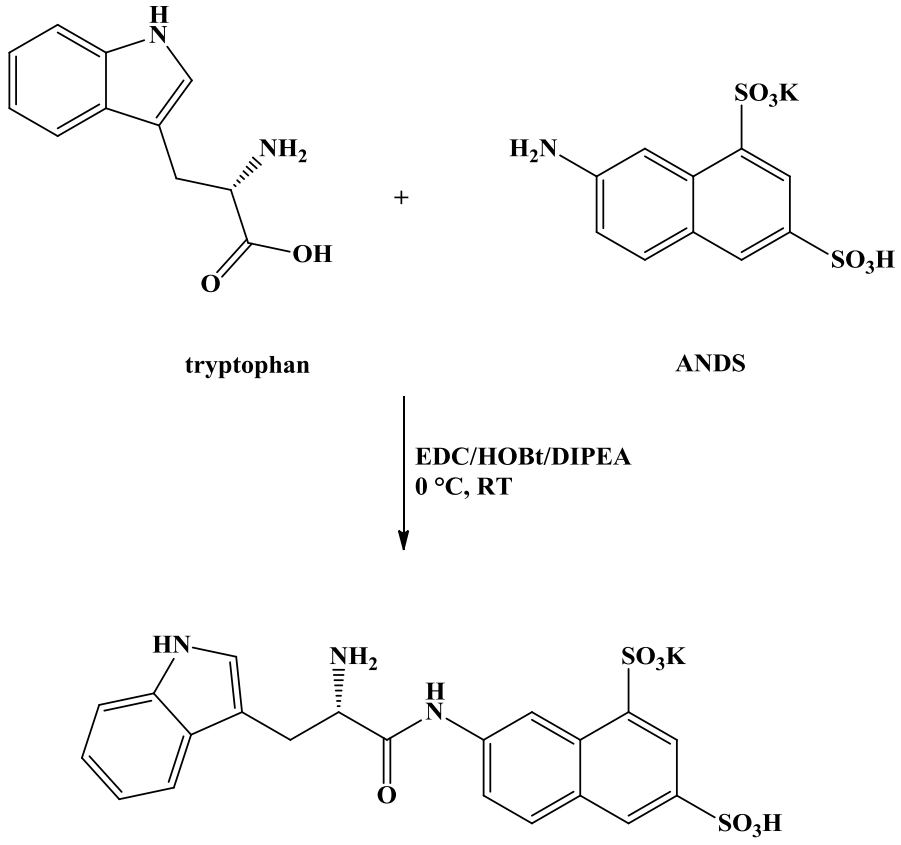

potassium (*S*)-7-(2-amino-3-(1*H*-indol-3-yl)propanamido)-3-sulfonaphthalene-1-sulfonate

9

The carboxylic acid of the amino acid (tryptophan) was activated by using EDC at ambient temperature. The amine (ANDS) was added to the activated amino acid followed by HOBt and DIPEA at ambient temperature and further the reaction was allowed to proceed at RT. The amide (**9**) formation was monitored using TLC, which showed that the amide formation was only upto 50% after overnight reaction and the reaction yield remained unchanged even with increase in the reaction time. The side products like urea and unreacted HOBt were removed by washing the final residue with diethyl ether. The generated amide product was recovered from methanol by triturating the filterate with ether.

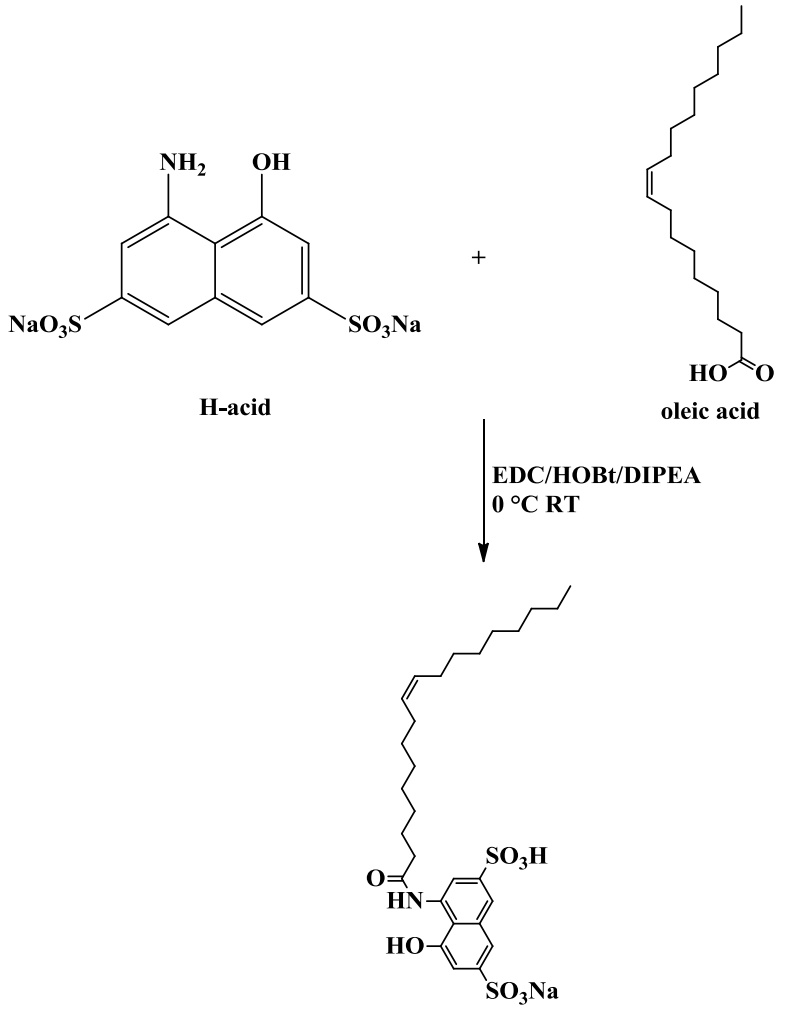

H-acid **oleic acid**

sodium 4-hydroxy-5-oleamido-7-sulfonaphthalene-2-sulfonate

10

The carboxylic acid of the oleic acid was activated by using zero length cross linker carbodiimide (EDC) at low temperature. The amine (H-acid) was added to the activated oleic acid followed by addition of HOBt and DIPEA at ambient temperature. HOBt serves as a catalytic additive and DIPEA acts as a base to facilitate the efficient conversion of acid and amine to amide. The amide formation (**10**) was regularly checked using TLC and the side products (urea) and unreacted components (HOBt) in methanol was neutralized and removed by rotator evaporation. The amide product was recovered from methanol by trituration of the residue with ether.

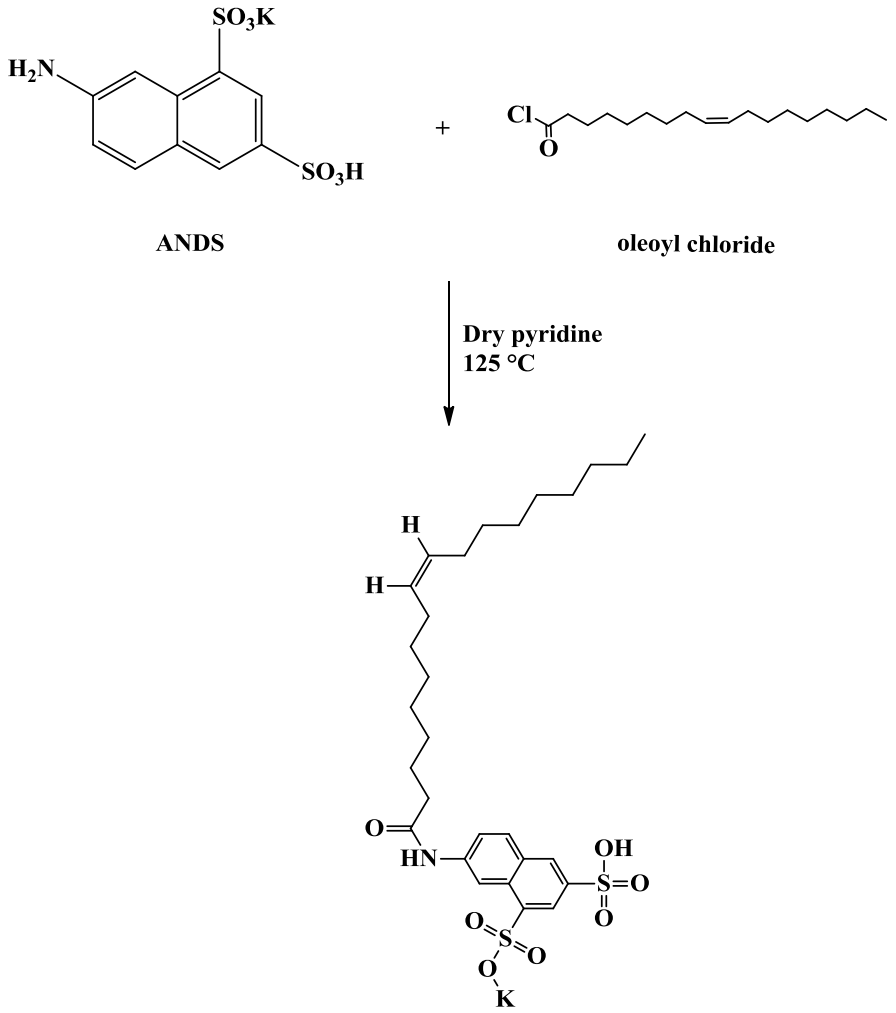

potassium 7-oleamido-3-sulfonaphthalene-1-sulfonate

11

The peptide bond (in compound (**11**)) was achieved between the oleoyl chloride and ANDS substrate at high temperature under inert atmosphere via a modified literature procedure[217]. The slow addition of dry pyridine into the heated reaction mixture (oleoyl chloride and ANDS) resulted in the evolution of HCl gas from the reaction. The completion of the reaction was monitored using TLC for 2 days. The excess pyridine from the reaction was removed by distillation. The resulting solid residue was soluble in chloroform which was in contradiction to the reports from the literature, wherein the obtained solid residue was only soluble in methanol (could be due to usage of different unsaturated acids). However, the sticky product could be obtained by washing with methanol and followed by trituration with ether. These products were only amenable to negative ion FAB mass spectral analysis, as reported for most of the naphthalene sulfonates[164].

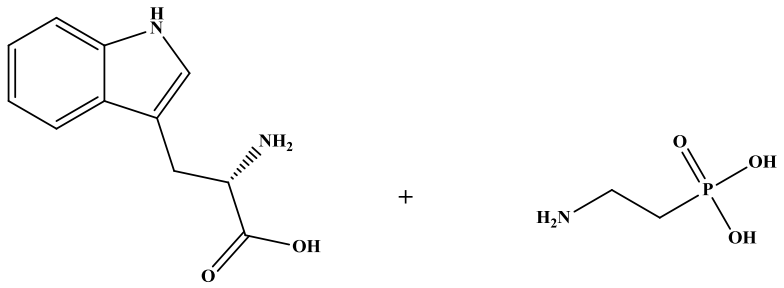

Tryptophan **2-aminoethylphosphonic acid (AEP)**

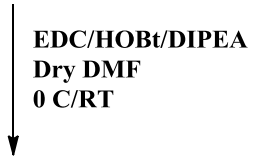

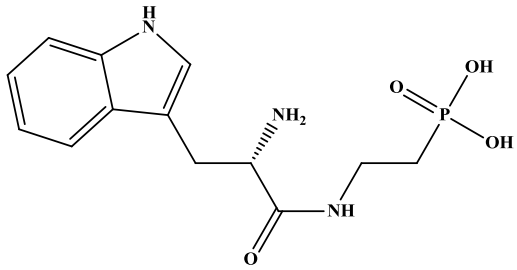

(*S*)-2-(2-amino-3-(1*H*-indol-3-yl)propanamido)ethylphosphonic acid

12

The carboxylic acid of the amino acid (tryptophan) was activated by using EDC and the amine (AEP) was added to the activated amino acid, followed by addition of HOBt and DIPEA at ambient temperature. Further, the reaction was allowed to proceed overnight at RT. The amide formation was continuously monitored using TLC and after reaction completion the side products and excess reagents were removed by washing the residue with ether. However, the amide (**12**) could not be completely recovered from methanol by ether extraction and via re-crystallization from aqueous solution. Therefore, the product was recovered by rotatory evaporation from the reaction mixture.

2.3. Synthesis of iron oxide cores

Magnetic nanoparticles used for medical and diagnostic imaging applications can be synthesized via different methods like micro-emulsions[165], sol-gel syntheses[166], sonochemical reactions[167], hydrothermal reactions[168], hydrolysis and thermolysis of

precursors[169], flow injection syntheses[170], and electrospray syntheses[171]. In this thesis, the cores of the iron oxide nanoparticles were synthesized by employing two different methods namely co-precipitation (aqueous phase) and thermal decomposition (organic phase) respectively. One of the major limitations of co-precipitation synthetic strategy is that it yields only polydispersed nanoparticles, however, the reaction yield from co-precipitation is very high and further facilitates MR imaging as the synthesized nanoparticles are available as aqueous suspensions. Conversely, nanoparticles prepared by thermal decomposition are highly monodispersed, but suffers from low yield and problems related to their transfer from organic into aqueous phase.

2.3.1. Synthesis of Iron oxide nanoparticles (10 nm) by the co-precipitation method

The iron oxide nanoparticles with 10 – 12 nm core diameters were prepared via co-precipitation of ferric and ferrous salts (2:1 molar ratio) by using alkaline bases like sodium hydroxide, ammonia or tetramethyl ammonium hydroxide (TMAOH) (pH range between 8 and 14). The first controlled preparation of superparamagnetic iron oxide nanoparticles was performed and reported by Massart[172]. In our study, magnetic nanoparticles were prepared by a modified Massart method, in which the iron precursors in acidic solutions are simultaneously added into a base in order to propagate the growth of the nanoparticles. The particles synthesized with Fe^{2+}/Fe^{3+} ratios between 0.4 and 0.6 are effective enough to be used as MR contrast agents[173-175]. The Fe_3O_4 formation may be represented chemically as follows

$$Fe^{2+} + 2Fe^{3+} + 8OH^- \longrightarrow Fe_3O_4 + 4H_2O$$

The co-precipitation was carried out under inert atmosphere and at 80°C in order to remove the dissolved oxygen from the aqueous medium which might induce oxidation of the iron cores (Fe_3O_4) to form maghemite. Bubbling nitrogen gas through the solution not only protects against critical oxidation of the magnetite but also reduces the particle size when compared to synthetic methods without removing oxygen[176;177].

The magnetite is immediately formed as a black precipitate due to the addition of the base (NaOH) that induces nanoparticle nucleation. The crystal growth of the magnetite is allowed to proceed for 20 min by stirring them at 1000 rpm. In magnetite, Fe^{3+} ions are distributed in the octahedral (Oh) and tetrahedral (Td) sites, and Fe^{2+} ions are distributed in the octahedral (Oh) sites of the inverted spinel structure (Fe_3O_4: $[Fe^{3+}]_{Td}[Fe^{3+}Fe^{2+}]_{Oh}O_4$).

In order to stabilize the as-prepared nanoparticles in solution without any aggregation, the negative surface charge of the nanoparticles (originating from hydroxyl groups and oxo-bridges) was protonated by addition of aqueous HCl acid (pH 2) and converted into positively charged surface. The high proton (H^+) concentration also converts the magnetite into maghemite without any change in the particle size[178].

$$Fe_3O_4 + 2H^+ \longrightarrow \gamma Fe_2O_3 + Fe^{2+} + H_2O$$

Under acidic conditions, surface Fe^{2+} ions are desorbed as hexa-aqua complexes in solution. In line with this, the size sorting process was reported on cationic Massart nanoparticles using nitric acid as an electrolyte and allowed to fractionate the particle size distribution with a very good yield[179].

The size, shape and composition of the synthesized magnetic nanoparticles depends on the type of salts used (e.g., chlorides, sulfates, nitrates), the Fe^{2+}/Fe^{3+} ratio, the reaction temperature, the pH value and ionic strength of the media. Table 2.1.0 displays different reaction conditions which are optimized to yield nanoparticles with reasonable dispersity that suits their use in biomedical applications.

In another synthetic strategy, iron oxide nanoparticles (10 nm) were prepared in a rapid and economical method at ambient temperature without using inert atmosphere and elevated temperature. In this method, the Fe^{2+}/Fe^{3+} salts in water were stirred for 10 min at RT, in order to completely dissolve the iron salts and to form a homogeneous solution. Further, the co-precipitation was achieved by addition of ammonia into the above iron salt solution. The magnetite crystal growth was allowed to proceed for 10 min at 1200 rpm at ambient temperature. Excess of ammonium ions, chloride anions from the magnetic fluid suspensions were removed by washing three times with de-ionized water. The removal of free chloride anions from the solution was confirmed by testing an aliquot with silver nitrate solution which results in curdy white precipitate with chloride anions. Finally, the magnetic fluids were suspended in aqueous hydrochloric acid (pH 2) at low temperatures.

Additionally, iron oxide nanoparticles were prepared by co-precipitation and stabilized via using a non-polymeric binding of alkaline tetramethyl ammonium hydroxide (TMAOH). After washing with water, the pH of the magnetic particles was slightly basic (around 8 – 8.5) and further with increase in storage time, the nanoparticle agglomerates and sediments down which makes them unsuitable for coating purposes. The agglomeration could be avoided by removing the big aggregates via centrifugation.

Furthermore, lanthanides doped magnetic nanoparticles with 10 nm average diameter were prepared by a modified Massart (co-precipitation) method. It is known that doped

nanoparticles generated using co-precipitation display physico-chemical characteristics almost similar to that of undoped magnetite nanoparticles[180].

Table 2.1.0. Stabilization of different parameters involved in the synthesis of cores of iron oxide nanoparticles. The highlighted conditions (in italics and underlined) indicate the optimized parameters necessary to yield highly dispersed nanoparticles.

Temperature (°C)	NaOH concentration (M)	Stirring speed (rpm)	Reaction time (min)	Stability in solvents and solutions
80	*0.5*	*Mechanical stirring (1000 rpm)*	*20*	*Stable in glucose, diethyl glycol, DMF, DMSO, methanol*
20, 40, 60	1.0, 1.5	Magnetic stirring (1000 – 1200 rpm)	20	Unstable in citric acid, acetonitrile, PBS buffer, and saline solution.

2.3.2. Synthesis of iron oxide nanoparticles (5-6 nm) by the co-precipitation method

Iron oxide nanoparticles (5-6 nm) were prepared in a simple and facile way at ambient temperature without the influence of inert atmosphere and high temperature. In this method, the Fe^{3+}/Fe^{2+} salts (2:1 molar ratio) in water was stirred for 10 min at RT to generate a homogeneous solution. The aqueous solution of iron salts were co-precipitated by using ammonia. The magnetite crystal growth was allowed to proceed for 20 min at 1200 rpm at ambient temperature. It is known that, with increasing in the reaction time the size of the nanoparticles decreases (i.e. 10 nm to 5-6 nm). Excess of ammonium ions, chloride anions from the magnetic fluid suspensions were removed by washing three times with de-ionized water. The free chloride anions removal was confirmed by silver nitrate test. Further, the magnetic fluids were suspended and stabilized without agglomeration in aqueous hydrochloric acid (pH 2). The big agglomerates in the magnetic fluid were removed by sonication at ambient temperature which was aided by filtration through 0.22 µm filter units. Furthermore, high-speed centrifugation removes the remnant agglomerates from the magnetic fluid. The supernatant solution containing highly dispersed nanoparticles was collected and stored at low temperature.

2.3.3. Synthesis of iron oxide nanoparticles by the thermal decomposition method

2-pyrrolidione (2-Py) serves as a solvent for high-temperature thermal decomposition reaction and also involves in surface modification of the generated magnetite nanocrystals via coordination, which renders them water-soluble and increases the colloidal stability of nanoparticles[181]. Trace amount of water in 2-Py was removed by using molecular sieves 4A and $Fe(acac)_3$ addition to 2-Py resulted in red color solution which was sonicated for 7 min and refluxed at 250-300 °C under inert atmosphere. The carbon monoxide produced during the synthesis was quenched by purging into a transition metal complex solution. The reaction intermediate (azetidine) is known to be actively involved in the catalytic hydrolysis of the iron acetylacetonate precursor[182]. Iron oxide nanoparticles generated by thermal decomposition resulted in black solution, which could not be precipitated using methanol. The final residue obtained after rotatory evaporation was washed several times with acetone and dried in hot air oven. 2- Py adsorbed magnetic nanoparticles were dispersed in water with sonication. The size and shape of these magnetic nanoparticles can be tuned by altering the reaction time and temperature respectively.

Oleic acid is a surfactant widely used to stabilize the magnetic nanoparticles via the coordination that occurs between the carboxylic acid groups (oleic acid) and the nanoparticles[183;184]. The interaction between carboxylates and metal atom is known to occur via carboxylate head in four different forms: monodentate, bridging (bidentate), chelating (bidentate), and through ionic interaction[185]. Thermal decomposition of iron precursor ($Fe(acac)_3$) in the presence of oleic acid was carried out in organic phase under nitrogen atmosphere. The magnetite crystal growth increases at high temperature as displayed by the change in color (red to yellow to black). The magnetic particles could not be precipitated from black solution by ethanol addition. Therefore, excess ethanol was rotatory evaporated and nanoparticles were recovered by centrifugation. The nanoparticles displayed agglomeration which prevented them from re-dispersing in water. In line with this, Sun, et al., reported the thermal decomposition of $Fe(acac)_3$ in presence of surfactants like oleic acid and oleylamine to generate monodispersed magnetite nanoparticles[186].

In another synthesis strategy, oleic acid based stabilization of the magnetic nanoparticles was demonstrated. Here, the nanoparticles were generated using iron (II) precursor at elevated temperature. The iron (II) in the alkaline iron (II) precursor solution was oxidized to iron (III) by using $(NH_4)_2S_2O_8$ and resulted in black solution respectively. The black solution was formed by $(NH_4)_2S_2O_8$ (oxidant) addition, to the alkaline iron (II) precursor solution. Oleic acid in toluene was added to the reaction mixture and heated to generate the oleic acid capped magnetic nanoparticles, and isolated by precipitation in

acetone. A dark sticky precipitate was obtained in a low yield. The magnetic nanoparticles (solid) were highly soluble in toluene, chloroform and tetrahydrofuran thus providing stable organosols. The transfer of the oleic acid stabilized nanoparticles into water was not successful.

The surface of the commercial ferrofluid (EMG 911) extracted from mineral oil was covered by oleic acid and could be readily re-dispersed in toluene. These hydrophobic nanoparticles displayed a mean diameter around 10 nm and resulted in agglomerates upon drying due to strong hydrophobic interactions between their surfaces[220]. The ferrofluid (EMG 911) served as control particles and the properties (physical and chemical) of them after coating with silica were compared to the magnetic nanoparticles generated in our laboratory, thus paving way for efficient designing of versatile MR contrast agents. Indeed, there were problems associated with EMG 911 during silica coating like aggregation, phase separation etc.

2.4. Estimation of the iron concentration in nanoparticles

The total iron concentration of the magnetic nanoparticles was determined by using three different techniques/methods such as titrimetry, colorimetry and mass spectrometry (ICP-MS) respectively. Inductively coupled mass spectrometry (ICP-MS) estimates the total iron concentration in nM, but has drawbacks like long measurement time and high cost. Titrimetry and colorimetry are fast and convenient techniques used to determine iron concentration in µM range. The total iron (Fe^{3+}) concentration of the uncoated and coated nanoparticles was determined prior to their *in vitro* and *in vivo* investigations.

2.4.1.Titrimetry

Total iron content of the magnetic nanoparticles was estimated using EDTA standard solution (Idranal for metal titration). EDTA was standardized using the standard zinc solution (0.01 M) in bicarbonate-carbonate buffered solution (pH = 10.0). Eriochrome Black T acts as an indicator under basic conditions and displays the end point by change in color from wine red to purple blue.

The total iron in the magnetic fluids was dissolved by boiling them with HCl acid and the color of solution changes from black to slight yellow. In this method, the iron in the sample was completely oxidized to Fe^{3+} by an oxidizing agent ($(NH_4)_2S_2O_8$) which turns the solution completely into yellow. The Fe^{3+} forms a wine red complex with sulfosalicylic acid (Figure 2.1.0) and a buffer is added additionally to stabilize the Fe (III) complex. The solution is titrated with standardized EDTA to give yellow color as the end point. The total

iron content of magnetic nanoparticles with 10 nm and 5-6 nm core diameters was determined by titration as 233 mM and 143 mM respectively.

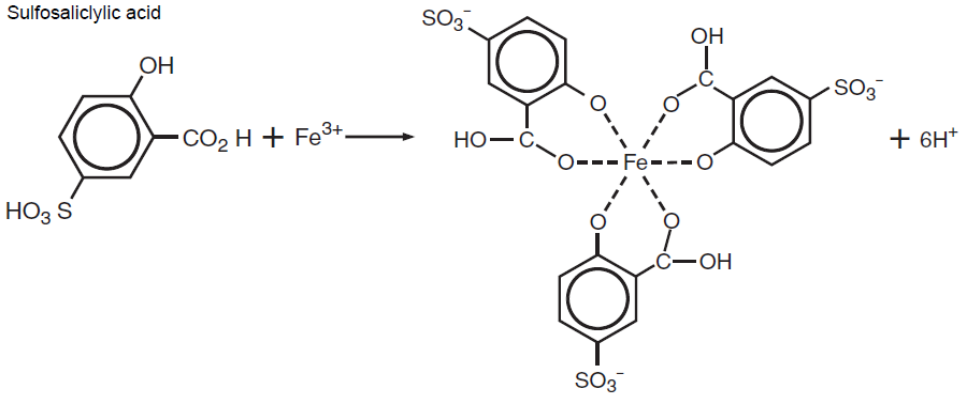

Figure 2.1.0. Schematic diagram of complex formed between iron (III) and sulfosalicylic acid during the titrimetric estimation of iron concentration.

2.4.2. Colorimetry

Magnetic nanoparticles (Fe(II)) were completely oxidized to Fe(III) by aqua regia ($3HCl/HNO_3$). Fe(III) forms a red complex with disodium-1,2-dihydroxy-3,5-benzene disulfonic acid (tiron) as shown in Figure 2.1.1. The complexation (via two hydroxyl groups) is facilitated under basic conditions by using a phosphate buffer (pH 9-10). The total iron content of magnetic nanoparticles with 10 nm and 5-6 nm core diameters determined by tiron colorimetric method is in line with the results obtained from titration.

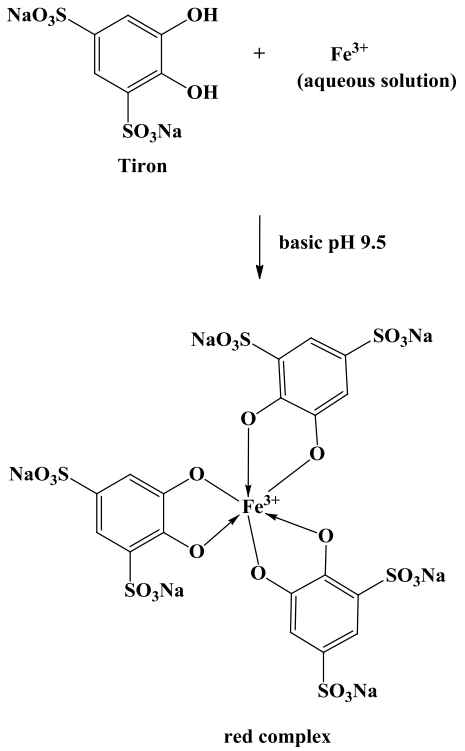

Figure 2.1.1. Tiron complexes with iron (III) under basic conditions to form the tiron coordinated red complex

2.4.3. Mass spectrometry

Iron oxide nanoparticles were digested and oxidized using nitric acid and hydrogen peroxide under microwave irradiation. Further, these digested acidic solutions were diluted in water and the total iron content of the samples was estimated based on the standard calibration in nM concentration. Table 2.1.1 shows ICP-MS results of total iron concentration of different magnetic cores prepared using different base concentration (NaOH, NH_3).

Table 2.1.1. Total iron concentration of the iron cores prepared using different base concentration as determined by ICP-MS.

No.	Base used	Iron cores (uncoated)	Elements in the sample	Total iron concentration mg/mL
1.	1.5 M NaOH	Uncoated	Fe, O, H	20.211
2.	0.5 M NaOH	Uncoated	Fe, O,H	9.247
3.	1.0 M NaOH	Uncoated	Fe, O, H	4.596
4.	25% NH_3	Uncoated	Fe, O, H	8.000

2.5. Different magnetic nanoparticles

In this section, different magnetic nanoparticles generated based on various coating strategies will be discussed. In magnetic nanoparticles, the surface iron atoms act as Lewis acids and coordinate with molecules that donate lone-pair electrons. Therefore, in aqueous solutions, the Fe atoms coordinate with water, which dissociates readily to leave the iron oxide surface hydroxyl functionalized. These hydroxyl groups are amphoteric and may react with acids or bases[179]. The magnetic nanoparticles can be stabilized by using any one of the following coatings such as monomeric stabilizers (carboxylates, phosphates), inorganic materials (silica, gold), polymer stabilizers (dextran, polyethylene glycol, polyvinyl alcohol, alginate, chitosan) respectively. This thesis deals with the design and development of new bimodal MR contrast agents based on silane, mixed silane, non-polymeric, and fluorescent non-polymeric coatings. The specificity of the MR contrast agents was promoted by conjugation to peptides, which can be further visualized (imaged) in cells and animals by including a fluorescent tag. Most of the conjugation chemistry in this thesis was achieved via the available free amine groups from different coatings. The physico-chemical properties of different magnetic nanoparticles were studied using various techniques and their suitability as versatile MR contrast agents was evaluated successfully for intended *in vitro* and *in vivo* bio-medical applications.

2.6. Synthesis of Ln-USPIO nanoparticles

The first synthesis strategy in generating multimodal contrast agents was performed by doping the iron oxide nanoparticles with lanthanide (Ln) metal ions via a modified co-precipitation protocol respectively. Here, magnetic fluids were synthesized by using different concentrations of base (NaOH) in order to generate nanoparticles with different sizes. Lanthanides like Eu,Gd,Tb were incorporated into the crystal lattice of the iron oxide nanoparticles, so that its emission at long wavelength could be efficiently used for fluorescence imaging. Due to insufficient loading of lanthanides into the iron lattice, the anticipated fluorescence was not observed either by fluorescence (spectroscopy and microscopy) techniques. It is reported in the literature that the effective lanthanide emission could be accomplished by conjugating the organic dyes, whose emission matches the absorption of lanthanides, so that it could act as antenna in transferring the absorbed energy to the lanthanides[187;188]. In line with this, fluorescent naphthalene sulfonates (ANDS and H-acid) were used as an antenna to transfer the absorbed energy. However, the fluorescent antenna conjugated lanthanides showed diminished fluorescence, due to the low level of loaded lanthanides inside the iron crystal lattice and further, the emission of naphthalene

sulfonates did not spectrally match with the lanthanides absorption wavelength (discussed in detail under section 2.6.1).

During the doping synthesis of magnetite, the iron (III) ions are replaced by different molar equivalents of either one or more lanthanide ions namely Gd(III), Eu(III) and Tb(III) as indicated in Table 2.1.2. The synthesis of Ln-doped USPIO (Ln-USPIO) was achieved in aqueous phase (single step) via co-precipitation of iron and lanthanide salts together. With increase in the amount of lanthanides replacing iron (i.e. up to 20%) did not lead to any fluorescence originating from the doped magnetic core. The nanoparticles were stored at pH 2 after doping, to prevent them from agglomeration. However, the doped lanthanides might get lost from the magnetite crystal lattice due to their storage under highly acidic solution that could promote leaching of the lanthanide from the crystal lattice. The reason for failure in generating Ln-USPIO is due to the considerable difference in size observed between iron (III) (Fe(III): 69.0 to 78.5 pm (cationic radius) and Fe(II): 75.0 to 92.0 pm (cationic radius)) and lanthanide (III) metal ions (Gd(III), Eu(III), Tb(III): 100.8 to 108.7 pm (cationic radius)), which does not facilitate replacement by lanthanides. In line with our observation, it was shown that only less amount of gadolinium (III) can be incorporated into the iron crystal lattice[189]. It was shown that using dextran polymers during doping synthesis might facilitate loading of more lanthanides into the iron crystal lattice. However, it is not fully demonstrated by the authors, how the fluorescence originating from Ln-USPIO could be efficiently used for optical imaging purposes both at the *in vitro* and *in vivo* levels[190]. In addition, Ln-USPIO could also be synthesized in organic phase which involves many steps and yields highly mono-dispersed magnetic crystals[191]. Inspite of their excellent physico-chemical properties, they do suffer from loss of fluorescence from lanthanides and from change in the magnetic properties compared to undoped magnetites. To increase the stability of the Ln-USPIO, and to prevent the leaching of the lanthanides from the crystal lattice of magnetites, they were further coated with either 3-aminopropyl trimethoxysilane (APTMS) or tetraethyl orthosilicate (TEOS) or via mixed coating of APTMS and TEOS in organic phase respectively. One of the main advantages of having magnetic nanoparticle surface covered with silica is the availability of free surface silanol groups that could react with coupling agents covalently in order to attach the target specific ligands[192;193]. For example, amine groups have been introduced on the surface of silica-coated magnetite nanoparticles by hydrolysis and condensation of an organosilane such as APTES (3-aminopropyl triethoxy silane), which facilitates further functionalization with biomolecules[194-196].

Prior to *in vitro* evaluation, the total iron concentration of APTMS coated Ln-USPIO was determined using ICP-MS. The results clearly indicated the drop in the iron

concentration after silica coating of non-doped magnetite synthesized using different base concentration (Table 2.1.3) in comparison to the uncoated ones as shown in Table 2.1.1. The drop in iron concentration may be attributed to loss of magnetic nanoparticles during the work up due to their extensive exchange between aqueous and organic phase. Contrarily, the total iron concentration of Eu-doped magnetic fluid synthesized using 1.5 M NaOH remained unchanged before and after silane coating.

The TEOS coating of the magnetic nanoparticles leaves free silanol groups, which could be used for further conjugation with biomolecules. These silanol groups were generated *in situ* through the hydrolysis and condensation reaction of the TEOS that occurs on the nanoparticles surface[197-199]. Further, the silica-coated magnetic particles were coated with APTMS to introduce stability as well as free amino groups that might enable further functionalization with biomolecules or fluorescent dyes (Figure 2.1.2). Silica coating of Ln-USPIO with TEOS and APTMS does not solve the problem of lanthanides leaching from the iron crystal lattice. Further, silica coating could also be influenced by different parameters like change in pH, solvents/solutions, temperature, stirring speed etc. Therefore, these paramaters have to be carefully tuned and checked in order to achieve a protective thin layer of silane coating respectively.

Table 2.1.2. Different types of generated lanthanides (Eu, Gd, Tb) doped USPIO coated with silane were listed in this table.

Fe molar percentage (%)	Lanthanides Molar percentage (%)		
	Eu (III)	Gd (III)	Tb (III)
95	5	-	-
95	-	5	-
95	-	-	5
90	-	5	5
98	-	2	-
98	-	-	2
96	-	2	2
96	2	2	-
96	-	2	2
85	15	-	-
80	20	-	-

Table 2.1.3. Total iron concentration of silica coated and Ln-USPIO (coated and silica uncoted) as determined by ICP-MS.

No.	Base	Iron cores (coated/uncoated)	Elements in the sample	Total iron concentration mg/mL
1.	1.5 M NaOH	coated	Fe,C,N,Si,O,H	1.575
2.	0.5 M NaOH	coated	Fe,C,N,Si,O,H	1.363
3.	1.0 M NaOH	coated	Fe,C,N,Si,O,H	2.619
4.	1.5 M NaOH	uncoated	Fe,O,Eu,H	10.125
5.	1.5 M NaOH	coated	Fe,C,N,Si,Eu,O,H	3.404

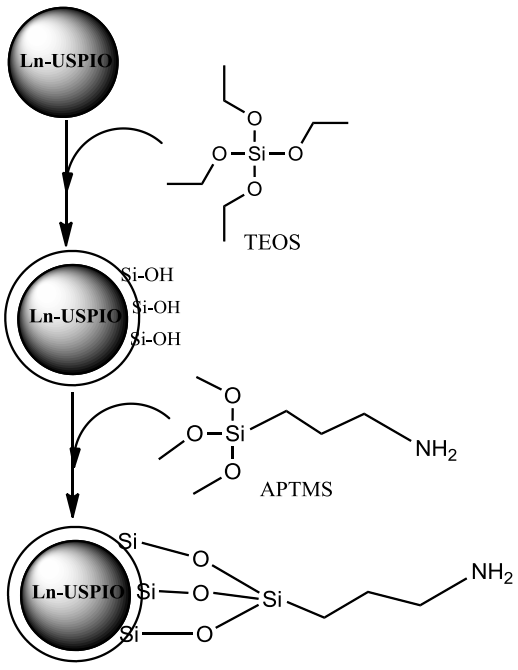

Figure 2.1.2. Schematic diagram of mixed silane coating (TEOS and APTMS) achieved for lanthanide (Eu,Gd,Tb)doped iron oxide nanoparticle.

2.6.1. Physico-chemical characterization of Ln-USPIO

The physical and chemical properties of Ln-USPIO were evaluated using TEM, powder XRD, fluorescence spectroscopy and ICP-OES techniques. Further evaluation of Ln-USPIO was not performed due to lack of plausible imaging properties (fluorescence and high magnetization) that are suitable for *in vivo* MR and optical imaging techniques.

TEM measurements indicated that there is difference observed in core diameters of Eu-doped magnetic nanoparticles synthesized by using different base concentration (0.5 and 1.5 M NaOH) respectively. TEM measurements of 5% Eu-doped USPIO coated with APTMS showed spherical nanoparticles with an average core diameters of 7.78 ± 1.35 nm (0.5 M NaOH) and 10.46 ± 1.41 nm (1.5 M NaOH) respectively (Figure 2.1.3A, 2.1.3B). In addition, TEM measurements of USPIO prepared by using base at different concentration and coated with APTMS also displayed spherical nanoparticles with an average core diameters of 12.73 ± 2.47 nm (0.5 M NaOH); 14.86 ± 2.79 nm (1.0 M NaOH); and 10.46 ± 1.81 nm (1.5 M NaOH) as shown in Figure 2.1.3C, 2.1.3E, 2.1.3D. TEM measurements of USPIO (0.5 M NaOH) coated with mixed silanes (APTMS and TEOS) displayed a mean core diameter of 10.35 ± 1.74 nm (Figure 2.1.3F). On comparing the core diameters of the doped nanoparticles with the non-doped ones, one could clearly visualize that lanthanide doping does not influence the overall mean core diameter of the nanoparticles. However, in contrast to the nanoparticles prepared by using 0.5 M NaOH, there are notable discrepancies over the mean diameter of the doped with the non-doped ones, which could be attributed to the problems associated with the synthesis strategy and size analysis.

The crystallinity and chemical composition of 2% Gd-doped USPIO coated with TEOS was measured using powder XRD technique. These measurements indicated that the nanoparticles are crystalline with low amounts of amorphous constituents (Figure 2.1.4). The diffraction patterns of doped nanoparticles coated with TEOS are in close agreement with the diffraction patterns reported for the magnetite, which clearly indicated that the lanthanide (Gd) incorporation into the crystal lattice is relatively low and it does not alter the crystal lattice of the magnetite.

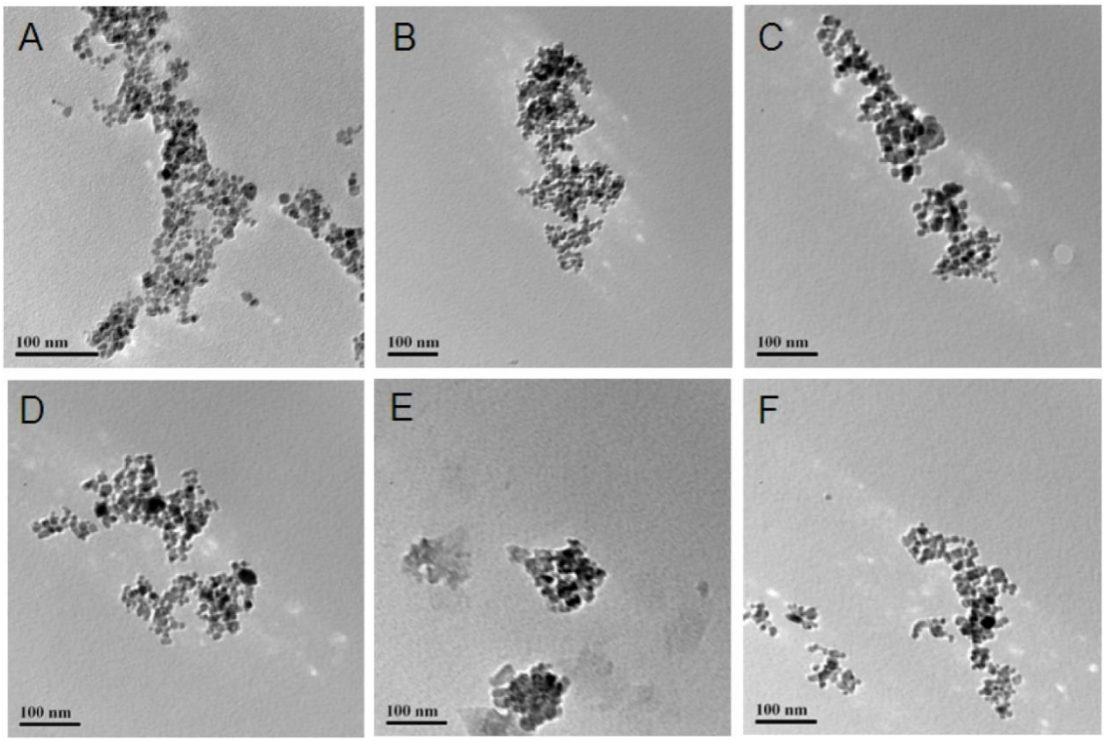

Figure 2.1.3. TEM images of 5% Eu-doped USPIO synthesized using 0.5 M NaOH and coated with APTMS (A); 5% Eu-doped USPIO (1.5 M NaOH) coated with APTMS (B); USPIO (0.5 M NaOH) coated with APTMS (C); USPIO (1.5 M NaOH) coated with APTMS (D); USPIO (1.0 M NaOH) coated with APTMS (E) and USPIO (0.5 M NaOH) coated with APTMS and TEOS (F) respectively.

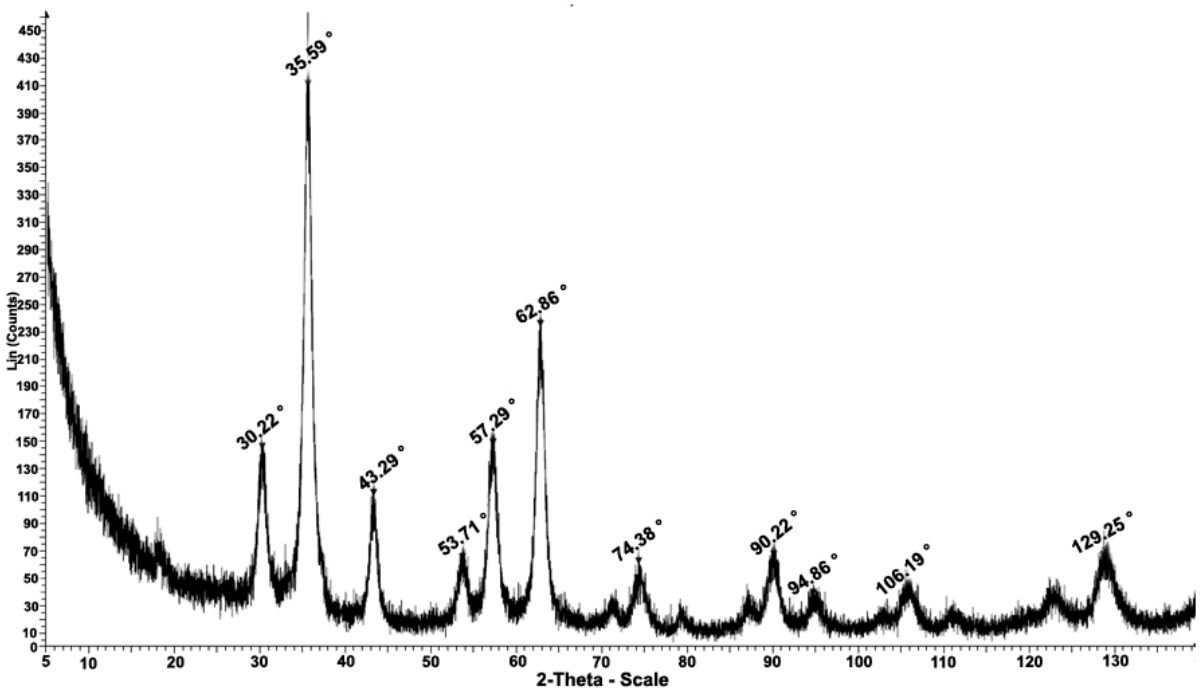

Figure 2.1.4. Powder X-ray diffraction pattern of 2% Gd doped USPIO coated with TEOS.

To generate fluorescence from the lanthanide, inside the Ln-USPIO nanoparticles, they were coated with aromatic molecules such as naphthalene sulfonates, which could act as an antenna in transferring the energy to the lanthanides. To this end, ANDS and H-acid (as ligands for antenna effect) are used for coating the lanthanide doped magnetic cores. Unfortunately, the anticipated energy transfer did not occur between the coated naphthalene sulfonates and the doped lanthanides due to relatively large difference between the emission wavelength of aromatic moieties and the excitation wavelength of lanthanides. Therefore, the naphthalene's failed to act as antenna´s in transferring energy to the lanthanides as shown via the absorption and fluorescence spectroscopy of 20% Eu-doped USPIO coated with ANDS (Figure 2.1.5A and 2.1.5B) and H-acid (Figure 2.1.5C and 2.1.5D) respectively. The spectra in Figure 2.1.5 clearly indicated that the absorption and emission originated only from the naphthalene sulfonates, which were coated over the Ln-USPIO despite of being loaded with lanthanides. Further, coating trials should be performed with a fluorophore which could spectrally overlap with lanthanide´s absorption respectively.

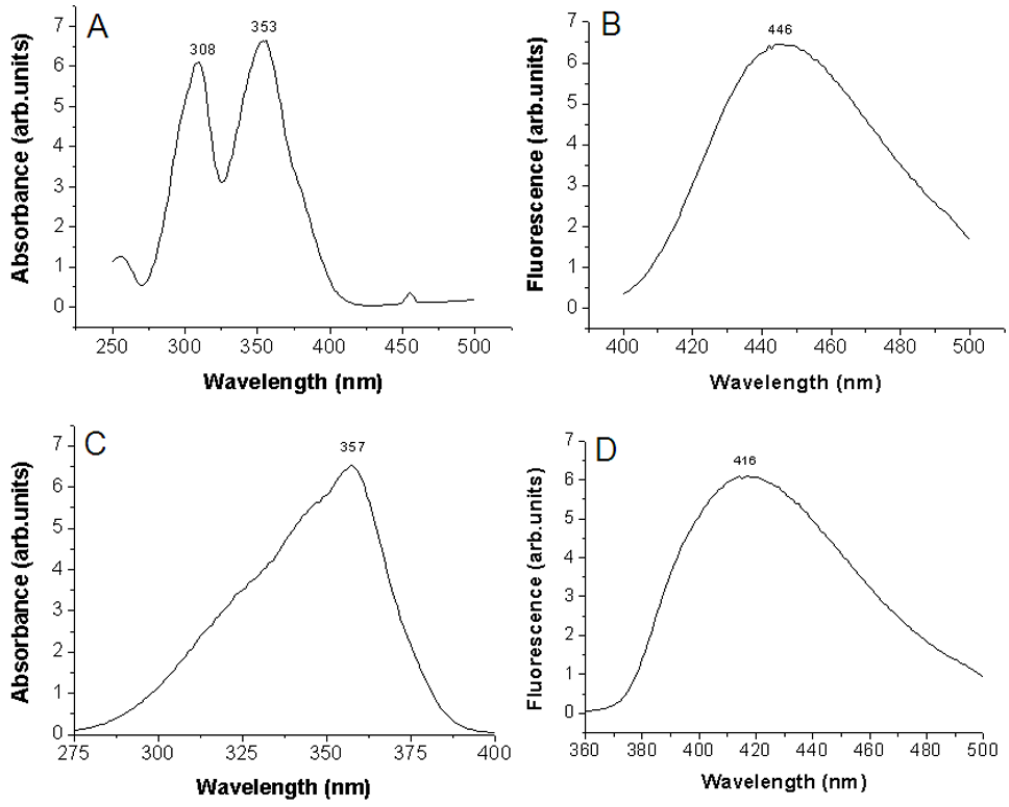

Figure 2.1.5. Absorption and fluorescence spectra of the magnetofluorescent nanoparticles in water. Absorption spectrum of 20% Eu-doped USPIO coated with ANDS (A); fluorescence spectrum of 20% Eu-doped USPIO coated with ANDS (B); absorption spectrum of 20% Eu-doped USPIO coated with H-acid (C); and fluorescence spectrum of 20% Eu-doped USPIO coated with H-acid.

The amount of lanthanide doped inside the crystal lattice of the iron oxide nanoparticles was measured by ICP-OES. These measurements explicitly showed that only very low percentage of lanthanides (Eu, Gd, Tb) were incorporated inside the core of the nanoparticles (Table 2.1.4). These observations are in line with reports that claimed low percentage of doped lanthanide inside the metallic nanoparticles[189].

Table 2.1.4. Weight percentage of lanthanides (Eu, Gd, Tb) in Ln-USPIO coated with silane as determined by ICP-OES.

Sample	Fe weight percentage (%)	Si weight percentage (%)	Eu weight percentage (%)	Gd weight percentage (%)	Tb weight percentage (%)
5 % Eu-USPIO-APTMS	2.736 ± 0.018	0.103 ± 0.001	0.024 ± 0.0002	-	-
5% Gd-USPIO-APTMS-TEOS	5.942 ± 0.030	0.304 ± 0.002	-	0.011 ± 0.0004	-
5% Tb-USPIO-APTMS-USPIO	4.983 ± 0.044	0.194 ± 0.001	-	-	0.009 ± 0.0004

Due to the lack of anticipated fluorescence and low loading of lanthanides in Ln-USPIO, these nanoparticles could not be employed as an ideal candidate for multimodal imaging techniques. In spite of different experimental trials in increasing the percentage of doped lanthanides in the iron nanoparticles, we were unable to develop a promising multimodal nanoparticle formulation that facilitates the bio-medical application. Therefore, the focus of the work was shifted in search of new molecules and iron nanoparticles (monodispersed) for generating the magnetofluorescent nanoparticles respectively.

2.7. Magnetofluorescent nanoparticles via dye conjugation (APTMS USPIO)

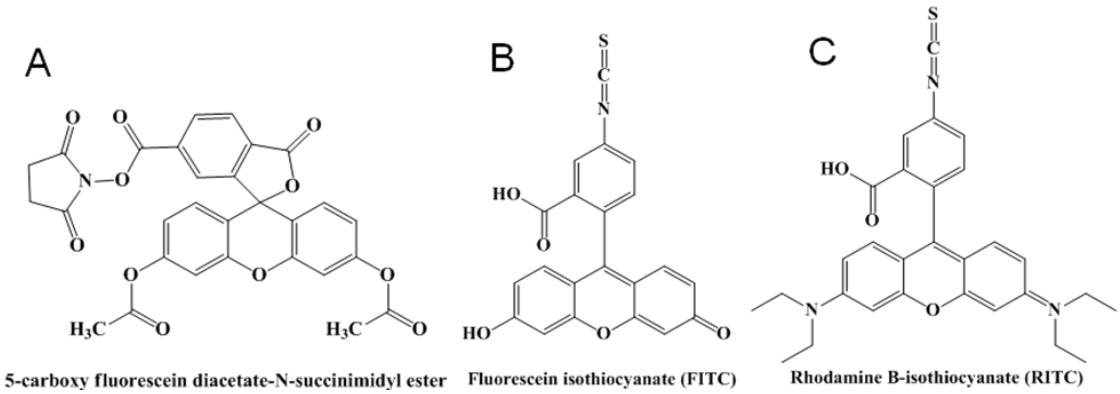

Figure 2.1.6. Chemical structures of different dyes conjugated to APTMS-USPIO. (A) 5-carboxy fluorescein diacetate-N-succinimidyl ester; (B) Fluorescein isothiocyanate (FITC) and (C) Rhodamine B-isothiocyanate (RITC) respectively.

The amino group available in the silane (APTMS) coated USPIO were conjugated to the fluorophores (FITC, RITC etc.) either through activated carboxylic groups (succinimidyl ester) (Figure 2.1.6A) or via isothiocyanate groups (Figure 2.1.6B, 2.1.6C). The conjugation of 5-carboxy fluorescein diacetate-N-succinimidyl ester occurs only under basic reaction conditions. The dye conjugation was achieved by incubation at low temperature in the dark respectively. The excess of unreacted dye was removed through dialysis against water at low temperature for 2 days. The fluorescence microscopy and spectroscopy techniques revealed reasonable fluorescence intensity for FITC and RITC nanoparticles (see appendices section). However, these nanoparticles suffered from low stability due to agglomeration, which could be attributed to the DMSO that was used to dissolve the fluorophores induces agglomeration on admixing with aqueous USPIO solution. In addition, the APTMS-USPIO was conjugated to biomolecules like streptavidin via well known glutaraldehyde conjugation techniques. Further, the FITC-labeled biotin (bio-FITC) was conjugated to the streptavidin functionalized nanoparticles at low temperature in the dark. The excess bio-FITC dye was removed by extensive dialysis against water at low temperature which was frequently monitored using fluorescence spectroscopy. However, due to insufficient conjugation and silane coating, these nanoparticules were de-stabilized due to agglomeration after storing them for extended period of time. Although, these conjugation techniques generated promising multimodal contrast agents for MR and optical imaging, these systems did not show stability under physiological conditions which paves way for further rigorous experiments.

2.8. Synthesis of NUSPIO nanoparticles

Due to the failure of Ln-USPIO in creating fluorescence suited for optical imaging, the second synthesis strategy for generating multimodal contrast agents was focused on non-polymeric coatings, which could be achieved via biocompatible naphthalene sulfonates respectively. Naphthalene USPIO (NUSPIO) nanoparticles were synthesized by coating USPIO with the non-polymeric molecules (ANDS and H-acid) to achieve a thin layer of coating at ambient temperature. After incubation, the modified USPIO was purified either by dialysis or by resin exchange technique.

NUSPIO were prepared using H-acid (80 mmoles/mL) and USPIO (10 mg/mL, pH 2) by incubation for 1h at ambient temperature[226]. Purification of the NUSPIO was performed using cellulose ester dialysis membrane with 10/100 kD molecular weight cut off or by using visking membrane (dialysis) with similar molecular weight cut off. Excess of uncoated H-acid was removed by dialysing NUSPIO against water at 4 °C. Slight reddish brown color originating due to the diffusion of unreacted H-acid into the water is observed after dialysing NUSPIO for 2-3 h. The dialysing water was replaced for every 4 h in order to facilitate removal of excess H-acid from NUSPIO which was often monitored using fluorescence spectroscopy. The final pH of the NUSPIO remains acidic (pH 4-5) after dialysis against water for 2-3 days. In order to increase their stability under physiological conditions which facilitate the *in vitro* and *in vivo* applications, NUSPIO were dialysed against solutions and buffers (pH 7) at low temperature (4 °C).

Resin exchange technique is also employed for the purification of NUSPIO by gliding them through the activated acidic resin and subsequently washed with water (several times) to remove the unreacted H-acid respectively. The resulting resin exchanged nanoparticles displayed pH 4 and further it was glided through the activated basic resin for neutralization. The total iron concentration of the NUSPIO was low after passing through the basic resin and further, due to washing several times with water. The NUSPIO after exchange with basic resin resulted only in agglomerated nanoparticles, which could be attributed to the acidic nature of H-acid which strongly interacts with the basic resin thus leading to the shearing of the coating from the surface of the nanoparticles. However, dialysing the NUSPIO against water at low temperature and further exchanging them with basic resin generated nanoparticles with reasonable stability. The NUSPIO displayed stability in buffers (HEPES, MES, MOPS), dextran, glucose solutions and in cell culture media respectively. NUSPIO displayed agglomeration when dialysed against PBS buffer and 0.15 M NaCl solution.

2.8.1. Physico-chemical characterization of NUSPIO

The physical and chemical properties of NUSPIO were evaluated using TEM, MRI, DLS, powder XRD, FT-IR, Raman, UV-Vis, fluorescence spectroscopy and cyclic voltammetry. The most relevant physical-chemical characterization results of NUSPIO required for the evaluation of its imaging properties (characteristics) are presented in this section.

NUSPIO were generated by coating the iron oxide nanoparticles with a thin layer of monomeric organic biocompatible molecules. These molecules attach to the iron oxide nanoparticles based on their fixation site i.e. phosphonates, phosphonic acids, sulfonic acids, carboxylic acids etc. The Figure 2.1.7 shows a binding mode of H-acid via two sulphonic acid groups to the iron oxide nanoparticles.

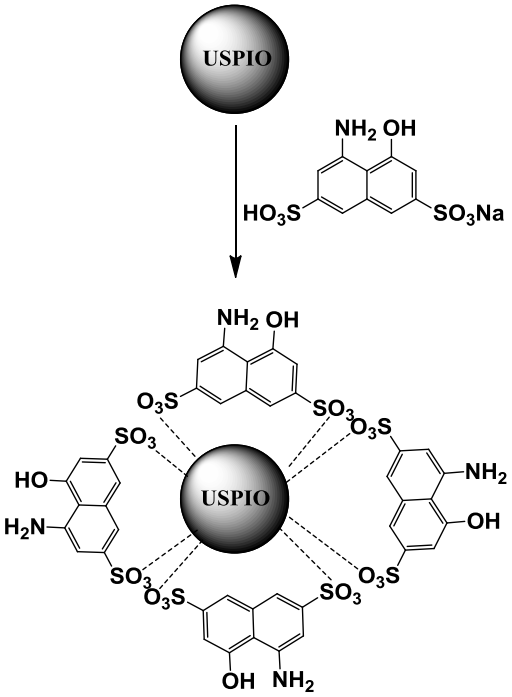

Figure 2.1.7. Schematic diagram shows the USPIO coated with non-polymeric H-acid respectively.

TEM measurements of NUSPIO indicated spherical morphology with low aggregation and displayed a significant change in the diameters of NUSPIO, prepared using different purification methods (dialysis and resin exchange technique) respectively. The anticipated core diameter for uncoated USPIO was about 10 - 15 nm. The core diameters of the NUSPIO generated by H-acid coating purified by dialysis against water and neutralized by PBS/0.15 M NaCl solution were 23.75 ± 5.93 nm and 19.11 ± 3.93 nm respectively (Figure 2.1.8A, 2.1.8B). The size of the nanoparticles after dialysis with PBS/NaCl increased due to anticipated agglomeration that occurred due to high concentration of phosphate anions

(PBS) and high ionic strength (NaCl). These observations might be attributed to the strong interaction of phosphate anions with USPIO compared to the naphthalene sulfonates (H-acid). Whereas, the core diameter of the NUSPIO generated by dialysis against water, and exchanged via basin resin for neutralization resulted in 12.51 ± 1.93 nm (Figure 2.1.8C). In addition, the average diameter of the iron oxide nanoparticles doped with 10% H-acid (pH ~ 5) dialysed against water indicated 10.08 ± 1.74 nm (Figure 2.1.8D) without showing any deviation from the expected mean diameter of the nanoparticles. Increase in pH (pH 7) of the H-acid-doped USPIO may lead to agglomeration and will result in increase in overall diameters of the nanoparticles. The stability of these nanoparticles could be increased without any agglomeration by dialysing against HEPES buffer (pH 7.2).

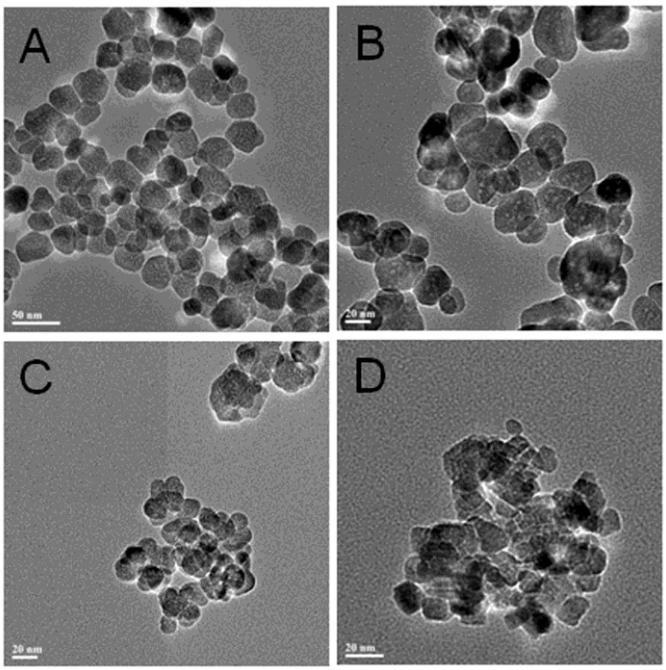

Figure 2.1.8. TEM images of NUSPIO (H-acid) purified by different ways: (A) dialysed against water and PBS; (B) dialysed against water and NaCl solution (0.15 M); (C) dialysed against water and neutralized by exchange with basic resin (amberlite IRA 95); and (D) USPIO doped with 10% H-acid and dialysed against water. All dialysis procedures were carried out at low temperature.

Dynamic light scattering (DLS) results of NUSPIO (H-acid) purified by dialysis against water and neutralized by different buffers are shown in Figure 2.1.9. Nanoparticles with low hydrodynamic diameter (D_h) was reported to foster reasonable pharmacokinetic characteristics thus facilitating their intended *in vivo* application[200]. The D_h of 10% H-acid doped USPIO after dialysis against water displayed few micrometers (~2 µm; Figure 2.1.9A). The large D_h could be attributed to the agglomeration that occurred due to lack of protective coating for the iron oxide nanoparticles. NUSPIO after dialysis against water and HEPES buffer exhibited a mean D_h around 300 nm (Figure 2.1.9B). However, NUSPIO prepared

after purification by dialysis against water and neutralized by 0.15 M NaCl, and PBS buffer showed mean D_h of 600 nm (Figure 2.1.9C) and 1 µm (Figure 2.1.9E) respectively. In addition, NUSPIO purified by dialysis against water and neutralized by exchanging them with basic resin displayed mean D_h of about 300 nm with an additional size distribution at 1 µm (Figure 2.1.9D). These D_h results clearly show that NUSPIO agglomerates heavily in the PBS buffer and in addition, the role of basic resin in removing excess H-acid is questionable due to their inefficiency in discriminating the monodispersed nanoparticles fraction from their agglomerated counterparts. The NUSPIO prepared by dialysis against water and neutralized by NaCl solution displayed a large D_h due to high concentration of salts that induce agglomeration. The commercially available USPIO (EMG 911) with 10 nm core diameter, dispersible in toluene were used as control nanoparticles (as gold standard) for evaluating the characteristics of NUSPIO. The H-acid coating of EMG 911 was achieved in 3 days by using two phase (aqueous and organic) system and purified by dialysis against water at low temperature. The H-acid coated EMG 911 indicated D_h around 50 nm (Figure 2.1.9F). The two phase reaction system between H-acid and EMG 911suffered from slow reaction and low reaction yield due to the insufficient interaction of H-acid with the surfactant covered EMG 911 surface respectively.

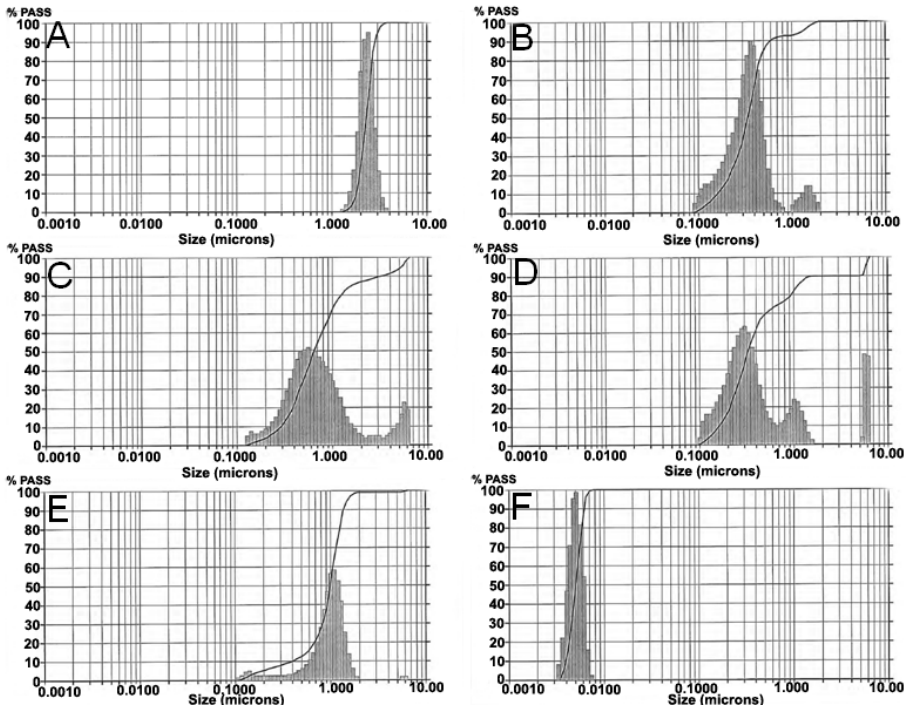

Figure 2.1.9. Hydrodynamic size analysis (DLS) of NUSPIO (H-acid) and purified by different methods (dialysis and resin exchange technique): A-F: (A) USPIO doped with 10% H-acid and dialysed against water; (B) dialysed against water and HEPES buffer; (C) dialysed against water and 0.15 M NaCl solution; (D) dialysed against water and neutralized by exchange with basic resin (amberlite IRA 95); (E) dialysed against water and PBS buffer; and (F) EMG 911 coated with H-acid and purified by dialysis against water.

The crystal structure of the NUSPIO purified by dialysis against water was confirmed by powder XRD measurements. These XRD results indicated that NUSPIO are crystalline with negligible amounts of amorphous constituents (Figure 2.2.0), which was in close agreement with the reported diffraction patterns emerging from the crystal structure of magnetite. However, as expected additional peaks with very low intensities related to the diffraction patterns of haematite are also found in Figure 2.2.0, which could be attributed to the discrepancies arising due to the utilized synthesis strategy (co-precipitation).

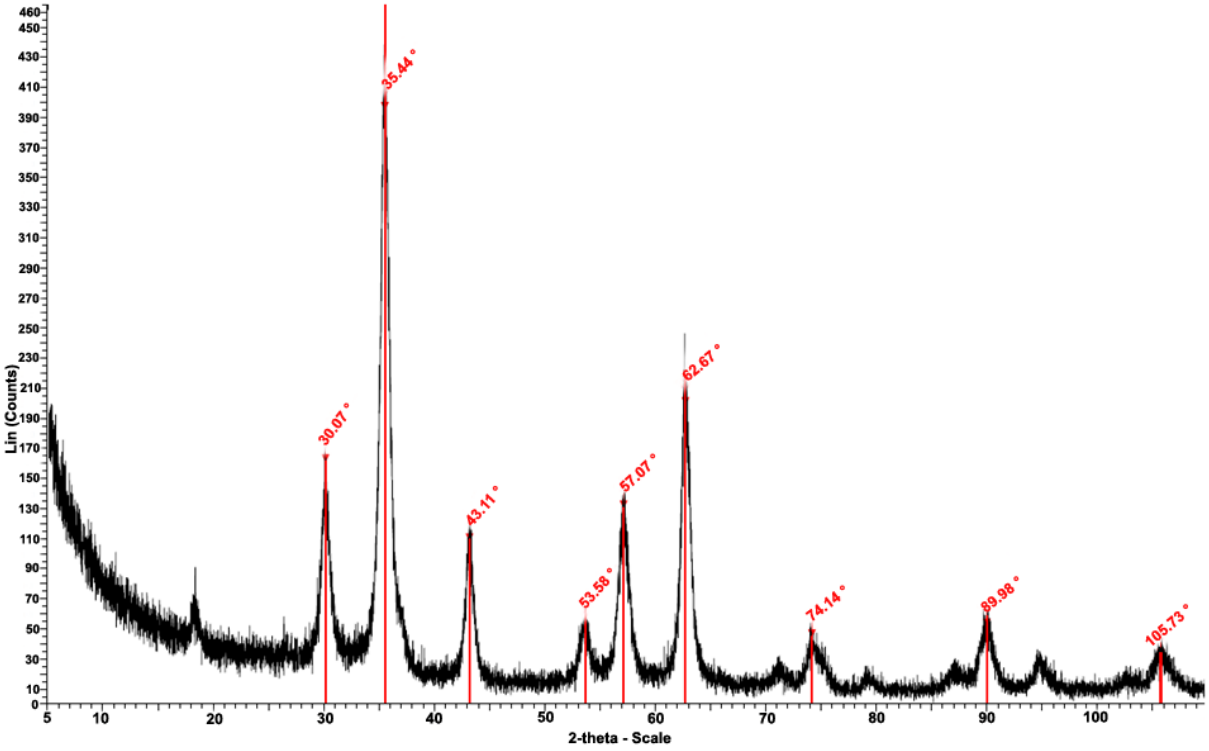

Figure 2.2.0. Powder diffraction pattern of NUSPIO (H-acid) purified by dialysis against water at low temperature.

The MR relaxivity measurements of the NUSPIO were performed in buffers (HEPES, PBS) or in de-ionized water at RT using a clinical MR scanner (Siemens Symphony, 1.5 T). The high relaxivities and contrast enhancement of iron oxide nanoparticles obtained in MRI are highly dependent on the crystalline nature of the iron cores respectively[201;202]. In line with this, the NUSPIO purified by dialysis against water and HEPES buffer displayed high relaxivity values with r2 = 138.12 ± 4.25 $s^{-1}mM^{-1}$ and r1 = 1.0058 ± 0.45 $s^{-1}mM^{-1}$ respectively (Figure 2.2.1A). These NUSPIO neutralized by HEPES buffer displayed stability and exhibited high T_2 relaxation times without showing any visible agglomeration under the influence of the external magnetic field of (1.5 T). The relaxivity values of NUSPIO purified by dialysis against water and PBS buffer were r2 = 81.99 ± 4.54 $s^{-1}mM^{-1}$ and r1 = 4.7917 ± 0.42 $s^{-1}mM^{-1}$ (Figure 2.2.1B). However, these NUSPIO stabilized by PBS buffer showed relatively low stability (high agglomeration) due to the shearing of the H-acid coating

because of their strong interaction of phosphate anions with the nanoparticle surface compared to the sulfonates. Therefore, the insufficient surface coverage of iron oxide nanoparticles by H-acid leads to observed low relaxivity values.

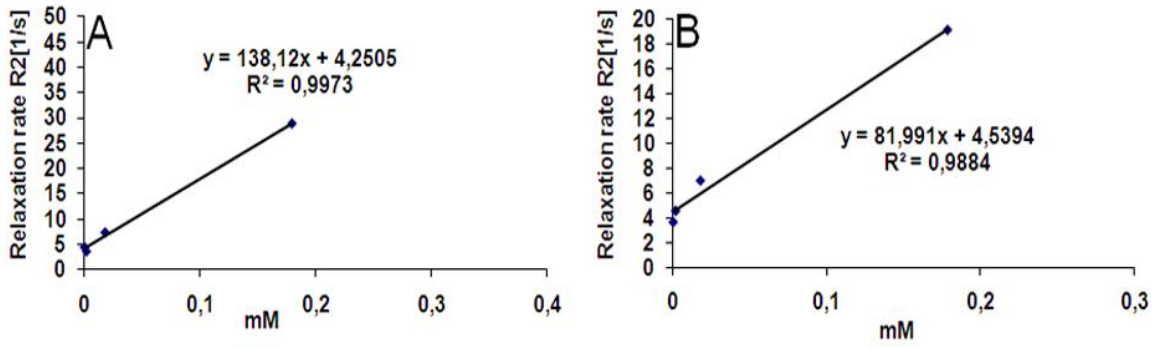

Figure 2.2.1. MR relaxivity of NUSPIO (H-acid) purified by dialysis. A-B: dialysis against water and HEPES buffer (A); and dialysis against water and PBS buffer (B) respectively.

Functional groups in H-acid and NUSPIO were characterized by using FT-IR spectroscopy [Perkin Elmer - Spectrum 100 FT-IR Spectrometer] using the KBr pellet technique with a resolution of 4 cm^{-1}. USPIO showed anticipated ν(Fe-O) bands at 562 and 627 cm^{-1}. H-acid displayed unbound ν(S=O) bands at 1072 and 1090 cm^{-1}; ν(S-O) band at 869 cm^{-1}; ν(SO_3^-) asymmetric stretch bands at 1147,1167,1188 and 1221 cm^{-1}; and ν(SO_3^-) symmetric stretch band at 1030 cm^{-1} respectively (Figure 2.2.2A). The ν(S-O) band disappeared due to binding of H-acid in NUSPIO which indicated the binding of the sulfonate groups to the nanoparticles. The ν(S=O) band of H-acid in NUSPIO shifted to 1041 cm^{-1} and ν(SO_3^-) asymmetric stretch band shifted to 1183 cm^{-1}. Additionally, an intense broad band appeared at 575 cm^{-1} after binding of H-acid with USPIO (Figure 2.2.2B).

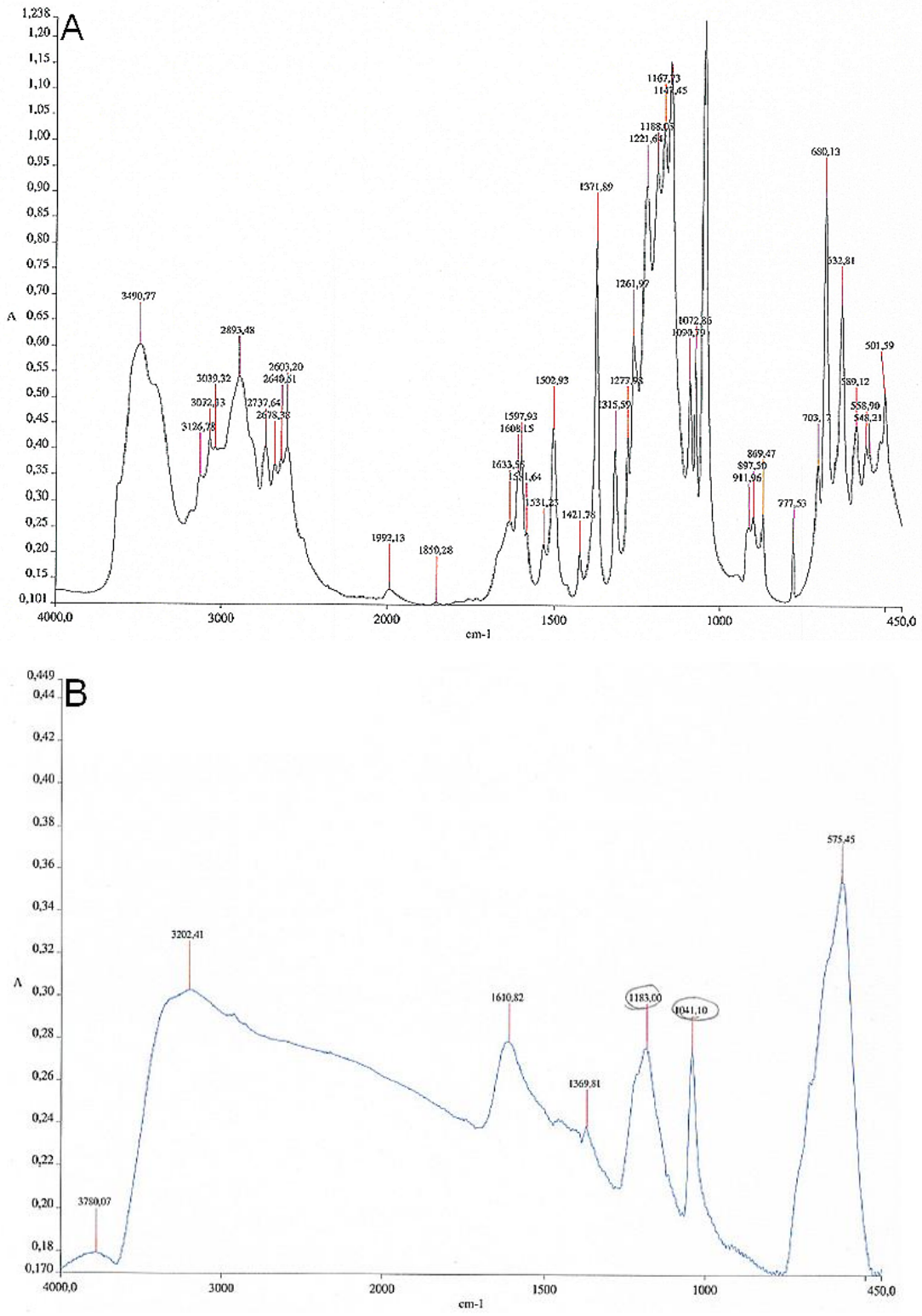

Figure 2.2.2. FT-IR spectra of (A) H-acid; and (B) NUSPIO (H-acid).

The fluorescence properties of H-acid were evaluated using fluorescence spectroscopy. The fluorescence emission of H-acid in water occurred at 430 nm when excited at 340 nm or at 360 nm. The fluorescence spectroscopy results showed a red shift in the emission maxima of H-acid (416 to 430 nm) with increase in pH , which could be attributed

to the deprotonation of H-acid at alkaline pH (Figure 2.2.3A) and further due to the phototautomerization that occurs in the excited state[203]. Furthermore, under acidic conditions, H-acid exists in the protonated form and displayed a blue shift with decreased fluorescence intensity. Additionally, a peak at 380 nm with very low fluorescence intensity was also observed under acidic conditions (Figure 2.2.3A).

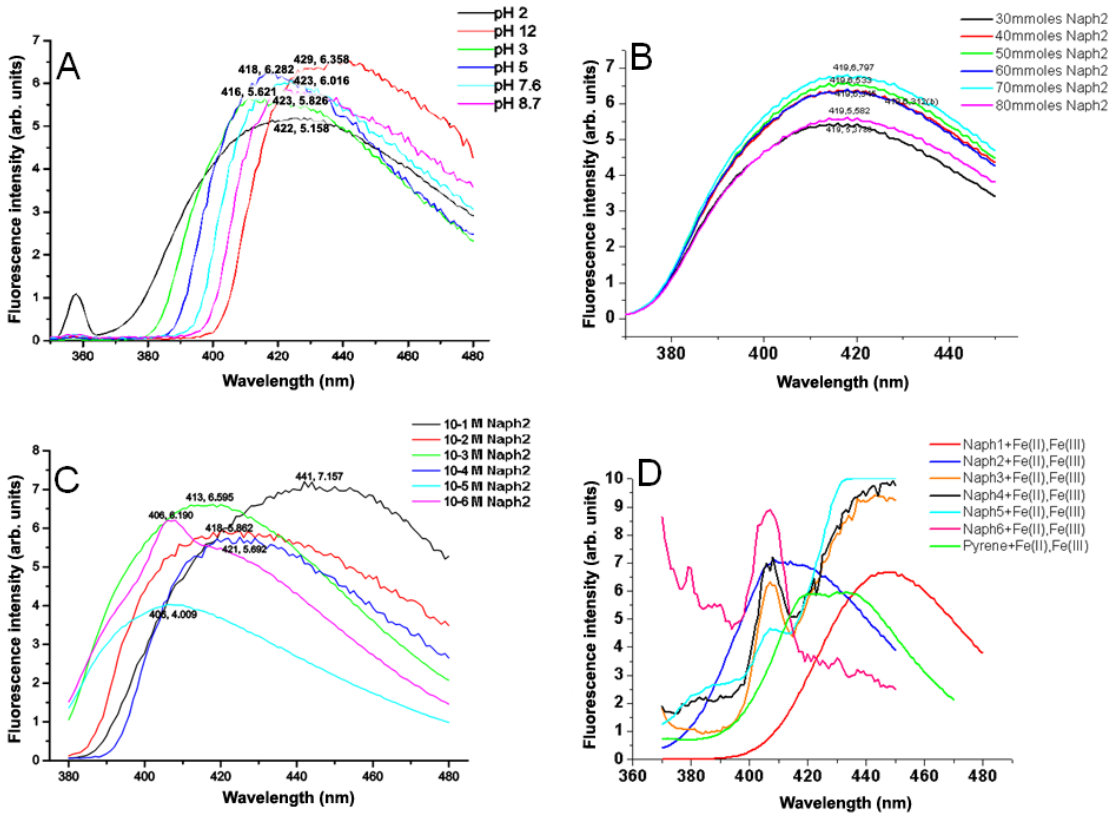

Figure 2.2.3. Fluorescence emission spectra of H-acid shown in water. A-F: (A) H-acid in different pH (pH 2 - 12) ; (B) different H-acid coating concentration (30 – 80 mmoles); (C) different H-acid concentration (10^{-1} M to 10^{-6} M) and (D) change in fluorescence of different naphthalene sulfonates and pyrene sulfonate after addition of Fe(II) and Fe(III) ions respectively.

H-acid is known to exist in two forms (i.e. protonated and as zwitterions) in the excited state under acidic conditions or in neutral solution (pH 7)[204]. The fluorescence spectra of H-acid in water indicated an increase in the fluorescence intensity with increasing H-acid coating concentrations (30-80 mmoles) (Figure 2.2.3B). Further, the fluorescence emission maxima of H-acid under acidic conditions were red shifted (405 nm to 441 nm) with increase in concentration (10^{-6}M to 10^{-1}M) (Figure 2.2.3C). The change in fluorescence of ANDS, H-acid, Naphthol blue black (Naph 3), 1-hydroxy-3,6-naphthalene disulfonic acid monosodium salt (Naph 4), 3-hydroxy-2.7-naphthalene disulfonic acid monosodium salt (Naph 5), Sodium 5-acetamido-4-hydroxy-3-(phenyldiazenyl) naphthalene-2,7-disulfonate (Naph 6), and pyrene trisulfonic acid after addition of aqueous solution of iron salts

($2Fe^{3+}/Fe^{2+}$) was studied by fluorescence spectroscopy (Figure 2.2.3D). Addition of iron salts to different naphthalene sulfonates and pyrene sulfonate resulted in the formation of coordination complexes that displayed distinct color with small change in fluorescence emission compared to free ligands (color, fluorescence) respectively. Further, ammonia addition to these complexes resulted in the generation of iron oxide nanoparticle via quick degradation of the coordination complexes (see appendices section for further fluorescence spectra). The fluorescence ability of USPIO (10 mg/mL) coated with ANDS and H-acid (80 mmoles/mL) were evaluated using fluorescence microscopy. The NUSPIO coated with ANDS and purified by dialysis (water, PBS/HEPES buffer) displayed blue fluorescence under the fluorescence microscope. (see appendices section).

2.8.2. In vitro results of NUSPIO

The biocompatibility of NUSPIO was evaluated using different assays (TUNEL and LDH assays) and trypan blue staining. Further, the cellular uptake of NUSPIO was evaluated using fluorescence microscopy respectively.

The cytotoxicity was evaluated using the TUNEL assay in which RPMI8226 cells were incubated with NUSPIO (H-acid) for 3 h. The TUNEL positive cells (apoptotic cells) were stained red by the TUNEL reagents and nuclei of the cells were stained blue with DAPI (Figure 2.2.4). The TUNEL positive and negative cells were counted using fluorescence microscope with 10X magnification by choosing five to six fields of view.

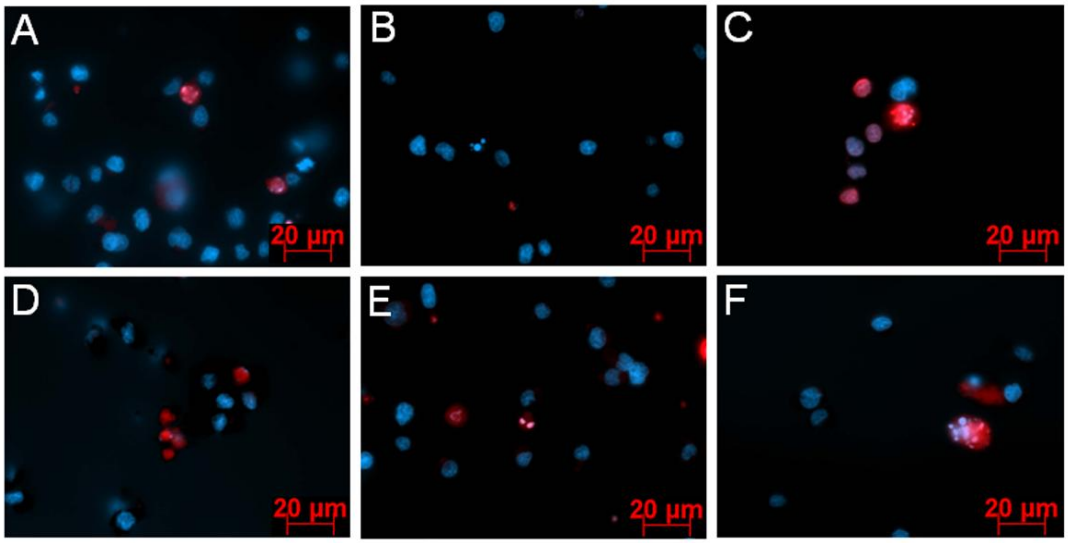

Figure 2.2.4. Cytotoxicity of NUSPIO (H-acid) determined by using TUNEL assay. RPMI8226 cells incubated for 3 h with NUSPIO. A-F: (A) Medium; (B) TUNEL negative control; (C) TUNEL positive control; (D) NUSPIO (3.0 µmol/mL); (E) NUSPIO (0.3 µmol/mL); and (F) NUSPIO (0.03 µmol/mL).

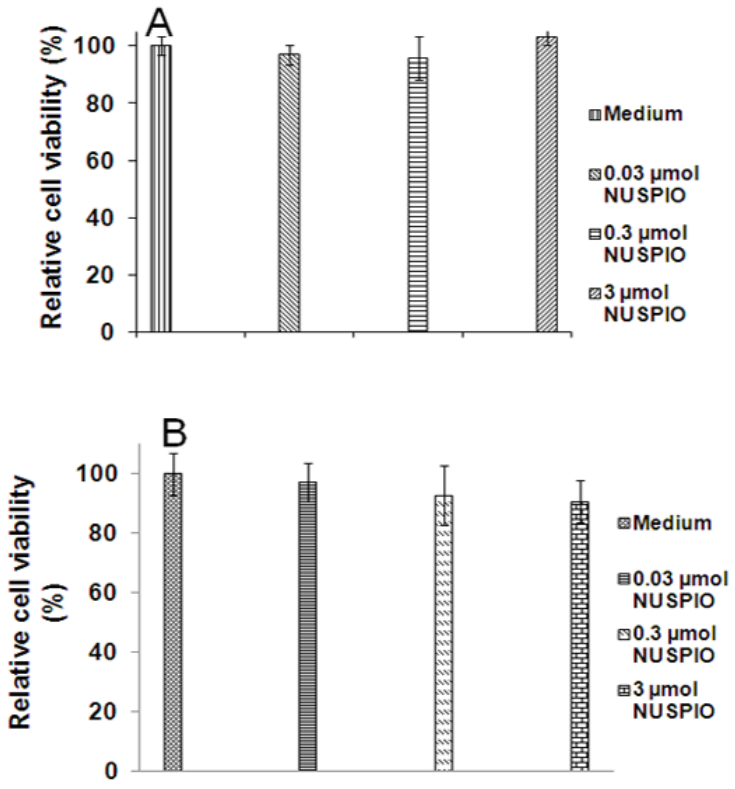

Figure 2.2.5. Cytotoxicity of NUSPIO (H-acid) was evaluated using TUNEL assay and trypan blue staining. TUNEL assay was performed by incubating RPMI8226 cells for 3 h with NUSPIO (A); and Trypan blue staining was performed for RPMI8226 incubated with NUSPIO (3 h) (B) respectively. Data presented as mean ± SD (n=3).

The relative cell viability of RPMI8226 cells (0.5 x 10^6 cells) after treatment with NUSPIO (3h) were calculated relative to the total viable cells available in the medium control (treated as 100% cell viability). The assay was performed in triplicates. With increase in NUSPIO concentration from 0.03 µmol Fe/mL to 3.0 µmol Fe/mL, the cells did not show any relevant loss in cell viability and they also well tolerated the high dosage of NUSPIO (3.0 µmol Fe/mL) (Figure 2.2.5A). The high viability exhibited by cells incubated with 3.0 µmol Fe/mL of NUSPIO compared to the control (medium) could be attributed to the error associated with cell counting under the fluorescence microscope.

Cytotoxicity results from trypan blue staining of RPMI8226 cells (2 x 10^6 cells) incubated with NUSPIO (3 h) revealed only a slight decrease in cell viability. The cytotoxicity results also indicated a direct correlation that prevailed between the cell viability and the NUSPIO concentration in the growth medium. With 3.0 µmol Fe/mL of NUSPIO there was a slight decrease in the cell viability compared to the control cells (medium) respectively (Figure 2.2.5B).

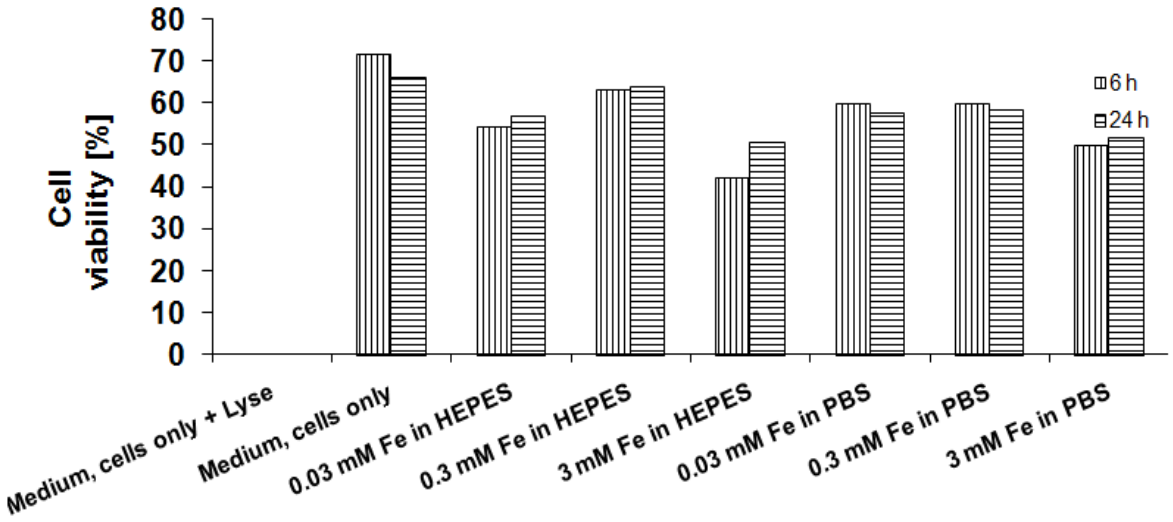

Figure 2.2.6. Cytotoxicity of NUSPIO (H-acid) evaluated using LDH assay in which RPMI8226 cells were incubated with NUSPIO for 6 hand 24 h in three different concentration (3.0, 0.3, 0.03 µmol Fe/mL) respectively.

Additionally, the cytotoxicity induced by NUSPIO on RPMI8226 cells was studied using LDH assay. Here, RPMI8226 cells were incubated (6 h, 24 h) with NUSPIO (H-acid) purified by dialysis against water and neutralized by HEPES/PBS buffers in triplicates and at three different iron concentrations (3.0, 0.3, 0.03 µmol Fe/mL). The positive control was generated by lysing the cells using a lysis buffer. The cells without NUSPIO treatment served as a negative control. The LDH assay indicated decreased cell viability with 3 µmol Fe/mL of NUSPIO after 6 h and 24 h incubation (Figure 2.2.6). Further, the decrease in viability of cells incubated with NUSPIO stabilized in HEPES buffer (3 µmol Fe/mL) compared to NUSPIO stabilized in PBS buffer could be attributed to low toxicity induced by HEPES in specific cell types (reported) or due to the error associated with the measurements that originated due to the interaction of NUSPIO in the medium and LDH at high concentrations. However, in the case of other NUSPIO concentration (0.3, 0.03 µmol Fe/mL) at different incubation times, there was no relevant loss in cell viability.

The intracellular uptake of NUSPIO (ANDS) in PC-3 (prostate cancer) and MDA-MB-231(breast cancer) was evaluated using fluorescence microscopy. Both cell types were incubated (3 h) in triplicates with medium (Figure 2.2.7A, 2.2.7D), ANDS (3 µmol/mL; Figure 2.2.7B, 2.2.7E) and NUSPIO (3 µmol Fe/mL; Figure 2.2.7C, 2.2.7F) respectively. The cells highly internalized ANDS which was shown by their blue fluorescence inside the two different cell types (2.2.7B and 2.2.7E) respectively. However, the cells did not show fluorescence (blue) from the NUSPIO (ANDS) which could be attributed to quenching of ANDS fluorescence (ANDS excited state tautomerization and paramagnetic USPIO). Furthermore, the internalization of NUSPIO could be observed from Figure 2.2.7C and 2.2.7F (images (bright field) without fluorescence overlay), which should be further

supported and validated using Prussian blue staining for internalized NUSPIO nanoparticles respectively.

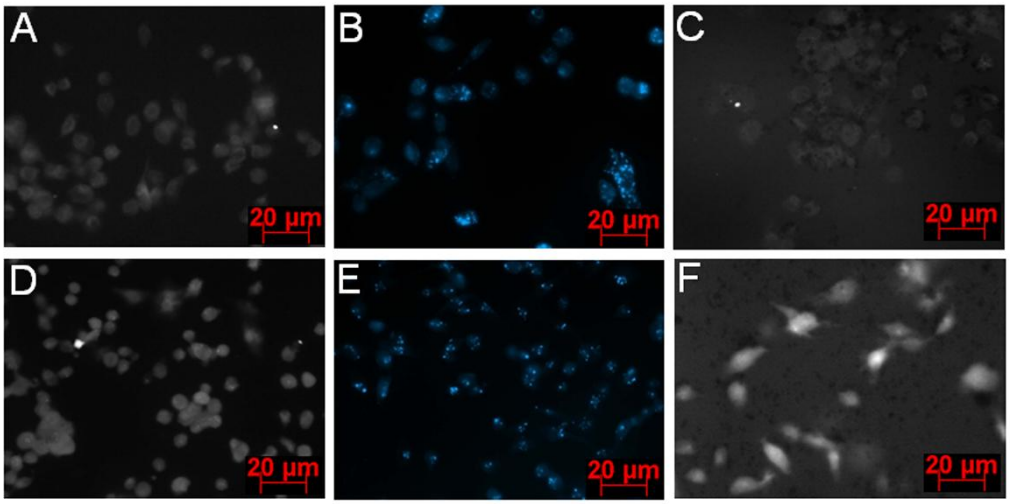

Figure 2.2.7. Cellular uptake studies of NUSPIO (ANDS) by PC-3 and MDA-MB-231 cells after 3 h studied using fluorescence microscopy. Bright field image of PC-3 cells incubated with medium (A); fluorescence image of PC-3 incubated with ANDS (3.0 µmol/mL) B-C: fluorescence image of PC-3 incubated with ANDS (3.0 µmol/mL) (B) and NUSPIO (3.0 µmol Fe/mL). Bright field image of MDA-MB-231 incubated with medium (D); E-F: fluorescence image of MDA-MB-231 incubated with ANDS (3.0 µmol/mL) (D) and NUSPIO (3.0 µmol/mL) (E) respectively.

2.9. USPIO coated with different naphthalene sulfonates

USPIO (2 mg/mL) were coated with different naphthalene sulfonates (30,40,50 mmol/mL) like sodium 4-hydroxy-5-oleamido-7-sulfonaphthalene-2-sulfonate (compound **10**), potassium 7-oleamido-3-sulfonaphthalene-1-sulfonate (compound **11**), potassium (s)-7-(2-amino-3-(1H-indol-3-yl)propanamido)-3-sulfonaphthalene-1-sulfonate (compound **9**), 1-(6-hydroxy-2-naphthoyloxy)ethane-1,1-diyldiphosphonic acid (compound **8**), sodium 3,3-(1´Z)-(4,4´-((E)-ethene-1,2-diyl)bis(4,1-phenylene))bis(diazene-2,1-diyl)bis(5-amino-4-hydroxynaphthalene-2,7-disulfonate) (compound **5**), sodium 3,3´-(1´Z)-(4,4´-((E)-ethene-1,2-diyl)bis(3-sulfonato-4,1-phenylene))bis(diazene-2,1-diyl)bis(5-amino-4-hydroxynaphthalene-2,7-disulfonate) (compound **6**) by incubation for 1 h at ambient temperature. After incubation, the naphthalene sulfonates coated nanoparticles were purified by washing several times with water aided by a permanent magnet. NUSPIO synthesized using compound **10** and **11** displayed a reasonable blue fluorescence, and exhibited a low degree of agglomeration respectively.

However, NUSPIO synthesized by using compounds **5**,**6**,**8** and **9** for coating at different concentration did not show any fluorescence (because of the quenching that occurred due to the interaction of hybrid H-acid/ANDS moiety with the paramagnetic

USPIO) and some of them were highly unstable due to strong agglomeration which originated from insufficient surface coverage of iron oxide nanoparticles.

2.9.1. USPIO coated with new non-polymeric ligands

In line with the previous non-polymeric coating strategy, USPIO were coated with some new ligands like 2-(6-hydroxy-2-napthamido)ethylphosphonic acid (compound **7**), 4-(4-((R)-hydroxy((2S,4S,8R)-8-vinylquinuclidin-2-yl)methyl-6-methoxyquinolinium-1-yl)butane-1-sulfonate (compound **4**), 4-(9-aminoacridinium-10-yl)butane-1-sulfonate (compound **3**), thiamine monophosphonic acid (TMP), sodium 8-hydroxy-3,6-dihydropyrene-1,3,6-trisulfonate by 1 h incubation at ambient temperature. After incubation, the nanoparticles were purified by removing the unreacted ligands via water washing guided by a permanent magnet. The sulfonates based non-polymeric ligand system did not provide nanoparticles with better coating and often resulted in quenching and agglomeration. Therefore, phosphonic acid based ligand system such as TMP was employed to achieve the coating for USPIO, which displayed sufficient fluorescence and reasonable stability under physiological conditions for few days (~3 days). However, with increase in the storage time TMP coated USPIO resulted in agglomeration.

In conclusion, NUSPIO prepared using ANDS displayed low fluorescence emission compared to NUSPIO prepared via H-acid (quenched fluorescence), which makes them unsuitable for MR and optical imaging. In spite of the enormous experimental work in generating NUSPIO with blue fluorescence, we were unable to develop a formulation which could ideally serve as an appropriate candidate for both imaging techniques. Therefore, the search for biocompatible ligands, which could be used for generating fluorescent, non-polymeric coated monodispersed USPIO, was performed.

2.10. Synthesis of FLUSPIO nanoparticles

The first two synthesis strategies i.e. Ln-USPIO and NUSPIO, failed in generating magnetofluorescent nanoparticles suitable for cellular labeling and MR *in vivo* imaging. Therefore, the flavins received much attention as the coating molecules due to their characteristics such as biocompatibility, inherent fluorescence, phosphate groups and targeting ability respectively. These flavin (FMN) decorated USPIO were utilized as versatile MR contrast agent via more pronounced RCP targeting and designated as fluorescent USPIO (FLUSPIO) respectively.

USPIO nanoparticles prepared by co-precipitation were coated with non-polymeric fluorescent FMN, which strongly binds to the iron oxide core via phosphate groups (Figure

2.2.8a). The FMN coating was achieved in aqueous solutions of USPIO and FMN (at pH 4) under sonication at ambient temperature. The coating of USPIO with FMN alone did not lead to an efficient and stable coverage of the entire nanoparticle surface, which might be due to steric hindrance caused by the isoalloxazine ring of FMN. Consequently, by visual inspection nanoparticle sediments were found indicating nanoparticle agglomeration. In addition, the nanoparticle surface should not be covered entirely with FMN due to the quenching of green fluorescence that occurs at high concentrations. GMP is less bulky and contains a phosphate group (similar to that of FMN), which strongly chemisorbs to the iron oxide surface during the non-polymeric coating. Both, FMN and GMP are negatively charged molecules and their binding to USPIO results in a negative surface charge of FLUSPIO at pH 7.0, thus providing colloidal stabilization. Therefore, the addition of GMP was necessary to stabilize the colloidal suspension and to complete the surface coverage. Furthermore, GMP also allows for further functionalization with biomolecules (peptides, antibodies etc.) using standard conjugation techniques via the amine group available in the guanine moiety.

2.10.1. Physico-chemical characterization results of FLUSPIO

The physical and chemical characteristics of generated FLUSPIO were evaluated using different techniques such as transmission electron microscopy (TEM), scanning electron microscopy (SEM), atomic force microscopy (AFM), dynamic light scattering (DLS), powder X-ray diffraction (XRD), superconducting quantum interface device (SQUID), thermogravimetric analysis (TGA), energy dispersive X-ray absorption (EDX), fluorescence spectroscopy, fourier transform infrared spectroscopy (FT-IR), magnetic resonance imaging (MRI), time of flight secondary ion mass spectrometry (TOF-SIMS), X-ray photoelectron spectroscopy (XPS), fluorescence quantum yield. Characterization results from AFM. XPS, quantum yield, TOF-SIMS, powder XRD are presented in the appendices section.

Transmission electron microscopy (TEM), dynamic light scattering (DLS) and scanning electron microscopy (SEM) were used to characterize the FLUSPIO. TEM analysis of USPIO, and FLUSPIO showed nanoparticles with an average iron core diameter of 5 ± 1 nm (Table 2.1.5 and Figure 2.2.8b-c). SEM was used to study the surface morphology of the nanoparticles. SEM images of USPIO and FLUSPIO confirmed the spherical surface morphology, with an average particle diameter of 23.19 ± 4.62 nm (USPIO) and 27.76 ± 4.76 nm (FLUSPIO) (Figure 2.2.8d-e). The increase in size observed in SEM could be attributed to the clustering of the nanoparticles that occurs due to drying and/or to the conductive layer of sputtered gold on the nanoparticles surface. The thin layer of non-polymeric coating yields nanoparticles with a low hydrodynamic diameter (D_h) which enhances the uptake of

nanoparticles into tissues[226]. The FLUSPIO in HEPES buffer showed an average (D_h) of 97 ± 3 nm with a low polydispersity index (PDI) of 0.16. The broad average D_h, which can be observed in Figure 2.3.2a-b, is an average of several runs, which displayed similar D_h with comparable PDI values. The increase in average D_h of FLUSPIO in HEPES buffer may derive from the hydration shell and could be further increased by minor agglomeration which arises from the tendency of smaller iron cores to form clusters, which are not sterically stabilized by FMN and GMP. However, these DLS results of FLUSPIO are in line with the characteristics of clinically approved/used MR contrast agent Resovist (4 nm core size), which displayed D_h around ~60 nm. In comparison to FLUSPIO, USPIO, show stability only at pH 2 without any surface coverage with coating molecules, and displayed a large D_h with a broad size distribution at pH 7 (252 ± 66 nm), due to aggregation between the iron cores at increasing pH (Table 2.1.5 and Figure 2.3.2a-b).

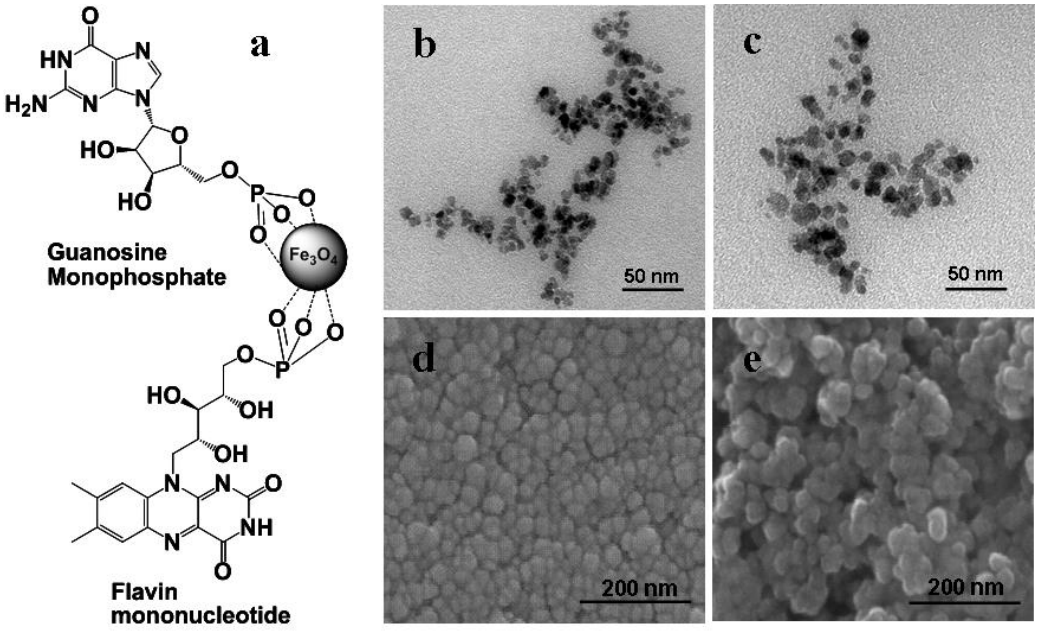

Figure 2.2.8. Preparation of FLUSPIO. a: Schematic diagram showing the mode of binding of FMN and GMP to the iron oxide cores in FLUSPIO. b-c: TEM images of USPIO (b) and FLUSPIO (c). Quantitative analysis of the images reveals that both types of nanoparticles have a core diameter of 5±1 nm and a narrow size distribution. d-e: SEM images of USPIO (d) and (e) FLUSPIO, displayed spherical morphology. Quantitative analysis indicated an average diameter of 23±4 nm (USPIO) and 27±4 nm (FLUSPIO) respectively.

Zeta potential measurements were performed to determine the surface charge, electrophoretic mobility and colloidal stability of the USPIO and FLUSPIO particles at pH 2, 7 and 13 (Table 2.1.5). Under acidic conditions, USPIO had a positive zeta potential due to their highly protonated surface hydroxyl and oxygen groups. USPIO agglomerated immediately in PBS buffer and saline solution (0.9% NaCl). A negative zeta potential was observed for FLUSPIO, which fosters for colloidal stability of the nanoparticles at neutral pH

and usually leads to better pharmacokinetic properties. FLUSPIO were stable in physiological pH in water, HEPES buffer and in 5% glucose solution. However, after 15 min, aggregation was observed in PBS buffer and saline solution (0.9% NaCl) by visual inspection, likely because of the high ion concentrations and electrostatic interactions. No aggregation was found in cell culture media, most probably due to colloidal stabilization of FLUSPIO by serum proteins (Figure 2.2.9).

Table 2.1.5. Physico-chemical characterization results of USPIO and FLUSPIO

Sample	TEM diameter	Hydrodynamic diameter [nm]	Zeta potential in different pH solutions [mV]			MR Relaxivities at 3T in water	
	[nm]	HEPES buffer	pH 2	pH 7	pH 13	r2[$s^{-1}mM^{-1}$]	r1[$s^{-1}mM^{-1}$]
USPIO	5.5 ± 1.1	252 ± 66	32.83 ± 1.53	18.93 ± 2.46	–0.01 ± 0.03	n.d[c].	n.d[c].
FLUSPIO	5.6 ± 1.7	97 ± 3	4.59 ± 2.48	–31.13 ± 1.70	–31.70 ± 2.76	202.64 ± 0.48	2.13 ± 0.04
Resovist	4.2[a]	45.87 ± 0.09[b]	n.d.	-34.36 ± 2.30	n.d.	221.11 ± 0.61	5.21 ± 1.40

[a] Size of polycrystalline iron oxide with multiple single crystals and its reported relaxivity values[205] [b] Hydrodynamic diameter of Resovist in water and its approximate zeta potential at pH 7 [c] Relaxivity of USPIO at pH 7 could not be determined because of aggregation and susceptibility artefacts.

The stability of FLUSPIO in different cell culture media and physiological solutions (HEPES, saline, PBS) were evaluated merely by visual inspection. To this end, FLUSPIO were diluted in RPMI (Figure 2.2.9A) and McCoy's cell culture media (Figure 2.2.9B), both supplemented with 10% FBS, 5% glucose solution (Figure 2.2.9C), 25 mM HEPES buffer pH 7.2 (Figure 2.2.9D), saline solution (0.9%) (Figure 2.2.9E), and PBS buffer (Figure 2.2.9F) to reach a final concentration of 3.0 µmol Fe/mL, respectively. Photographs were taken after filling the suspensions into cuvettes at 0 min, 15 min, 1 h. In contrary to the agglomeration of FLUSPIO after 15 min in PBS buffer and saline (0.9% NaCl) solution, no visible aggregation was found within 1 h if FLUSPIO were incubated with one of the FBS enriched cell culture media. Similarly, FLUSPIO displayed reasonable stability in HEPES buffer without any visible agglomeration respectively.

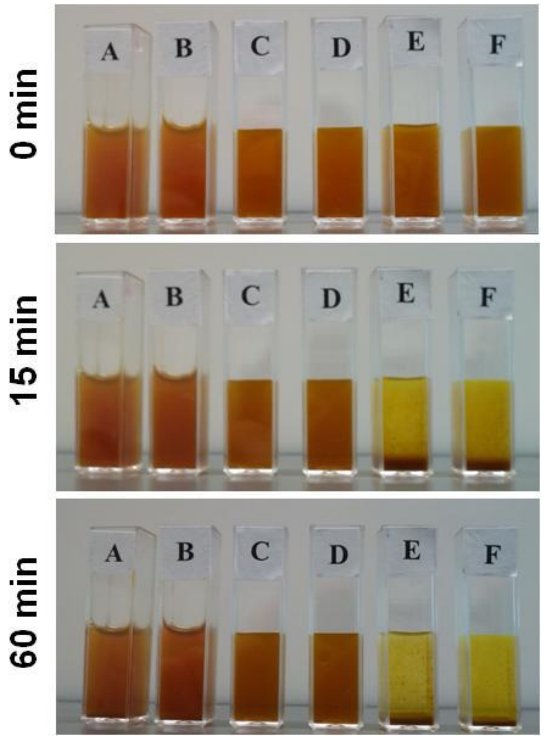

Figure 2.2.9. Photographs of FLUSPIO in RPMI cell culture medium (A), McCoy's cell culture medium (B), 5% glucose solution (C), HEPES buffer (D), saline solution (E), and PBS buffer (F) after 0 min, 15 min, 1 h respectively.

X-ray powder diffraction (XRD) analysis was used to determine the chemical composition and crystalline of the FLUSPIO. The XRD patterns of FLUSPIO could be assigned to (220), (311), (400), (422), (511), and (440) reflections of the spinal structure of magnetite (JCPDS No. 19-0629) (Figure 2.3.0). The observed diffraction peaks of generated USPIO are consistent with the expected diffraction patterns of Fe_3O_4. These peaks are also present in FLUSPIO, together with three other diffraction peaks. The additional peaks in FLUSPIO diffract gram at approximately 23.4 and 27.6° (2θ) are broad and are thus due to a material with low crystallite size, whereas the third additional peak at approximately 31.8° (2θ is sharp which is due to a material with larger crystallite size). The crystalline nature of their iron cores explains the high relaxivities of FLUSPIO found in MRI experiments. Fourier-transform infrared (FTIR) spectroscopy confirmed the binding of FMN and GMP phosphate groups to nanoparticles, and this was validated by comparing the spectra of free FMN and GMP and unmodified USPIO (Figure 2.3.2c). The chemical composition of the surface (concentration of FMN, GMP) was analyzed by energy-dispersive X-ray spectroscopy (EDX), Vaskovsky phosphate determination, elemental analysis and thermogravimetry (TGA). As expected from the theoretically calculated ratio of phosphate to iron, the Fe:P ratio of the fluorescent nanoparticles determined by EDX was 1:0.231. This was further supported by the Vaskovsky phosphate determination (Table 2.1.6) and elemental analysis. Elemental analysis (C/H/N) revealed C 14.80%, H 2.65% and N 4.47% by weight

(expected C 13.45%, H 1.43% and N 4.55%) for FLUSPIO. TGA of the FLUSPIO showed a weight loss of 24% when heated to 600 ºC (Figure 2.3.1). This account for the decomposition of the surface coating (FMN and GMP), as well as for the dehydration of the inorganic matrix (theoretically calculated weight loss: 23 %).

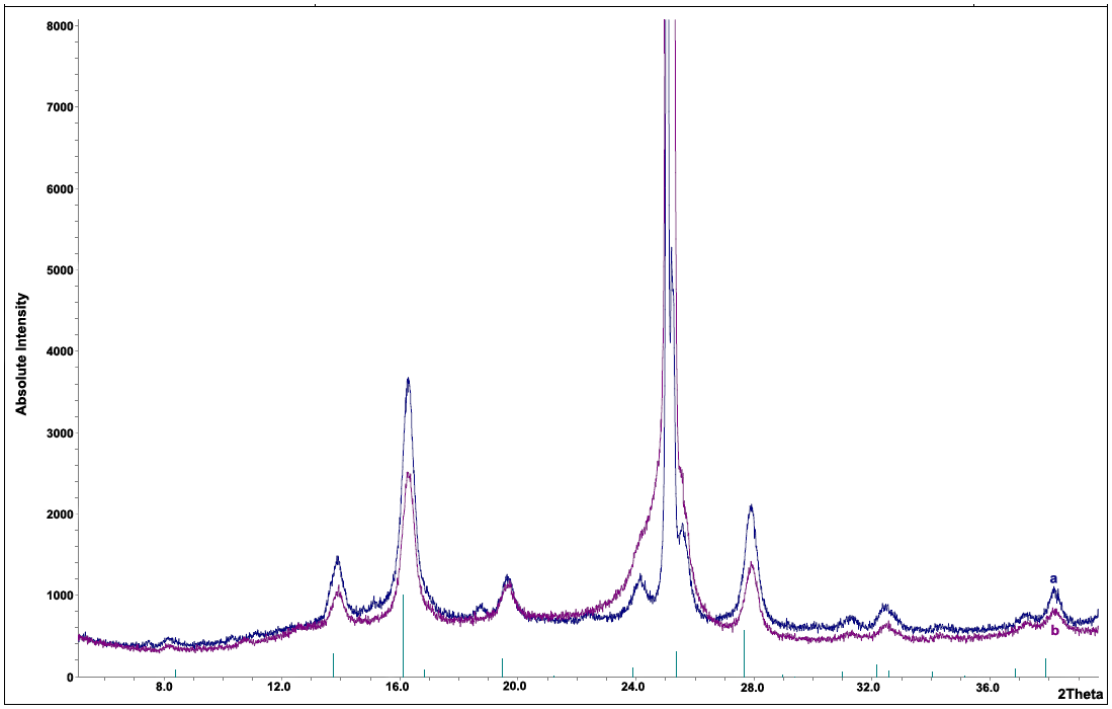

Figure 2.3.0. X-ray diffraction patterns of (a) USPIO and (b) fluorescent USPIO nanoparticles (FLUSPIO)

Table 2.1.6. Total phosphate content deriving from the non-polymeric molecules (FMN and GMP) on the surface of FLUSPIO.

Sample	Iron amount (µg)	Phosphorous amount (µg)	Fe:P ratio
FLUSPIO	223.38	45.28	1:0.203

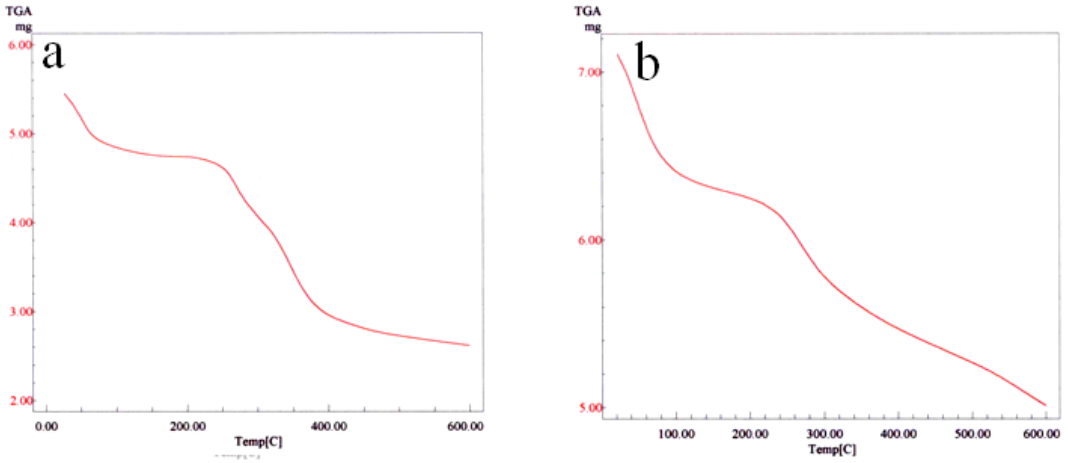

Figure 2.3.1. TGA curves of (a) FMN (b) FLUSPIO respectively.

Fourier-transform infrared (FTIR) spectroscopy confirmed the binding of FMN and GMP phosphate groups to the nanoparticles, which was validated by comparing the spectra of free FMN,GMP and unmodified USPIO (Figure 2.3.2c). Functional groups in FMN, GMP and USPIO were characterized by FT-IR spectroscopy (with 4 cm^{-1} resolution) of the KBr pellets. USPIO showed ν(Fe-O) bands at 562 and 627 cm^{-1}. FMN displayed unbound ν(P=O) band at 1181 cm^{-1} and ν(P-OR) bands at 927, 983 and 1045 cm^{-1}. For GMP free ν(P=O) bands occur at 1120 and 1180 cm^{-1} and ν(P-OR) bands occur at 905, 937 and 974 cm^{-1}. The ν(P=O) band disappeared due to binding of FMN and GMP in FLUSPIO which indicates binding of the phosphate groups to the nanoparticles. The ν(P-OR) band of FMN in FLUSPIO shifted to 994 and 1090 cm^{-1}.

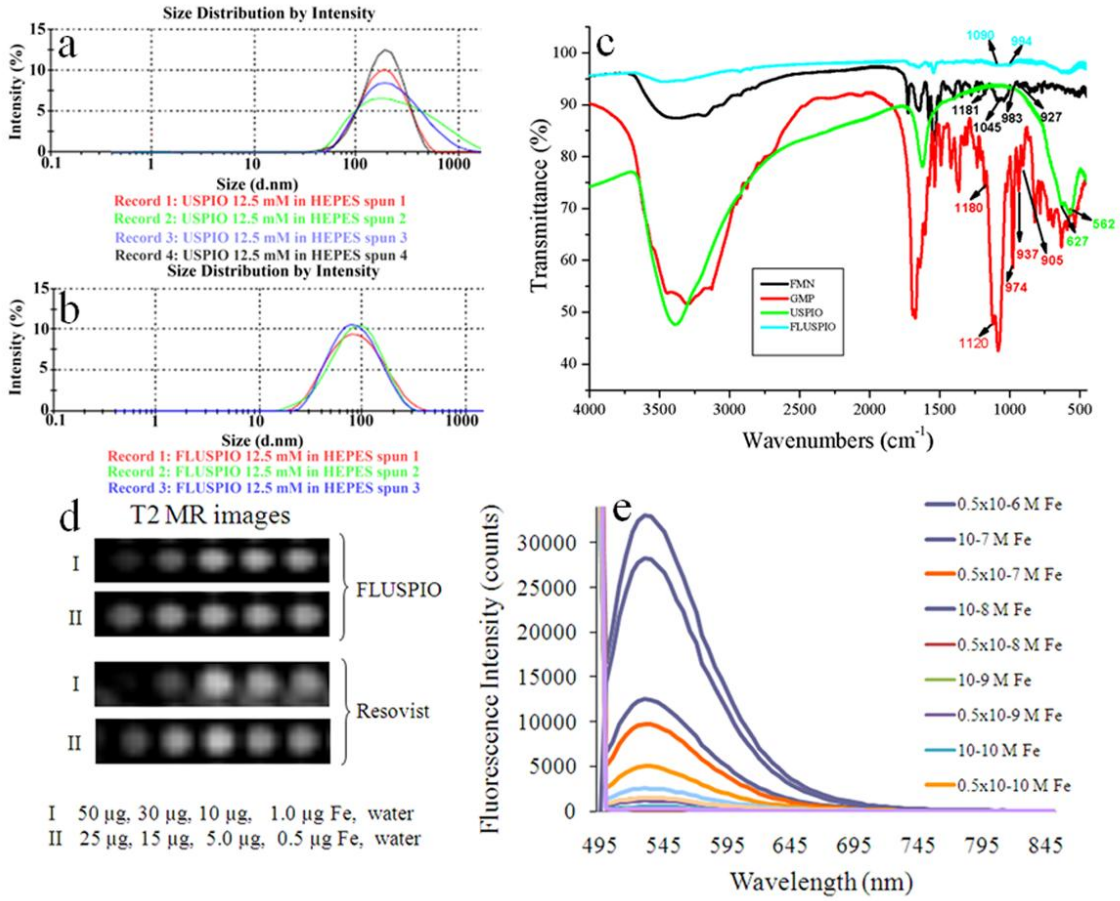

Figure 2.3.2. Physico-chemical characterization of FLUSPIO. DLS analysis of (a) USPIO and (b) FLUSPIO. (c). FT-IR spectra of FLUSPIO with reference to free FMN, GMP and uncoated USPIO. (d). T_2-weighted MR images of FLUSPIO (50 – 0.005 µg) in comparison to Resovist in water. (e) Fluorescence emission spectrum of FLUSPIO at different concentration in water (0.5×10^{-6} M to 0.5×10^{-10} M Fe).

2.10.1.1. Magnetic Properties of FLUSPIO

The superparamagnetic behavior of the FLUSPIO was studied by SQUID magnetometry, at a constant temperature of 290 K and a field of ± 5 T. The magnetization vs field curve was compared to that of unmodified USPIO and showed the expected regular progression for superparamagnetic substances (Figure 2.3.3)[177]. The MR relaxivity of the FLUSPIO in de-ionized water at ambient temperature and at 3 T was found to be similar to that of the clinically used MR contrast agent Resovist (FLUSPIO: r2 = 202.64±0.48 $s^{-1}mM^{-1}$, Resovist: r2 = 221.11±0.61 $s^{-1}mM^{-1}$; Table 2.1.5 and Figure 2.3.2d), thereby confirming their excellent MR contrast enhancement properties.

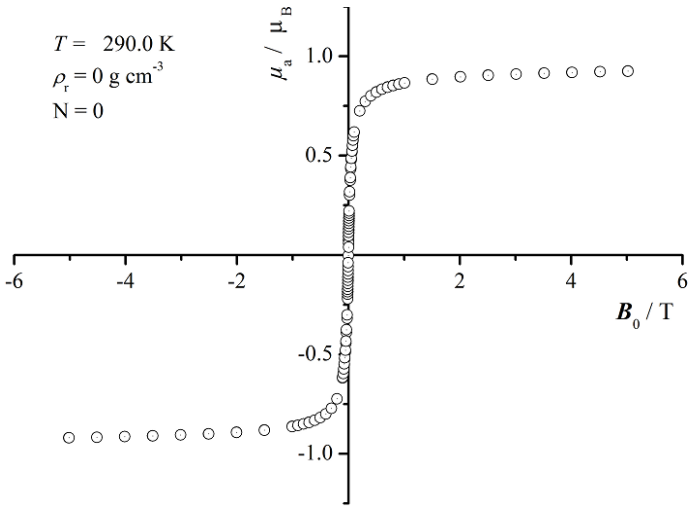

Figure 2.3.3. Magnetization versus applied field of FLUSPIO measured at T = 290 K (± 5 T)

2.10.1.2. Fluorescence Properties of FLUSPIO

Fluorescence spectroscopy and microscopy of the FLUSPIO revealed a high fluorescence intensity due to the photoluminescence of the FMN fluorophore associated with the nanoparticle surface[206]. The fluorescent nanoparticles can be excited in a wide wavelength range (250-500 nm), resulting in an intense green emission at 530 nm respectively (Figure 2.3.2e, 2.3.4 and 2.3.5). The absolute quantum yield without referring to a standard fluorophore was determined to elucidate the difference in quantum yield between free FMN and FMN on the FLUSPIO. Importantly, it was found that the association of FMN to the surface of the FLUSPIO did not affect the quantum efficiency of the dye (see appendices section).

The absorbance spectrum of USPIO, FMN, FMN with GMP and FLUSPIO was recorded in water and various buffer solutions (data not shown) using TECAN Infinite M200 (Tecan Austria GmbH) plate reader. The absorbance spectrum of FMN, FMN with GMP and FLUSPIO showed absorption peaks at 376 nm and 450 nm, respectively (Figure 2.3.4). After exposing them for 3 days to daylight, the absorption spectrum showed a peak maximum at 358 nm and a shoulder at 468 nm without any significant change in the absorption intensity (Figure 2.3.4).

The fluorescence of FLUSPIO was recorded in water and various buffer solutions (TRIS, TES, HEPES, sodium phosphate)(data not shown) at RT using the TECAN Infinite M200 (Tecan Austria GmbH) plate reader (iron concentration range: 10^{-6} M to 10^{-12} M). No change in the emission intensity of FMN was observed when mixed with GMP. FMN was excited at 452 nm and 468 nm and its intense emission occurred at 530 nm. The FLUSPIO showed more intense fluorescence due to presence of huge amount of luminescent centres per

nanoparticle (fluorescence spectroscopy and microscopy). FMN and FLUSPIO were exposed to daylight for three days in order to study the effect of daylight on their emission intensity. After three days, only a moderate decrease of 40% in their emission intensity was found, which proves that FLUSPIO are sufficiently stable enough without photobleaching (Figure 2.3.5).

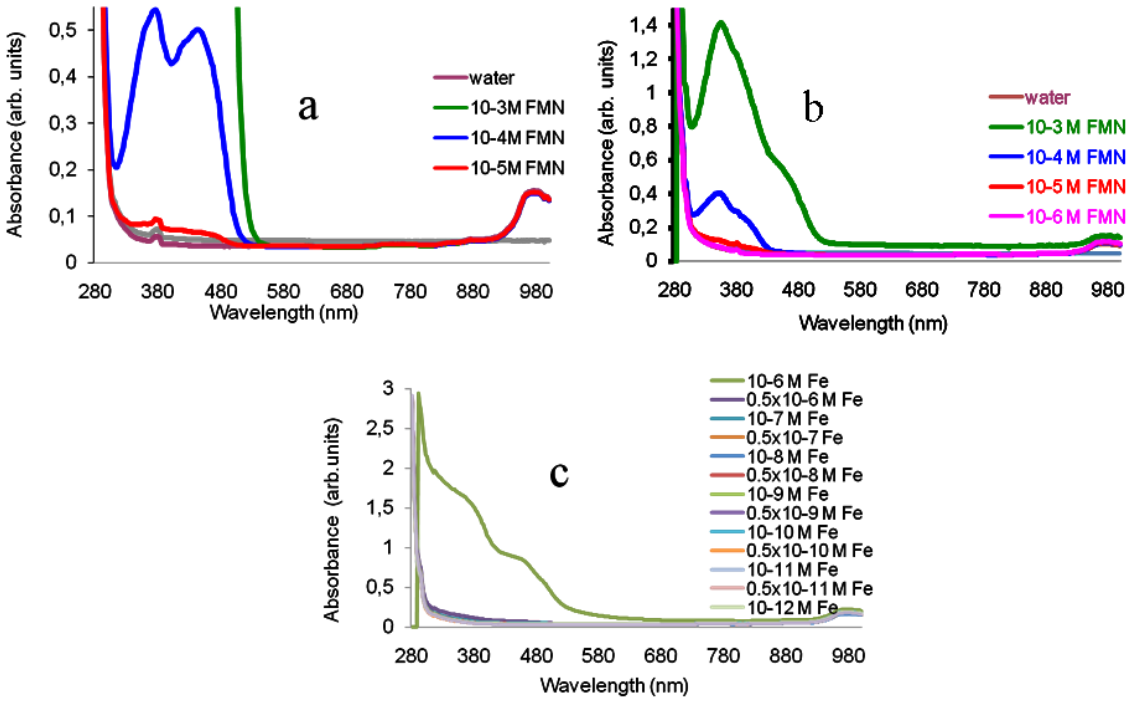

Figure 2.3.4. Absorption spectra of (a) FMN (no daylight exposure), (b) FMN (daylight exposure, three days), (c) FLUSPIO measured in water.

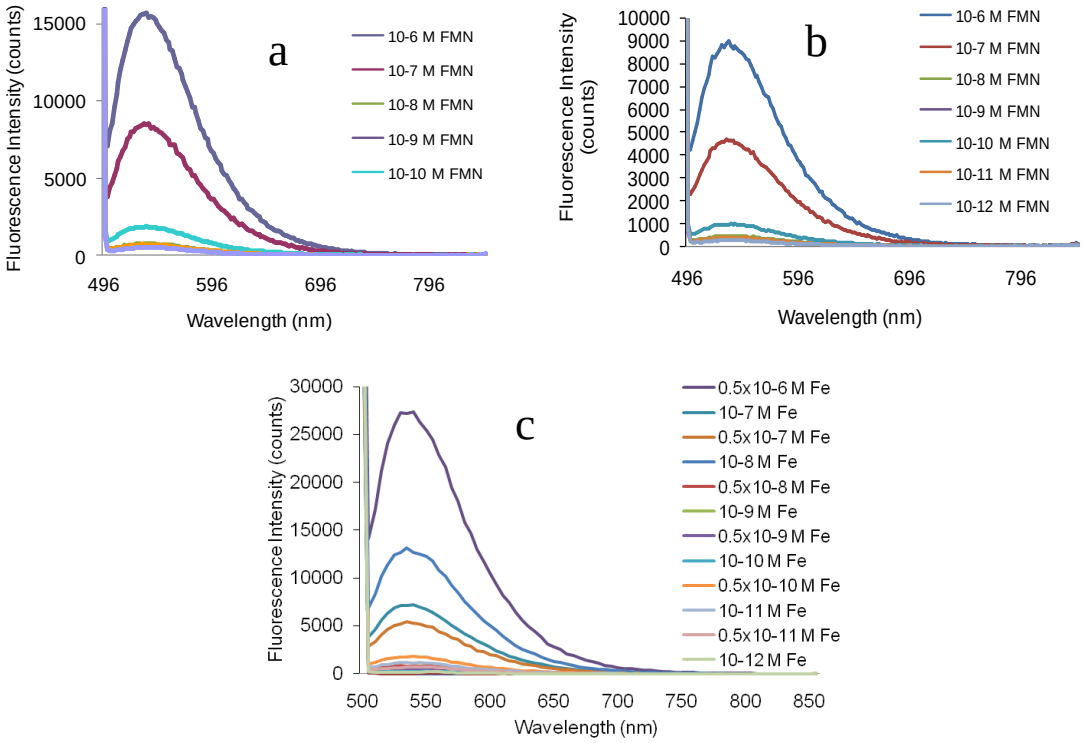

Figure 2.3.5. Fluorescence spectra of FMN in water with (a) no daylight exposure (b) daylight exposure (3 days). Emission spectra of FLUSPIO in water with (c) daylight exposure (3 days) respectively.

2.10.2. In vitro evaluation of FLUSPIO

After successful physico-chemical characterization, the biocompatibility of FLUSPIO was evaluated using different cytotoxicity assays and staining (staining: Trypan blue and 7-AAD, assays: TUNEL and MTT, and direct cell counting). Further, the cellular labeling efficacy of FLUSPIO was studied using MRI, TEM, fluorescence microscopy and ICP-MS respectively.

2.10.2.1. Cytotoxicity Assay

The biocompatibility of the FLUSPIO was investigated using PC-3 cells (human prostate cancer cells) and HUVEC (as an example of activated endothelial cells). As shown in Figure 2.3.6 and 2.3.7, neither trypan blue staining nor TUNEL staining (common assays used for determining the cytotoxicity of iron oxide nanoparticles)[207] indicated any significant change in cell viability at relevant cell labeling concentrations (i.e. up to 0.3 µmol Fe/mL). This observation was further confirmed by flow cytometry, in which 7-AAD (7-amino actinomycin D) was used to label dead cells, suggesting that the FLUSPIO are highly biocompatible (Figure 2.3.8).

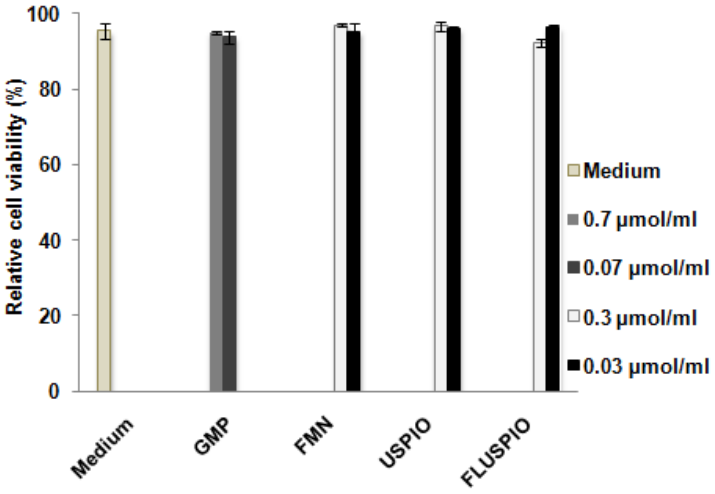

Figure 2.3.6. Relative viability of PC-3 cells determined by trypan blue staining after 24 h incubation with USPIO and FLUSPIO (0.3, 0.03 µmol Fe/mL) in the cell growth medium, respectively.

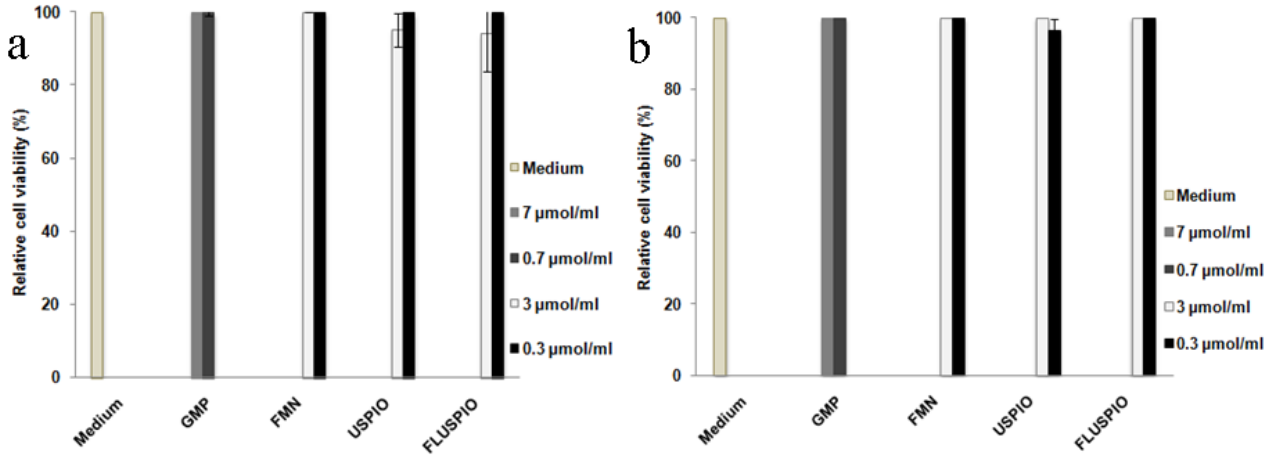

Figure 2.3.7. Data from the TUNEL assay showing the percentage of viable cells after 3 h incubation: (a) PC-3 cells, (b) HUVEC respectively.

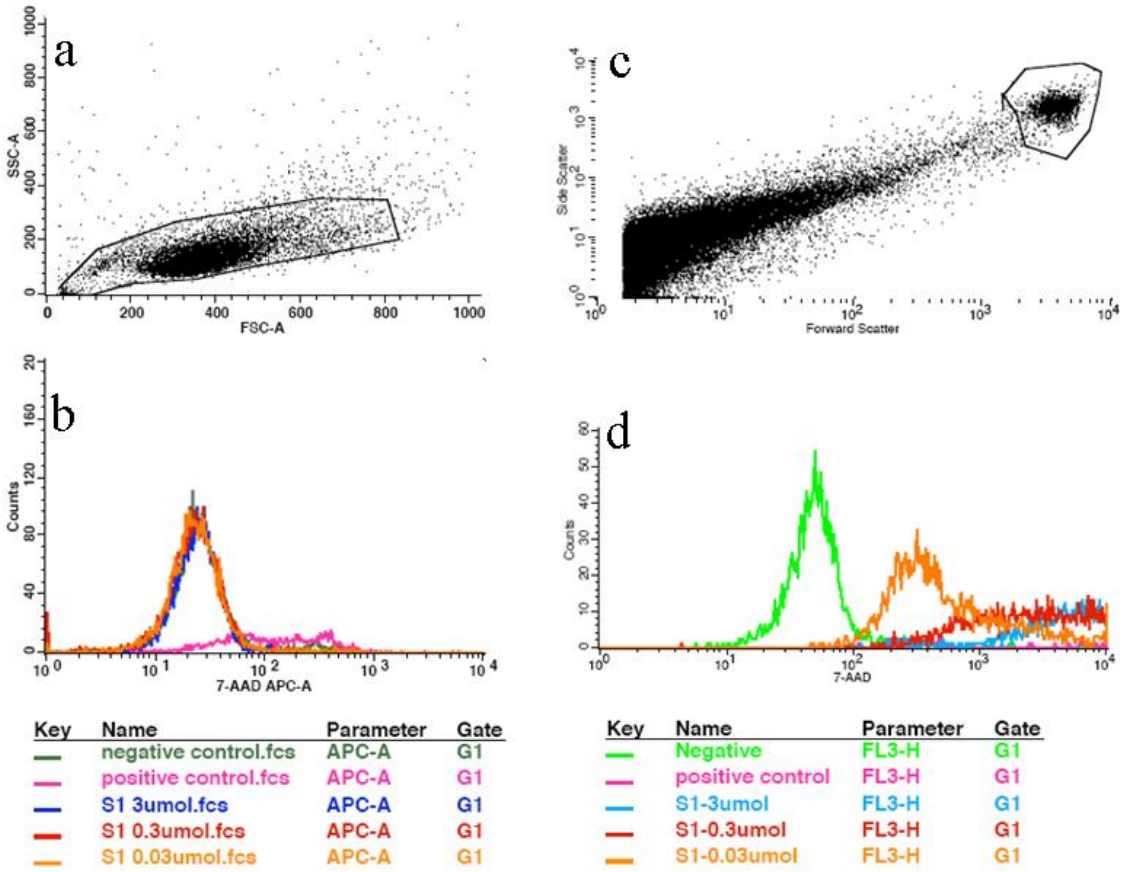

Figure 2.3.8. Flow cytometry analysis of PC-3 cell viability after incubation with FLUSPIO (S1) in which dead cells were stained with the 7-AAD dye (FL3 (APC channel)). Negative controls (dot plot), on which gating was performed, were incubated with medium for 3h (a) and 24h (c). PC-3 cells incubated with different iron concentrations (3.0, 0.3, 0.03 µmol Fe/mL) of FLUSPIO for 3h (b) and 24h (d) did not show any change in viability at cell labeling concentrations up to 0.3 µmol Fe/mL. In Figure (d) the peak from the positive control was shifted to the right respectively.

2.10.2.2. Cellular Labeling and Competition (MRI and ICP-MS)

Subsequently, the cellular labeling efficiency and the uptake of FLUSPIO were investigated by MRI (at 3.0 T). The cells were labeled with FLUSPIO, re-suspended in 10% gelatin (9 x 10^6 cells/0.3 mL; 0.3 µmol Fe/mL, 30 min and 1 h) and the R2 relaxation rates were determined. PC-3 cells in gelatin showed a significantly higher R2 relaxation rate after 1 h of incubation with FLUSPIO (5.08±1.44 s^{-1}, $p<0.001$) than with USPIO (2.28±0.19 s^{-1}), indicating a higher cellular uptake of FLUSPIO (similar R2 values for FLUSPIO were obtained after 30 min incubation). Furthermore, the specificity of FLUSPIO uptake was investigated via competitive blocking of RCP with free FMN[208-210]. After the addition of free FMN to PC-3 cells and subsequent incubation with FLUSPIO for 30 min, the R2 relaxation rate was significantly reduced (10-fold FMN competition; 4.33±0.70 s^{-1}, $p<0.05$; 100-fold FMN competition: 3.19±0.58 s^{-1}, $p<0.001$; FLUSPIO incubation alone: 5.08±1.44 s^{-1}). Similar results were obtained when blocking RCP with free FMN for 1 h. In this case,

the corresponding R2 relaxation rates were 3.84±0.81 s^{-1} (10-fold FMN competition) and 3.87±0.69 s^{-1} (100-fold FMN competition), respectively (Figure 2.3.9a-b). The higher cellular uptake of FLUSPIO compared to USPIO and the capability of free FMN to block FLUSPIO internalization in PC-3 cells was confirmed by the quantification of the intracellular iron contents using inductively coupled plasma mass spectrometry (ICP-MS, Figure 2.3.9e, Table 2.1.7).

In line with this, also HUVEC showed a significantly higher uptake of FLUSPIO (30 min: 3.69±0.45 s^{-1}, 1 h: 7.23±0.64 s^{-1}) than of USPIO (30 min: 1.98±0.17 s^{-1}, 1 h: 2.03±0.06 s^{-1}; Figure 2.3.9c-d). Competition experiments with free FMN confirmed the specificity of the RCP-mediated uptake of FLUSPIO in HUVEC. After RCP blocking by free FMN for 30 min, the R2 relaxation rate of HUVEC was decreased with respect to FLUSPIO alone (100-fold FMN competition: 1.73±0.07 s^{-1}; 10-fold FMN competition: 1.95±0.18 s^{-1}). Even after 1 h of FLUSPIO incubation, the uptake was still significantly lower in presence of 10-(2.54±0.53 s^{-1}) and 100-fold excess (1.60±0.12 s^{-1}) of free FMN (Figure 2.3.9c-d). Together, these findings convincingly show that the RCP-mediated uptake of FLUSPIO by human prostate cancer cells (PC-3) and HUVEC is significantly higher than that of USPIO.

The less pronounced reduction of the relaxation rates (R2) by 10-fold FMN competition in PC-3 cells in comparison to HUVEC is most probably related to the higher unspecific nanoparticle uptake in these cells in comparison to RCP-mediated FLUSPIO internalization (Figure 2.3.9f). To the best of our knowledge, the regulation of RCP expression is still unclear. However, with increase in metabolic activity, cells are expected to have a higher demand for Rf. The Rf uptake in cells is facilitated by RCP. The increased uptake of Rf (FLUSPIO) by metabolically active cells points to an up regulation of RCP expression. Thus, we hypothesize that the RCP expression level is linked to the metabolic activity of the cell. Unfortunately, the expression levels of RCP on the PC-3 and HUVEC cell surface could not be determined (and correlated to the MR findings) due to lack of a human RCP-binding antibody.

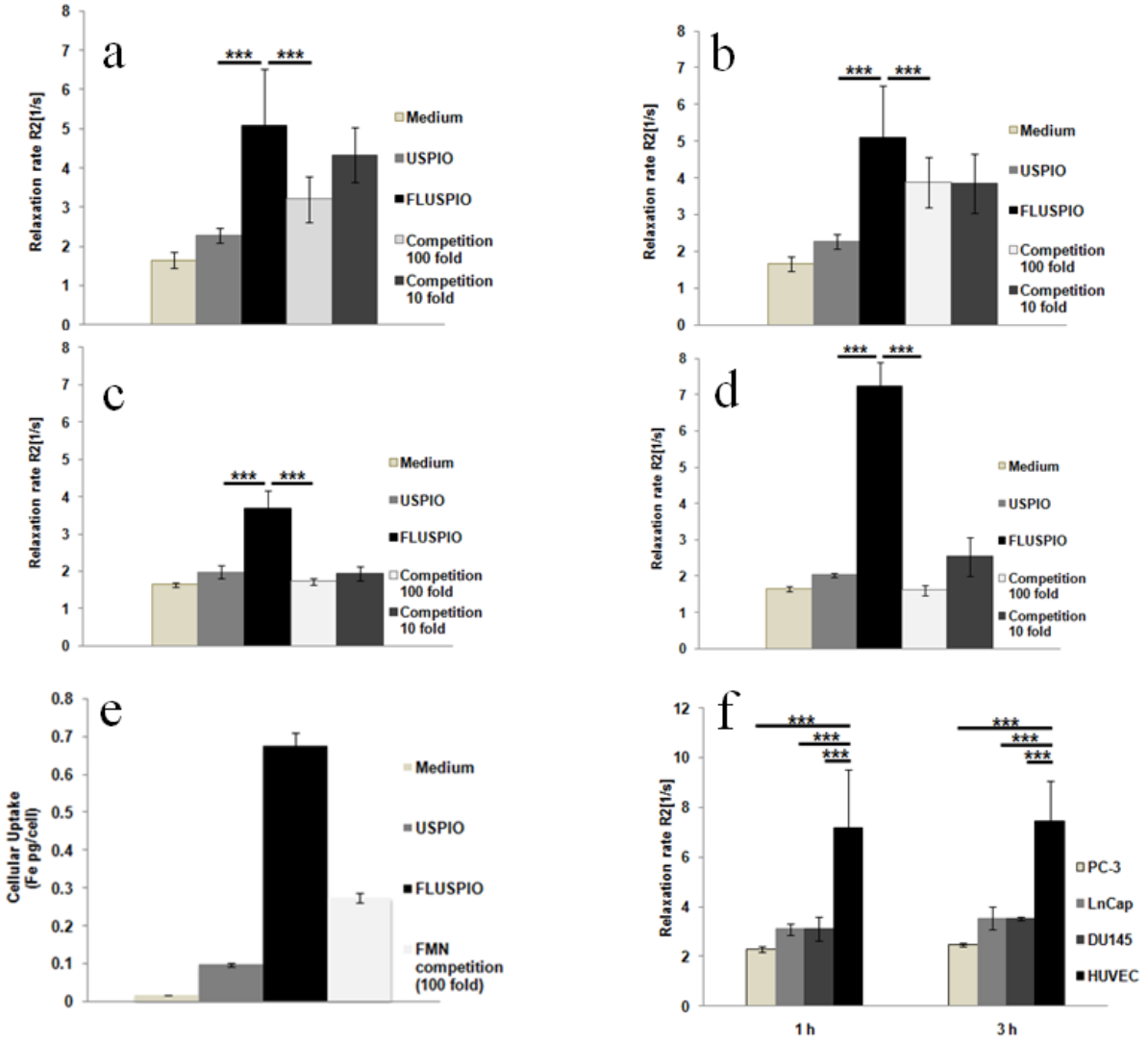

Figure 2.3.9. FLUSPIO uptake analyzed by means of MR and ICP-MS. a: R2 relaxation rates of PC-3 cells in gelatin (9.0 x10^6 cells/0.3 mL) incubated with 0.3 µmol Fe/mL of USPIO, FLUSPIO and FLUSPIO plus free FMN (10- and 100-fold excess, for competition purposes) for different time intervals, i.e. 30 min (a) and 1 h (b). c: R2 relaxation rates of HUVEC in gelatin (1.0 x10^6 cells/0.3 mL) incubated with 0.3 µmol Fe/mL of USPIO, FLUSPIO and FLUSPIO plus free FMN (10- and 100-fold excess) for 30 min (c) and 1 h (d). e: ICP-MS determination of intracellular iron content in PC-3 cells after a 1 h incubation with USPIO, FLUSPIO and FLUSPIO in the presence of excess FMN (100-fold excess). (f). R2 relaxation rates of three different prostate cancer cell lines and HUVEC (2 x 10^6 cells/0.3 mL for each; in gelatin) incubated with 0.3 µmol Fe/mL of FLUSPIO for 1 h and 3 h. In all cases, two-sided student t-tests were performed to address statistical significance. ***: $p<0.001$.

Table 2.1.7. Uptake of USPIO, FLUSPIO and FLUSPIO under competition with FMN in PC-3 cells (2 x 10^6 cells/0.3 mL) after 1h incubation (ICP-MS)

ICP-MS iron content [pg Fe/cell]		
USPIO (0.3 µmol Fe/mL)	FLUSPIO (0.3 µmol Fe/mL)	FMN (100 fold)
0.097 ± 0.003	0.675 ± 0.31	0.274 ± 0.04

Interestingly, FLUSPIO were found to be taken up much more efficiently by HUVEC than by PC-3 cells, which may be due to cell type-specific characteristics of activated endothelial cells. To investigate this interesting phenomenon in more detail, and to confirm FLUSPIO uptake in different cancer cells, a comparative MR relaxometry study was performed using PC-3, LnCap and DU-145 cells. All of these three prostate cancer cell lines are known to express RCP,[151] and all three showed a high uptake of FLUSPIO. Remarkably however, in all cases, the R2 relaxation rate of HUVEC was found to be more than twice as high as that of the prostate cancer cell lines (Figure 2.3.9f). Together, these findings suggest that FLUSPIO are highly suitable for targeting and labeling (angiogenic) endothelial cells [208-210].

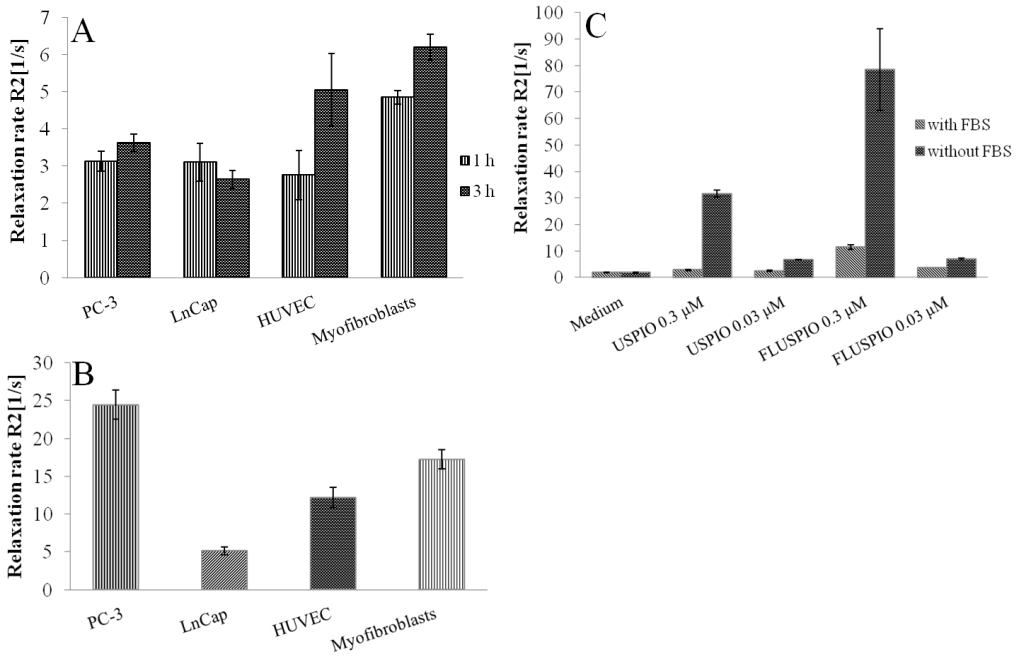

Figure 2.4.0. FLUSPIO uptake analyzed by MRI. R2 relaxation rates of PC-3, LnCap, myofibroblast cells and HUVEC in gelatin (2.0 x10^6 cells/0.3 mL) incubated with 0.3 µmol Fe/mL of FLUSPIO for different time intervals, i.e. 1 h and 3 h (A). R2 relaxation rates of PC-3, LnCap, myofibroblast cells and HUVEC in gelatin (2.0 x10^6 cells/0.3 mL) incubated with 0.3 µmol Fe/mL of double coated FMN USPIO for 1 h (B). R2 relaxtion rates of PC-3 cells in gelatin (2.0 x 10^6 cells/0.3 mL) incubated for 3 h with USPIO, FLUSPIO in McCoy´s medium with and without FBS supplements (C) respectively.

Further, the cellular labeling efficiency and the uptake of FLUSPIO in four different cells (PC-3, LnCap, HUVEC, and myofibroblasts) were investigated by MRI (at 3.0 T). The cells were labeled with FLUSPIO, re-suspended in 10% gelatin (2.0 x 10^6 cells/0.3 mL; 0.3 µmol Fe/mL, 1 h and 3 h) and the R2 relaxation rates were determined. R2 relaxation rates after 1 h incubation (Figure 2.4.0A) are 3.12±0.27 s^{-1} (PC-3), 3.11±0.51 s^{-1} (LnCap), 2.76±0.65 s^{-1} (HUVEC), 4.84±0.18 s^{-1} (Myofibroblasts) and after 3 h incubation (Figure 2.4.0A) are 3.62±0.24 s^{-1} (PC-3), 2.64±0.24 s^{-1} (LnCap), 5.04±0.98 s^{-1} (HUVEC) and 6.19±0.35 s^{-1} (Myofibroblasts) respectively. These results clearly show the increase in FLUSPIO uptake in HUVEC and myofibroblast cells with increase in incubation time, which could be related to cell-type specific characteristics of fibroblast cells. To validate the specific uptake of FLUSPIO is due to the RCP specific ligand, four different cells were incubated for 1 h with double coated FMN USPIO and relaxation rates were measured. The relaxation rates after 1 h incubation are 24.15±1.93 s^{-1} (PC-3), 5.14±0.50 s^{-1} (LnCaP), 12.18±1.38 s^{-1} (HUVEC), 17.23±1.24 s^{-1}(myofibroblasts) which confirmed the RCP-mediated specific uptake in different cell types (Figure 2.4.0B). The inhibitory effect of FBS on USPIO, FLUSPIO uptake by PC-3 cells was evaluated using MR relaxometry (Figure 2.4.0C). The FLUSPIO and USPIO (0.3 µmol Fe/mL) diluted in the PC-3 cell growth medium without FBS enrichment displayed high R2 relaxation rate (FLUSPIO: 78.58±15.41 s^{-1} and USPIO: 31.63±1.30 s^{-1}) compared to the medium enriched with FBS (FLUSPIO: 11.45±0.80 s^{-1} and USPIO: 2.86±0.23 s^{-1}) respectively. The high uptake of FLUSPIO and USPIO in the absence of FBS clearly demonstrates the unspecific interaction between the nanoparticles and serum proteins of the FBS enriched medium thereby inhibiting the cellular uptake of the nanoparticles.

2.10.2.3. Fluorescence Microscopy and TEM

In vitro experiments on PC-3 cells and HUVEC were also performed to evaluate the cellular labeling efficiency of FLUSPIO. The TEM images in Figure 2.4.1a-d show that after 3 h and 6 h, FLUSPIO strongly accumulated inside endosomes, while USPIO were not taken up effectively. The high uptake of FLUSPIO by PC-3 cells was confirmed by fluorescence microscopy (Figure 2.4.2a-f) and flow cytometry (Figure 2.4.3). A strong green fluorescence of the cells was observed after FLUSPIO incubation (Figure 2.4.2a-f). The perinuclear fluorescence pattern strongly suggests (likely) endosomal localization of the FLUSPIO and supports the results observed from the TEM studies.

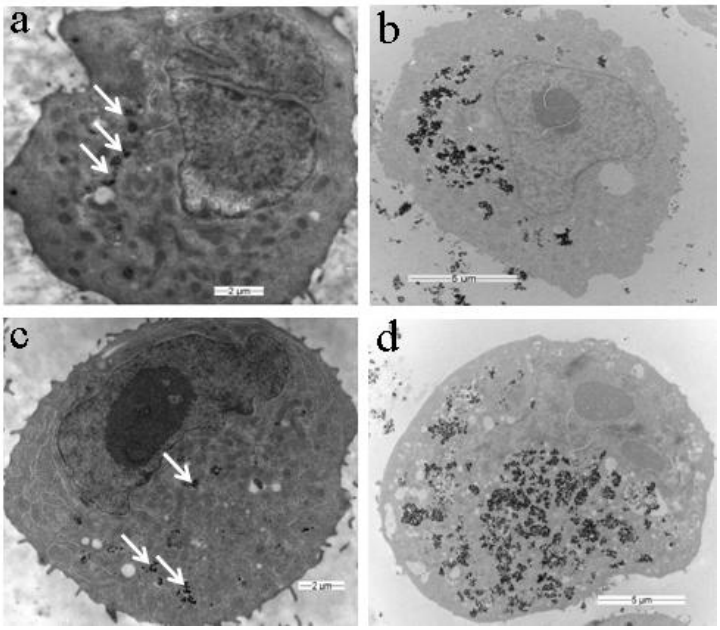

Figure 2.4.1. FLUSPIO uptake analyzed by TEM. a-d: TEM images of PC-3 cells incubated with USPIO and FLUSPIO at an iron concentration of 3.0 µmol Fe/mL. After 3 h (a and b) and 6 h (c and d) of incubation, PC-3 cells have internalized only a small amount of uncoated USPIO (a and c; see arrows), while there is strong uptake for FLUSPIO (b and d).

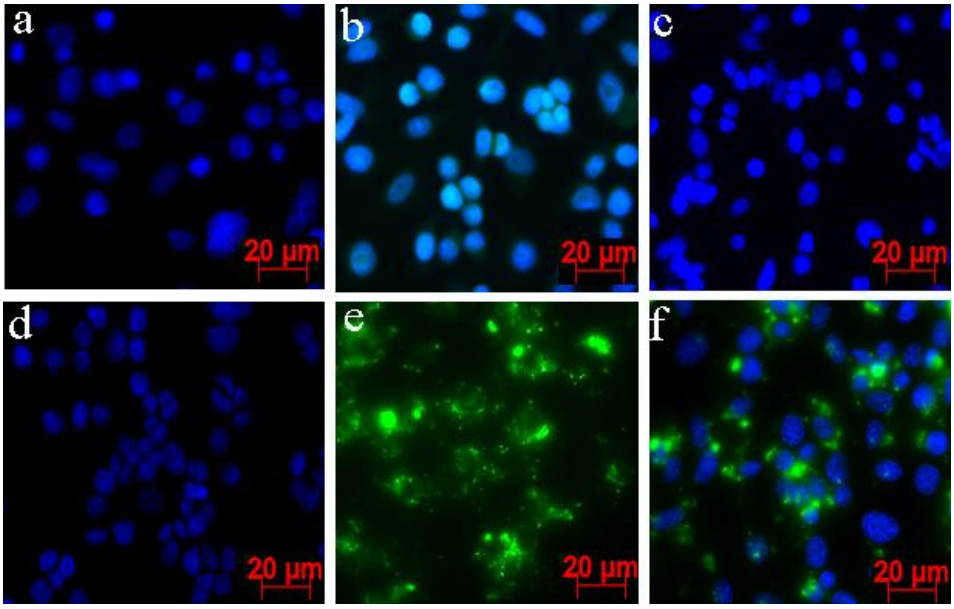

Figure 2.4.2. FLUSPIO uptake analyzed by means of fluorescence microscopy. a-f: Fluorescence microscopy images of PC-3 cells incubated for 3 h with FLUSPIO (0.5 µmol Fe/mL). Nuclei are counterstained with DAPI. a: Blank medium. b: FMN. c: GMP. d: USPIO. e: FLUSPIO without DAPI. f: FLUSPIO plus DAPI. The images clearly show the vesicular (likely endosomal) localization of the FLUSPIO.

PC-3 cells on glass cover slips were incubated for 3 h with FLUSPIO and controls (see above) at 37 °C, 5% CO_2 and 95% relative humidity. Medium was removed and cells were washed three times with 1 mL PBS. Further, cells were fixed on cover slips using 0.5 mL of 100% ethanol and dried at RT. Nuclei of cells were stained with DAPI (Figure 2.4.2 a-

f). The green fluorescence of FLUSPIO was analyzed in the FITC channel (FL1 channel) and the high cell labeling efficiency with fluorescence microscopy and flow cytometry was demonstrated.

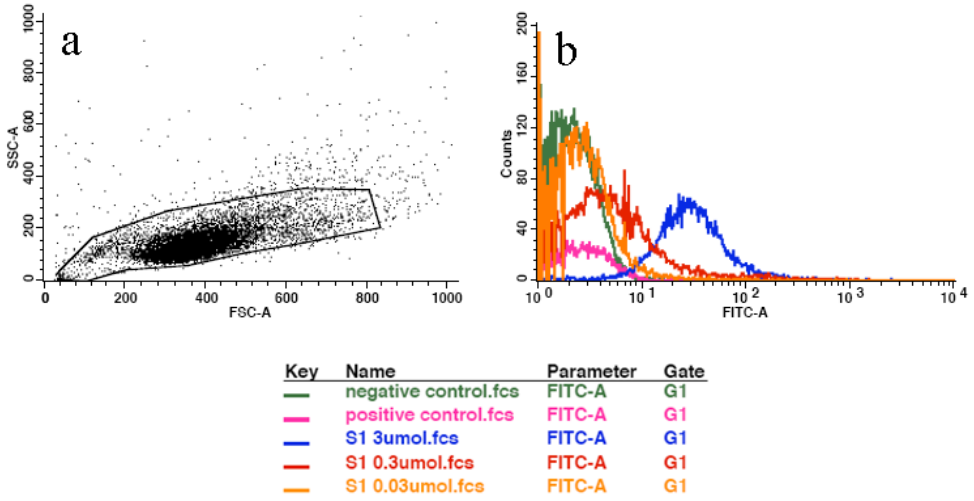

Figure 2.4.3. Flow cytometry of PC-3 cells after incubation with FLUSPIO (S1). (a): negative control cells (dot plot) incubated for 3 h on which gating was performed; (b): PC-3 cells incubated with FLUSPIO (3 h) show an increase in fluorescence intensity with increasing FLUSPIO iron concentration

Furthermore, the dose- and time-dependency of nanoparticle uptake was investigated by incubating PC-3 and HUVEC cells with FLUSPIO of different iron concentrations (3.0, 0.3, 0.03 µmol Fe/mL) in the respective cell culture media for different incubation periods. As shown in Figure 2.4.4 and 2.4.5, MR relaxometry of these cells showed increased R2 relaxation rates of FLUSPIO with increasing dose and incubation time.

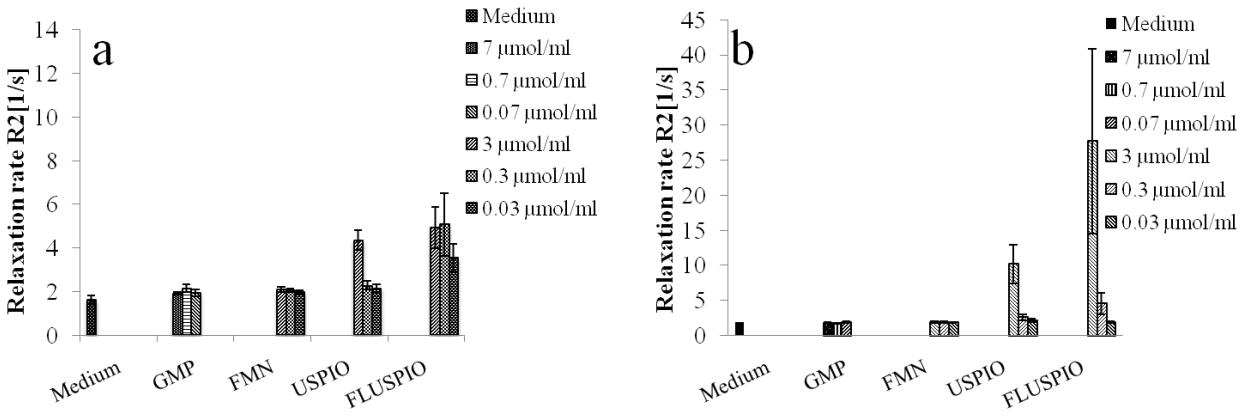

Figure 2.4.4. R2 relaxation rate of gelatin gels containing (a) PC-3 cells and (b) HUVEC (2 x 10^6/0.3 mL) after 1 h incubation.

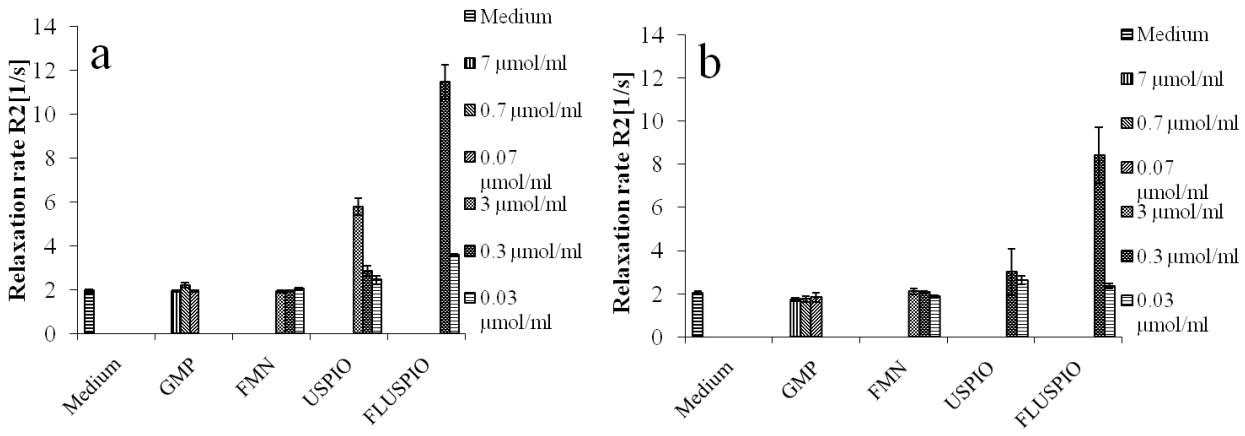

Figure 2.4.5. R2 relaxation rate of gelatin gels containing (a) PC-3 cells and (b) HUVEC (2 x 10^6/0.3 mL) after 3 h incubation.

In summary, we here introduce RCP targeting as an effective way to specifically transport (iron oxide-based) nanomaterials into metabolically active tumor and endothelial cells. In this context, USPIO with an adsorptive fluorescent coating of FMN and GMP (FLUSPIO) were synthesized, which are stable at physiological pH and show an intense fluorescence as well as high R2 relaxation rate in MRI. The high RCP-mediated uptake of FLUSPIO by activated endothelial and cancer cells suggest them as promising tools for molecular MRI and cell tracking experiments. As a follow up application (*in vivo*) study for FLUSPIO, we will investigate whether FLUSPIO specifically accumulate in tumors and/or tumor endothelial cells after intravenous injection. We assume that *in vivo*, FLUSPIO will mostly target activated endothelial cells, thereby enabling molecular MR and optical imaging of tumor angiogenesis respectively.

2.11. Synthesis of FAD USPIO nanoparticles

After having achieved the traits essential for imaging, such as successful coating, stability under physiological conditions and high cellular labeling efficacy for FLUSPIO, we tried to extend this promising fluorescent flavin based coating to USPIO by using FAD (flavin analogues) in order to generate nanoparticles with a very high MR-cellular labeling profile and for highly specific *in vivo* targeting of the riboflavin carrier protein (RCP) respectively. In this aspect, FAD USPIO nanoparticles were generated by adapting similar synthesis protocol as pursued for FLUSPIO. Here, also a mixed coating for USPIO of fluorescent FAD and non-polymeric GMP was achieved in two simple steps at ambient temperature (Figure 2.4.6A). The reasons for including GMP in this coating were congruent to that of FLUSPIO as explained in section 2.10 respectively.

2.11.1. Physico-chemical characterization results of FAD USPIO

The physico-chemical properties of FAD USPIO were evaluated using TEM, SEM, DLS, Zeta potential, TGA, FT-IR, powder XRD, EDX, MRI, fluorescence spectroscopy and microscopy respectively. The characterization results obtained from above techniques will be discussed in this section.

TEM analysis of USPIO, and FAD USPIO showed nanoparticles with an average iron core diameter of 5.8 ± 1 nm (Table 2.1.8 and Figure 2.4.6B-C) similar to that of FLUSPIO diameters. SEM images of USPIO and FAD USPIO confirmed the spherical surface morphology, with an average particle diameter of 23.19 ± 4.62 nm (USPIO) and 35.83 ± 5.69 nm (FAD USPIO) (Figure 2.4.6D-E). There was an increase in size of FAD USPIO observed in SEM compared to FLUSPIO which could be attributed to the nanoparticles prone to clustering upon drying. The FAD USPIO in HEPES buffer showed an average hydrodynamic diameter (D_h) of 265 ± 2.48 nm with a low polydispersity index (PDI) of 0.23 (2.4.8A-B) higher than FLUSPIO D_h values. The discrepancies observed in the D_h values between the flavin coated nanoparticles could be attributed to the lack of centrifugation for FAD USPIO compared to FLUSPIO. The average D_h of FAD USPIO in 10% glycine, 5% glycine, saline, PBS are 272.90 ± 28.63 nm (PDI = 0.35); 256.46 ± 3.91 nm (PDI = 0.26); 872.76 ± 75.69 nm (PDI = 0.25); 707.93 ± 66.33 nm (PDI = 0.22) respectively. The increase in average D_h of FAD USPIO in saline and PBS clearly indicates agglomeration due to high electrostatic interaction between USPIO and different anions respectively. USPIO showed stability only at pH 2 and displayed an increase in D_h at pH 7 (393 ± 35.37 nm) with PDI equal to 0.84, due to agglomeration that occurred at increasing pH (Table 2.1.8 and Figure. 2.4.8A-B).

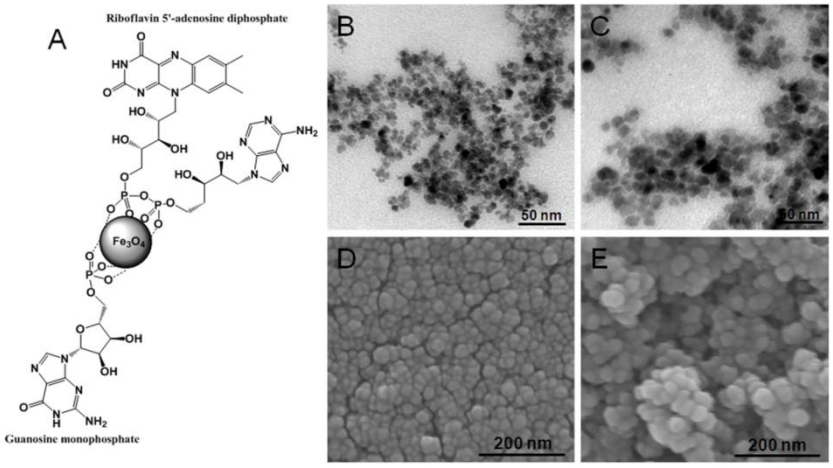

Figure 2.4.6. Preparation of FAD USPIO. A: Schematic diagram showing the mode of binding of FAD and GMP to the iron oxide cores in FAD USPIO. B-C: TEM images of USPIO (B) and FAD USPIO (C). Quantitative analysis of the images reveals that both types of nanoparticles have a core diameter of 5.8±1 nm and a narrow size distribution. D-E: SEM images of USPIO (D) and (E) FAD USPIO, displayed spherical morphology. Quantitative analysis indicated average diameters of 23±4 nm (USPIO) and 35.83±5.69 nm (FAD USPIO) respectively.

Zeta potential measurements were performed to determine the surface charge, electrophoretic mobility and colloidal stability of the USPIO and FAD USPIO particles at pH 2, 7 and 9 (Table 2.1.8). Under acidic and physiological conditions USPIO displayed a positive zeta potential due to their highly protonated surface hydroxyl and oxygen groups. Further, under basic conditions USPIO displayed a negative zeta potential which could be attributed to the deprotonation of surface groups respectively. FAD USPIO displayed a negative zeta potential under physiological and basic conditions which facilitates their *in vivo* application and bolster better pharmacokinetic properties. Under acidic conditions, FAD USPIO displayed a positive zeta potential as anticipated due to prominent protonation at this pH. FAD USPIO was stable at physiological pH in water, HEPES buffer and in 5% glucose solution. No aggregation was found in cell culture media, most probably due to the colloidal stabilization of FAD USPIO by serum proteins.

X-ray powder diffraction (XRD) analysis was used to determine the chemical composition and crystallinity of the FAD USPIO. The majority of the nanoparticles were crystalline in nature, with low amounts of amorphous constituents which was validated by comparing with magnetite diffraction patterns (Figure 2.4.7). The crystalline nature of their iron cores explains the high relaxivities of FAD USPIO found in the MRI experiments.

Table 2.1.8. Physico-chemical characterization results of USPIO and FAD USPIO (PDI = polydispersity index)

Samples	TEM size	Hydrodynamic size (nm)			Zeta potential (mV)		
	(nm)	pH 2 (PDI)	pH 7 (PDI)	pH 9 (PDI)	pH 2	pH 7	pH 9
USPIO	5.97 ± 1.18	18.50 ± 0.22 (0.26)	393.43 ± 35.57 (0.84)	575.30 ± 86.26 (0.73)	27.03 ± 3.74	33.80 ± 5.02	-27.36 ± 1.14
FAD USPIO	5.83 ± 1.05	327.50 ± 25.63 (0.49)	265.23 ± 2.48 (0.23)	382.70 ± 15.59 (0.42)	24.50 ± 1.61	-27.96 ± 0.11	-25.83 ± 2.06

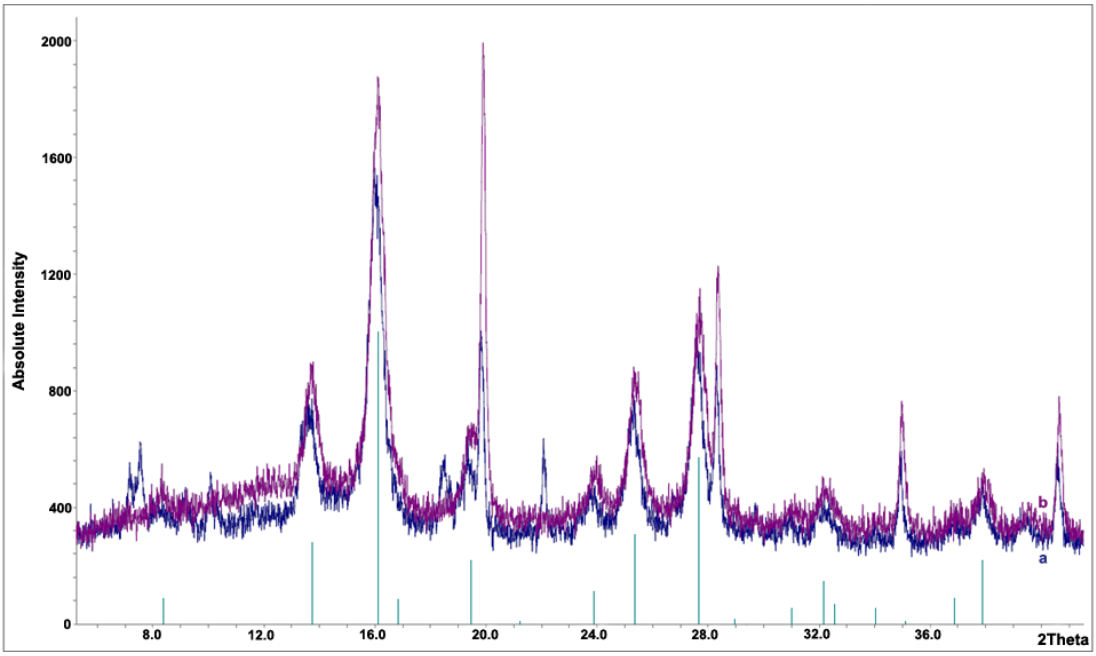

Figure 2.4.7. X-ray diffraction patterns of generated (a) USPIO and (b) fluorescent nanoparticles (FAD USPIO) respectively.

Fourier-transform infrared (FTIR) spectroscopy confirmed the binding of FAD and GMP phosphate groups to nanoparticles, and this was validated in comparison to free FAD and GMP and unmodified USPIO spectra (Figure 2.4.8C). Functional groups in FAD, GMP and USPIO were characterized by FT-IR spectroscopy (with 4 cm^{-1} resolution) of KBr pellets. USPIO showed ν(Fe-O) bands at 583 and 629 cm^{-1}. FAD displayed unbound ν(P=O) bands at 1116 cm^{-1} and ν(P-OR) bands at 949 and 1078 cm^{-1}. For GMP free ν(P=O) bands occured at 1121 and 1190 cm^{-1} and ν(P-OR) bands occur at 905, 935, 979, 1006 and 1021 cm^{-1}. The ν(P=O) band disappeared due to the binding of FAD and GMP in FAD USPIO which indicated the binding of the phosphate groups to nanoparticles. The ν(P-OR) band of FAD in FAD USPIO shifted to 992 and 1050 cm^{-1}.

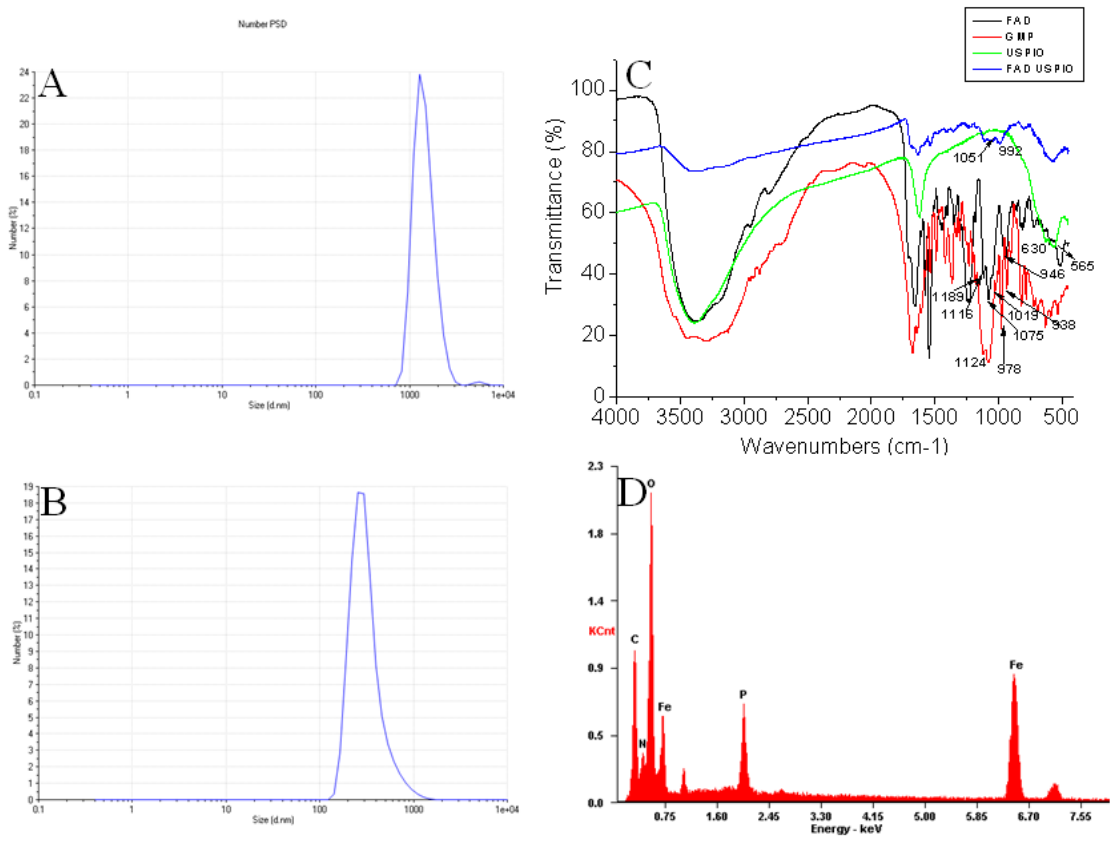

Figure 2.4.8. Physico-chemical characterization of FAD USPIO. DLS size measurements of USPIO (A) and FAD USPIO (B) in water. USPIO displayed agglomeration at pH 7 in water due to lack of surface coating. FT-IR spectra of FAD, GMP, USPIO, and FAD USPIO (C) indicated that binding of FAD/GMP occurs via phosphate groups. EDX spectrum of FAD USPIO (D) displayed the peaks (K*counts*) for phosphorous and iron respectively.

The chemical composition of the surface (concentration of FAD, GMP) was analyzed by energy-dispersive X-ray spectroscopy (EDX), Vaskovsky phosphate estimation, elemental analysis and thermogravimetry (TGA). As expected from theoretically calculated ratios, the Fe:P ratio of the fluorescent nanoparticles determined by EDX was 1:0.145 (Figure 2.4.8D). This was further supported by the Vaskovsky phosphate estimation (Table 2.1.9) and elemental analysis.

Table 2.1.9. Total phosphate content deriving from the non-polymeric molecules (FAD and GMP) on the surface of FLUSPIO (Vaskovsky phosphate determination).

Sample	Iron amount (µg)	Phosphorous amount (µg)	Fe:P ratio
FAD USPIO	223.38	5.807	1:0.026

The elementary analysis of FAD USPIO revealed C 16.21%, H 2.58% and N 8.20% by weight (expected C 15.45%, H 2.2% and N 7.25%) for FAD USPIO. TGA of the FAD USPIO showed a weight loss of 26% when heated to 600 ºC (Figure 2.4.9). This accounts for the decomposition of the surface coating (FAD and GMP), as well as for the dehydration of the inorganic matrix (expected theoretical weight loss: 27 %).

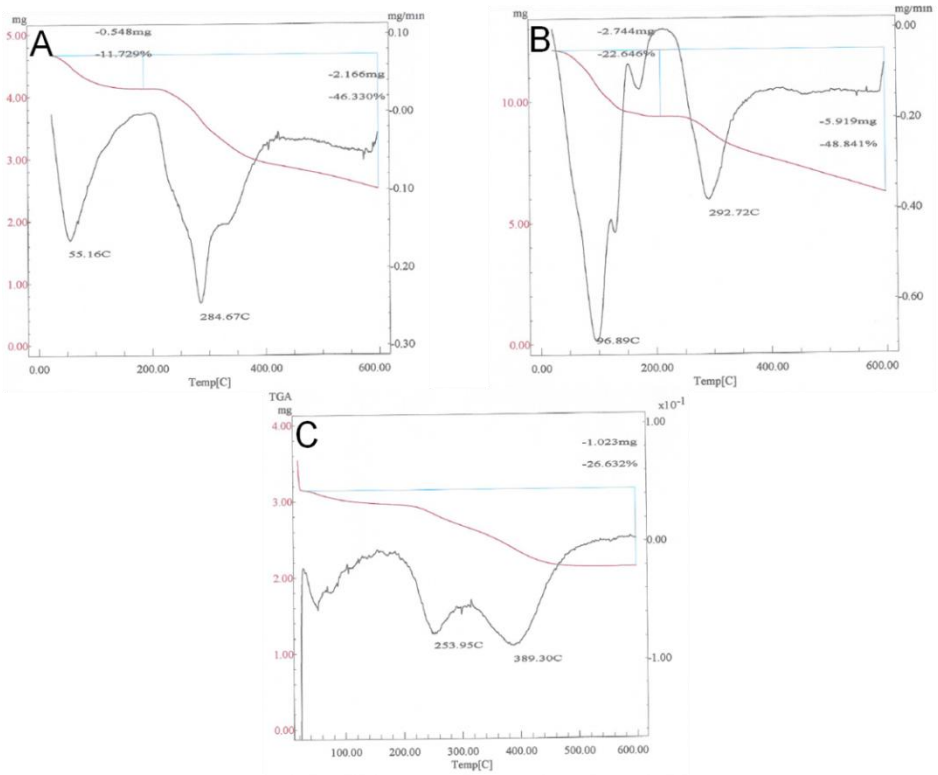

Figure 2.4.9. TGA curves of (A) FAD (B) GMP and (C) FAD USPIO respectively.

2.11.1.1. Magnetic Properties of FAD USPIO

The MR relaxivity of the FAD USPIO in de-ionized water (slightly basic) at RT at 3 T was found to be similar to that of the clinically used MR contrast agent Resovist (FAD USPIO: r2 = 136.22±0.46 $s^{-1}mM^{-1}$, Resovist: r2 = 144.36±0.92 $s^{-1}mM^{-1}$; thereby confirming their excellent contrast enhancement properties.

2.11.1.2. Fluorescence Properties of FAD USPIO

Fluorescence spectroscopy and microscopy of the FAD USPIO revealed a high fluorescence intensity due to the photoluminescence of the FAD fluorophore associated with the nanoparticle surface[206]. The fluorescent nanoparticles can be excited in a wide wavelength range (250-500 nm), resulting in an intense green emission at 530 nm. The absorbance spectrum of FAD and FAD USPIO was recorded in water using a TECAN

Infinite M200 (Tecan Austria GmbH) plate reader. The absorbance spectrum of FAD and FAD USPIO showed absorption peaks at 378 nm and 450 nm, respectively (Figure 2.5.0A and 2.5.0B). The fluorescence of FAD USPIO was recorded in water at RT (iron concentration range: 10^{-6} M to 10^{-12} M). FAD was excited at 452 nm and 468 nm and its intense emission occurred at 530 nm. The FAD USPIO showed more intense fluorescence due to the presence of a huge amount of luminescent FAD centres per nanoparticle (fluorescence spectroscopy and microscopy)(Figure 2.5.0C, 2.5.0D and 2.5.1).

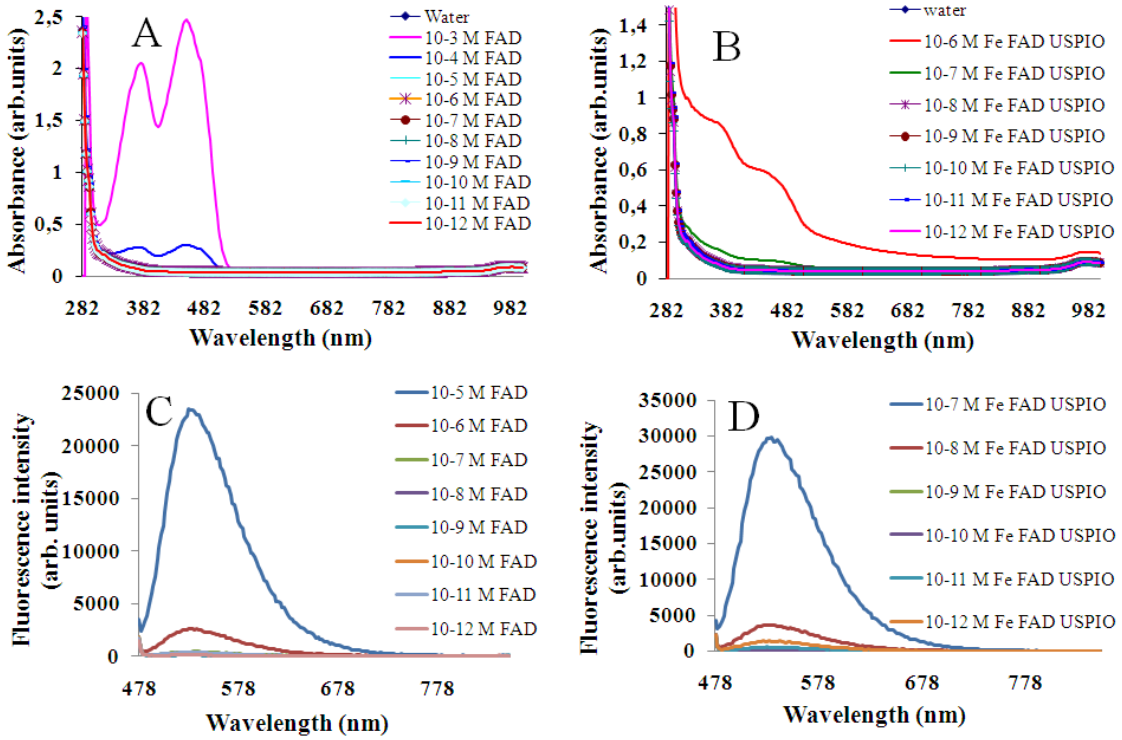

Figure 2.5.0. Absorption spectra of (A) FAD (B) FAD USPIO and fluorescence spectra of (C) FAD and (D) FAD USPIO recorded in water respectively.

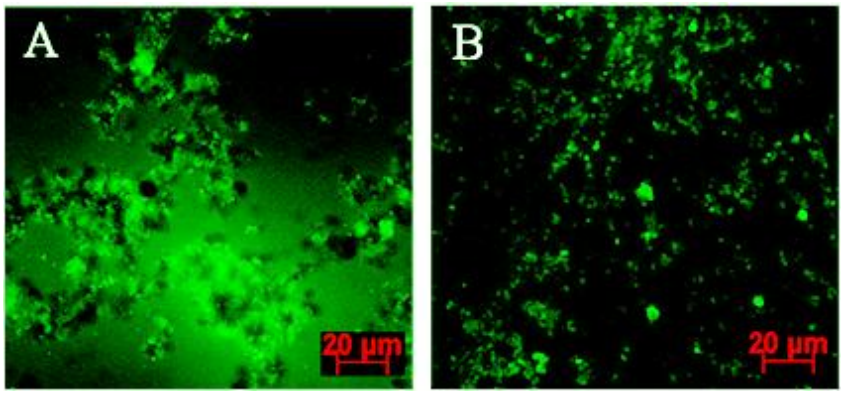

Figure 2.5.1. Fluorescence microscopy images of (A) FLUSPIO and (B) FAD USPIO recorded with 20X magnification respectively.

2.11.2. In vitro evaluation of FAD USPIO

The biocompatibility of the generated FAD USPIO was checked using cytotoxicity assays and staining (staining: Trypan blue and 7-AAD, assay: MTT) respectively. Further, the cellular labeling efficacy of FAD USPIO was evaluated using MRI and fluorescence microscopy.

2.11.2.1. Cytotoxicity Assay

The biocompatibility of the FAD USPIO was investigated using LnCap cells (human prostate cancer cells). As shown in Figure 2.5.2, neither trypan blue staining nor MTT assay indicated any significant change in cell viability at relevant cell labeling concentrations (i.e. up to 0.3 µmol Fe/mL). This observation was further confirmed by flow cytometry, in which 7-AAD (7-amino actinomycin D) was used to label dead cells, suggesting that the FAD USPIO is highly biocompatible (Figure 2.5.3).

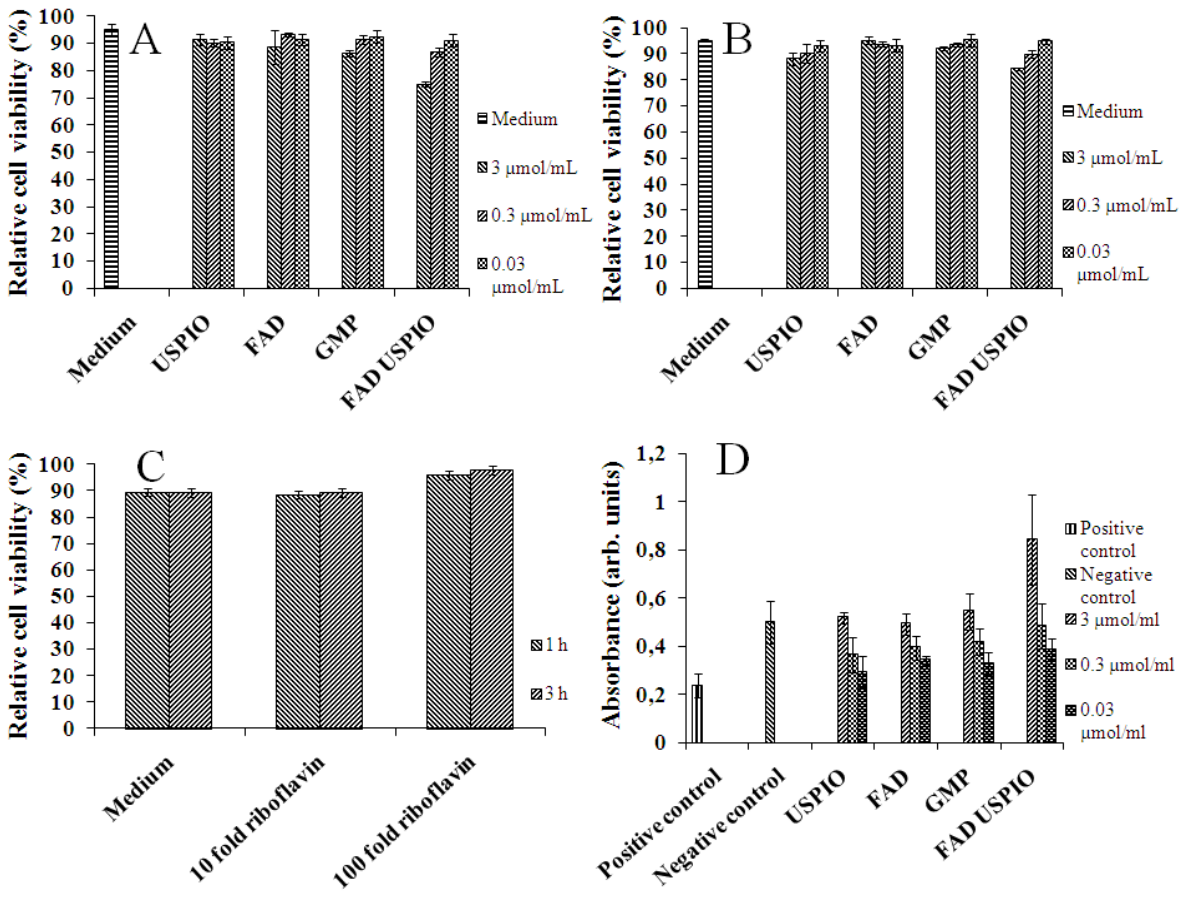

Figure 2.5.2. Relative viability of LnCap cells determined by trypan blue staining after (a) 3 h; (b) 24 h incubation of USPIO, FAD USPIO with 3.0, 0.3, 0.03 µmol Fe/mL in the cell growth media; (c) Rf (10- and 100- fold competition) for 1 h and 3 h and (D) MTT assay of LnCap cells incubated with FAD USPIO and controls for 4 h. The trypan blue staining and MTT assay results didn't show any relevant loss in LnCap cell viability respectively.

The viability of the LnCap cells after incubation with FAD USPIO at three different labeling concentrations (3.0, 0.3, 0.03 µmol Fe/mL) were evaluated using trypan blue staining and MTT assay. Cells were cultured, incubated for two different time points (3 h and 24 h), stained with trypan blue and dead cells (stained blue) were counted analogous to FLUSPIO. Trypan blue staining results did not show any loss in viability at relevant cell labeling concentrations (0.3 µmol Fe/mL). These viability results were further confirmed by MTT assay. Additionally, the effect of excess Rf (10- and 100-fold) used for competition purposes on cell viability was also evaluated using trypan blue staining. The trypan blue results indicated that there was no cytotoxicity exhibited by excess of Rf on LnCap cells.

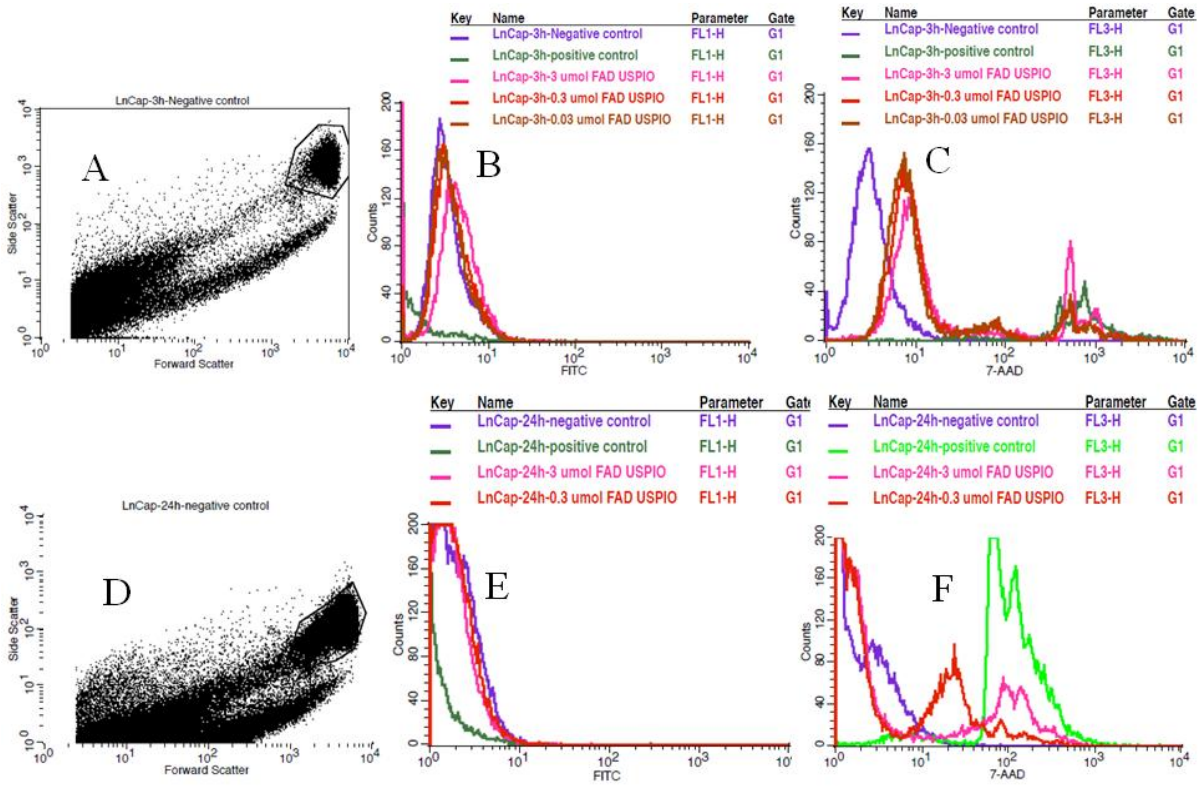

Figure 2.5.3. Flow cytometry analysis of LnCap cell viability after incubation with FAD USPIO in which dead cells were stained with the 7-AAD dye (FL3 (APC channel)). Negative controls (dot plot), on which gating was performed, were incubated with medium for 3 h (A) and 24 h (D). LnCap cells incubated with different iron concentrations (3.0, 0.3, 0.03 µmol Fe/mL) of FAD USPIO for 3 h (C) and 24 h (F) show no relevant loss of viability at cell labeling concentrations (0.3 µmol Fe/mL). The increase in green fluorescence could be detected in FL1(FITC channel) after 3 h (B) and 24 h (diminished fluorescence) (E) incubation with increase in FAD USPIO concentration respectively.

2.11.2.2. Cellular Labeling and Competition (MRI)

The cellular labeling efficiency and the uptake of FAD USPIO were investigated by MRI (at 3.0 T). Triplicates were used per condition. The cells were labeled with FAD USPIO, re-suspended in 10% gelatin (2 x 10^6 cells/0.3 mL; 0.3 µmol Fe/mL, 30 min and 1 h) and the R2 relaxation rates were determined. LnCap cells in gelatin showed a significantly

higher R2 relaxation rate after 1 h incubation with FAD USPIO (135.56±36.78 s^{-1}, $p<0.001$) than with USPIO (2.76±0.43 s^{-1}), indicating a significant higher cellular uptake of FAD USPIO (similar R2 values for FAD USPIO were obtained after 30 min incubation). Furthermore, the specificity of FAD USPIO uptake was investigated via competitive blocking of RCP with free Rf[208-210]. After the addition of free Rf to LnCap cells and subsequent incubation with FAD USPIO for 30 min, the R2 relaxation rate was significantly reduced (10-fold Rf competition; 8.51±0.42 s^{-1}, $p<0.001$; 100-fold Rf competition: 3.46±0.94 s^{-1}, $p<0.001$; FAD USPIO incubation alone: 69.91±27.43 s^{-1}). Similar results were obtained when blocking RCP with free Rf for 1 h. In this case, the corresponding R2 relaxation rates were 7.76±1.42 s^{-1} (10-fold Rf competition) and 2.22±0.15 s^{-1} (100-fold Rf competition), respectively (Figure 2.5.5A-B).

Similarly, the LnCap cells in the FAD based competition experiments also showed a significantly higher uptake of FAD USPIO (30 min: 57.63±9.15 s^{-1}, 1 h: 82.93±14.49 s^{-1}) than of USPIO (30 min: 4.59±0.25 s^{-1}, 1 h: 4.75±0.64 s^{-1}; Figure 2.5.5C-D). Competition experiments with free FAD confirmed the specificity of the RCP-mediated uptake of FAD USPIO in LnCap cells. After RCP blocking by free FAD for 30 min, the R2 relaxation rate of LnCap cells was lower compared to the ones incubated with FAD USPIO alone (100-fold FAD competition: 22.41±2.01 s^{-1}). Even after 1 h of FAD USPIO incubation, the uptake was still significantly lower in the presence of 100-fold excess (47.48±6.57 s^{-1}) of free FAD (Figure 2.5.5C-D). Together, these experimental insights adequately show that the RCP-mediated uptake of FAD USPIO by LnCap cells is intensely higher than that of plain USPIO. Furthermore, the uptake of FAD USPIO in PC-3 cells displayed under competition (100 fold Rf and FMN) was enormously higher than that of USPIO (the relaxation rates are shown in Table 2.2.0).

The LnCap cells and HUVEC were labeled with FAD USPIO, re-suspended in 10% gelatin (2 x 10^6 cells/0.3 mL; 0.3, 0.03 µmol Fe/mL, 1 h) and the R2 relaxation rates were determined. HUVEC in gelatin showed a significantly higher R2 relaxation rate compared to LnCap after 1 h of incubation with FAD USPIO (0.3 µmol Fe/mL, 58.34±6.74 s^{-1}, $p<0.001$) than with USPIO (3.74±0.35 s^{-1}), indicating a higher cellular uptake of FAD USPIO. Similarly, the LnCap cells also displayed a significant higher R2 relaxation rate after 1 h incubation with FAD USPIO (0.3 µmol Fe/mL, 28.83±12.18 s^{-1}, $p<0.005$) than with USPIO (2.85±0.06 s^{-1}), respectively (Figure 2.5.5F). The higher uptake of FAD USPIO in HUVEC compared to LnCap cells could be attributed to cell type specific characteristics of activated endothelial cells. Remarkably, the R2 relaxation rate of HUVEC was found to be twice as high as that of the prostate cancer cell lines (Figure 2.5.5F). Together, these MR findings

suggest that FAD USPIO is highly suitable for targeting and labeling (angiogenic) endothelial cells.

Table 2.2.0. Uptake of USPIO, FAD USPIO and FAD USPIO under competition with FMN and Rf in PC-3 cells (2 x 10^6 cells/0.3 mL) after 1 h incubation (MRI)

R2 relaxation rate [1/s]			
USPIO (0.3 µmol Fe/mL)	FAD USPIO (0.3 µmol Fe/mL)	FMN (100 fold)	Rf (100 fold)
3.351 ± 0.239	67.56 ± 9.49	46.74 ± 4.21	2.45 ± 0.21

Furthermore, the time-dependency of nanoparticle uptake was investigated by incubating three different prostate cancer cells (PC-3, DU-145, and LnCap) with FAD USPIO (0.3 µmol Fe/mL) which are known to express RCP, in the respective cell culture media for two different incubation periods (1 h and 3 h) respectively. As shown in Figure 2.5.4, MR relaxometry of these cells showed high R2 relaxation rates for FAD USPIO compared to USPIO with increase in the incubation times. LnCap displayed the highest uptake (shown by R2 relaxation rates) for the FAD USPIO nanoparticles among the three prostate cancer cells.

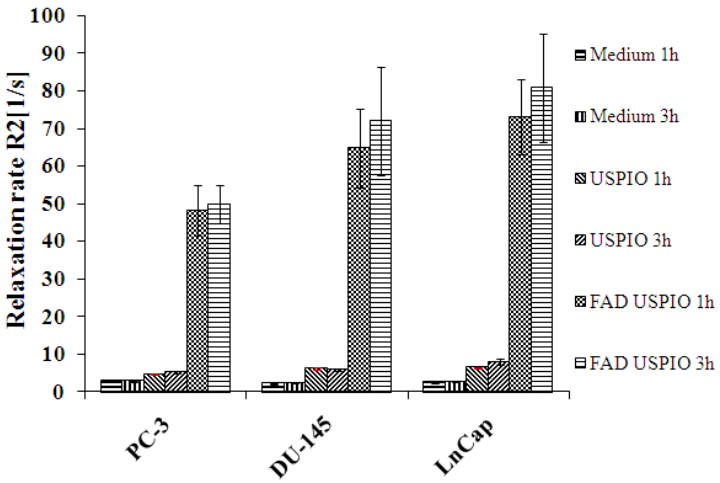

Figure 2.5.4. R2 relaxation rates of three prostate cancer cells (PC-3, DU-145 and LnCap) incubated with FAD USPIO and USPIO for 1 h and 3 h respectively.

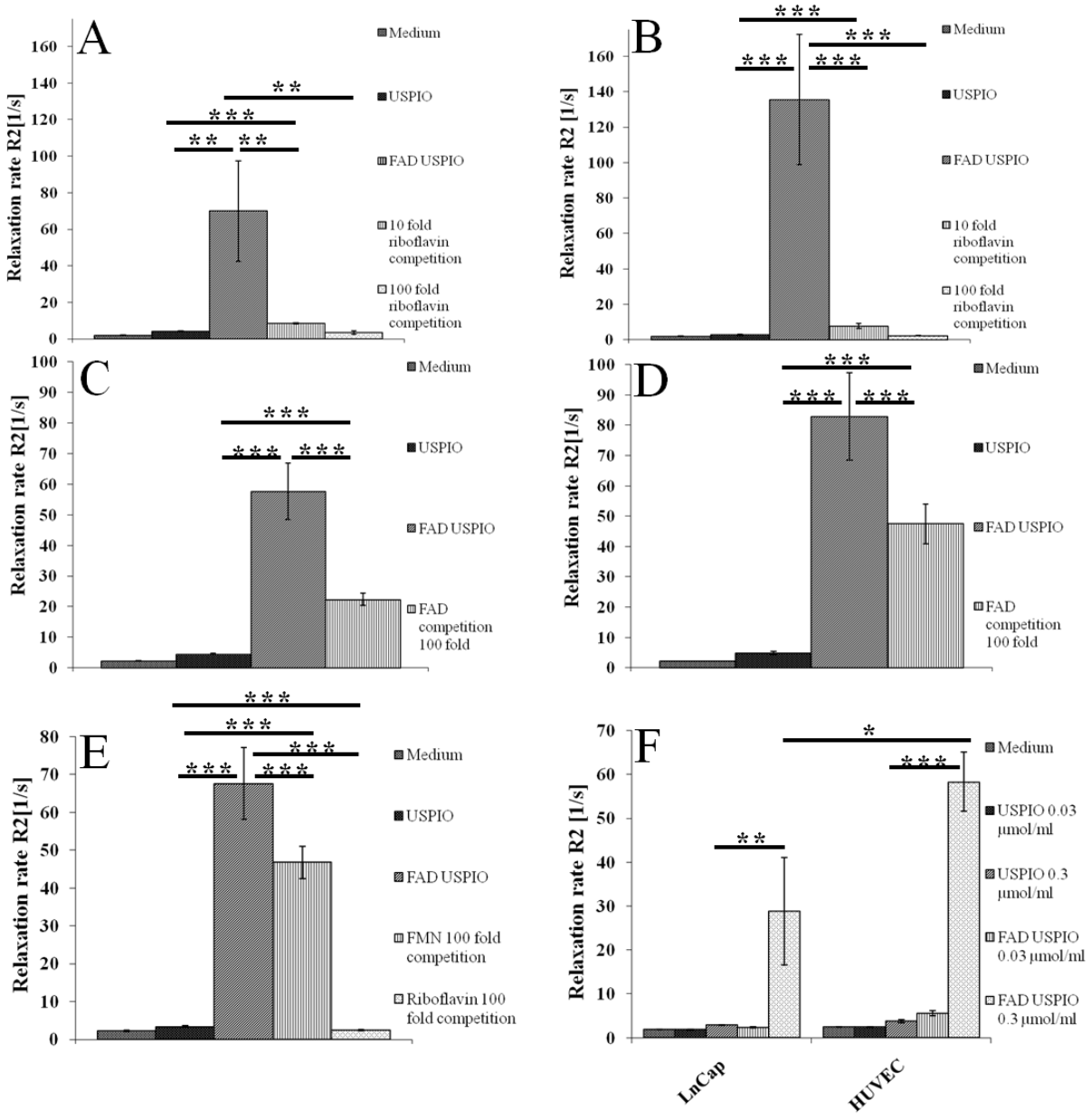

Figure 2.5.5. FAD USPIO uptake analyzed by MRI A-D: R2 relaxation rates of LnCap cells in gelatin (2.0 x10^6 cells/0.3 mL) incubated with 0.3 µmol Fe/mL of USPIO, FAD USPIO, FAD USPIO plus free Rf (10- and 100-fold excess) (30 min (A), 1 h (B)), and FAD USPIO plus free FAD (100-fold excess for competition purposes)(30 min (C), 1 h (D)). (E): R2 relaxation rates of PC-3 in gelatin (2.0 x10^6 cells/0.3 mL) incubated with 0.3 µmol Fe/mL of USPIO, FAD USPIO and FAD USPIO plus free FMN and Rf (100-fold excess) for 1 h. (F): R2 relaxation rates of LnCap and HUVEC (2 x 10^6 cells/0.3 mL for each; in gelatin) incubated with 0.3 and 0.03 µmol Fe/mL of USPIO, FAD USPIO for 1 h. In all cases, two-sided student t-tests were performed to address statistical significance. ***: $p<0.001$; **:$p<0.005$; *:$p<0.01$.

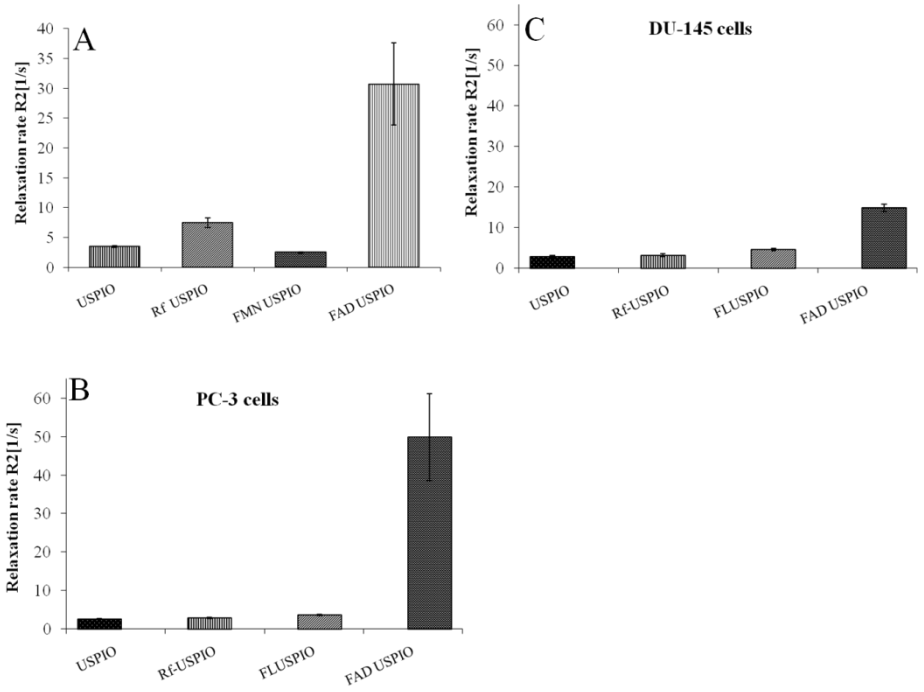

Figure 2.5.6. Rf-USPIO, FLUSPIO, and FAD USPIO cellular uptake analyzed by MRI. R2 relaxation rates of PC-3 cells in gelatin (2.0 x 10^6 cells/0.3 mL) incubated for 3 h with 0.3 µmol Fe/mL of double coated (twice coated with Rf and metabolic analogues) Rf USPIO, FMN USPIO, and FAD USPIO (A). The controls (medium, Rf, FMN, FAD) from (A) were not shown for better clarity. R2 relaxation rates of PC-3 (2.0 x 10^6 cells/0.3 mL)(B) and DU-145(2.0 x 10^6 cells/0.3 mL) (C) in gelatin incubated for 3 h with Rf-USPIO, FLUSPIO and FAD USPIO. The controls (medium, GMP, Rf, FMN, FAD) from (B) and (C) are not shown for better clarity.

The cellular uptake of Rf and its metabolic analogues coated USPIO by different prostate cancer cells was evaluated using MR relaxometry measurements. In this regard, the USPIO double coated with Rf, FMN, FAD i.e. Rf USPIO, FMN USPIO, and FAD USPIO cellular uptake in PC-3 cells after 3 h incubation displayed high R2 relaxation rates for double coated FAD USPIO compared to plain USPIO. R2 relaxation rates of the nanoparticles double coated with endogenous RCP ligand are 7.47±0.83 s^{-1} (Rf-USPIO), 2.51±0.08 s^{-1} (FMN USPIO), 30.72±6.90 s^{-1}(FAD USPIO) compared to USPIO (3.47±0.16 s^{-1}) (Figure 2.5.6A) respectively. The cellular uptake of three different flavin based nanoparticles (Rf-USPIO, FLUSPIO, and FAD USPIO coated with GMP for stabilization) was studied in PC-3 (Figure 2.5.6B) and DU-145 cells (Figure 2.5.6C). Among the fluorescent nanoparticles generated by flavin coating i.e. Rf-USPIO, FLUSPIO, and FAD USPIO, high R2 relaxation rates were displayed by FAD USPIO in gelatin after 3 h incubation (PC-3: 2.92±0.17 s^{-1}; DU-145: 3.19±0.32 s^{-1} for Rf-USPIO), FLUSPIO (PC-3: 3.67±0.16 s^{-1}; DU-145: 4.59±0.33 s^{-1}) and FAD USPIO (PC-3: 49.87±11.33 s^{-1}; DU-145: 14.92±0.86 s^{-1}) than that of USPIO alone (PC-3: 2.60±0.12 s^{-1}; DU-145: 2.84±0.28 s^{-1}) respectively.

2.11.2.3. Fluorescence Microscopy (Cell uptake and competition)

In vitro experiments on LnCap cells were also performed to evaluate the cellular labeling profile of FAD USPIO. The high uptake of FAD USPIO by LnCap cells was confirmed by fluorescence microscopy (Figure 2.5.7A-F) and flow cytometry (Figure 2.5.3B and 2.5.3E). A strong green fluorescence from the cells was observed after FAD USPIO incubation (3 h) (Figure 2.5.7A-F). The perinuclear fluorescence pattern strongly suggests the endosomal localization of the FAD USPIO. In addition, the specificity of FAD USPIO for RCP was confirmed using fluorescence microscopy by competitively blocking their uptake by free Rf (10- and 100- fold excess). In Figure 2.5.7G and 2.5.7H, FAD USPIO uptake by LnCap cells is competitively blocked using free Rf, which could be clearly visualized by reduction in the green fluorescence of FAD USPIO respectively.

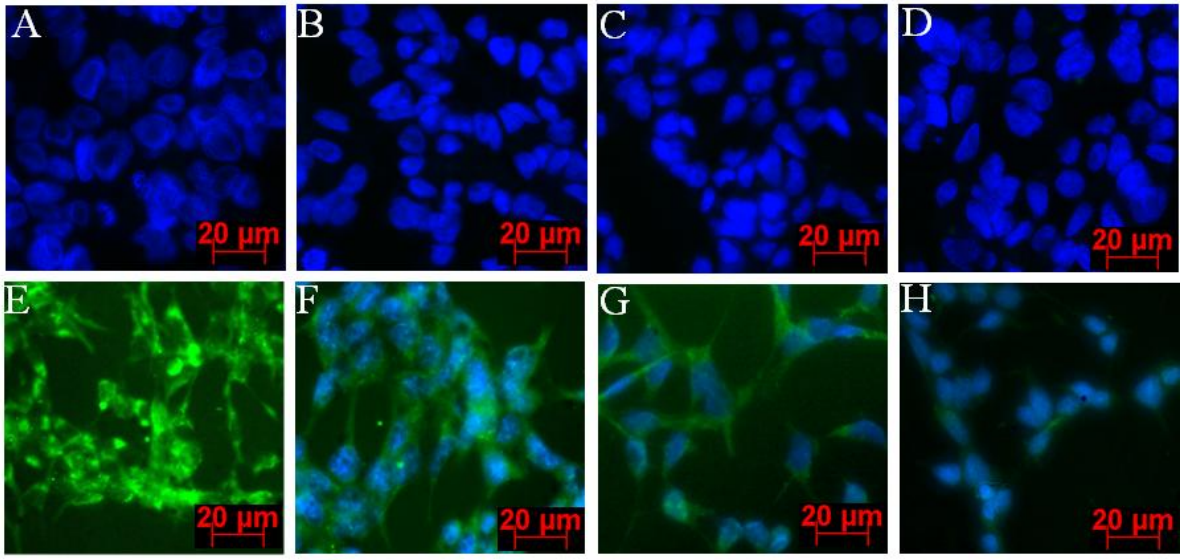

Figure 2.5.7. FAD USPIO uptake and Rf competition (10- and 100-fold excess) in LnCap cells analyzed by means of fluorescence microscopy. A-F: Fluorescence microscopy images of LnCap cells incubated for 3 h with FAD USPIO (3.0 µmol Fe/mL). Nuclei are counterstained with DAPI. A: Blank medium. B: FAD. C: GMP. D: USPIO. E: FAD USPIO without DAPI. F: FAD USPIO plus DAPI. The images clearly show the vesicular (likely endosomal) localization of the FAD USPIO. G-H: FAD USPIO (0.3 µmol Fe/mL) uptake by LnCap cells was competitively blocked by Rf (10- and 100-fold competition) after 1 h incubation. The competition effect clearly indicates the RCP-mediated uptake of FAD USPIO by LnCap cells.

2.11.3. In vivo evaluation of FAD USPIO

The FAD USPIO displayed intense cell labeling efficacy for metabolically active cells (prostate and activated endothelial cells) compared to their antecedent FLUSPIO. RCP-mediated uptake of FAD USPIO (*in vitro*) profile was further advanced to *in vivo* targeting investigations. Prior to the intended *in vivo* studies the pharmacokinetic profile of FAD

USPIO was checked by blood half life studies. Additionally, *in vivo* MR findings of FAD USPIO were validated using histology and supported by Prussian blue staining respectively.

2.11.3.1. Blood half life of FAD USPIO

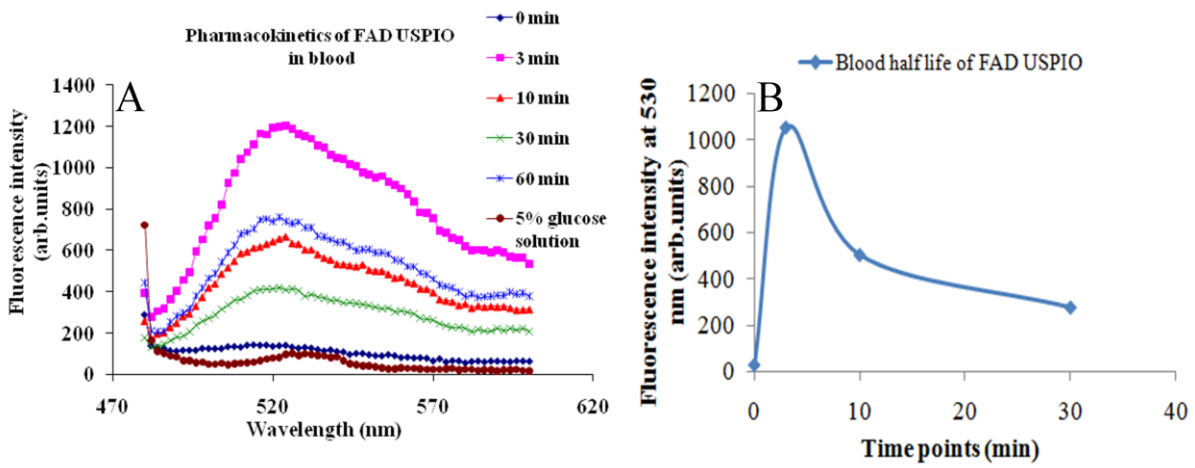

Figure 2.5.8. Blood half life of FAD USPIO as determined using fluorescence spectroscopy. Male nude (CD1) mouse (n=1) was intravenously injected with FAD USPIO (900 µmol Fe/Kg) and fluorescence from FAD USPIO (emission at 530 nm) in blood at different time points (0, 3, 10, 30 and 60 min) was measured using fluorescence spectroscopy respectively.

The blood half life of FAD USPIO was determined using CD1 male nude mouse (n=1), which was administered with 900 µmol Fe/Kg of FAD USPIO (130 µL) and their circulation time in the blood was followed using fluorescence spectroscopy. The FAD on FAD USPIO was excited using either 450 or 468 nm as the excitation wavelength and the emission intensity was measured at 530 nm in the blood. The auto fluorescence from blood was subtracted by including the blood collected prior to i.v. injection of the nanoparticles which is used as the control. The blood samples (FAD USPIO in blood), withdrawn from the mouse at different time points, were diluted in 5% glucose solution prior to the fluorescence measurements. The FAD USPIO displayed a reasonable blood half life of 10 min (Figure 2.5.8A and 2.5.8B). The increase in blood half life after 60 min could be attributed to the error associated with the measurements and fluorescence originating from the remnant nanoparticles (may be agglomerates) in blood. As a follow up study, more number of mice will be used for determining the half life of FAD USPIO in blood in order to draw statistical conclusions.

2.11.3.2. In vivo MR imaging of FAD USPIO

The *in vivo* specificity of FAD USPIO for RCP was evaluated in CD1 male nude mice bearing LnCap tumor xenografts. Resovist was used as a control group for the *in vivo* study. The specific uptake of FAD USPIO was shown by the increase in R2 relaxation rates after 1 h and 3 h incubation in comparison to the Resovist. R2 relaxation rates of FAD USPIO/Resovist (n=3) after 1 h and 3 h incubation are 21.86±3.85 s^{-1}/6.43±3.88 s^{-1} and 13.97±4.91 s^{-1}/3.24±4.16 s^{-1} respectively (Figure 2.6.0E). Additionally, visual inspection of the T_2*-weighted images of LnCap tumors after 1 h and 3 h of injection of FAD USPIO showed clearly the accumulation of the specific probe in the centre and periphery of the tumor compartment due to the decrease in T_2* signal intensity (indicated by arrows in Figure 2.5.9E-F). Contrarily, T_2*-weighted images of LnCap tumors after 1 h and 3 h of injection of Resovist showed less or no signal intensity reduction in the tumor borders (Figure. 2.5.9A-C). Furthermore, the color coded R2 relaxation pixel map supported the visual observations from T_2*-weighted images and confirmed the specificity of FAD USPIO for RCP compared to Resovist in LnCap tumor xenografts (Figure 2.5.9G-L).

To verify the observed FAD USPIO specificity (MR findings), histology and Prussian blue staining was performed. Histological sections of LnCap tumors previously injected with Resovist and FAD USPIO were stained for blood vessel density using CD-31 (red) and nuclei were stained with DAPI (blue)(Figure 2.6.0A-B). LnCap tumor sections displayed a high vascularity with many mature vessels facilitating the accumulation of the specific probe (FAD USPIO) in the endothelial cells of the tumor xenografts. Further, to confirm the high intratumor accumulation of the probe Prussian blue staining was performed. The Prussian blue images clearly show the accumulation of the RCP-specific probe (FAD USPIO) after 3 h incubation as indicated by arrows in Figure 2.6.0D respectively. In contrast, the Prussian blue images of the control LnCap tumors after 3 h incubation, did not show any accumulation of Resovist (Figure 2.6.0C).

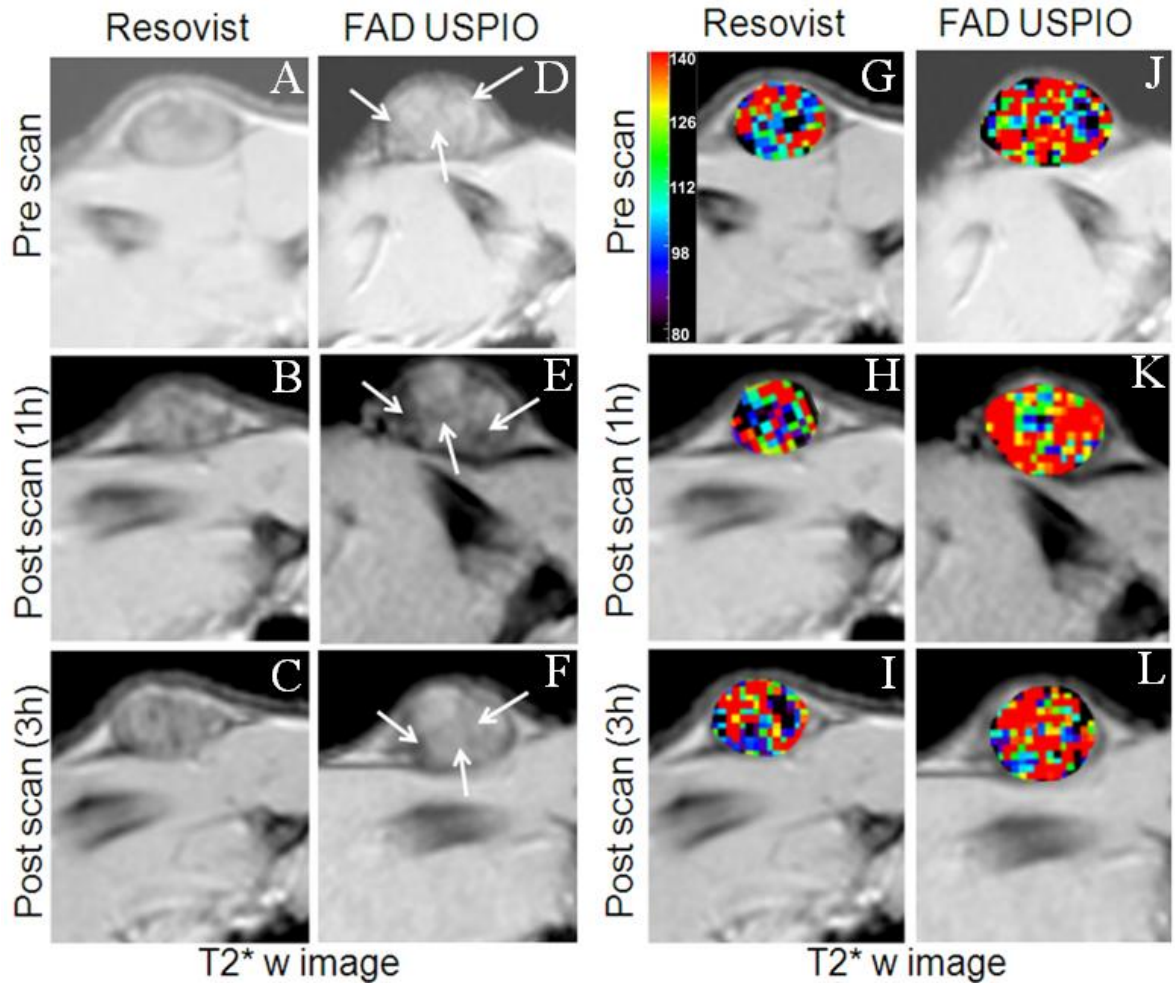

Figure 2.5.9. T_2*-weighted MR images (transversal slice) of CD1 male nude mice bearing s.c. LnCap tumors before and after 1 h and 3 h i.v. injection of Resovist (A-C) and FAD USPIO (D-F) respectively. The focal areas with strong and heterogeneous signal intensity (SI) decrease are observed in the tumor center and periphery after 1 h of injection of FAD USPIO (arrows in E) and less intense heterogeneous SI decrease are observed in tumor periphery after 3 h incubation (arrows in F). Only few spots with high susceptibility are found at the margin of the control tumor after injection of the Resovist (A). No decrease in signal was observed in control tumors by visual inspection after 1 h and 3 h incubation (B-C). The color coded R2 relaxation pixel map was overlayed on T_2*-weighted MR images of Resovist (G-I) and FAD USPIO (J-L) respectively. The increase in R2 relaxation rate after 1 h of injection of FAD USPIO are observed in tumor center and periphery (displayed as organisch red color pixel map in K) and similarly after 3 h incubation the increase in relaxation rate (R2) is shown in L. In contrast, the control tumor didn't show any change in the R2 relaxation rates (1 h and 3 h) after injection of the Resovist (H and I) respectively.

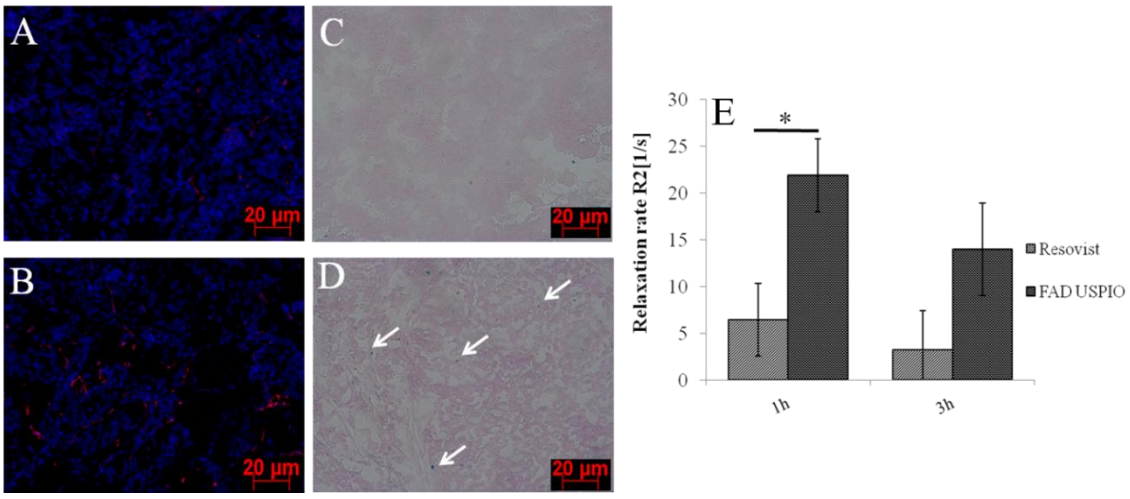

Figure 2.6.0. Immunofluorescence and Prussian blue staining images of LnCap tumors and prostate gland. Histological sections of LnCap tumors previously injected with Resovist (A), FAD USPIO (B) in which (blood vessel-)density were studied by staining with CD-31(red) and nuclei with DAPI (blue). Both control and FAD USPIO tumor sections displayed CD-31-positive vessels. In addition, Prussian blue staining of tumors showed considerable accumulation of FAD USPIO (arrows in D) while control tumors (C) displayed less or no accumulation of the Resovist respectively. E, change of R2 relaxation rates in LnCap tumors (n=3) after injection of FAD USPIO and Resovsit respectively. The specificity of the FAD USPIO probe for RCP in LnCap tumors after 1 h and 3 h incubation was clearly indicated by increase in R2 values compared to the Resovist. Two sided student ttest was performed to address the statistical significance *: $p<0.01$ respectively.

In summary, FAD coating of iron oxide nanoparticles rendered them fluorescent and highly specific for targeting the RCP *in vivo*. Further, FAD decorated USPIO proved itself as a better candidate for MR-cellular labeling than FLUSPIO and displayed intense accumulation in the prostate cancer tumors via targeting RCP. Hence, these FAD USPIO could be used as a tool for *in vivo* MR imaging and subsequently the MR findings could be validated by histology. As a follow up study, blood half life of FAD USPIO will be increased by conjugation of long circulating ligands (PEG spacer) and further, optimization of its imaging properties (magnetism and fluorescence) will be carried out in order to generate nanoparticles with even better *in vivo* targeting ability respectively.

Chapter 3.
Conclusion and Outlook

In this thesis three different synthesis attempts were made to generate the magnetofluorescent nanoparticles under aqueous reaction conditions by using simple and straightforward formulation techniques. Initially, lanthanide incorporation into the magnetic nanoparticles was tested and evaluated, followed by naphthalene sulfonates-coated nanoparticles, and finally non-polymeric flavin-coated magnetofluorescent nanoparticles were developed.

Firstly, lanthanides were incorporated into iron oxide nanoparticles (via doping) for the attempted generation of magnetofluorescent nanoparticles. The synthesis of lanthanide-doped iron oxide nanoparticles (Ln-USPIO) was achieved by replacing molar percentages of iron(III) by lanthanide (Eu(III), Tb(III), Yb(III)) metal ions under aqueous reaction condition. However, the Ln-USPIO synthesis only leads to a low level of lanthanides inside the iron oxide crystal lattice, due to size-based difference between the lanthanide and iron cations. As a consequence, the fluorescent properties of the particles were not satisfying. Furthermore, Ln-USPIO storage under highly acidic conditions might lead to leaching of the lanthanides inclusion from the iron oxide crystal structure. As further trials, the lanthanide inclusion in USPIO may be increased by a protective coating of (bio-)polymers (dextran, chitosan, PEG, PVA, PVP, PEO) thus preventing its leaching from Ln-USPIO.

Secondly, NUSPIO were generated by incubating naphthalene disulfonic acids (H-acid and ANDS) with iron oxide nanoparticles under aqueous acidic conditions at ambient temperature. The final nanoparticles were purified using dialysis or resin exchange techniques, and neutralized using ideal buffers (HEPES, PBS, MOPS, etc.). However, NUSPIO failed to display any fluorescence under the fluorescence microscope, which could be explained based on quenching of naphthalene sulfonates fluorescence by the paramagnetic species (magnetic nanoparticles), via the static and dynamic electron transfer reactions. As further investigations, sonication and mixed coating with small molecules (AMP, GMP) to avoid steric hindrance should be tested for generating fluorescent NUSPIO.

Finally, the first fluorescent and non-polymeric coating of iron oxide nanoparticles was achieved based on the endogenous flavin analogues such as flavin mononucleotide (FMN) and flavin adenine dinucleotide (FAD). Additionally, the importance of the riboflavin carrier protein (RCP) and its role in mediating the uptake of the fluorescent nanoparticles by prostate cancer cells and activated endothelial cells was demonstrated. The magnetofluorescent nanoparticles (FLUSPIO/FAD USPIO) were generated in aqueous reaction conditions at ambient temperature, by first sonicating FMN or FAD with magnetic nanoparticles followed by a coating with GMP in order to avoid steric hindrance between the bulky isoalloxazine rings of FMN or FAD respectively. The FLUSPIO and FAD USPIO were stable under physiological conditions and displayed an intense green fluorescence. FLUSPIO

and FAD USPIO showed high relaxivity values similar to Resovist (clinical MR contrast agent) in water and HEPES buffer, respectively. The biocompatibility of FLUSPIO and FAD USPIO was confirmed using different cytotoxicity assays and staining (assays: TUNEL and 7-AAD labeling; staining: trypan blue). The high cellular uptake of FLUSPIO/FAD USPIO by activated endothelial and cancer cells is anticipated to be mediated by RCP, since blocking/saturating this carrier protein with free FMN/FAD/Rf attenuated nanoparticle uptake. Using activated endothelial cells and different prostate cancer cell lines, the suitability of FLUSPIO/FAD USPIO for MR- and fluorescent cell tracking purposes was demonstrated. The *in vivo* specificity of FAD USPIO was confirmed by MRI and further validated through histology studies (immunohistochemistry and Prussian blue staining). However, the mechanistic aspects of FLUSPIO and FAD USPIO uptake (i.e. RCP mediated uptake) in metabolically active (cancer and activated endothelial) cells have to be dealt critically in future by performing rigorous experimental investigations.

In follow-up analyses, we aim to investigate the fluorescence and target specificity of USPIO with different core diameters by employing flavin and its derivatives (Rf, FMN, FAD) as an adsorptive, fluorescent and non-polymeric coating. In addition, we will investigate the accumulation and target specificity of FLUSPIO in tumors and/or tumor endothelial cells. We presume that *in vivo*, FLUSPIO will mostly target activated tumor endothelial cells, thereby enabling molecular MR and optical imaging of tumor angiogenesis. Nevertheless, the concept of targeting RCP is not only limited to USPIO. FMN could also serve as a versatile building block in generating contrast agents for other imaging modalities. For instance, small FMN-containing molecular probes could be synthesized for nuclear imaging techniques such as PET and SPECT, and they could serve as a platform to develop novel diagnostic tools for monitoring tumor metabolism and progression.

Chapter 4.

Experimental Section

4.1. Materials

4.1.1. List of chemicals

Sigma Aldrich Chemie GmbH, Steinheim, Germany

Iron (III) chloride ($FeCl_3$, >97%), Iron (II) chloride tetrahydrate ($FeCl_2.4H_2O$, >99%), Sodium hydroxide (NaOH, 98%), 5-sulfosalicylic acid dehydrate (≥ 99% for metal titration), IDRANAL III standard solution (EDTA-Na_2, reagent for metal titration,0.1 M), N-[Tris(hydroxymethyl)methyl]-2-aminoethanesulfonic acid sodium salt (TES, ≥99%), Potassium bromide (KBr, ≥99%), 3-aminopropyltrimethoxy silane (APTMS, 97%), Tetraethyl orthosilicate (TEOS, 98%), Europium (III) chloride hexahydrate ($EuCl_3.6H_2O$, 99.9% trace metal basis), Gadolinium (III) chloride hexahydrate ($GdCl_3.6H_2O$, 99% titration), Terbium (III) chloride hexahydrate ($TbCl_3.6H_2O$, 99.9% trace metal basis), Riboflavin-5`-monophosphate sodium salt dihydrate (Flavin mononucleotide, FMN, 73-79% fluorimetric grade), Oleic acid (Ph Eur), Glutaraldehyde solution (25% wt in H_2O), Thiamine monophosphate chloride dihydrate (TMP, ≥ 99%), D-(+)-Glucose (≥99.5%), 7-amino-1,3-naphthalene disulfonic acid monopotassium salt (≥98%; ANDS, fluorescent grade), 4-amino-5-hydroxy-2,7-naphthalene disulfonic acid disodium salt (H-acid, 85%), Etidronic acid monohydrate (≥95% (T)), Fluorescein-5(6)- isothiocyanate (FITC, 90% (HPLC)), Quinine hydrochloride dihydrate (≥99% (NT); suitable for fluorescence), 9-aminoacridine hydrochloride monohydrate (≥96% (AT), purum for fluorescence), DL-Tryptophan (≥99%), N-hydroxysuccinimide (NHS, 98%), Bromotrimethyl silane (TMBS, 97%), Diethyl vinyl phosphate (97%), N,N`-dicyclohexylcarbodiimide (DCC, 99%), N-(3-Dimethylaminopropyl)-N′-ethylcarbodiimide hydrochloride (EDC, commercial grade), DOWEX 50WX8 (20/50 Mesh, strongly acidic, H^+ form), Amberlite IRA 95 resin (weakly basic), 1,4-butane sultone (≥99 (GC)), 2-pyrrolidinone (99%), Silicagel for column chromatography (60 Å pore size, mesh (230 to 400)), Iron (III) acetylacetonate ($Fe(C_5H_7O_2)_3$, 97%), Tetramethyl ammonium hydroxide solution (TMAOH, ACS reagent,1M solution), Iron (II) sulfate heptahydrate ($FeSO_4.7H_2O$, reagent plus, ≥99%), N,N`-diisopropylcarbodiimide (DIC, ≥98% (GC)), N-ethyldiisopropylamine (DIPEA,≥98% (GC)), 1-hydroxybenzotriazole hydrate (HOBt, ≥97% (T)), 2-aminoethyl dihydrogen phosphate (AEP, 98%), Diethylazodicarboxylate (DEAD, puriss, ~40% in toluene), (Diacetoxyiodo)benzene (purum, ≥98% (AT)), Triphenylphosphine (purum, ≥95% (GC)), (4-dimethylamino)pyridine (DMAP, reagent plus, 99%), Sephadex G25 (medium), Disodium Molybdenum oxalate (puriss, p.a)

Carl Roth GmbH & Co. KG, Karlsruhe, Germany

Ammonia solution (NH_3, ≥25%), Hydrochloric acid (HCl, 37%), Ammonium peroxodisulfate ($NH_4S_2O_8$, ≥98%), Sodium acetate (CH_3COONa, ≥99%), N-(2-Hydroxyethyl)piperazine-N′-(2-ethanesulfonic acid) (HEPES, ≥99.5%), N,N-dimethylformamide (DMF, ≥99.8% for synthesis), spectrum dialysis membrane (Molecular weight cut off 10,000 and 5,000), visking membrane (Molecular weight cut off 14,000).

Applichem GmbH, Darmstadt, Germany

Zinc sulphate heptahydrate ($ZnSO_4.7H_2O$, p.a), Eriochrome Black T (analytical grade for metal titration), PBS buffer (10X Dulbecco`s powder), Riboflavin (Rf, 98-100% analytical grade), Riboflavin-5`-adenosine diphosphate disodium salt dihydrate (Flavin adenine dinucleotide, FAD, 95-98% analytical grade), Guanosine-5`-monophosphate disodium salt hydrate (GMP, 98%), Adenosine-5`-monophosphate disodium salt dihydrate (AMP, 99%), Gelatin (ph. Eur, powder), Pyridine for analysis.

MercK KGaA/VWR, Darmstadt, Germany

TLC Silicagel $60F_{254}$ 25 Al sheets 20X20cm, hydrazine hydrochloride (puriss), perchloric acid (70-72%)).

4.2. Methods

4.2.0. Different physico-chemical characterization techniques

4.2.1. Transmission electron microscopy (TEM)

The morphology, size, and size distribution of the generated nanoparticles were characterized by TEM (EM 400 T (Philips, Eindhoven, The Netherlands) with an accelerating voltage of 60 kV (TEM accelerating range 30 – 120 kV). USPIO, FLUSPIO, FAD USPIO were embedded in 2 % agarose, rinsed with distilled water and dehydrated with ethanol (30 %, 50%, 70%, 90%, 100 %). Subsequently, they were embedded in Epon, polymerized 8 h at 37 °C, 56 h at 60 °C, and then cut into 70 – 100 nm thick slices using Leica EM UC6, Reichert Ultracut S loaded with LKB knife maker 7801 Type A. TEM micrographs were recorded using SIS Morada (11 Mpix) digital camera. The particle size and size distributions were calculated using an image analysis program (iTEM software, Olympus, Germany) and by measuring the diameter of at least 200 particles. TEM measurements of the cellular uptake of the USPIO and FLUSPIO by prostate cancer cells were performed similar to the above described procedure. The uranyl acetate and lead citrate contrast of the cells for different cell

organelles embedded in the Epon polymer was performed using LKB ultrastainer. The morphology, size and size distribution of NUSPIO, Ln-USPIO were characterized by TEM (Jeol 2100F, Japan). These nanoparticle suspensions were directly deposited onto a carbon-coated copper grid and air dried at RT and further examined using TEM respectively. Dr. Jörg Bornemann, Pathology Institute, University Clinics RWTH Aachen University performed TEM measurements.

4.2.2. Scanning electron microscopy (SEM)

The surface morphology of the nanoparticles was characterized by SEM [FEI (PHILIPS) ESEM XL 30 FEG; EDAX Falcon genesis, resolution 2 nm, sample chamber pressure 3.0 nbar – 7.5 mbar] with an accelerating voltage of 20 kV (SEM accelerating range 200 V – 30 kV). USPIO, FLUSPIO, and FAD USPIO in water were dried by dehydrating them with different percentages of ethanol (25%, 50%, 70-75%, 90-95%, 100%). Finally, trace amounts of water were removed by treating them with propylene oxide. Further, samples were dried and mounted on the glass cover slip, which is kept over the specimen stub, and a conductive glue (silver paste or graphite) was applied between them in order to have connectivity as well as conductivity between them. Mr. Manfred Bovi, Pathology Institute, University Clinics RWTH Aachen University performed SEM measurements.

4.2.3. Atomic force microscopy (AFM)

A drop (5 μL) of the sample (USPIO, FLUSPIO) solutions was deposited onto a polymer membrane providing a very flat surface for visualizing nanoparticles (Nucleopore 0.1μm, Whatman). These samples were left to dry in a fume hood for 1.5 h. A circular shaped deposit was formed. Structurally the circular deposit consists of a tidemark which is a high concentration of the particle aggregates formed on the edge of the dried droplet, and the central region enclosed where a low concentration of the particle aggregates is evident. Tapping mode imaging was subsequently performed on both of these regions.

All AFM images were taken in the Tapping Mode on a Multimode Nanoscope IIIa instrument (Veeco, USA) using Budget Sensors Tap300 probes. Imaging parameters were continually adjusted to provide the best resolution and phase contrast. Images are shown with topography on the left and phase images on the right. Both images are recorded simultaneously from the same area of sample. Phase images can highlight features not shown clearly in the topography, and present contrast based on variations in mechanical or surface

chemical material properties. Dr. Matt Bunker, Molecular Profiles Ltd, Nottingham, UK performed AFM measurements.

4.2.4. Dynamic light scattering (DLS)

Dynamic light scattering (DLS) measures Brownian motion and relates this to the size of the nanoparticles. Brownian motion is the random movement of particles due to the bombardment by the solvent molecules that surround them. DLS is concerned with measurement of particles suspended within a liquid. The larger the particle, the slower will be the Brownian motion. Smaller particles are "kicked" further by the solvent molecules and move more rapidly. The temperature also needs to be maintained as constant; otherwise convection currents in the sample will cause the non-random movements that will ruin the correct interpretation of size. The velocity of the Brownian motion is defined by a property known as the translational diffusion coefficient (D). DLS measurements were conducted with glass cuvette with square aperture (PCS1115) by using a Nanosizer ZS (Malvern Instruments, Malvern, United Kingdom). DLS of USPIO, FLUSPIO, and FAD USPIO were measured using Nanosizer ZS in different physiological solutions in addition to acidic and basic solutions respectively. The NUSPIO particle size prepared by different purification methods were measured in water at 23.6 °C using MICROTRAC-UPA 150 using polystyrene cuvettes and 386 mV as reflected power respectively. DLS measurements were performed at the DWI, RWTH Aachen University.

4.2.5. Zeta potential

The liquid layer surrounding the nanoparticle consists of two parts (regions); an inner region (stern layer) where the ions are strongly bound and an outer (diffuse) region where they are less firmly associated. Within the diffuse layer there is a notional boundary, inside which the ions and particles form a stable entity. When a particle moves (e.g., due to gravity), ions within the boundary move it. Those ions beyond the boundary stay with the bulk dispersant. The potential at this boundary (surface of hydrodynamic shear) is the zeta potential. The surface charge of USPIO, FLUSPIO and FAD USPIO nanoparticles was determined by measuring the zeta potential as a function of the pH value of USPIO and FAD USPIO suspensions with clear disposable zeta cell (DTS1060C) by using a zetasizer (Nano sizer, Malvern Instruments). Zeta potential measurements were performed at the DWI, RWTH Aachen University.

4.2.6. X-ray powder diffraction (XRD)

The crystal structures of the USPIO, FLUSPIO, and FAD USPIO particles were characterized by using the powder diffractometer STOE STADI P equipped with an IP-PSD detector and CuKα_1 –radiation (1.54059Å; STOE & Cie, Darmstadt, Germany) source. The diffraction pattern of the nanoparticles was compared with STOE STADIMP diffractometer equipped with a PSD detector and MoKα_1 –radiation (0.70932Å) source where the fluorescence from iron is eliminated. The crystal structure of Ln-USPIO and NUSPIO nanoparticles were characterized by using the powder diffractometer equipped with a monochromatic x-ray source (CuKα1 1.5406 A) and calibrated against NIST1976 Corundum standard reference material. Scans were recorded from 10 to 140° (2θ), with a 0.10° (2θ) step and a counting rate of 1.2 s per step at RT. Dr. Paul Müller, Inorganic Chemistry Institute, RWTH Aachen University and Dr. Matt Bunker, Molecular Profiles Ltd, Nottingham, UK performed powder XRD measurements.

4.2.7. Fourier-Transform Infra Red (FT-IR)

Functional groups in FMN, GMP, FAD, Naphthalene sulfonates, USPIO, FLUSPIO, NUSPIO, and FAD USPIO were characterized by using FT-IR spectroscopy [Perkin Elmer - Spectrum 100 FT-IR Spectrometer] using the KBr pellet technique with a resolution of 4 cm^{-1}. Mr. Maik Jacob, from Prof. Peter Comba´s group, Inorganic Chemistry Institutes, University of Heidelberg performed FT-IR measurements.

4.2.8. Elemental analysis (C,H,N analysis)

The organic elementary analysis of FLUSPIO and FAD USPIO was performed in the analytical laboratories of the Chemical Institutes at the University of Heidelberg on a Vario EL analysis instrument with a thermal conductivity detector (Elementar, Germany).

4.2.9. Thermo gravimetric analysis (TGA)

Thermo gravimetric analysis of fluorescent FMN, GMP, FAD, FLUSPIO, and FAD USPIO was performed using a Shimadzu TGA-50H device, by heating the samples in an alumina crucible in presence of inert nitrogen atmosphere at a heating rate 20 °C/min from 0 to 600 °C. Mr. Friedrich Haulena, DWI, RWTH Aachen University performed TGA measurements.

4.2.10. SQUID magnetometry

The magnetic susceptibility of the fluorescent nanoparticles (FLUSPIO) and USPIO was determined using SQUID magnetometry (Quantum Design MPMS-5XL) in the field range of B = 5.0 to – 5.0 T and at RT (T = 290.0 K). The data were corrected for the sample holder (Teflon capsules) and the diamagnetic contribution of the compound. Mr. Manfred Spieldrich, Inorganic Chemistry Institute, RWTH Aachen University performed the SQUID measurements.

4.2.11. MR relaxometry

Nuclear MR relaxometry of FLUSPIO and FAD USPIO nanoparticles was performed in a clinical 3T whole-body MR scanner (PHILIPS Achieva, The Netherlands) using a knee coil (SENSE-flex-M, PHILIPS, The Netherlands) at RT in University Clinics RWTH Aachen University. FLUSPIO and FAD USPIO were diluted in deionized water at concentrations ranging from 0.001 to 100 µg of Fe/0.3 mL. For MR measurements 0.3 mL/well of diluted FLUSPIO/FAD USPIO solution was filled in custom made phantoms (Greiner 96 well Flat Transparent Polystyrol microplate, Germany). Transverse relaxation times (T_2) were measured in 2 D scan mode using a multi-slice, multi shot spin echo sequences with 90° excitation pulses followed by a train of equally spaced 180° refocusing pulses [TR = 1500 ms, mTR = 1189 ms, TE = 8.1 ms (shortest), number of echoes = 20, inter-echo spacing = 8.1 ms, FOV = 130 x 162.5, reconstruction matrix = 64 x 81, voxel size = 2 x 2, slice thickness = 3 mm, slice orientation = coronal, scan mode = multishot (MS)]. Transverse relaxation times (T_2) were measured in 3 D scan mode using a multi-slice, multi shot spin echo sequences with 90° excitation pulse followed by a train of equally spaced 180° refocusing pulses [TR = 1500 ms, mTR = 716 ms, TE = 11.8 ms (shortest), number of echoes = 20, inter-echo spacing = 12 ms, FOV = 130 x 162.5 x 18 mm, reconstruction matrix = 64 x 81, voxel size = 2 x 2 x 3, slice orientation = coronal, scan mode = 3 D, TSE turbo direction = Y]. T_2 relaxation times were calculated by a linear fit of logarithmic region of interest (ROI) signal amplitudes versus echo time (TE). Longitudinal relaxation times (T_1) were determined using a multi shot spin echo sequences with 10° excitation pulse without refocusing pulse [TR = 6.8 ms, TE = 3.3 ms (shortest), number of echoes = 1, FOV = 170 x 148.75 mm, reconstruction matrix = 152 x 130, voxel size = 1.12 x 1.11, slice thickness = 5 mm, slice orientation = coronal, scan mode = 2 D, cardiac synchronization = ECG trigger, cardiac frequency = 30]. Relaxivities r1 and r2 were determined by a linear fit of the inverse relaxation times as a function of the iron concentrations. Nuclear MR relaxometry of the NUSPIO nanoparticles was performed using a clinical 1.5 T whole-body MR system (Siemens Symphony, Erlangen,

Germany) in combination with a custom-made radio frequency coil for excitation and signal reception. The radio frequency coil was designed as a cylindrical volume resonator with an inner diameter of 83 mm and a usable length of 120 mm. To optimize the available signal-to-noise ratio, manual tuning and matching of the coil's resonance circuitry was performed for each measurement. NUSPIO nanoparticles were diluted in distilled water at concentrations between 0.001 and 100 µg of Fe/mL. For MR measurements 0.5 mL NUSPIO dilutions were filled in 1 mL Eppendorf vials each. T_2 relaxation times were measured using a standard Carr-Purcell-Meiboom-Gill pulse sequence (TR = 2000 ms, TE range 30-960 ms, 32 echoes, FOV = 134 x 67 mm, matrix 128 x 64, slice thickness 10 mm, BW = 40, NEX = 3). T_1 relaxation times were determined using a T_1w saturation recovery turbo FLASH sequence, thereby varying the inversion time, TI(TR = 7160 ms, TE = 1.67 ms, TI = 900-4000 ms, FOV = 200 x 150 mm, matrix 52 x 128, slice thickness 2 mm), respectively.

4.2.12. Fluorescence Spectroscopy and Microscopy

The absorbance spectra of USPIO, FMN, FMN with GMP, and FLUSPIO were recorded in water and various buffer solutions using the TECAN Infinite M200 (Tecan Austria GmbH) plate reader at RT (iron concentration range: 10^{-6} M to 10^{-12} M). FAD, FAD USPIO absorbance spectra were only recorded in water. The absorbance measurements were performed on a 96-well plate (Greiner Bio-one 96 well flat transparent polystyrol microplate, Germany). Additionally, the absorbance spectra of the moieties (i.e. FMN, FLUSPIO) in water were recorded after 3 d exposure to daylight. The fluorescence spectra of FMN and FLUSPIO were recorded in water and various buffer solutions (TRIS, TES, HEPES, sodium phosphate) at RT using the TECAN Infinite M200 (Tecan Austria GmbH) plate reader (iron concentration range: 10^{-6} M to 10^{-12} M). FAD, FAD USPIO fluorescence spectra were only recorded in water respectively. The fluorescence measurements were performed using a 96-well plate (Greiner Bio-one 96 well, F-bottom (chimney well), fluorotrac 600 black polystyrene microplate, Germany). Further, we exposed FMN and FLUSPIO to daylight for 3 days in order to study the effect of daylight on their emission intensity.

The fluorescence spectra of organic dyes (naphthalene sulfonates, FITC, RITC) and NUSPIO was measured in water and different buffer solutions using aminco-bowman series 2 fluorescence spectrophotometer (Thermo electron corporation, Germany).

The fluorescence intensity of FLUSPIO and FAD USPIO nanoparticles was checked using a fluorescence microscope (Axio Imager M2, Carl Zeiss, Germany). Additionally, fluorescence intensity of Ln-USPIO, NUSPIO was evaluated using an epifluorescence

microscope (Olympus, Model BX50, Germany) with an added fluorescence device respectively. In brief, 3 to 5 µL of the fluorescent nanoparticles in water was placed in the microscopic observation slides (75 x 26 mm, R. Langenbrinck, Emmendingen, Germany) and they were fixed with a cover slip (round, 12 mm, Carl Roth GmbH, Karlsruhe, Germany). Further, the samples were directly examined under the fluorescence microscope for their fluorescence intensity and for visualizing the surface morphology and shape (spherical morphology and degree of agglomeration) of the nanoparticles. These preliminary microscopic examinations were carried out for all batch preparations and their fluorescence ability was validated prior to their intended *in vitro* experiment.

4.2.13. Energy dispersive X-ray (EDX) analysis

The chemical composition of the FLUSPIO and FAD USPIO nanoparticles was determined by SEM [FEI (PHILIPS) ESEM XL 30 FEG; EDAX Falcon genesis]. FLUSPIO and FAD USPIO in water were dried under high vacuum conditions. Further, the dry samples were mounted on specimen stub with silver paste or graphite and EDX spectrometric analysis was measured by employing 20 kV as the EDX accelerating voltage.

4.2.14. NMR spectroscopy

NMR spectra were recorded at 199.92 MHz (^{1}H) and (^{13}C) on a Bruker DRX200 instrument. For ^{1}H and ^{13}C spectra, the respective solvent peak was used as reference for the chemical shift δ. In case of the TMS added deutrated solvent, the peak from TMS was used as the reference for the chemical shift δ. For the chemical investigation using NMR, deutrated chloroform, water, methanol and DMSO was used respectively. The following abbreviations are used for signal multiplicities: s = singlet, d = doublet, t = triplet, q = quartet, br = broad singlet or broad multiplet, m = multiplet. The measurements were performed at Inorganic Chemistry Institute, Heidelberg University.

4.2.15. Mass spectrometry

4.2.15.1. ESI Mass spectrometry

Electrospray ionization (ESI) mass spectrometry is a “soft” (i.e. fragmentation free) method for the analysis of charged molecules and supramolecular compounds present in the solution. Analysis of small organic molecules, metal complexes, biomolecules (peptides), nucleic acids, spacers (polyethylene glycol and derivatives) and phospholipids can be carried

out using ESI Mass spectrometry. ESI mass spectra of the samples were measured in methanol on an ICR Apex-Qe instrument using ESI pos HPmix 550-2800 m/z and ESI neg Arginin 100-900/150-1300 m/z methods. The measurements were performed at the Institute of Organic Chemistry, Heidelberg University.

4.2.15.2. TOF-SIMS Spectrometry

Time-of-Flight Secondary Ion Mass Spectrometry (TOF-SIMS) uses a pulsed primary ion beam to desorb and ionize species from a sample surface. The resulting secondary ions are accelerated into a mass spectrometer, where they are mass analyzed by measuring their time-of-flight from the sample surface to the detector. There are three different modes of analysis in TOF-SIMS; 1) mass spectra are acquired to determine the elemental and molecular species on a surface; 2) images are acquired to visualize the distribution of individual species on the surface; and 3) depth profiles are used to determine the distribution of different chemical species as a function of depth from the surface.

An image is generated by rastering a finely focused beam across the sample surface. Due to the parallel detection nature of TOF-SIMS, the entire mass spectrum is acquired from every pixel in the image. The mass spectrum and the secondary ion images are then used to determine the composition and distribution of sample surface constituents.

TOF-SIMS provides spectroscopy for characterization of chemical composition, imaging for determining the distribution of chemical species, and depth profiling for thin film characterization. TOF-SIMS analysis of FMN, GMP, and FLUSPIO were carried out in order to evaluate the chemical composition of the fluorescent nanoparticles. Dr. Matt Bunker, Molecular Profiles Ltd, Nottingham, UK performed TOF-SIMS measurements.

4.2.15.3. ICP-MS Spectrometry

The amount of iron present in nanoparticles (USPIO, APTMS-USPIO and FLUSPIO) was determined by high-resolution sector field ICP-MS (Element 2, Thermo Electron, Bremen, Germany) equipped with an autosampler (ASX-100, CETAC, Omaha, NE). Data were acquired at medium resolution (4000) using rhodium (5 ppb) as an internal standard. A PFA spray chamber equipped with a PFA 100 microflow nebulizer (CETAC) was used for sample introduction. The instrument was tuned and calibrated via infusion of a 1 ng/mL multi element standard solution (Merck, Darmstadt, Germany). Digestion of the USPIO, APTMS-USPIO and FLUSPIO was performed in a closed vessel microwave reaction system (CEM,

Kamp-Linfort, Germany) after addition of 53% nitric acid (60%) at 3 bar and 600 Wfor 50 min. Samples were diluted 1:200 in H_2O. Calibration was linear between 2 and 150 ng/mL iron (r>0.999). The iron content was expressed in nanograms of iron per mL. Mr. Sven Thöree, Hygiene department, University Clinics RWTH Aachen University performed ICP-MS measurements.

4.2.16. pH meter

pH values were adjusted at 25 ºC with a Mettler Toledo pH meter equipped with a KCl electrode and calibrated with pH standard solutions at pH 4.01,7.00 and 9.21 respectively.

4.2.17. X-ray photon electron spectroscopy

X-ray photoelectron spectroscopy (XPS) is a surface chemical analysis technique with the capability of determining elemental composition, oxidation state, empirical formula and impurities present in a sample. XPS takes advantage of the photoelectric effect. It measures the kinetic energy of the electrons that are ejected from a sample after irradiation by x-rays. The kinetic energy of an ejected electron is related to the binding energy of that electron for a certain atom. In this way, binding energies can be used to assign peaks to atoms in a typical spectrum. XPS of USPIO and FLUSPIO were measured in order to evaluate the coating efficiency of FMN, GMP through their binding energy to the surface of iron oxide nanoparticles. Dr. Matt Bunker, Molecular Profiles Ltd, Nottingham, UK performed XPS measurements.

4.2.18. Absolute quantum yield and fluorescence lifetime measurements

Absolute quantum yield measurements of FLUSPIO was measured using a custom made fluorescence set up (integrated sphere set up) without using any fluorophore standard which is often used in determining the relative quantum yield. Fluorescence lifetime of FLUSPIO was measured in order to evaluate the lifetime of FMN on the USPIO surface and to check their photostability. Dr. Ute Resch, BAM Federal Research Institute, Berlin performed absolute quantum yield and fluorescence lifetime measurements.

4.3. Ligand synthesis

Column chromatography was performed using 230 – 400 mesh silica gel. Thin-layer chromatography (TLC) was performed using TLC Silicagel $60F_{254}$ 25 Al sheets 20X20 cm (Merck KGaA, Darmstadt, Germany). Solvents for organic synthesis were of standard quality (*p.a.* grade) and used without further purification. Dry solvents were purchased form Sigma-Aldrich, stored over molecular sieves and used without further purification. All chemicals were used without further purification. The hydrochloride from 9-aminoacridine and quinine hydrochlorides was removed by washing it with the saturated K_2CO_3 and further they were extracted with ethyl acetate. The separated organic layer was dried over Na_2SO_4 and rotatory evaporated to generate 9-amino acridine and quinine respectively.

4.3.1. Synthesis of (2-([2-(Diethoxy-phosphoryl)ethyl]-naphthalen-1-ylmethyl-amino)-ethyl)-phosphonic acid diethyl ester

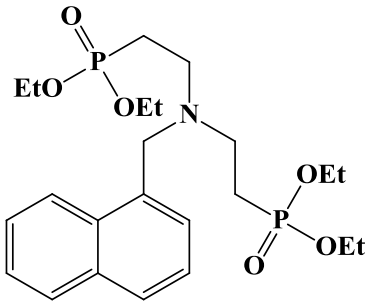

1

In a typical synthesis, a mixture of aminomethylnaphthalene (0.5 g, 3.18 mmol) and diethyl vinylphosphonate (3.13 g, 19.08 mmol, 6 equiv) in 10 mL of dry methanol was refluxed for 5 days[211]. The solvent was evaporated and the crude product was purified by column chromatography using silica gel as the solid phase and a mixture of CH_2Cl_2-methanol (20:1=v:v) as the mobile phase. The product was separated as a colourless gummy liquid (Yield 50%).

Molecular Formula: $C_{23}H_{37}NO_6P_2$ Molecular weight : 485.59

^{1}H-NMR (400 MHz, $CDCl_3$): δ = 8.05 (m, 2H, CH), 7.67 – 7.80 (m, 4H, CH), 7.33 – 7.46 (m, 8H), 4.18 (m, 8H, CH_2), 2.96 (m, 4H, N-CH_2), 1.89 – 2.05 (m, 4H, CH_2-P), 1.19 (m, 12 H, CH_3)

^{13}C-NMR (400 MHz, $CDCl_3$): δ = 133.8, 132.8, 127.7, 126.9, 125.2, 124.6, 122.5 (CH), 60.72 (PO-C), 49.97, 42.09 (N-C), 26.6, 23.8 (P-H_2C), 15.4 (H_3C)

4.3.2. Synthesis of [2-naphthalen-1-ylmethyl-(2-phosphono-ethyl)amino]ethyl]-phosphonic acid

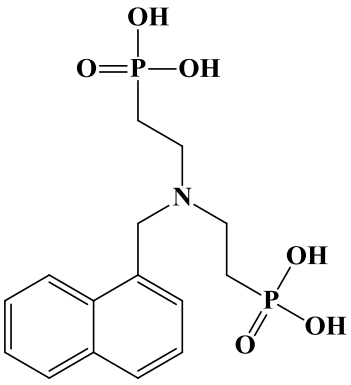

2

To a solution of (2-([2-(diethoxy-phosphoryl)ethyl]-naphthalen-1-ylmethyl-amino)-ethyl)-phosphonic acid diethyl ester (0.08 g, 0.16 mmol), in dry CH_2Cl_2 (5 mL), bromotrimethylsilane (0.4 g, 2.6 mmol, 16 equiv) was added in three different portions at 15 min intervals. The mixture was stirred for 60 min after the addition of the last portion. Evaporation of the solvent along with excess bromotrimethylsilane under reduced pressure afforded the crude product which was washed and triturated with hexane (3 X 15 mL) to get the pure product as a white solid (Yield 50%).

Molecular Formula: $C_{15}H_{21}NO_6P_2$ Molecular weight: 373.28

^{1}H-NMR (400 MHz, CD_3OD): δ = 8.24 (d, 1H), 8.03 (t, 2H), 7.52 – 7.77 (m, 4H), 4.09 (m, 2H), 2.21 – 2.43 (m, 4H), 1.33 (m, 4H)

^{13}C-NMR (400 MHz, CD_3OD): δ = 135.4, 132.6, 131.7, 130.5, 130.1, 128.6, 128.3, 127.6, 126.5, 124.0 (CH), 64.08 (C-C), 43.0. 43.8 (N-CH_2), 25.8, 25.0, 23.0, 22.2 (P-C)

4.3.3. Synthesis of 4-(9-aminoacridinium-10-yl)butane-1-sulfonate

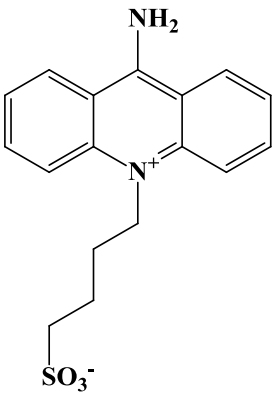

3

In brief, toluene (30 mL), 9-aminoacridine (0.68 g, 3.5 mmol) and 1,4-butane sultone (0.54 mL, 5.25 mmol) were heated under reflux for 3 days[212]. Further, the reaction mixture was allowed to cool to RT. The resulting orange solid was filtered and washed with acetone. Furthermore, they were re-crystallized with methanol and ethanol mixture (1:2) by gentle warming and cooling them to RT and then at 4°C. The crystals were collected and dried in vacuum (Yield 45%).

Molecular Formula: $C_{17}H_{18}N_2O_3S$ Molecular Weight: 330.40

^{1}H-NMR (400 MHz, DMSO d6): δ = 8.65 (m, 2H, CH), 8.47 (m, 2H, CH), 8.24 (m, 2H, CH), 8.10 (m, 2H, CH), 7.52 – 7.68 (m, 2H, CH), 4.65, 4.79 (m, 2H, N-CH_2), 2.50 (m, 2H, S-CH_2), 1.67 (m, 2H, S-CH_2-CH_2), 1.94 (m, 2H, N-CH_2-CH_2)

4.3.4. Synthesis of 4-(4-((R)-hydroxy((2S,4S,8R)-8-vinylquinuclidin-2-yl)methyl)-6-methoxyquinolinium-1-yl)butane-1-sulfonate

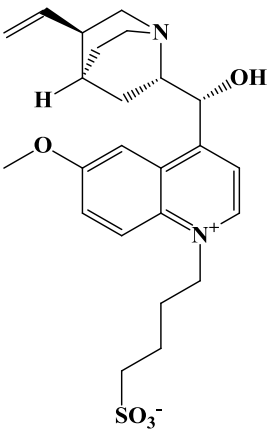

4

The mixture of 1,4-butane sultone (0.16 mL, 1.57 mmol) and quinine (0.34 g, 1.04 mmol) in 10 mL of toluene was heated under reflux for 21 h. The reaction mixture was allowed to cool to RT. The resulting pink solid was filtered and washed with toluene and acetone. Further, the crude product was re-crystallized with methanol and ethanol mixture (1:2). The crystalline solid was collected and dried in vacuum (Yield 97%).

Molecular Formula: $C_{24}H_{32}N_2O_5S$ Molecular weight: 460.59

^{1}H-NMR (400 MHz, D_2O): δ = 8.65 (m, 1H, CH), 7.72 – 7.86 (m, 2H, CH), 7.63 (br, 1H, CH), 7.32 (m, 1H, CH), 7.19 (m, 1H, CH), 7.07 (m, 1H, CH), 5.87 (s, 1H, C=CH), 5.08 (br, 2H, $C=CH_2$), 4.86 (m, 3H, N^+-CH_2, C-CH), 3.98 (m, 3H, O-CH_3), 3.58 (br, 1H, C-OH), 2.86 (br, 1H), 2.19 – 2.29 (m, 5H), 1.99 (br, 5H), 1.26 (m, 2H)

4.3.5. Synthesis of sodium 3,3'-(1'Z)-(4,4'-((E)-ethene-1,2-diyl)bis(4,1-phenylene))bis(diazene-2,1-diyl)bis(5-amino-4-hydroxynaphthalene-2,7-disulfonate)

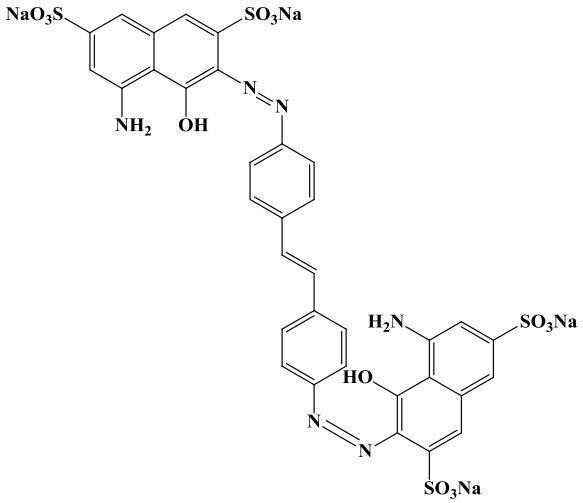

5

A mixture of 4,4'-diaminostilbene dihydrochloride (0.25g, 0.88 mmol), 5 mL of water and 0.37 mL of 37% HCl was heated until the solution was clear. After cooling the above solution down to 0 – 5 °C, $NaNO_2$ (0.122g, 1.76 mmol) in a minimum amount of water was added dropwise to the solution and the diazotization was continued for 2 h (colour of the solution changed from light brown to reddish brown). The as-prepared diazonium salt was added into the coupling solution having H-acid (0.663 g, 1.94 mmol) dissolved in 50 mL of water at pH 7 and further to facilitate the coupling reaction, the pH of the solution was maintained between 8 and 9 (color of H-acid changed from brown into dark violet colour). Further, the solution was stirred for 2 h and 25 mL of NaCl solution (3 wt%) was added to the

final solution[213;214]. The precipitate formed was filtered, washed with water and dried in a vacuum oven. The crude product was purified by refluxing in ethanol for 2 h, which was filtered and washed with hot ethanol and subsequently dried in oven (Yield 50%).

Molecular Formula: $C_{34}H_{22}N_6Na_4O_{14}S_4$ Molecular weight : 958.79

^{1}H-NMR (400 MHz, D_2O): δ = 7.48 -7.59 (br, 3H, CH), 7.09 – 7.29 (br, 8H, CH), 6.93 (br, 2H, C=CH)

4.3.6. Synthesis of sodium 3,3'-(1'Z)-(4,4'-((E)-ethene-1,2-diyl)bis(3-sulfonato-4,1-phenylene))bis(diazene-2,1-diyl)bis(5-amino-4-hydroxynaphthalene-2,7-disulfonate)

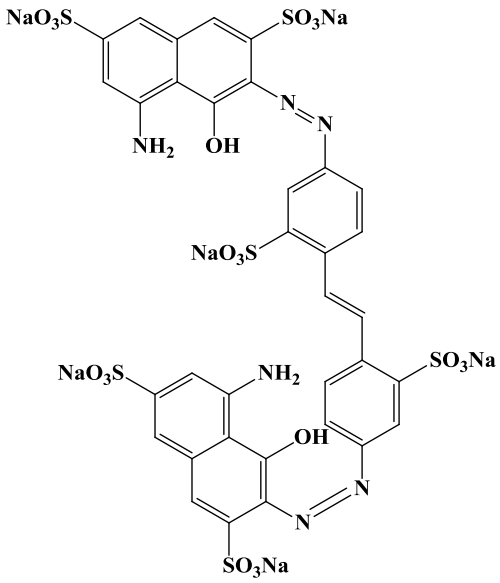

6

A mixture of 4,4'-diamino-2,2'-disulfonato stilbene dihydrochloride (0.25g, 0.67 mmol), 5 mL of water and 0.37 mL of 37% HCl was heated until the solution became clear. After cooling the above solution to 0 – 5 °C, aqueous solution of $NaNO_2$ (0.093g, 1.35 mmol) was added dropwise to the above acidified solution and the diazotization was continued for 2 h (colour of the solution changed from light brown to reddish brown). Then, H-acid (0.506g, 1.48 mmol) was dissolved in 50 mL of water at pH 7. Without further purification the diazonium salt liquor was added into the coupling solution and pH of the solution was maintained between 8 and 9 (color of H-acid changed from ivory (cream) into dark violet colour). The reaction mixture was stirred further for 2 h and 25 mL of NaCl solution (3 wt%) was added in order to quench the reaction. The resulting crude product was refluxed in

ethanol for 2 h, filtered and washed with hot ethanol and subsequently dried in oven (Yield 50%).

Molecular Formula: $C_{34}H_{20}N_6Na_6O_{20}S_6$ Molecular weight : 1162.88

^{1}H-NMR (400 MHz, D_2O): δ = 8.09 (br, 4H, CH), 7.94 (br, 2H, CH), 7.80 (br, 2H, CH), 7.60 (br, 2H, CH), 7.36 (br, 2H, CH), 7.17 (br, 2H, CH), 7.04 (br, 2H, HC=CH)

4.3.7. Synthesis of 2-(6-hydroxy-2-naphthamido)ethyl phosphonic acid

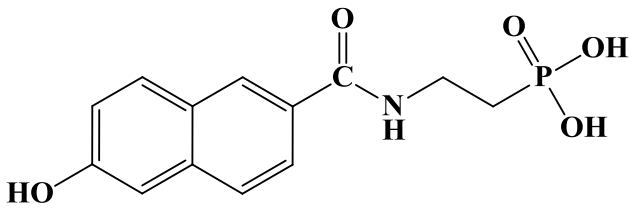

7

The carboxylic acid group of 6-hydroxy-2-naphthoic acid (0.20g, 1.06 mmol) was activated in dry DMF (15 mL) by adding 1-ethyl-3-(3-dimethylaminopropyl)carbodiimide (EDC) (0.24g, 1.27 mmol) at 0 ºC for 10 min. To further enhance the activation of carboxylic group and to increase the reaction yield, 1-hydroxybenzotriazole (HOBt) (0.17g, 1.27 mmol) and N,N-diisopropylethylamine (DIPEA) (0.58 mL, 3.40 mmol) were added[215]. 2-aminoethyl phosphonic acid (0.22 g, 1.59 mmol) was added to the above solution at 0 ºC. The reaction mixture was stirred at 0 ºC for 2 – 5 h. Further, the reaction was allowed to proceed overnight at RT. The completion of the reaction was checked and monitored using TLC (70% chloroform and 30% methanol). The reaction mixture was filtered and DMF was removed and dried. Final residue after drying was dissolved in minimum amount of water and extracted twice with diethyl ether. The final product is recrystallized from water (Yield 55%).

Molecular Formula: $C_{13}H_{14}NO_5P$ Molecular weight : 295.23

^{1}H-NMR (400 MHz, CD_3OD): δ = 7.83 – 7.88 (m, 2H, CH), 7.70 – 7.75 (m, 2H, CH), 7.42 – 7.57 (m, 2H, CH), 3.28 – 3.31 (m, 2H, NH-CH_2), 2.14 (br, 2H, P-CH_2)

4.3.8. Synthesis of 1-(6-hydroxy-2-naphthoyloxy)ethane-1,1-diyldiphosphonic acid by Mitsunobu reaction

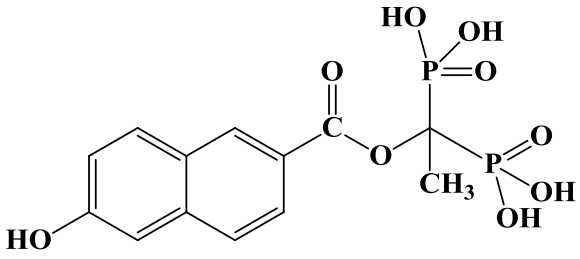

8

6-hydroxy-2-naphthoic acid (0.185 g, 0.98 mmol) and 1-hydroxyethane-1,1-diyldiphosponic acid (0.20 g, 0.89 mmol) was dissolved in anhydrous DMF (7.5 mL). To the DMF solution, triphenylphosphine (0.468 g, 1.78 mmol), diethyl azodicarboxylate (DEAD)(0.041 mL, 0.089 mmol) and iodosobenzene diacetate (0.575 g, 1.78 mmol) were added[216]. The reaction mixture was stirred at RT for 16 – 24 h and the completion of the reaction was checked using TLC. After completion of the reaction, the DMF was removed by rotatory evaporation and the final residue was diluted in minimum amount of water and solubility was facilitated by sonication followed by washing twice with diethyl ether for removal of organic impurities. The final product was recrystallized from water (Yield 45%)

Molecular Formula: $C_{13}H_{14}N_9O_2$ Molecular weight : 376.19

^{1}H-NMR (400 MHz, D_2O): δ = 8.80 – 8.84 (br, 1H, CH), 8.61 – 8.69 (br, 1H, CH), 8.10 – 8.14 (br, 2H, CH), 7.95 (br, 1H, CH), 7.76 – 7.80 (br, 1H, CH), 1.55 – 1.71 (m, 3H, CH_3)

4.3.9. Synthesis of potassium (S)-7-(2-amino-3-(1Hindol-3-yl)propanamido)-3-sulfonaphthalene-1-sulfonate

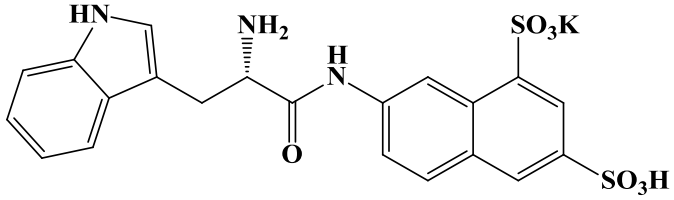

9

The carboxylic acid group of tryptophan (0.20g, 0.97 mmol) was activated in dry methanol (15mL) by adding 1-ethyl-3-(3-dimethylaminopropyl)carbodiimide (EDC) (0.23g,

1.17 mmol) at 0 ºC for 10 min. To further promote the activation of carboxylic group, 1-hydroxybenzotriazole (HOBt) (0.16g, 1.17 mmol) and N,N-diisopropylethylamine (DIPEA) (0.54 mL, 3.13 mmol) were added. ANDS (0.53 g, 1.47 mmol) was added to the above solution at 0 ºC. The reaction mixture was stirred at 0 ºC for 2 – 3 h and further allowed to proceed overnight at RT. The completion of the reaction was monitored using TLC (60% chloroform and 40% methanol). The methanol from reaction mixture was rotatory evaporatored. The residue obtained was washed with chloroform and hexane in order to remove the impurities. Further, the residue was dissolved in methanol and the solution was filtered and triturated with diethyl ether to extract the pure product. (Yield 45%)

Molecular Formula: $C_{21}H_{18}KN_3O_7S_2$ Molecular weight : 527.61

^{1}H-NMR (400 MHz, D_2O): δ = 8.30 – 8.48 (m, 1H, CH), 7.73 (m, 1H, CH), 7.67 -7.68 (m, 2H, CH), 7.08 – 7.16 (m, 2H, CH), 7.33 – 7.36 (m, 1H, CH), 7.00 (br, 1H, CH), 3.46, 3.17 (m, 2H, C-CH_2)

4.3.10. Synthesis of sodium 4-hydroxy-5-oleamido-7-sulfonaphthalene-2-sulfonate

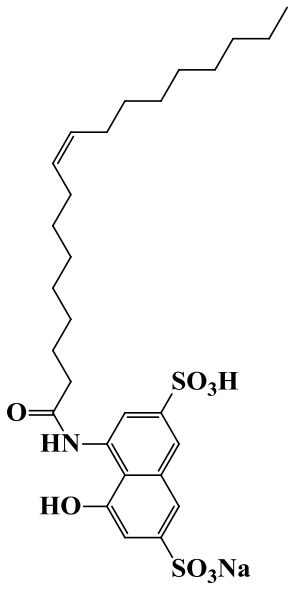

10

The carboxylic acid group of oleic acid (0.20g, 0.71 mmol) was activated in dry methanol (10 mL) by adding 1-ethyl-3-(3-dimethylaminopropyl)carbodiimide (EDC) (0.16g, 0.85 mmol) at 0 ºC for 10 min. The activation of carboxylic group was promoted and to increase the reaction yield, HOBt (0.11g, 0.85 mmol) and DIPEA (0.38 mL, 3.2 mmol) were

added. H-acid (0.36 g, 1.06 mmol) was added to the above solution at 0 ºC. The reaction mixture was stirred at 0 ºC for 5 h[217] and further reacted overnight at RT. The reaction mixture in methanol was neutralized with drops of acetic acid in methanol to pH 7. The methanol was rotatory evaporated and the residue obtained was washed with chloroform and hexane. Further, the residues were dissolved in methanol and filtered followed by trituration with diethyl ether to generate the pure product. (Yield 50%)

Molecular Formula : $C_{28}H_{40}NNaO_8S_2$ Molecular weight : 605.74

^{1}H-NMR (400 MHz, D_2O): δ = 7.07 – 7.36 (m, 4H, CH), 7.26 (br, 1H, OC-NH), 5.35 (m, 2H, HC=CH), 2.37 (m, 2H, OC-CH_2), 2.05 (m, 4H, H_2C-CH=CH-CH_2), 1.64 (m, 2H, OC-CH_2-CH_2), 1.27 (m, 20H, CH_2), 0.91(m, 3H,CH_3)

4.3.11. Synthesis of potassium 7-oleamido-3-sulfonaphthalene-1-sulfonate

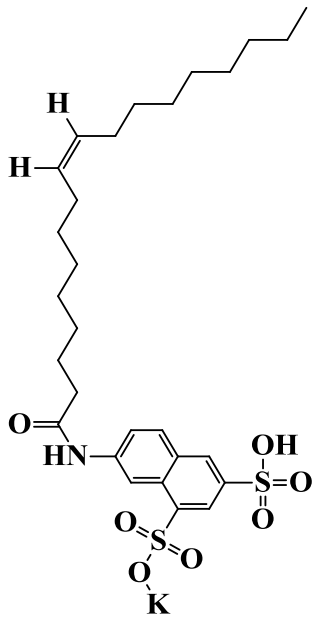

11

ANDS (0.25g, 0.69 mmol) and oleoyl chloride (2.06 mL, 6.23 mmol) were heated to 120 – 125 °C followed by addition of dry pyridine (20 mL) which was further heated under reflux for 4 h. Excess pyridine was removed by distillation and the solid mass thus obtained was dissolved in chloroform. Further, they were washed twice with methanol and filtered. The filtrate was triturated with diethyl ether and the separated solid was filtered to yield the product (Yield 40%)

Molecular Formula: $C_{28}H_{40}KNO_7S_2$ Molecular weight : 605.85

^{1}H-NMR (400 MHz, D_2O): 11.08 (s, 1H, exchangeable with D_2O), 9.13 (s, 1H, CH), 8.66 (s, 1H, CH), 8.18 (s, 1H, CH), 7.88 (br,1H, CH), 7.65(br, 1H, CH), 5.45 (m, 2H, HC=CH), 2.42 (m, 2H, OC-CH_2), 2.14 (m, 4H, H_2C-CH=CH-CH_2), 1.72 (m, 2H, OC-CH_2-CH_2), 1.40 (s, 18 H, CH_2), 1.00 (s, 3H, CH_3).

4.3.12. Synthesis of (S)-2-(2-amino-3-(1H-indol-3-yl)propanamido)ethyl phosphonic acid

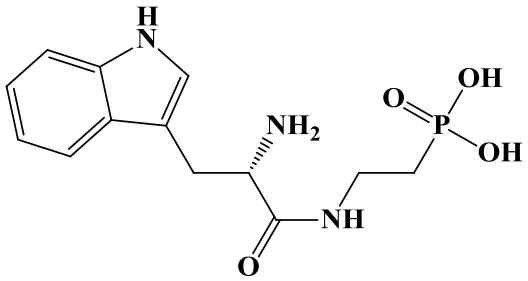

12

The carboxylic acid group of tryptophan (0.20g, 0.98 mmol) was activated in dry DMF (15 mL) by adding 1-ethyl-3-(3-dimethylaminopropyl) carbodiimide (EDC) (0.23g, 1.17 mmol) at 0 ºC. The activation was facilitated by HOBt (0.16g, 1.17 mmol) and DIPEA (0.53 mL, 3.13 mmol) addition. 2-aminoethyl phosphonic acid (0.21 g, 1.46 mmol) was added to the above solution and the reaction mixture was stirred at 0 ºC for 2 – 5 h. Then, the reaction was allowed to react at RT for 24 h. The completion of the reaction was often checked using TLC (85% chloroform and 15% methanol). Excess DMF from the reaction mixture was removed under high vacuum. Then it was washed with chloroform, filtered and filterate was evaporated. The residue after drying was dissolved in methanol and extracted twice with diethyl ether. The final product could not be recovered from the above solvents. Methanolic solution of the final product was heated and allowed to crystallize at 4°C. Unfortunately, the product didn't crystallize out of the methanolic solution.

Molecular Formula: $C_{13}H_{18}N_3O_4P$ Molecular weight : 311.27

4.4. Iron oxide nanoparticles synthesis (USPIO)

The iron oxide nanoparticles were prepared either in aqueous or in organic phase. In aqueous solution, they were prepared by co-precipitation of ferric and ferrous salts by using a base. In organic phase, nanoparticles were prepared under thermal decomposition of iron precursors and the solvent used itself acts as a capping agent that stabilizes the generated iron oxide nanoparticles.

4.4.1. Synthesis of iron oxide nanoparticles (10-12 nm)

Ultrasmall superparamagnetic iron oxide nanoparticles (USPIO), were prepared as described below[172]. An aqueous solution of sodium hydroxide (250 mL, 0.5 M) was maintained at 80 ºC in a three necked reaction flask with mechanical stirring and further it was degassed using inert nitrogen as the cover gas. Aqueous solutions of $FeCl_3$ (25mL, 1 M in 0.2M HCl) and $FeCl_2$ (25 mL, 0.5M in 0.2M HCl) were added to a mechanically stirred solution of NaOH within 5 min under an inert nitrogen atmosphere at 80 °C. On addition a black precipitate of magnetite is formed immediately. The nanoparticle formation was allowed to proceed for 20 min at 80 °C. After the reaction time, subsequently the nanoparticles formed were cooled to ambient temperature. The nanoparticles were separated from the parent solution by using an external magnetic field, and washed three times with de-ionized water, and dispersed into 100 mL of aqueous hydrochloric acid (0.01 M). The size of the magnetic cores was tuned by varying the concentration of the basic solution used for the nanoparticle synthesis (1.0, 1.5 M NaOH).

4.4.2. Synthesis of iron oxide nanoparticles (10 nm)

Ultrasmall SuperParamagnetic Iron Oxides (USPIO) nanoparticles were synthesized by co-precipitation of ferrous (Fe^{2+}) and ferric (Fe^{3+}) salts in aqueous alkaline conditions by a modified one-part synthesis protocol[178]. We used stoichiometric ratio of $2Fe^{3+}$:Fe^{2+}, 16 mmol (2.66 g) of $FeCl_3$ and 8 mmol (1.63 g) of $FeCl_2.4H_2O$ which was dissolved in 190 mL de-ionized water at RT by magnetic stirring for 10 min. Under vigorous stirring, 10 mL of 25% NH_3 were poured down the vortex of the iron solution. Immediately, magnetite was formed as a black precipitate. After stirring for 10 min, the nanoparticles were washed thrice with water and finally magnetic fluids were dispersed in 100 mL of aqueous hydrochloric acid (0.1 M) and stored at pH 2 for further investigations.

4.4.3. Synthesis of iron oxide nanoparticles (5-6 nm)

USPIO were synthesized by co-precipitation of ferrous (Fe^{2+}) and ferric (Fe^{3+}) salts in aqueous alkaline conditions by a modified one-part synthesis protocol[178]. Stoichiometric ratio of $2Fe^{3+}$:Fe^{2+}, 16 mmol (2.66 g) of $FeCl_3$ and 8 mmol (1.63 g) of $FeCl_2.4H_2O$ was

dissolved in 190 mL de-ionized water at RT by magnetic stirring for 10 min. Under vigorous stirring, 10 mL of 25% NH_3 was poured down the vortex of the iron solution. The magnetite was formed as a black precipitate. After stirring for 20 min, the nanoparticles were washed thrice with water and cationic ferrofluid was prepared by washing two times with 0.1 M HCl solution under the influence of external magnetic field using a rare-earth magnet. Magnetic fluids were dispersed in 100 mL of aqueous hydrochloric acid (0.1 M). The USPIO were further sonicated for 20 min with ultrasonic cleaner (Ultrasonic cleaner, 30 W, VWR GmbH, Germany) at ambient temperature. Consequently, the sonicated nanoparticles were filtered through 0.22 µm filter units in order to get rid of the agglomerates. Additionally, USPIO were centrifuged at 20,000g for 20 min at ambient temperature in order to remove big aggregates. The final ferrofluid was collected and stored at 4 ºC at pH 2 for further use. The colloidal dispersion is stable for 2-3 months at ambient temperature.

4.4.4. Synthesis of 2-pyrrolidione stabilized iron oxide nanoparticles (5 nm)

Iron oxide nanoparticles with small core diameter (5 nm) were synthesized by the thermal decomposition of iron acetylacetonate in the presence of 2-pyrrolidione at high temperatures (250-270ºC)[181;182]. A typical synthesis yielding iron oxide nanoparticles with 5-nm particle diameter is described below. 20-mL of 2-pyrrolidione solution containing 2.0 mmol $Fe(acac)_3$ was first purged with nitrogen to remove the oxygen and then heated. After being refluxed at high temperature (250 -300 °C) for 10 min, the reaction system was cooled to RT. The iron oxide nanoparticles were precipitated from the black solution by addition of methanol into the 2-pyrrolidione solution which resulted in a dark-brown precipitate. The precipitate was washed with acetone for several times in order to remove the excess 2-pyrrolidione and then dried in air. The final black powder was found to be soluble in water and 2-pyrrolidione. The weak interaction between 2-pyrrolidione and USPIO could be exploited and further functionalized with different coating molecules (Figure 4.1.1). The nanoparticles obtained indicated an average diameter of 5±1.2 nm as reported in the literature.

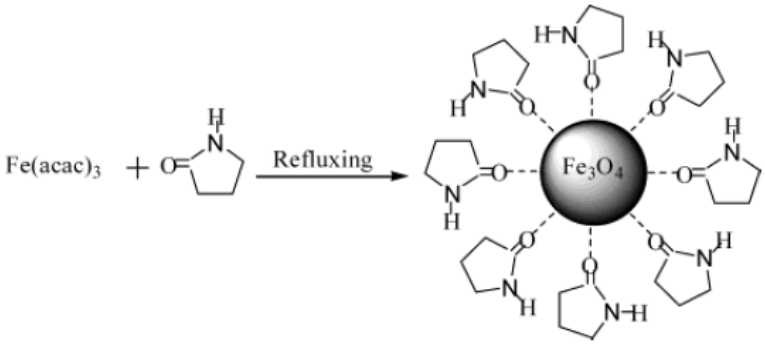

Figure 4.1.1. The schematic figure shows the iron oxide nanoparticles (5 nm) stabilized with the capping ligand (2-pyrrolidione) synthesized via thermal decomposition technique respectively.

4.4.5. Synthesis of oleic acid stabilized iron oxide nanoparticles (7 nm)

Oleic acid stabilized iron oxide nanoparticles (7 nm) were synthesized by a modified thermal decomposition protocol. In a typical synthesis, $Fe(acac)_3$(2 mmol), 1,2-hexadecanediol (10 mmol), benzyl ether (20 mL, 105 mmol), oleic acid (6 mmol) and oleyl amine (6 mmol) were mixed together and stirred magnetically under nitrogen flow. The temperature of the mixture was raised to 200 ºC. Initially, the color of the reaction mixture was blood red and with increase in temperature the color changed to yellow. The mixture was heated at 200 ºC for 30 min under a blanket of nitrogen. Further, the mixture was refluxed at 200-250 ºC for 7-8 h which resulted in the brownish black solution which was cooled to RT. The iron oxide nanoparticles were retrieved from the above solution by addition of 75 mL of ethanol, followed by centrifugation at 900 rpm for 15 min. The resulting blackish brown precipitate was dried and used for further characterization[218]. Iron oxide nanoparticles with increased size can be synthesized by using the above nanoparticles with 7 nm diameter as seeds to grow in the iron precursor solution ($Fe(acac)_3$).

4.4.6. Synthesis of oleic acid stabilized iron oxide nanoparticles (8 nm)

USPIO cores were synthesized and stabilized with oleic acid by a modified synthesis protocol. In a typical synthesis, to a solution of $(NH_4)_2Fe(SO_4)_2.6H_2O$ (2.04g, 5 mmol) in 50 mL of de-ionized water were added KOH (1.14g, 20 mmol) in 20 mL water followed by dropwise addition of $(NH_4)_2S_2O_8$ (0.38 g,1.6 mmol) in 10 mL water. Subsequently, 1.5 mL (4.7 mmol) of oleic acid in 30 mL toluene was added and the mixture was heated (95 ºC) at reflux for 30 min. After cooling the reaction mixture to RT, the organic layer was extracted by using toluene for three to four times. The aqueous layer was collected and discarded. The organic layer was dried over anhydrous sodium sulphate to remove trace amounts of water. Then the solution was poured slowly into acetone and further centrifuged at 900 rpm for 10 min. The precipitated iron oxide nanoparticles were collected and washed three times with acetone, air dried and used for further characterization[219]. The ligand exchange reactions could be performed in order to bring the oleic acid stabilized iron oxide nanoparticles into

water. This could be achieved by exchanging them with either betaine- or carboxyethylsilane triol in ethanol and stirring for 24 h at RT followed by centrifugation and washing with ethanol and dried. The resulting solid is easily dispersible in water affording clear hydrosols of high concentration.

4.4.7. Commercial iron oxide nanoparticles (EMG 911)

Iron oxide nanoparticles were extracted from a commercial available ferrofluid as reported. In a typical process, 20 mL of acetone was added to 1 mL of ferrofluid EMG 911 (Ferrotec, Nashua, NH) and shaken vigorously to extract iron oxide nanoparticles from the dispersion medium (light mineral oil). The nanoparticles were then collected with the aid of a permanent magnet. This extraction procedure was repeated 5 times. These extracted iron oxide nanoparticles were dried in oven at 60 ºC for 1 h and finally re-dispersed in 20 mL of toluene by sonication for 1 h[220]. These magnetic nanoparticles can be coated with silane molecules in the organic phase. The magnetic characteristics and stability of these nanoparticles (control nanoparticles) were compared with iron oxide nanoparticles generated in our laboratory.

4.4.8. Synthesis of lanthanide-doped iron oxide nanoparticles (10-12 nm)

Lanthanide doped USPIO were prepared using the Massart method with a small modification[210]. An aqueous solution of sodium hydroxide (250 mL, 0.5 M) was maintained at 80 ºC in a three necked reaction flask with mechanical stirring and further it was degassed using inert nitrogen as the cover gas. Iron (III) chloride was partly replaced by lanthanide (III) chloride (Eu, Gd, Tb) in different molar percentages (2%, 5%, 15%, 20%). Aqueous solutions of $FeCl_3$ and $LnCl_3$(Eu,Gd, Tb) (25mL, 1 M in 0.2M HCl) and $FeCl_2$ (25 mL, 0.5M in 0.2M HCl) was added to a mechanically stirred solution of NaOH within 5 min under an inert nitrogen atmosphere at 80 °C. On addition a black precipitate of magnetite is formed immediately. The nanoparticle growth (nanoparticle formation) proceeds for 20 min at 80 °C. After the reaction time, subsequently the nanoparticle formed was cooled to ambient temperature. The nanoparticle was separated from the parent solution by using an external magnetic field, and further washed three times with de-ionized water, and dispersed into 100 mL of aqueous hydrochloric acid (0.01 M).

4.4.9. Synthesis of iron nanoparticles with TMAOH

USPIO were also synthesized by co-precipitation using tetramethyl ammonium hydroxide (TMAOH) as the base for precipitation of iron salts. For magnetite synthesis, 1 M ferric chloride ($FeCl_3$ >99%) and 2 M ferrous chloride tetrahydrate ($FeCl_2.4H_2O$ >99%) were prepared by dissolving iron salts in 2 M HCl solutions, respectively[221]. In a typical

experimental procedure, 10 mL of 1 M $FeCl_3$ solution was mixed with 2.5 mL of 2 M $FeCl_2$ solution in a flask. This solution was stirred, followed by the slow addition of 21 mL of 25% (w/w) $N(CH_3)_4OH$, until a pH 13 was reached. Vigorous stirring was continued for 20 min. The solution color could be seen to alter from orange to black, leading to a black precipitate. The precipitated nanoparticles were isolated via using a permanent magnet. The supernatant was discarded by decantation. The precipitate was washed three times in order to remove excess ions and tetramethyl ammonium salt in the suspension. Finally, the washed precipitates were dispersed in de-ionized water for further investigation.

4.5. Estimation of total iron concentration in nanoparticles

The total iron concentration of the magnetic fluids was determined by using either one of the following methods/techniques such as titration, colorimetry and ICP-MS respectively.

4.5.1. Titration of iron oxide nanoparticles

Total iron content of the nanoparticles was estimated by performing the titration for iron against an EDTA standard solution. The EDTA solution was first standardized using standard zinc solution prior to its use in iron estimation.

4.5.1.1. Standardization of the EDTA solution

A standard zinc solution (0.01 M) was prepared as a stock solution. A 10 mL aliquot from the stock of 0.01 M standard zinc solution was transferred into a 250 mL Erlenmeyer flask and the pH of the solution was adjusted by addition of 20 mL of the bicarbonate-carbonate buffer solution (pH 10.0 ± 0.1) which was prepared by using Na_2CO_3 (30g/L and pH adjusted using 6 M HCl). To this solution three drops of Eriochrome Black T indicator (0.25 g in 50 mL of absolute ethanol) were added and mixed well. The color of the solution changed into pink color. The solution was titrated with 0.01 M EDTA solution until the color changed to pure blue at the end point. The titration was repeated to get concordant titre values. The exact concentration of the EDTA solution was calculated from the standardization (titration) with standard zinc solution.

4.5.1.2. Estimation of the iron(III) content with standardized EDTA

The determination of the total iron content of USPIO suspensions by titration is based on complexation of Fe^{3+} with sulfosalicylic acid. Briefly, 0.5 mL of the USPIO solution was added into Erlenmeyer flasks (250 mL) followed by addition of 10 mL of 0.5 N HCl to dissolve the iron oxide nanoparticles. The solution was heated (100 °C) until it turned yellow. To the boiling solution small amounts of $(NH_4)_2S_2O_8$ were added in order to completely oxidize the remaining Fe(II) to Fe(III). Then, the solution was diluted with 40 mL of de-

ionized water to get a colorless or pale yellow colored solution. The solution pH was adjusted to ~ 2.5 using 1M Na($OOCCH_3$) and pH change was monitored with the pH meter. Then, 0.1 mL of sulfosalicylic acid indicator was added and the color of the solution changed from yellow to pink due to complexation with Fe^{3+}. Further, the solution was heated to 40-50 °C and titrated immediately against the standard 0.01M EDTA solution. The end point was the appearance of the yellow color[222]. The titration was repeated to get concordant titre values. The iron concentration of NUSPIO, FLUSPIO, FAD USPIO (0.5 mL) was determined by using the above described protocol.

4.5.2. Colorimetric estimation of the iron concentration

The determination of USPIO total iron content with Tiron is based on the complexation of Fe^{3+} with Tiron[223;224]. The Fe^{2+} in the USPIO suspension was oxidized to Fe^{3+} by adding 300 µL of a mixture containing 37% HCl/65 % HNO_3 in a volume ratio (3:1). The required volume of deionized water was added to the sample in order to obtain the respective dilution factor (solution A) as shown in Table 4.1.1 and Table 4.1.2. Then, the procedure for the colorimetric iron determination was performed. To 500 µL of solution A, 100 µL of iron complexing reagent i.e. aqueous solution of 0.25 M Tiron (4,5-Dihydroxy-1,3-benzenedisulfonic acid) was added. Further, 500 µL of 4 M KOH solution, and 1000 µL of phosphate buffer pH 9.5 (prepared by using 0.2 mole (71.6g) $Na_2HPO_4.12H_2O$ and 4 mL of 1 M KOH in 600 mL de-ionized water and made up to 1L) were added to the solution containing Tiron. Further, the absorption of the solution was measured at λ = 480 nm. Each sample was analysed in threefolds. To obtain a linear calibration curve, the same procedure was followed with aqueous Fe^{3+} solutions with known iron concentrations (10 - 100 µg/mL).

Table 4.1.1. Preparation of standard iron solutions for calibration (iron standard stock solution: 1 mg Fe/mL)

Nr.	µg Fe/mL	Iron standard solution (µL)	37% HCl (mL)	65% HNO_3 (mL)	De-ionized water(mL)
0	0	0	0.3	0.1	2.1
1	10	25	0.3	0.1	2.075
2	20	50	0.3	0.1	2.05
3	30	75	0.3	0.1	2.025
4	50	125	0.3	0.1	1.975
5	70	175	0.3	0.1	1.875
6	100	250	0.3	0.1	1.85
7	150	375	0.3	0.1	1.725

Table 4.1.2. Dilution series for the probe

Dilution factor	probe (mL)	37% HCl (mL)	65% HNO_3 (mL)	De-ionized water (mL)
2	1.0	0.24	0.08	0.68
5	0.4	0.24	0.08	1.28
10	0.2	0.24	0.08	1.48
15	0.133	0.24	0.08	1.547
20	0.1	0.24	0.08	1.58
25	0.08	0.24	0.08	1.60
30	0.0667	0.24	0.08	1.613
40	0.05	0.24	0.08	1.63
50	0.04	0.24	0.08	1.64
75	0.0267	0.24	0.08	1.6533
100	0.025	0.3	0.1	2.075

4.5.3. Total iron concentration determination by ICP-MS

The amount of iron present in the nanoparticles was determined by high-resolution sector field ICP-MS (Element 2, Thermo Electron, Bremen, Germany) equipped with an autosampler (ASX-100, CETAC, Omaha, NE). Data were acquired at medium resolution

(4000) using rhodium (5 ppb) as an internal standard. A PFA spray chamber equipped with a PFA 100 microflow nebulizer (CETAC) was used for sample introduction. The instrument was tuned and calibrated via infusion of a 1 ng/mL multi element standard solution (Merck, Darmstadt, Germany). Digestion of the USPIO, APTMS-USPIO, FLUSPIO was performed in a closed vessel microwave reaction system (CEM, Kamp-Linfort, Germany) after addition of 53% nitric acid (60%) at 3 bar and 600W for 50 min. Samples were diluted 1:200 in H_2O. Calibration was linear between 2 and 150 ng/mL iron (r>0.999). The iron content was expressed in nanograms of iron per mL.

4.6. Different coating strategies for iron oxide nanoparticles.

Iron oxide nanoparticles generated in this thesis, were synthesized by the co-precipitation method. The stability of the iron oxide nanoparticles decreased if there was no surface coverage (coating) which resulted in agglomeration. The ferrofluid is stable by changing their negative surface charge to positive by protonating their surface with addition of an acid. To further increase the stability, the surface was covered with either polymer or bio-compatible organic molecules (non-polymer) in order to make them stable at physiological pH and suitable for *in vitro* and *in vivo* bio-medical applications.

4.6.1. Silane coating of iron oxide nanoparticles (10 nm)

Iron oxide nanoparticles (10 nm) prepared by modified co-precipitation method were coated with a protective thin layer of silane by using 3-aminopropyltrimethoxy silane (APTMS)[210] as the coating molecule. In brief, USPIO cores (100 mL, 10 mg/mL) stored under acidic conditions were washed three times with methanol by retrieving the nanoparticles with the aid of a permanent magnet. The nanoparticles were isolated from the methanol washings by centrifugation at 20,000 g for 10 min respectively. The ferrofluid was suspended in 30 mL of dry methanol under inert nitrogen atmosphere. The methanolic solution of the nanoparticles was added to 70 mL of dry toluene placed in 250 mL reaction flask, which was equipped with a condenser, and maintained under inert nitrogen atmosphere. At 110 °C, an aliquot of APTMS (0.1 mL, 0.573 mmol) was added quickly to the ferrofluid in the reaction mixture followed by a 10 h reflux at 110 °C under nitrogen purging respectively. After reflux, the reaction mixture was cooled to RT. Further, the reaction mixture was suspended in methanol (50 mL) and sonicated for 10 min in order to disperse the agglomerated nanoparticles that originated due to the frequent exchange of solvents. The nanoparticles were recovered from methanol by using a permanent magnet, followed by washing with water. Furthermore, the silane coated nanoparticles were washed two times simultaneously with methanol (50 mL) to remove toluene and two times with water (50 mL)

to remove methanol. The nanoparticles lost during different washing steps were recovered by centrifuging them at 20,000 g for 10 min. Finally, the silane coated nanoparticles were suspended in 100 mL of water and stored at 4°C for further use. A similar coating protocol was followed for coating the iron oxide nanoparticles with 5 nm as the average core diameter respectively.

4.6.2. Mixed silane coating of iron oxide nanoparticles (10 nm)

10 nm USPIO and Ln-USPIO (Ln = Eu,Gd,Tb) were prepared by co-precipitation using aqueous alkaline solution (0.5 M NaOH). The nanoparticles were coated simultaneously with two different silanes namely APTMS and TEOS. In a typical coating procedure, USPIO (100 mL, 10 mg/mL) at pH 2 were washed three times with methanol by retrieving the nanoparticles with a permanent magnet. The nanoparticles were recovered from the methanol washings by centrifugation at 20,000 g for 10 min. The ferrofluid was suspended in 30 mL of dry methanol and added to dry toluene (70 mL) in a three necked round bottom flask (250 mL), which was equipped with a condenser and maintained under inert atmosphere. At 110 °C, APTMS (0.05 mL, 0.286 mmol) and TEOS (0.043 mL, 0.192 mmol) were added to the reaction mixture either simultaneously or after 5 h of reaction completion by sequential addition of APTMS followed by TEOS and vice versa respectively. The reaction mixture was refluxed with stirring for 10 h at 110 °C under nitrogen purging. After reflux, the reaction mixture was cooled to RT. Then, the nanoparticles were transferred into the methanol (50 mL) and sonicated for 10 min. Further; the mixed silane coated nanoparticels were washed for three times simultaneously with methanol (50 mL) and water (50 mL). The nanoparticles from different washing steps were recovered by centrifugation at 20,000 g for 10 min. Finally, the mixed silane coated nanoparticles were suspended in 100 mL water and stored at 4°C for further use.

In addition, the nanoparticles (USPIO and Ln-USPIO (Ln = Gd, Eu, Tb)) prepared by a modified co-precipitation method were coated with a thin layer of protective silane by using TEOS (0.1 mL, 0.478 mmol) [225]. Further, the procedure followed for silane coating was similar to the one described above. The TEOS coated nanoparticles were suspended in 100 mL water and stored at 4°C for further investigations.

4.6.3. Synthesis of NUSPIO

The USPIO were coated with the following non-polymeric molecules to yield fluorescent naphthalene coated USPIO (NUSPIO): 7-amino-1,3-naphthalene disulfonic acid monopotassium salt (ANDS), 4-amino-5-hydroxy-2,7-naphthalene disulfonic acid

monosodium salt (H-acid), Naphthol blue black (Naph 3), 1-hydroxy-3,6-naphthalene disulfonic acid monosodium salt (Naph 4), 3-hydroxy-2,7-naphthalene disulfonic acid monosodium salt (Naph 5), Sodium 5-acetamido-4-hydroxy-3-(phenyldiazenyl) naphthalene-2,7-disulfonate (Naph 6), 2,2´-(naphthalene-1-ylmethylazanediyl)bis(ethane-2,1-diyl) diphosphonic acid (Naph 7). The coating strategy was followed by slight modification of the reported procedure. In brief, different concentrations of the above non-polymeric molecules (30, 40, 50, 60, 70 and 80 mmol/L) were added to the suspension of iron oxide nanoparticles (Fe = 10 g/L). After 1 h incubation at 20 °C, the nanoparticles were dialyzed against water for 2 days and neutralized by dialysing for 3 days against buffers or NaCl solution (0.15 mol/L) at different temperatures (4 °C and RT). The purification methods (dialysis and resin exchange), performed after non-polymeric coating, will be discussed in detail under the section (4.7.1 and 4.7.2). The incubation time and dialysis temperature were varied in order to study their influence/effect on the stability of the non-polymeric coated iron oxide nanoparticles[226].

4.6.3.1. Synthesis of USPIO coated with different naphthalene sulfonates

The USPIO were coated with the following non-polymeric molecules (synthesized): sodium 4-hydroxy-5-oleamido-7-sulfonaphthalene-2-sulfonate, potassium 7-oleamido-3-sulfonaphthalene-1-sulfonate, potassium (s)-7-(2-amino-3-(1H-indol-3-yl)propanamido)-3-sulfonaphthalene-1-sulfonate, 1-(6-hydroxy-2-naphthoyloxy)ethane-1,1-diyldiphosphonic acid, sodium 3,3-(1´Z)-(4,4´-((E)-ethene-1,2-diyl)bis(4,1-phenylene))bis(diazene-2,1-diyl)bis(5-amino-4-hydroxynaphthalene-2,7-disulfonate), sodium 3,3´-(1´Z)-(4,4´-((E)-ethene-1,2-diyl)bis(3-sulfonato-4,1-phenylene))bis(diazene-2,1-diyl)bis(5-amino-4-hydroxynaphthalene-2,7-disulfonate) which were anticipated to display fluorescence that might aid MR cellular labeling studies and further facilitate the co-validation of the results obtained via MRI.

To this end, the non-polymeric coating of USPIO (2g/L) was achieved using different concentration of the above naphthalene sulfonates (30, 40, 50 mmol/L) respectively. After 1 h incubation at 20 °C, the nanoparticles were washed several times with water via the aid of a permanent magnet. The fluorescence efficiency of final nanoparticles synthesized was evaluated using fluorescence spectroscopy and microscopy techniques.

4.6.3.2. Synthesis of USPIO coated with sulfonates and phosphates

The stability and fluorescence efficiency of the USPIO coated with different sulphonates was compared to the nanoparticles coated with phosphonic acids in the physiological solutions merely by visual inspection and validated through fluorescence spectroscopy and microscopy respectively. The different sulphonates and phosphates which were employed as non-polymeric coating molecules are 2-(6-hydroxy-2-napthamido)ethylphosphonic acid, 4-(4-((R)-hydroxy((2S,4S,8R)-8-vinylquinuclidin-2-yl)methyl-6-methoxyquinolinium-1-yl)butane-1-sulfonate, 4-(9-aminoacridinium-10-yl)butane-1-sulfonate, thiamine monophosphonic acid (TMP), sodium 8-hydroxy-3,6-dihydropyrene-1,3,6-trisulfonate respectively. The coating strategy followed was a modification from the reported procedure[226]. The concentrations of USPIO and non-polymeric molecules (sulfonates and phosphates) used were similar to the previously described procedure (section 4.6.3.1). After incubation (1 h), excess non-polymeric ligands were removed by washing several times with water (permanent magnet) respectively.

4.6.4. Synthesis of FLUSPIO

The fluorescent ultrasmall superParamagnetic iron oxides (FLUSPIO) nanoparticles were synthesized by sonication of fluorescent, non-polymeric flavin mononucleotide (FMN) and non-polymeric guanosine monophosphate (GMP) with USPIO in different concentrations. In brief, 5-6 nm iron oxide nanoparticles (8 mg/mL, 143 mmol) suspensions at pH 2 were sonicated with FMN (35 and 50 mmol) using an ultrasonic cleaner (30 W, VWR GmbH, Germany) for 1 h at ambient temperature. On FMN addition to USPIO the pH of the solution reached 4.0. After sonication, the FMN modified nanoparticles were purified by washing several times with water aided via the high gradient magnetophoresis. Further, FMN modified USPIO were treated with GMP (43, 50 and 64 mmol) and sonicated for 1 h at ambient temperature. Excess GMP was removed by washing the nanoparticles several times with water (high gradient magnetophoresis). The FLUSPIO were stored at low temperature for further use. FLUSPIO were also generated by performing the FMN coating in combination with adenosine monophosphate (AMP) or with thiamine monophosphate (TMP).

In addition, double FMN coating of USPIO was achieved by following similar protocol as described above. For this type of coating, iron oxide nanoparticles were coated twice with the FMN (35 mmol) and excess FMN was removed by washing them with water (high gradient magnetophoresis). The double FMN coated USPIO were stable and stored at 4 ^{o}C for further investigations.

4.6.5. Synthesis of FAD USPIO

The flavin adenine dinucleotide USPIO (FAD USPIO) were synthesized by sonication (1 h) of USPIO with FAD and GMP and further synthesis steps were followed analogues to the FLUSPIO synthesis (section 4.6.4). After sonication, purification of the FAD modified nanoparticles was achieved via high gradient magnetophoresis. After GMP coating, excess non-polymeric ligands was removed by washing with water to yield the fluorescent FAD USPIO nanoparticles.

In addition, USPIO coated two times with FAD was prepared by incorporating the above protocol. FAD (35 mmol) was coated twice over USPIO and further purified by employing high gradient magnetophoresis. Similarly, USPIO were also coated two times with riboflavin (35 mmol) for generating double coated riboflavin-USPIO respectively.

4.6.5.1. In situ coating of USPIO with non-polymeric molecules

Iron oxide nanoparticles synthesized by thermal decomposition of iron precursors at high temperatures were coated *in situ* using H-acid by employing a slight modification in the reported procedure[181]. 10 mL of 2-pyrrolidinone solution containing $Fe(acac)_3$ (0.35 g, 1 mmol) and H-acid (0.34 g, 1 mmol) were sonicated for 12 min. Then, the reaction mixture was purged with nitrogen to remove the dissolved oxygen and heated to reflux under nitrogen for 10 min at 250 ºC. The reaction system was cooled to RT. Further, methanol was added into 2-pyrrolidinone which resulted in dark brown precipitate which was washed several times with acetone and then dried. The modified nanoparticles were dialyzed against water at 4 ºC for two days in order to remove excess H-acid from the sample. The fluorescence of the nanoparticles was checked with fluorescence spectroscopy and microscopy techniques.

4.7. Different purification techniques used for magnetofluorescent nanoparticles

The purification of the non-polymeric coated iron oxide nanoparticles was achieved by employing three different techniques/methods such as dialysis, resin exchange and high gradient magnetophoresis respectively.

4.7.1. Dialysis

Excess non-polymeric molecules on iron oxide nanoparticles was removed by dialysis using the cellulose ester (CE) membrane spectra/por FloatALyzer G2 (MWCO 10, 100 kD)(SPECTRUM). The dimension of the CE membrane used are: length (10 cm), membrane

diameter (10 mm), top piece diameter (23 mm), flotation ring (38 mm), volume (5 mL) respectively. The features of the FloatALyzer G2 are screw-on cap (color coded for MWCO, polypropylene), silicon O-ring (leak proof and resealable), floatation ring (center to maintain buoyancy, polyethylene), top/bottom piece (polycarbonate), potting (polyurethane) respectively (Figure 4.1.2). The glycerol which was used to dry the CE membrane was removed from the membrane by washing it with water prior to the sample dialysis. The non-polymeric modified nanoparticles were loaded in the dialysis membrane and dialysed against water at 4 ºC for two days in order to remove excess non-polymeric molecules. The dialysed water was removed every 4 h and exchanged with fresh water to continue the sample dialysis. Further, the samples were dialysed against various buffers and solutions for neutralization (0.15 mol/L (NaCl, glucose, citric acid), PBS (1X), HEPES (25 mM), MOPS (20 mM), MES (20 mM), oxalate (20 mM), and tris buffer) at 4 ºC for 1-2 days.

Figure 4.1.2. The figure shows different parts of the cellulose ester membrane dialyser and displays different steps involved from the sample addition to the color coded membrane dialyser, dialysis technique and sample recovery after dialysis respectively.

Dialysis of the non-polymeric modified USPIO was also performed using visking membranes with different molecular weights. The glycerine from visking membrane was cleaned by washing either with warm water or by heating the membrane in 2% sodium bicarbonate and 1mM EDTA at 80 ºC for 30 min and rinsing it with distilled water. After cleaning, the membranes should be stored, fully immersed in one of the following solutions; 1% formaldehyde, 1% sodium benzoate or 0.1% sodium azide at 4 ºC. The dialysis technique followed for purification of non-polymeric modified nanoparticles with visking membrane was similar to the protocol described above.

4.7.2. Resin exchange method

Non-polymeric coated USPIO can be purified by employing a resin exchange method, in which the acidic and basic resin was used for better separation and purification of the sample. Dowex fine mesh resins are based on a microporous copolymer of styrene and divinylbenzene (DVB) that results in maximum resistance to oxidation, reduction, mechanical wear and breakage (Figure 4.1.3). This co-polymeric structure of dowex is insoluble in common solvents, thus facilitating the ionic exchange. The DOWEX 50 WX8 20/50 is a strong acid cation resin containing 8% DVB and X being the number describing the degree of resin cross linkage. The Dowex resin is activated by stirring them in water overnight and further washed with 1 M HCl and excess acid cations was removed by washing simultaneously with water until the resin pH reached 2.

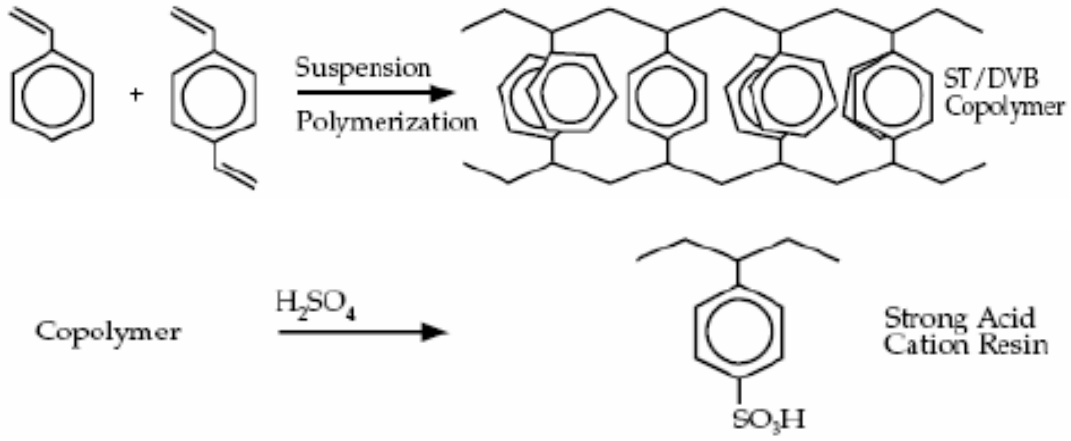

Figure 4.1.3. The schematic diagram shows the steps involved in synthesis of strong acidic cationic resin (DOWEX 50WX8) respectively.

Amberlite IRA 95 is a weakly basic anion exchanger with exceptional resistance to organic fouling. This resin is used for de-acidification, de-ionization of water where removal of strong mineral and organic acids is desired and for removal of heavy metals. The resin matrix consist of styrene divinylbenzene (macroreticular matrix) with active polyamine functional groups and particle size (16-50 mesh) which has working pH range (0 – 7). The amberlite resin is activated by stirring it in water overnight and further washing with 1 M NaOH. Excess base anions were removed by washing with water until the resin pH reached 8.0.

The non-polymeric modified nanoparticles were first acidified over 1 mL of an H^+ exchange resin (DOWEX 50WX8-20/50 Mesh) per mL of iron nanoparticle suspension. After 10 min of incubation at pH 4, the suspension was passed over 2 mL of a weakly basic OH^- resin (Amberlite IRA 95) for pH neutralization. After resin exchange, the nanoparticles were stored at low temperature.

4.7.3. High gradient magnetophoresis

High gradient magnetophoresis was performed using a MiniMacs separator (Miltenyi Biotech, Bergisch Gladbach, Germany) (Figure 4.1.4). To increase the separator efficiency, regions of high magnetic field gradient were produced to capture the magnetic nanoparticles as they flow by in their aqueous medium[227]. This efficiency can be achieved by loosely packing a flow column with a magnetizable matrix of wire (e.g., steel wool) and facilitating the magnetic fluid flow through the column under the influence of applied magnetic field. The steel wool is packed inside a 100 µL pipette tip and placed in a 3 mm gap between the two pole faces of a permanent magnet thus generating high gradient magnetic field which aids magnetic separation of the nanoparticles. Non-polymeric modified nanoparticles were passed through the steel wool and after separation each retentate was thoroughly washed with water to remove any non-adsorbed non-polymeric molecules (sulfonates, phosphate groups) remaining in the steel wool. Further, the pipette tip (holding the steel wool) was removed from the pole of the permanent magnet and the magnetic nanoparticle retentates were recovered and re-suspended from the filter matrix by washing with water.

Figure 4.1.4 The figure shows the set up which was used for high gradient magnetophoresis separation of coated magnetic nanoparticles. A high gradient magnetic field was generated by using steel wool in a pipette tip and by placing it between the poles of a permanent magnet. Excess coating molecules (FMN) was removed by washing the coated nanoparticles several times with water which results in the green solution respectively.

4.8. Total phosphate determination of FLUSPIO and FAD USPIO

4.8.1. Vaskovsky phosphate determination

Vaskovsky phosphate determination is based on the oxidative decomposition of the phospholipids and further, this phosphate determination could be applied to the iron oxide cores coated/functionalized with ligands containing phosphate groups respectively. The determination is based on the complexation of the inorganic phosphate with partially reduced molybdate metal ions under acidic conditions[228]. The stock solution for phosphate determination was prepared as follows, 3.81 mmol (0.40 g) $NH_2NH_2 \cdot 2HCl$ (Riedel-de Haën) and 41.33 mmol (10 g) $Na_2MoO_4 \cdot 2H_2O$ (Merck) were dissolved in 14 mL and 60 mL of 4 M HCl respectively. Both solutions were mixed and the mixture was heated to 80 ºC for 20 min on a water bath. The mixture was cooled to 25 °C and then 14 mL of concentrated H_2SO_4 was added with vigorously stirring. Then, de-mineralised water was added to a total volume of 100 mL(standard flask). The final stock solution can be stored in the dark for at least six months. The working solution was prepared by using 5.5 mL of the above-mentioned stock solution and 26 mL of 0.5 M H_2SO_4 which were made up to 100 mL using the de-mineralised water. The following procedure was performed for the actual phosphate determination: a mixture of 100 µL of a properly diluted sample and 100 µL of 70-72 % $HClO_4$ were introduced into a pyrex reagent tube and heated to 200-240 ºC for 45 min. The mixture was cooled to 25 °C and 1000 µL of working solution was added to it. Subsequently, the mixture was heated to 100 °C on a water bath for 20 min. After cooling to 25 °C, 1500 µL of 0.5 M H_2SO_4 are added and the absorbance was measured at 820 nm. The total phosphate concentration was determined on the basis of calibration curve. For this purpose solutions with a known phosphate concentration between 0.1 und 1.0 µmol/mL were treated in the similar way as the samples. For accuracy all samples were analysed threefold.

4.9. Conjugation of dyes/biomolecules to APTMS coated nanoparticles

Fluorescent iron oxide nanoparticles were generated by coupling different organic dyes such as 5-carboxyfluorescein diacetate-N-succinimidyl ester, fluorescein isothiocyanate (FITC), tetramethyl rhodamine isothiocyanate (TRITC) to the silane (APTMS) coated iron oxide nanoparticles via the free amino groups accessible from the APTMS coating respectively.

4.9.1. Coupling of 5-carboxyfluorescein diacetate-N-succinimidyl ester with APTMS USPIO

Coupling of 5-carboxyfluorescein diacetate-N-succinimidyl ester (dye) with APTMS USPIO was performed by following a slight modification in the reported protocol[229]. The APTMS coated USPIO (10 mg/mL) were retrieved from water using a permanent magnet and suspended in acetate buffer (pH 8.5). The stock solution of 5-carboxyfluorescein diacetate-N-succinimidyl ester (λex = 492 nm, λem = 517 nm) was prepared by dissolving 0.5 mg in 0.5 mL of DMSO and protected from light for further use. The dye solution in DMSO (50 – 100 µL) was added slowly to the silica coated USPIO suspension (pH = 8.5) in dark and the reaction vessel was covered with aluminium foil and allowed to react for 2 h at 4 ºC in the dark. Excess of activated fluorescein dye was removed from the reaction mixture by performing the dialysis against water at 4 ºC for 2 days.

4.9.2. Coupling of fluorescein isothiocyanate (FITC) with APTMS USPIO

APTMS coated USPIO was funtionalized with FITC by following a modified protocol[230]. The APTMS coated USPIO (10 mg/mL) were retrieved from water by using a permanent magnet and suspended in a buffer with pH 9. The dye stock solution of 1 mg/mL of FITC (λex = 494 nm, λem = 520 nm) was prepared using DMSO which was stored in the dark. The dye solution in DMSO (50 – 100 µL) was added slowly to each mL of silica coated nanoparticle (2 mg/mL) at pH 9 in dark and the reaction vessel was covered with aluminium foil and allowed to react for 8 h at 4 ºC in the dark. The reaction was quenched by addition of NH_4Cl (50 mM) and reacted for further 2 h to block the remaining isothiocyanate groups. Excess of activated fluorescein dye was removed from the reaction mixture by performing the dialysis against water at 4 ºC for 2 days.

4.9.3. Coupling of rhodamine isothiocyanate (TRITC) with APTMS USPIO

TRITC was conjugated with APTMS USPIO by superseding the reported coupling protocol with a slight modification[231]. The APTMS coated USPIO (2 mg/mL) were retrieved from water by using a permanent magnet and suspended in 0.1 M Na_2CO_3 solution with pH 9.0. The dye stock solution of 1 mg/mL of TRITC (λex = 544 nm, λem = 570 nm) was prepared using DMSO and protected from light respectively. The dye solution in DMSO (50 µL) was added slowly to each mL of silica coated nanoparticle (2 mg/mL) at pH 9 in dark and allowed to react for 8 h at 4 ºC in the dark. The reaction was quenched by addition of 50 µL of NH_4Cl (50 mM) and reacted for 2 h to block the remaining isothiocyanate groups.

Excess of activated rhodamine dye was removed from the reaction mixture by performing the dialysis against water at 4 ºC for 2 days.

4.9.4 Coupling of biotin-FITC to APTMS USPIO

Coupling of streptavidin to APTMS USPIO and further interaction with FITC labelled biotin was carried out by a modification in the reported protocol[232]. The APTMS coated USPIO were retrieved from water using a permanent magnet. The silica coated USPIO (10 mg/mL) were washed three times with 500 µL of PBS buffer. The amine groups present in the APTMS USPIO were activated using 200 µL of glutaraldehyde (5% aqueous solution) and 800 µL of PBS buffer by vacillating them for 4 h at RT. After vacillation, nanoparticles were recovered using a permanent magnet and washed thrice with PBS buffer and further 0.25 mg streptavidin was added. The reaction was allowed to proceed for 24 h by vacillation at RT. Excess streptavidin from the nanoparticles was removed by washing thrice with PBS buffer by retrieving nanoparticles with a permanent magnet. The stock solution of 1 mg of FITC labelled biotin (λex = 494 nm, λem = 520 nm) was prepared by dissolving it in 1 mL of PBS. The dye stock solution (30 µL) was added slowly to silica coated nanoparticle in dark and allowed to react for 10 min in the dark. Excess of FITC labelled biotin was removed either by dialysis against water at 4 °C or by high gradient magnetophoresis respectively.

4.10 In vitro experiments

4.10.1. List of equipments and accessories

Instrument	Model	Manufacturer
Laminar air flow cabinet	MSC-Advantage	Thermo Scientific Inc., Waltham, MA, USA
Waterbath (37 ºC)	Lauda AL12	Aqualine GmbH & Co. KG, Lauda-Königshofen, Germany
Suction pump	AA04	HLC, Bovenden, Germany
Incubator (37ºC, 5% CO_2, 95% relative humidity	C150	Binder Inc., Great River, NY, USA
Centrifuge	Multifuge 1L	Thermo Scientific Inc., Waltham, MA, USA
Microscope (Bright field)	Axiovert	Carl Zeiss MicroImaging GmbH, Germany
Fluorescence Microscope	- AxioObserver Z1 - Imager M2 - Olympus BX50	Carl Zeiss MicroImaging GmbH, Germany. Olympus, Germany.
Eppendorf pipette (10 µL, 100 µL, 200 µL and 1000 µL)	Transferpette S	Brand GmbH & Co. KG, Wertheim, Germany
Cryovial	Cryo S	Greiner Bio-one GmbH, Frickenhausen, Germany
Centrifuge	Fresco 21	Heraeus Germany
Image based cell analyser	Cedex XS	Innovatis AG, Bielefeld, Germany
Hemocytometer, Neubauer	0.100 mm depth 0.0025 mm^2	Brand, Wertheim, Germany
Autoclave	VE-40	Systec GmbH, Wettenberg, Germany
Cryocan (cell freezing)		Isotherm, Germany
Cryotom	CM 3050 S	Leica GmbH, Germany
Flow cytometer	FACS Calibur	BD Bioscience, Heidelberg, Germany

4.10.1.2. List of reagents

Reagent	Composition	Manufacturer
DPBS	Phosphate buffered saline without $CaCl_2$ and $MgCl_2$	GIBCO Invitrogen, Grand Island, NY, USA
RPMI 1640	Without L-Glutamine	GIBCO Invitrogen, Grand Island, NY, USA
RPMI 1640	With L-Glutamine	GIBCO Invitrogen, Grand Island,

		NY, USA
McCoy`s 5A	With Glutamax	GIBCO Invitrogen, Grand Island, NY, USA
DMEM	High glucose with Glutamax	GIBCO Invitrogen, Grand Island, NY, USA
Vasculife VEGF Endothelial cell culture medium	VascuLife Basal medium, VascuLife VEGF Lifefactors kit, rh FGF basic, Ascorbic acid, Hydrocortisone sulphate, FBS, L-Glutamine, rh IGF-1, rh EGF, rh VEGF, Heparin sulphate Life Factors	Cellsystems Biotechnologie Vertrieb GmbH, Troisdorf, Germany
Eagle`s minimum essential medium (MEM)	Modified to contain Earles Balanced Salt Solution, non-essential amino acids, 2 mM L-glutamine, 1 mM sodium pyruvate, and 1500 mg/L sodium bicarbonate	LGC Standards GmbH, Wesel, Germany
Fetal bovine serum (FBS)	South American origin	GIBCO Invitrogen, Grand Island, NY, USA
Pen/Strep	10,000 units/mL Penicillin 10,000 µg/mL Streptomycin	GIBCO Invitrogen, Grand Island, NY, USA
EDTA	0.05% in PBS	Merck KGaA. Darmstadt, Germany
Trypsin/EDTA	0.25% Trypsin; 0.05% EDTA in PBS buffer	GIBCO Invitrogen, Grand Island, NY, USA
DMSO	100% DMSO	SIGMA-ALDRICH Chemie GmbH, Steinheim, Germany
DAPI	100% DAPI	Merck KGaA, Darmstadt, Germany
Trypan blue	Microscopy grade	SIGMA-ALDRICH Chemie GmbH, Steinheim, Germany
7-amino actinomycin D	7-AAD viability staining solution in PBS and contains 0.09% NaN_3	NatuTec GmbH, an eBioscience Company, Frankfurt, Germany
In situ Cell Death Detection Kit, TMR red (TUNEL kit)	Enzyme solution (Terminal deoxynucleotidyl transferase from calf thymus recombinant in *E. Coli*, in storage buffer) and Label solution (Nucleotide mixture in reaction buffer)	Roche Diagnostics Deutschland GmbH, Mannheim, Germany
DNase I recombinant	RNase free	Qiagen GmbH, Hilden, Germany
Cell Proliferation kit I (MTT)	MTT labeling reagent and solubilization solution	Roche Diagnostics Deutschland GmbH, Mannheim, Germany
Cytotoxicity test kit (LDH)	Catalyst and dye solution	Roche Diagnostics Deutschland

		GmbH, Mannheim, Germany
Paraformaldehyde	4% paraformaldehyde	SIGMA ALDRICH Chemie GmbH, Steinheim, Germany
Triton X-100	0.1% Triton X-100	SIGMA ALDRICH Chemie GmbH, Steinheim, Germany
Sodium citrate	0.1 % Sodium citrate	Carl Roth GmbH & Co. KG; Karlsruhe, Germany
Permafluor mounting medium		Thermo Scientific Inc., Waltham, MA, USA

4.10.1.3. List of laboratory products

Product	**Manufacturer**
50 mL Falcon tubes	BD, Franklin Lakes, NJ, USA
Disposable pipettes (5mL, 10 mL, 25 mL, 50 mL)	Costar Stripettes, Corning, NY, USA
Pipette tips (10 µL,200 µL and 1000 µL)	TipOne by USA Scientific Inc., Ocala, FL, USA
Sterile glass Pasteur pipettes	Brand GmbH & CO. KG, Wertheim, Germany
T-25/T-75 cell culture flasks	Greiner Bio-one GmbH, Frickenhausen, Germany
Latex powder free gloves	MaiMed GmbH & CO. KG, Neuenkirchen, Germany
6-well plate	BD Falcon, Germany
24-well plate	BD Falcon, Germany
96-Flat transparent microplate	Greiner Bio-one, Frickenhausen,Germany
Petri dish (200 x 20 mm)	Greiner Bio-one, Frickenhausen,Germany
Cover slips, round (12 mm)	Carl Roth GmbH & Co. KG; Karlsruhe, Germany
Glass slides (76 x 26 mm)	R. Langenbrinck, Emmendingen, Germany
quadri PERM	Greiner Bio-one GmbH, Frickenhausen, Germany

4.11. Cell culture

4.11.1. PC-3 cell line

PC-3 cells initiated from a bone metastasis of a grade IV prostatic adenocarcinoma from a 62-year-old male Caucasian (Figure 4.1.5). Prostate cancer cells (PC-3 cell line) were purchased from ATCC (CRL-1435) and cultured by the reported procedure respectively.

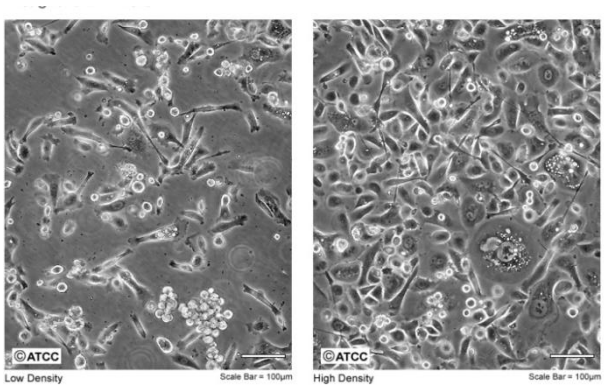

Figure 4.1.5. The figure shows PC-3 cell population grown in low and high density respectively.

4.11.2. DU-145 cell line

The DU-145 cells were established from the tumor tissue removed from the metastatic central nervous system lesion of a 69-year-old man with prostate carcinoma in 1975 (Figure 4.1.6). DU-145 cell lines were purchased from ATCC (HTB-81) respectively.

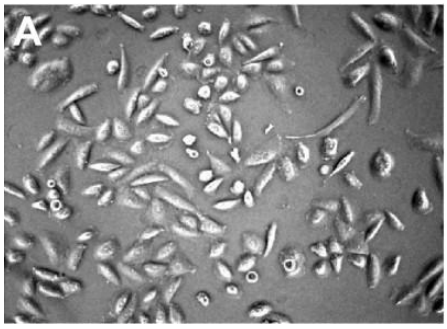

Figure 4.1.6. The figure shows DU-145 cell population grown in high density respectively

4.11.3. LnCap cell line

The LnCap cells were established from the left supraclavicular lymph node metastasis from a 50-year-old man with prostate carcinoma in 1977; cells were described to be androgen-sensitive (Figure 4.1.7). LnCap cell line was purchased from DSMZ (ACC.256) and was further expanded according to the following procedures.

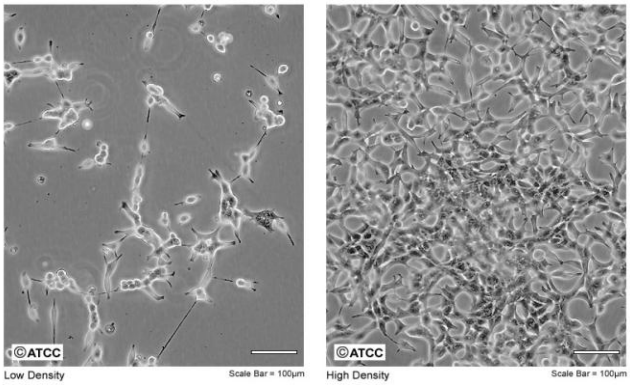

Figure 4.1.7. The figure shows LnCap cell population grown in low and high density respectively.

4.11.4. Human Umblical Vein Endothelial cells (HUVEC)

The endothelium is composed of a thin layer of endothelial cells (EC), which line the interior surface of blood and lymphatic vessels from the aorta to the smallest capillary. Endothelial cells vary in morphology and functions according to the type and size of the associated vessel. The cells were isolated from normal human adult tissues from different locations e.g., umbilical vein. Human Umbilical Vein Endothelial Cells (HUVEC) (Figure 4.1.8) were purchased from Promocell (C-12203, HUVEC pooled) and expanded according to the reported procedures.

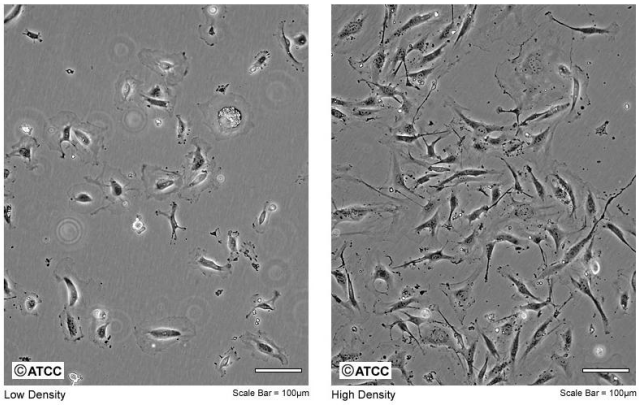

Figure 4.1.8. The figure shows HUVEC cell population grown in low and high density respectively.

4.11.5. Myofibroblasts

Myofibroblasts are thought to be derived from local resident mesenchymal cells, particularly fibroblasts, and further from smooth muscle cells, pericytes and endothelial cells. However, cellular origin of myofibroblasts was also reported to be emerged from bone-marrow-derived circulating fibrocytes (BMDCF) and epithelial-to-mesenchymal transformation (EMT) respectively. The process that involves the homing to local tissue sites

of BMDCF, under the influence of the local micro-environment appears to become myofibroblasts.

Myofibroblasts in granulation tissue and tumor stroma exhibit similarities in structure, immunophenotype and molecular activities. Wound healing myofibroblasts have the primary role of producing local concentration of matrix, a process supported by collagen synthesis and secretion. The myofibroblast has the same synthetic machinery as the fibroblast (rough endoplasmic reticulum, Golgi apparatus and collagen secretion granules). The myofibroblast has the same kind of myofilaments as in the smooth muscle cells but in reduced numbers and at the cell periphery: it also has the fibronexus which is not a distinctive feature of fibroblasts, smooth muscle cells and it lacks a lamina. The cellular machinery of the myofibroblasts and fibroblasts as shown in the Figure 4.1.9 are RER, rough endoplasmic reticulum, C, collagen secretion granules, G, Golgi apparatus, FA, focal adhesion, FF, fibronectin fibril, FNX, fibronexus, M, myofilaments respectively.

The myofibroblasts cells were kindly provided by Prof. Stefan Jockenhoevel, AME, Helmholtz Institute Aachen and further they were expanded according to the recommended cell culture protocols.

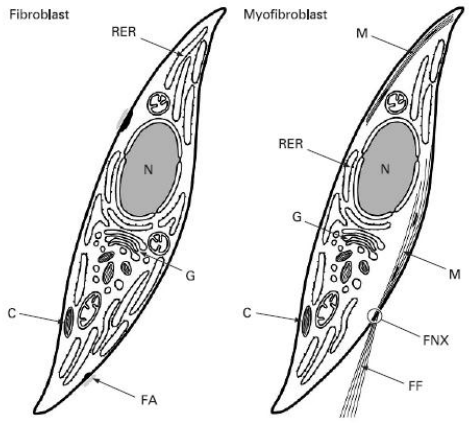

Figure 4.1.9. The figure shows the differences between fibroblast and myofibroblast cells respectively.

4.11.6. RPMI-8226 cell line

The RPMI-8226 cells were established from the peripheral blood of a 61-year-old man with multiple myeloma (IgG lambda-type) at diagnosis in 1966; described to produce and secrete only lambda light chains (but not heavy chains) (Figure 4.2.0). Human multiple myeloma cells (RPMI-8226 cell line) were purchased from DSMZ (ACC-402) and expanded further according to the suggested protocols.

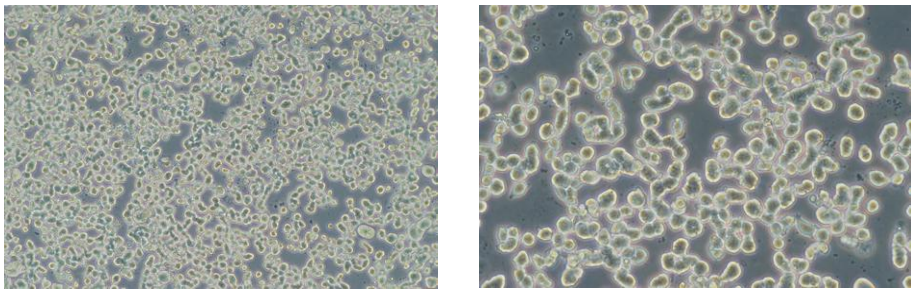

Figure 4.2.0. The figure shows RPMI-8226 cell population in low and high magnification (bright field microscope) respectively.

4.11.7. U87MG cell line

The U87MG cells were established from 44-year-old Caucasian woman with malignant glioma. This is one of a number of cell lines derived from malignant gliomas by J. Ponten and associates from 1966 to 1969(Figure 4.2.1). Human malignant glioma cells (U87MG cell line) were purchased from ATCC (HTB-14) and expanded according to the reported procedures.

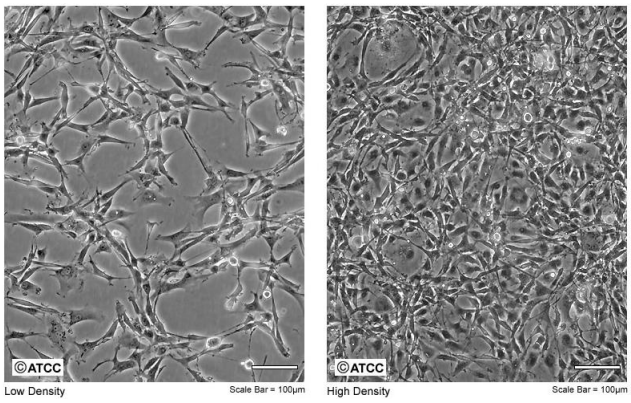

Figure 4.2.1. The figure shows U87MG cell population grown in low and high density respectively.

4.11.8. Cell culture media cocktails

The following cell culture media cocktail´s were used for culturing different cell types.

PC-3 cell line:

McCoy´s 5A with glutamax medium supplemented with 10% FBS and 1% Penicillin/Streptomycin.

DU-145 cell line:

RPMI 1640 without glutamine medium supplemented with 10% FBS and 1% Penicillin/Streptomycin.

LnCap cell line:

RPMI 1640 with glutamine medium supplemented with 20% FBS and 1% Penicillin/Streptomycin.

HUVEC:

DMEM with glutamax medium with high glucose content supplemented with 10% FBS and 1% Penicillin/Streptomycin.

Vasculife endothelial cell growth medium supplemented with endothelial cell growth factors.

Myofibroblasts:

DMEM with glutamax medium with high glucose content supplemented with 10% FBS and 1% Penicillin/Streptomycin

RPMI-8226 cell line:

RPMI 1640 without glutamine medium supplemented with 10% FBS and 1% Penicillin/Streptomycin

U87MG cell line:

Eagle´s minimum essential medium supplemented with 10% FBS and 1% Penicillin/Streptomycin.

4.11.9. General procedures for culturing different cell types

4.11.9.1. Cell thawing

Frozen cell suspensions were transferred from the cryovial into a 50 mL falcon tube with respective cell culture media (including supplements) and the cell suspensions were centrifuged at 1000 rpm for 5 min to remove the DMSO from the freezing medium. The supernatant medium was discarded and the cell pellet was resuspended in 10 mL of respective cell culture media with supplements. The cell suspension was transferred into the T25 cell culture flasks (Greiner bio-one, Germany) and incubated at 37 ºC, 5% CO_2 and 95% relative humidity.

4.11.9.2. Cell growth (cell propagation)

Once the cells reached 80-90% confluency in T25 cell culture flask (Greiner bio-one, Germany), the following protocol was followed: The old medium above the cells was removed and cells were washed with 10 mL PBS. Further, cells were trypsinized using 2 mL of Trypsin/EDTA (0.25%/0.5%) by 3 min incubation in the incubator. The trypsinization was stopped by addition of 8 mL of respective cell growth media. Then, 10 mL of cell suspension were transferred to a T75 cell culture flask (Greiner bio-one, Germany) which is further

diluted with 10 mL of respective cell growth media and grown in the incubator. Medium was renewed routinely (two to three times per week). After every medium change, confluency of the cells was examined under the bright field microscope.

4.11.9.3. Cell splitting (sub cultivation)

The cells were frequently passaged in order to avoid spontaneous differentiation and sub cultivated until they reach 90% confluency. Cells were split according to the following protocol. After removing the old medium, cells in T75 cell culture flask were washed with 10 mL PBS to remove traces of serum that contains trypsin inhibitor. Cells were trypsinized with 4 mL of trypsin/EDTA(0.25%/0.5%). The trypsinization was stopped by adding 16 mL of the cell growth media. Further, the amount of medium added depends on the splitting ratio attempted (Table 4.1.3). The following volumes were added to account for the desired splitting ratio.

Table 4.1.3. List of cell splitting ratios and volume added

Splitting ratio	Trypsin/EDTA (mL)	Medium (mL)	Total volume (mL)
1:2	4	4	8
1:3	4	8	12
1:4	4	12	16
1:5	4	16	20

4.11.9.4. Freezing cells

The cells were washed, trypsinated and the cell pellet was collected according to the above described procedure. Required amount of cells were frozen with 70% cell culture media, supplemented with 20% FBS, 10% DMSO and 1% Penicillin/Streptomycin and further stored at vapour phase liquid nitrogen temperature.

4.12. Mycoplasm test

Cell culture contamination by mycoplasms occur due to the contamination from individuals or contaminated cell culture media or cell culture supplements. Mycoplasma is a kind of bacteria that lacks a cell wall (Ryan, et al., 2004)[233]. It can induce cellular changes, including chromosome aberrations, metabolism changes and slow cell growth. Several techniques have been developed to detect mycoplasms such as polymerase chain reaction (PCR), plating on sensitive agar and staining with a DNA stain (e.g., Hoechst or DAPI). The

prostate cancer cells, myofibroblasts, myeloma cells and glioma cells were tested for mycoplasma contamination with DAPI DNA staining. The mycoplasma test was performed by following the below described protocol.

The cells were cultured in antibiotic-free (Streptomycin/Penicillin) cell growth media for 14 days and seeded onto sterile glass microscope slides. The cells were rinsed with PBS and placed in Carnoy`s fixative solution (75% methanol and 25% glacial acetic acid) for 15 min then they were air dried. Carnoy fixative is normally used to fix tissues that will be embedded in the paraffin. The regions of interest were marked using super PAP PEN IM3580 (Immunotech, Beckmann coulter company, France) into different squares (e.g., divide the region of interest into 4 x 2 squares) and UV fluorescent DNA stain (DAPI, 4`,6-diamidino-2-phenylindole) was added on each squares in drops until the square was filled. The concentrations used for DAPI staining were 2 µg/mL and 5 µg/mL. The cells were left in the dark in a humid metal chamber for 30 min.

This incubation time allows the infusion of the DAPI and its intercalation into the DNA between the bases and therefore allows the detection of DNA (nucleus) under ultraviolet light. The cells were then rinsed three times with PBS, mounted in mounting medium and covered by a cover slip. The samples were stored for long time at 4 ºC. The cells were viewed under the UV-Epifluorescent microscope (Imager M2, Carl Zeiss Microimaging, Germany) for extranuclear DNA-staining in the cytoplasm as an indicator of mycoplasma contamination. No cell contamination should be detected under the microscope prior to their *in vitro* investigations.

4.13. Cell viability assays

4.13.1. Trypan blue stain

The toxicity of the nanoparticles (FLUSPIO, FAD USPIO, NUSPIO) on prostate cancer cells (PC-3, LnCap), RPMI-8226 cells and HUVEC was investigated using trypan blue staining (trypan blue stain, Sigma-aldrich, Steinheim, Germany). Cell population of 2 x 10^6 cells were seeded in the 6-well plates (BD Falcon, Germany) and incubated for 24 h in the incubator. Medium was removed, and each well was washed with 2 mL of PBS buffer. Nanoparticles (FLUSPIO, FAD USPIO, NUSPIO) and controls were diluted in respective cell growth media, in order to have iron concentrations of 0.03, 0.3, 3.0 µmol Fe/mL, respectively. 1 mL of cell growth media comprising nanoparticles with different iron concentrations and respective controls were added to each well (6-well plate). Cells were

incubated for 3, 12 and 24 h. After incubation, medium was removed and transferred to 15 mL falcon tubes. Cells were washed once with PBS and subsequently trypsinized using 0.5 mL of trypsin/EDTA (0.25%/0.5%). The cell suspension was centrifuged at 1000 rpm (Multifuge, Thermo scientific, Germany) for 5 min and the supernatant medium was removed. The cell pellet was dissolved in 0.5 mL of respective fresh cell growth media. 50 µL of the cell suspension were mixed with 50 µL of the trypan blue staining solution (1:2). Trypan blue positive cells (dead cells) were counted using a Cedex XS (Innovatis AG, Germany) cell counter. The percentage of trypan blue positive cells as a function of the total cell number was calculated in order to determine the relative cell viability. Three samples per condition were analysed.

4.13.2. TUNEL assay

Toxicity of the nanoparticles (FLUSPIO and NUSPIO) on PC-3, HUVEC and RPMI-8226 cells was additionally evaluated using the In situ Cell Death Detection Kit, TMR red, (Roche Diagnostics GmbH, Mannheim, Germany). The cells ($1x10^5$ cells/mL) were grown on cover slips (12 mm, Carl Roth, Germany) inside the 24 well plates (Cell star, Greiner bio-one, Germany). Nanoparticles diluted in respective cell growth media (3.0, 0.3, 0.03 µmol Fe/mL) were added to the cells and incubated for 3 h. Duplicates were used (FLUSPIO). Triplicates were performed for NUSPIO toxicity investigation. After incubation, medium was removed and cells were washed three times with PBS buffer. Further, cells were fixed with 4% paraformaldehyde at RT for 15 min. Again, cells were washed three times with PBS buffer. After fixation, cells were permeabilised for 2 min using the permeabilisation solution [(0.1% Triton X-100 (Sigma Aldrich, Steinheim, Germany) and 0.1 % sodium citrate (Carl Roth, Germany)]. Cells were washed three times with PBS buffer and further dried at RT. Negative control cells were treated only with 50 µL of the labeling solution (without active enzyme). Positive control cells were generated by incubation with recombinant DNase I for 10 min in order to induce DNA strand break. 50 µL of TUNEL reaction mixture (label solution + active enzyme solution) were added to the positive control cells and to the cells, which were previously treated with controls and nanoparticles for 3 h. The TUNEL reaction mixture was incubated for 1 h at 37 °C in a humidified atmosphere in dark. After incubation, cells were washed three times with PBS for 10 min. Nuclei were counterstained with 4´,6´-diamino-2-phenylindole (DAPI, 5 µg/mL, Merck, Darmstadt, Germany). Viable and apoptotic cells were counted in five different fields of view/slide using a fluorescence microscope (AxioObserver Z1; Carl Zeiss GmbH, Germany). Images were acquired using a digital camera (AxioCam MRm; Carl Zeiss GmbH, Germany) with 10X magnification respectively.

4.13.3. MTT proliferation assay

MTT cell proliferation assay was used as the third method used to assess the cell viability. The Cell Proliferation Kit I (Roche Diagnostics GmbH, Mannheim, Germany) was designed to be used for the non-radioactive, spectrophotometric quantification of cell proliferation and viability in cell populations using the 96-well-plate format. The cleavage of the tetrazolium salt MTT (3-(4,5-dimethylthiazol-2-yl)-2,5-diphenyl tetrazolium bromide) into a blue colored product (formazan) by the mitochondrial enzyme succinate-dehydrogenase takes place only in living cells and amount of formazan produced is proportional to the number of cells (Figure 4.2.2).

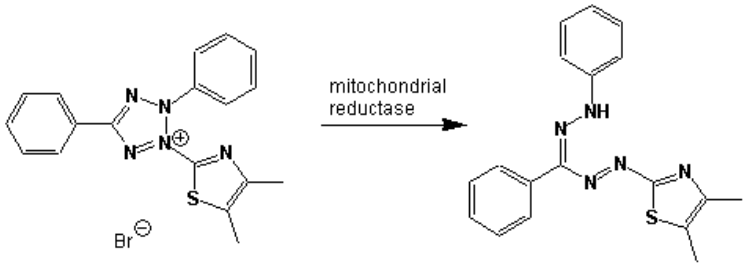

Figure 4.2.2. The figure shows the conversion of the tetrazolium salt (MTT) into formazan by mitchondrial reductase enzyme respectively.

Cells were grown in 96 well microplates by suspending them in 100 µL of respective cell growth media per well ($8x10^3$ cells/well). Incubation of the cells was carried out at 37 °C and 5% CO_2 for 24 h in the incubator. After incubation, cells were washed with warm cell culture medium without phenol red. Negative controls are the cells which was incubated with medium and 1 % FBS. Positive control is generated by adding 100 µL of triton X (0.5 %) and 100 µL of DMSO served as the blank control. Serial dilutions of the nanoparticles (FLUSPIO, FAD USPIO) were added to the cells in triplicates with final iron concentrations of 3.0, 0.3, and 0.03 µmol Fe\mL. 100 µL of samples (FLUSPIO, FAD USPIO and controls) in the cell growth media was introduced to the cells and further incubated for 3 h. The medium was removed after the incubation. Further, 100 µL of cell growth media were added to each well and trace amount of remnant nanoparticles and controls were removed. 20 µL of MTT solution (5 mg /mL of tetrazolium salt in PBS) were added to the each well, which were subsequently incubated for 4 h. Excess MTT-solution was removed after the incubation. The converted dye (formazan crystals) was solubilized with 150 µL of DMSO and stored at RT overnight to enhance the solubility of the samples. Further, trituration was performed in order to dissolve the converted dye completely. Absorbance of the converted dye was measured at 570 nm with background subtraction at 690 nm. Relative viability of the cells was calculated with reference to the negative control cells which were presumed to be 100% viabile.

4.13.4. LDH cytotoxicity assay

Cytotoxicity of the nanoparticles (NUSPIO) on PC-3 cells was also tested using LDH kit (Roche Diagnostics GmbH, Mannheim, Germany). The Cytotoxicity Detection Kit (LDH) was designed to be used as a precise, fast and simple colorimetric alternative to quantitative cytotoxicity/cytolysis based on the measurement of LDH activity released from the damaged cells into the supernatant of the incubated cell growth medium. The culture supernatant was collected cell-free and incubated with the reaction mixture from the kit. The LDH activity is determined in an enzymatic test: In the first step NAD^+ is reduced to $NADH/H^+$ by the LDH-catalyzed conversion of lactate to pyruvate. In the second step the catalyst (diaphorase) transfers H/H^+ from $NADH/H^+$ to the Iodotetrazolium chloride (INT) which is reduced to formazan (Figure 4.2.3, Table 4.1.4).

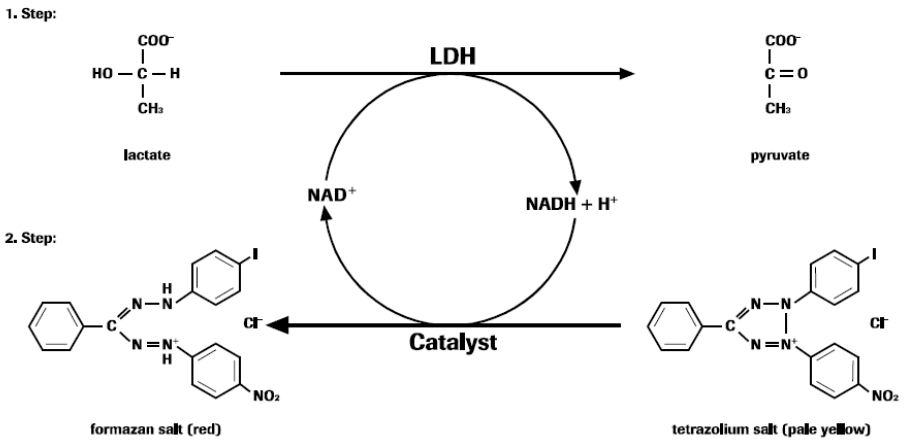

Figure 4.2.3. The schematic figure shows the different conversion steps related to LDH activity. The first step involves LDH mediated conversion of lactate into pyruvate and second step involves catalytic conversion of the tetrazolium salt into formazan salt respectively.

Table 4.1.4. Contents of LDH assay.

Label	Contents/function
Catalyst	Diaphorase/NAD^+ mixture, lyophilizate, stabilized
Dye solution	Iodotetrazolium chloride (INT) and sodium lactate

PC-3 cells (2 x 10^4 cells/well) were grown by suspending them in 100 µL of cell growth medium (DMEM/McCoy`s 5A with glutamax medium and 1-2% BSA (bovine serum albumin)) in 96 well microplates (Greiner bio-one, Germany). Cells were incubated at 37 °C and 5% CO_2 for 24 h in the incubator for the cells to adhere on the surface of the plate. After incubation, cells were washed with warm (37 °C) PC-3 growth medium. The assay medium

from the adherent cells was removed (to avoid LDH activity released from the cells during the overnight incubation step) and 100 µL of fresh cell growth medium was added to each well. 100 µL of the nanoparticle diluted in the PC-3 cell culture medium (3.0, 0.3, 0.03 µmol Fe/mL) was transferred into wells with PC-3 cells. 200 µL of cell growth medium without nanoparticles was used in triplicates as a background control for the medium. Negative control was generated by incubating the cells with culture medium (100 µL) in triplicates. Positive controls were generated by addition of 100 µL Triton X-100 (0.5%) to the cells. The background control for the nanoparticles (without cells) was used in order to avoid interference from nanoparticle absorption on LDH assay, which was achieved by using 100 µL of the nanoparticles (3.0 µmol Fe/mL) in 100 µL of the cell culture medium. Triplicates were used. Cells were incubated with nanoparticles (3.0, 0.3, 0.03 µmol Fe/mL) for 6 and 24 h respectively. After incubation, 100 µL of supernatant was removed carefully (the cells at the bottom was not disturbed) and transferred into wells of an optically clear 96-well flat bottom microplate (Greiner bio-one, Germany). The LDH activity in these supernatants was determined by treating each well with 100 µL of the reaction mixture (freshly prepared: mix 250 µL of bottle 1 (catalyst) with 11.25 mL of bottle 2 (dye solution)) and incubating them for 30 min between 15 and 25 °C in the dark. The absorbance of the samples was measured at 490/492 nm in addition to a reference for the background subtraction (above 600 nm) using an ELISA microplate reader. Cell viability (%) was calculated by the following relation/formula (experimental value-negative control/positive control-negative control) x 100.

4.13.5. Flow cytometry analysis

7-amino actinomycin D (7-AAD) viability staining (eBioscience GmbH, Frankfurt, Germany) was used to determine the effect of the nanoparticles (FLUSPIO and FAD USPIO) on the viable cells by flow cytometry (FACS Calibur, BD Bioscience). Cells (PC-3, LnCap cells and HUVEC) were grown in petridishes (200 X 20 mm; Greiner bio-one, Germany) until they reached 80% confluency. For the FACS analysis $4x10^5$ cells (PC-3, LnCap) and $2x10^5$ cells (HUVEC) in 300 µL were used. Positive controls were generated by exposing the cells to 2 mL of triton X-100 (0.5%) for 10 min in the incubator. Nanoparticles (FLUSPIO and FAD USPIO) were diluted in the respective cell growth media of PC-3, LnCap and HUVEC with the different iron concentrations (3.0, 0.3, 0.03 µmol Fe/mL). 10 mL of medium containing the nanoparticles were added to the cells and incubated at different time periods (3 h, 24 h). After incubation, medium was removed and cells were washed three times with PBS supplemented with 2% FBS. Cells were trypsinized by adding 2 mL of

trypsin/EDTA (0.25%/0.5%) and by 3 min incubation in the incubator. Trypsinization was stopped by adding 8 mL of the respective cell growth media to the cells. Further, they were centrifuged at 1000 rpm for 5 min in order to bring down the cells in the suspension. The cell pellet was re-suspended in 300 µL PBS supplemented with 2% fetal calf serum. The cell suspension (245 µL) was stained with 5 µL of 7-AAD viability staining solution by incubating them in the dark at RT for 20 min prior to the FACS measurement. The fluorescence intensity of 7-AAD was determined in the FL3 (7-AAD) channel of the flow cytometer for the nanoparticles (at three different concentrations) inside the cells and for the controls (positive, negative) respectively.

4.13.6. Direct cell viability counting method

The direct cell viability counting method was applied to assess the viability of the PC-3 cells after incubation with different iron concentrations of FLUSPIO nanoparticles. The PC-3 cells ($1x10^5$ cells/mL) were seeded into a 24 well plate (BD Falcon, Germany) and then incubated overnight to adhere onto the surface (24 well plate). Subsequently, the medium was removed and cells were washed once with PBS buffer. Negative controls were generated by incubating the cells with PC-3 cell growth medium. FLUSPIO nanoparticles were diluted in the growth medium to reach a final iron concentration of 3.0, 0.3, 0.03 µmol Fe/mL and further incubated for 3 h, 6 h, 12 h, 24 h, 48 h and 72 h respectively. After incubation, the medium containing the nanoparticles was removed and cells were washed three times with PBS. Cells were trypsinized. Finally, the cells were suspended in the medium and counted with the aid of a bright field microscope/cedex cell counter. The viability of the cells incubated with different FLUSPIO concentration were calculated relatively (drop in cell viability) in comparison to the total viable cell population of the negative control which was treated as 100% viable cells respectively.

4.14. Fluorescence microscopy

4.14.1. Fluorescence cell labeling by FLUSPIO/FAD USPIO nanoparticles

The fluorescence efficiency of the FLUSPIO nanoparticles in labeling the prostate cancer cells (PC-3) was evaluated by fluorescence microscopy. PC-3 cells (0.5×10^6 cells) were seeded into the wells of 24-well plates (BD Falcon, Germany) which were already loaded with cover slips (12 mm, Carl Roth, Germany). Cells were incubated for 24 h to adhere on the cover slips respectively. Subsequently, the medium was removed and cells

were washed once with PBS. FLUSPIO nanoparticles (0.5 – 1.0 µmol Fe/mL) and controls (USPIO, FMN: 3.0 µmol/mL, GMP: 7.0 µmol/mL), diluted in the PC-3 cell growth medium, were added (1 mL) to the cells and incubated for 3 h. After incubation, the medium was removed and cells were washed three times with 1 mL of PBS buffer. Then, the cells on the cover slips were fixed with 0.5 mL of 100% ethanol by incubating them for 10 min in RT. Furthermore, ethanol was removed and the coverslips were dried in RT. The cover slips were removed from the 24-well plates and the cell nuclei were stained with 500 µL of DAPI (10 µg/mL) by 30 min incubation in the dark. Excess DAPI was removed by washing with copious amount of water. Finally, the cover slips were fixed on the glass slides using the permafluor mounting medium and air dried prior to the fluorescence microscopic (AxioObserver Z1, Carl Zeiss Microimaging GmbH, Germany) evaluation. Triplicates were used for all conditions.

The fluorescence efficiency of FAD USPIO nanoparticles was evaluated in LnCap cells (0.5×10^6 cells) using fluorescence microscopy. The LnCap cells were seeded and further incubation procedure was followed analogous to that of FLUSPIO labeling. The FAD USPIO nanoparticles (3.0 µmol Fe/mL) and controls (USPIO, FAD: 3.0 µmol/mL, GMP: 7.0 µmol/mL) diluted in RPMI 1640 with glutamax medium supplemented with 10% FBS and 1% Pen/Strep were added (1 mL) in triplicates and incubated for 3 h respectively. Further, the cells were washed, trypsinized, fixed, stained with DAPI, and mounted on cover slips for analysis by fluorescence microscopy (analogous to FLUSPIO) respectively.

4.14.2. Competition experiments (Fluorescence Microscopy)

The fluorescence efficiency of the FAD USPIO nanoparticles for labeling the prostate cancer cells was mediated by riboflavin carrier protein (RCP) and their strong intracellular uptake was evaluated by fluorescence microscopy. The RCP dependant FAD USPIO uptake was proved by performing *in vitro* fluorescence competition experiments where RCP was blocked by free Rf in 10 and 100 fold excess. LnCap cells were seeded on the glass slides (76 x 26 mm) placed inside the quadriPERM chamber and incubated for 24 h. 2 mL of the LnCap cells suspension (0.5 – 1.0 million cells) in the RPMI 1640 with glutamax medium supplemented with 20% FBS and 1% Pen/Strep and 3 mL of LnCap cell growth medium was added to the quadriPERM chamber. The cells were incubated at 5% CO_2 and 37 °C for 48 h, until the cells reached 70-80% confluency. After incubation, the medium was removed from the wells and cells were washed once with PBS buffer. The FAD USPIO nanoparticles (0.3 µmol Fe/mL) were diluted in the LnCap cell growth medium. LnCap cells on the glass slides were pre-incubated with free Rf (10 and 100 fold in comparison to the concentration of FAD (Rf analogue) on the nanoparticles) in order to block the RCP that is responsible for the high

uptake of FAD USPIO. After 10 min incubation, medium with FAD USPIO was added and subsequently incubated for 1 h. After incubation, the medium was removed and cells were washed three times with PBS. Then, the cells were fixed with 5 mL of 100% ethanol for 10 min in RT. Excess ethanol was removed and the glass slides were dried at RT. Cell nuclei were stained with DAPI and processed as described before (section 4.14.1) prior to the fluorescence analysis.

4.14.3. Flow cytometry analysis of cells labelled with FLUSPIO and FAD USPIO

The fluorescence intensity of nanoparticles (FLUSPIO and FAD USPIO) inside the viable cells was determined by using flow cytometry (FACS Calibur, BD Biosciencs, Germany). Cells (PC-3 and LnCap cells) were grown in petridishes (200 X 20 mm; Greiner bio-one, Germany) until they reach 80% confluency. Flow cytometry analysis was performed with $4x10^5$ cells (PC-3, LnCap) in 300 µL. Positive controls were generated by exposing the cells to 2 mL of triton X-100 (0.5%) in the PBS buffer at 37°C. Nanoparticles (FLUSPIO and FAD USPIO) were diluted in respective cell growth media with different iron concentrations (3.0, 0.3, 0.03 µmol Fe/mL). 10 mL of the medium with the nanoparticles were added to the cells (incubation time: 3 h, 24 h). After incubation, medium was removed and cells were washed three times with PBS supplemented with 2% FBS. Cells were trypsinized. Trypsinization reaction was stopped by adding 8 mL of the respective cell growth media to the cells. Further, they were centrifuged at 1000 rpm for 5 min in order to bring down the cells in the suspension. The cell pellet was resuspended in 300 µL PBS with 2% fetal calf serum. The cell suspension (245 µL) was measured in the FL1 (FITC) channel in order to visualize the green fluorescence of FLUSPIO and FAD USPIO.

4.14.4. FLUSPIO uptake in prostate cancer cells (Bright field microscopy)

Additionally, the uptake of FLUSPIO by prostate cancer cells (PC-3 and DU-145) was evaluated using bright field microscopy. PC-3 and DU-145 cells were used at 80% confluency. The supernatant medium above the cells was removed and cells were washed with PBS. Then, the cells were trypsinized. Trypsinization was stopped by adding 16 mL of the respective cell growth media and cells were seeded on glass slides (76 x 26 mm) which were kept inside a quadriPERM chamber and incubated for 24 h. The supernatant medium was removed and the cells were washed once with PBS buffer. Cells were incubated with FLUSPIO for 3 h in different iron concentrations (3.0, 0.3, 0.03 µmol Fe/mL) in triplicates. After incubation, medium was removed and cells were washed three times with PBS buffer.

Then, the cells were fixed on the glass slides using 100% ethanol by 10 min incubation in RT. Ethanol was removed and the glass slides were dried in RT. The glass slides was removed from the quadriPERM chamber and cover slips were fixed on the glass slides using the permafluor mounting medium and dried prior to the analysis with the bright field microscope (AxioImagerD1, Carl Zeiss Microimaging GmbH, Germany).

4.15. TEM - FLUSPIO uptake by prostate cancer cells

The high competency of FLUSPIO in labeling prostate cancer cells (PC-3) was visualized using transmission electron microscopy (TEM). USPIO and FLUSPIO (3.0 µmol Fe/mL) were diluted in PC-3 cell growth medium. 11mL of medium containing either USPIO or FLUSPIO were added to the cells and incubated for 3 h and 6 h. After incubation, medium was removed and cells were washed thrice with PBS. Subsequently, cells were fixed in 3 % glutaraldehyde (in 0.1 M Soerensen's phosphate buffer [pH 7.4; 13 mM NaH_2PO_4 x H_2O; 87 mM Na_2HPO_4 x $2H_2O$]) by incubation for 22 h, and subsequently washed with 0.1 M Soerensen's phosphate buffer. Fixed cells were embedded in 2 % agarose, rinsed with distilled water and dehydrated with ethanol (80 % - 100 %). Finally cells were processed for embedding in Epon, by polymerizing 8 h at 37 °C and 56 hours at 60 °C, and then cut into 70 – 100 nm thick slices. After polymerization, cells were contrasted with uranyl acetate and lead citrate. The samples were analyzed with a PHILIPS EM 400 T microscope at 60 kV and micrographs were taken by an OLYMPUS CCD-Camera (MORADA)

4.16. Quantification of FLUSPIO intracellular uptake (ICP-MS)

4.16.1. In vitro FMN competition experiments

The increased FLUSPIO uptake by PC-3 cells mediated via RCP was also studied using ICP-MS technique by effectively blocking the RCP receptors with 10 and 100 fold excess of FMN respectively. PC-3 cells were cultured in respective cell growth medium and processed for FLUSPIO uptake analogous to the competition experiments performed for LnCap cells (as in section 4.14.2) respectively. FLUSPIO (0.3 µmol Fe/mL) and respective 10 and 100 fold excess of FMN was added to the PC-3 cells and incubated for 30 and 60 min. Triplicates of all conditions was performed. Further, after incubation the cells were washed, trypsinized, and centrifuged. The supernatant medium was discarded and the cell pellet (2 x 10^6 cells) was measured for the total iron content of the FLUSPIO internalized inside the PC-3 cells. Digestion of the cells was performed in a closed vessel microwave reaction system

(MLS ethos plus, MPV-100/HAT) by addition of 1.5 mL nitric acid (65%) to 1.5 mL hydrogen peroxide and 1 mL of internal standard (rhodium) using 1000 W for 45 min and by raising the temperature from RT to 210 ºC (left constant at 210 ºC for another 15 min). Samples were diluted in 1:100 in water.

The amount of the intracellular iron was determined using a high-resolution sector field inductively coupled plasma mass spectrometer [ICP-MS (Elan-DRCII, Perkin-Elmer)] equipped with an injector (2.0 mm i.d. Quartz, Part No.: WE02-3916). Data were acquired at medium resolution using rhodium as an internal standard. A Quartz Cyclonic spray chamber (Part No.: WE02-52222) equipped with a Meinhard Type A quartz nebulizer was used for the sample introduction. The instrument was tuned and calibrated via infusion of a 1 µg/mL rhodium standard solution. The iron content was expressed in picograms of iron per cell.

4.17. In vitro MR relaxometry

4.17.1. Phantom generation for FLUSPIO and FAD USPIO cellular uptake by different cell types

The intracellular uptake of the nanoparticles (FLUSPIO, FAD USPIO) by prostate cancer cells (PC-3, DU-145, LnCap) and endothelial cells (HUVEC) were investigated by determining the R2 relaxation rates using a clinical 3T MR scanner (PHILIPS Achieva, The Netherlands) in combination with a knee coil (SENSE-flex-M, PHILIPS, The Netherlands) at RT. The prostate cancer and endothelial cells were cultured according to the protocol described in section 4.11 respectively. Further, these cells were labelled using different concentration of FLUSPIO and FAD USPIO (3.0, 0.3, 0.03 µmol Fe/mL) by incubating them at different time periods respectively. Subsequently, the cells were washed and trypsinized as described in the previous sections. Furthermore, the incubated cells were centrifuged at 1000 rpm (Multifuge, Thermo scientific, Germany) for 5 min and supernatant medium was discarded. The cell pellet was re-suspended in 50 mL of PBS buffer and washed three times by performing the centrifugation as described above. The total cell number in the cell suspension was counted using a hemocytometer and cell pellet after PBS washing was dissolved in required volume of 10% gelatin solution to have 2 x 10^6 cells/0.3 mL as the final cell concentration. For MR measurements 0.3 mL/well of cell suspension in 10% gelatin was filled in the custom made phantoms (Greiner 96 well Flat Transparent Polystyrol microplate, Germany). The relaxation times T_1 and T_2 are measured according to the sequences parameters mentioned in section 4.2.11 respectively.

4.17.2. Comparison of FLUSPIO and FAD USPIO cellular uptake by different cell types

FLUSPIO efficiency in labeling prostate cancer cells, fibroblasts and endothelial cells were compared as these cells are kown to express different RCP levels. We believe that the high uptake of FLUSPIO is RCP dependant in above cells. The intracellular uptake of FLUSPIO nanoparticles in prostate cancer cells (PC-3, LnCap, DU-145), myofibroblasts and HUVEC was compared using MR tomography (R2 relaxation rates).

FLUSPIO nanoparticles were diluted in the respective cell growth media, to have a final iron concentration of 0.3 µmol Fe/mL for cellular labeling. 11 mL of cell culture medium with nanoparticles were added to each T75 flask with respective cells. Three samples per condition were analysed. Cells were incubated for 1 h and 3 h at 37 ºC, 5% CO_2 and 95% relative humidity. Cells were trypsinized and dissolved in 10% gelatin to have 2 x 10^6 cells/0.3 mL as the final cell concentration. R2 relaxation rates of the samples were determined as described before.

Similarly, the cellular uptake of FAD USPIO by prostate cancer cells (PC-3, DU-145, LnCap) mediated via RCP was studied in comparison to USPIO using MR relaxometry based on the R2 relaxation rates respectively. The three different prostate cancer cells were cultured according to the previously described protocols (section 4.11). FAD USPIO and USPIO (0.3 µmol Fe/mL) were diluted in the respective cell culture media and cells were labelled with 11 mL of medium containing nanoparticles. Triplicates of all conditions were performed. The cells with nanoparticles were incubated for 1 h and 3 h in the incubator. After incubation, cells were washed, trypsinized, centrifuged, and suspended in 10 % gelatin in order to have a total cell concentration of 2 x 10^6 cells/0.3 mL respectively. Further, the FAD USPIO cellular uptake was analyzed by measuring the R2 relaxation rates of the cells as described before. In line with the above described experiment (under identical experimental conditions), Rf-USPIO, FLUSPIO, and FAD USPIO cellular uptake by PC-3 and DU-145 cells were studied via the R2 relaxation rates (MR relaxometry) in order to determine the specific uptake of the probes mediated by different RCP ligands respectively.

In addition, the RCP mediated specific uptake of flavin coated nanoparticles by prostate cancer cells, fibroblasts and endothelial cells was studied by employing double FMN coated USPIO using MR relaxometry. The double FMN coated USPIO was diluted in the respective cell growth media to 0.3 µmol Fe/mL and 11 mL of this medium was used for labeling the cells by incubating them for 1 h respectively. Triplicates of the samples were analyzed. After incubation, cells were washed, trypsinized, centrifuged analogous to the *in vitro* phantom generation protocols. The cell pellet was diluted in 10% gelatine to have a cell

concentration of 2 x 10^6 cells/0.3 mL respectively. Further, the R2 relaxation rates of the labelled cells and controls were determined as described prior to MRI measurements. In line with the above described experimental conditions, double Rf coated USPIO, double FMN coated USPIO and double FAD coated USPIO cellular uptake by PC-3 cells were evaluated using MR relaxometry (R2 relaxation rates) in order to prove that the uptake is highly regulated via RCP.

4.17.3. Inhibition of FLUSPIO uptake by FBS in prostate cancer cells

The uptake of FLUSPIO by PC-3 cells in the absence of FBS was almost two to three folds in comparison to cells incubated with FLUSPIO in the presence of FBS. FLUSPIO and USPIO nanoparticles were diluted in McCoy`s 5A with glutamax medium supplemented only with 1% penicillin/streptomycin with and without FBS supplementation, to have a final iron concentration of 3.0, 0.3, 0.03 µmol Fe/mL to facilitate cellular labeling. 11 mL of medium with nanoparticles (USPIO and FLUSPIO) was added to each T75 flask. Cells were incubated for 3 h at 37 ºC, 5% CO_2 and 95% relative humidity. Cells were embedded in gelatin and measured by R2- relaxometry by using MR-sequences as described before. Three samples per condition were analysed.

4.18. In vitro competitive blocking of FLUSPIO/FAD USPIO uptake by different cells

Flavin (Rf, FMN, FAD) based competition experiments were performed in order to validate the uptake of FLUSPIO and FAD USPIO mediated via RCP respectively. The high intracellular uptake of FAD USPIO and FLUSPIO nanoparticles by prostate cancer cells (PC-3, LnCap, DU-145) and HUVEC was determined using MR tomography (R2 relaxation rates). For labeling cells, FAD USPIO, FLUSPIO nanoparticles and control (USPIO) were diluted in the respective cell growth media, in order to have a final iron concentration of 0.3 µmol Fe/mL. Cells were pre-incubated for 10 min with 10 mL of cell growth media containing 10 and 100 fold excess of one of the following RCP specific ligand (Rf, FMN, FAD) in order to block the highly expressed RCP. Subsequently, 10 mL of FLUSPIO and FAD USPIO (0.3 µmol Fe/mL) in respective cell growth media were added and further, cells were incubated for 30 or 60 min at 37 ºC, 5% CO_2 and 95 % relative humidity. Three samples per condition were analysed. After incubation, cells incubated with nanoparticles and excess RCP ligand (flavins) were washed, trypsinized and centrifuged. Finally, the cell pellet was diluted in 10 % gelatin to yield a final cell concentration of 2 x 10^6 cells/0.3 mL respectively. The R2 relaxation rates of the above cells in gelatin were determined using MR

relaxometry as described above to evaluate the flavin coated USPIO uptake by different cells mediated via the RCP.

4.19. Fluorescence imaging (Fluorvivo300 Indec imaging system)

Fluorvivo Model 300 Indec imaging system offers multicolor, simultaneous, GFP-RFP imaging with two additional excitation and emission filter sets, thus allowing at least three alternative probes to be imaged (see Table 4.1.4). Real time multicolor imaging and live video imaging and recording can be achieved with this system. The system finds its applications in basic research that include studies of gene expression and apoptosis, tumor growth and angiogenesis, and metastasis and invasion. Pre-clinical applications include drug screenings, drug targeting, and further validation of the animal models can also be achieved using this imaging system respectively.

The MR gelatin phantom`s from different experiments i.e FLUSPIO and FAD USPIO in prostate cancer cells, endothelial cells were scanned using FluorVivo300 Indec system before and after MR scan in order to co-validate the results obtained from MR relaxometry via fluorescence. Further, the fluorescence image`s (intensity) of these phantoms were compared with the relaxation rate`s (R2) from MR measurements which can be related to very high specific uptake of FLUSPIO, FAD USPIO nanoparticles in different cells.

Table 4.1.4. Table shows different channels available in the FluorVivo imaging system respectively.

Channel Name	Relevant Probes
GFP	GFP Cy2™ Qdot® 525
YFP	YFP
RFP	RFP Cy3 Alexa Fluor® 555 Alexa Fluor 568 Alexa Fluor 594 dsRed2 Katushka/mKate mCherry Qdot 605 Qdot 625
Texas Red	Texas Red mPlum Cy3.5
Cy5	Cy5 Cy5.5 Alexa Fluor 647 Alexa Fluor 660 Alexa Fluor 680 Qdot 655
Near Infrared	Cy7 Alexa Fluor 750

4.20. In vivo experiments with FAD USPIO

Ten CD1 male nude mice (Charles River Laboratories International, Inc., Wilmington, MA, USA) were used for the in vivo evaluation of FAD USPIO and Resovist. The male nude mice were generated from the transfer of the nude gene through a series of crosses and backcrosses. All animal experiments were approved by the governmental review committee on animal care.

4.20.1.1 Tumor Xenograft model: subcutaneous injection (s.c. injection)

For xenotransplantation, 4 x 10^6 LnCap cells in 100 µL matrigel (with small amount of medium) were subcutaneously injected into the right hind limb of each male nude mouse (n = 10). The tumors were left for 6-8 weeks to grow.

4.20.1.2. Assessment of tumor growth

Assuming that the tumor has an ellipsoid shape, the diameters were measured using a calliper and the tumor volume was calculated according to the volume formula of ellipsoid $V = ab^2\Pi/6$, where a & b being the longest and shortest diameters of the ellipsoid along 2 axes respectively.

4.20.1.3. MRI of tumor bearing mice

The nude mice bearing LnCap tumor were scanned using a solenoid sense-receive mouse coil manufactured by Philips in the clinical 3T MRI system under isoflurane anesthesia before and after i.v. injection of FAD USPIO and Resovist (1 h and 3 h). The tumor was non-invasively imaged using T_2w, T_2*w, T_1w image sequences. In addition, T_2 and T_2* relaxometry sequences was applied as described below.

Transverse relaxation times (T_2) were measured using a multi-slice, multi shot spin echo sequences with 90° excitation pulses followed by a train of equally spaced 180° refocusing pulses [TR = 1500 ms, TE = 18 ms (shortest), number of echoes = 20, FOV = 30 mm, matrix scan = 80, reconstruction matrix = 112, slice thickness = 1 mm, slice orientation = sagittal, scan mode = multishot (MS), scan technique = SE]. T_2 relaxation times were calculated by a linear fit of logarithmic region of interest (ROI) signal amplitudes versus echo time (TE). T_2 star relaxation times (T_2*) were measured using a multi-slice, multi shot spin echo sequences with 30º excitation pulse without refocusing pulse [TR = 1330 ms, TE 1= 10 ms, TE = 7.9 ms, number of echoes = 15, FOV = 30 mm, matrix scan = 80, reconstruction matrix = 112, slice thickness = 1 mm, slice orientation = sagittal, scan mode = multishot (MS), scan technique = FFE]. T_2 weighted (T_2w) images were acquired by measuring a

multi-slice, single shot spin echo sequences with 30º excitation pulse without refocusing pulse [TR = 800 ms, TE = 26 ms, number of echoes = 1, FOV =25 mm, matrix scan = 96, reconstruction matrix = 96, slice thickness = 1mm, slice orientation = sagittal, scan mode = M2D, scan technique = FFE]. T_2star weighted (T_2*w) images were acquired by measuring a multi-slice, multi shot spin echo sequences with 90º excitation pulses followed by a train of equally spaced 120º refocusing pulses [TR = 2391 ms, TE = 100 ms, number of echoes = 1, FOV = 25 mm, matrix scan = 128, reconstruction matrix = 144, slice thickness = 1mm, slice orientation = sagittal, scan mode = multishot (MS), scan technique = SE]. T_1weighted (T_1w) images were acquired by measuring a multi-slice, multi shot spin echo sequences with 90º excitation pulses followed by a train of equally spaced 115º refocusing pulses [TR = 500 ms, TE = 20 ms, number of echoes = 1, FOV = 150 mm, matrix scan = 304, reconstruction matrix = 512, slice thickness = 5mm, slice orientation = sagittal, scan mode = multishot (MS), scan technique = SE] respectively.

4.20.1.4. Injection of contrast agent (FAD USPIO)

The animals were randomly divided into two groups: Resovist (control, n=5), and FAD USPIO (n=5). The animals were injected with 130 µL of respective agents in 5% glucose solution with a total iron concentration of 900 µmol Fe/Kg. The injection process was performed under the FluorVivo 300 imaging system (GFP channel) in order to visualize the fluorescence of the FAD USPIO nanoparticles.

4.20.2. Prussian blue staining

Prussian blue staining was performed to localize USPIO, and FAD USPIO in the prostate cancers. The tumors were frozen in tissue tek (O.C.T. Compound, Sakura Finetek Europe B.V., Germany) and stored at -80°C. Thin sections (8 µm) of the tumor tissues were cut using a cryotom. Tumor tissues were first incubated with an aqueous solution of $K_4Fe(CN)_6$ (10%) for 5 min, then with a 1:1 mixture of $K_4Fe(CN)_6$ (10%) and hydrochloric acid (20%) for 30 min. Tissues were counterstained with Nuclear Fast Red (Carl Roth, Karlsruhe, Germany) for 10 min. After staining, tumor tissues were washed with water, dried with ethanol (70%, 80%, and 100% respectively), rinsed with xylene and embedded with coverslips for microscopic analysis (Imager M2, Carl Zeiss Microimaging GmbH, Germany).

4.20.3. (Immuno-)histological Staining of Tumors

The tumor slices on microscopic slides were stained for vascularization using a primary rat anti-mouse CD31 antibody (BD Biosciences, San Jose, CA) for 2 h (RT) in combination with a Cy3-labeled anti-rat IgG secondary antibody (Dianova GmbH,

Hamburg,) which was incubated for 30 min at RT, respectively. Nuclei in the tumor sections were counterstained with DAPI for 30 min. The slides were visualized using fluorescence microscope (Imager M2, Carl Zeiss GmbH, Germany) with different magnification (10X, 20X and 40X) and fields of view, respectively.

4.20.4. Pharmacokinetic profile of FAD USPIO in mouse blood (Blood half life)

Small volumes of blood (30 µL – 50 µL) were withdrawn intravenously from a male nude mouse (CD1) before injecting them with specific nanoparticles under the isoflurane anesthesia. The blood was diluted with 50 µL of 5% glucose solution which acts as a blank (5% glucose solution) and control (blood without nanoparticles). The FAD USPIO nanoparticles (900 µmol/Kg) in 5% glucose solution were injected in one mouse which was visualized under the FluorViVo 300 imaging system. After the injection, 30 – 50 µL of the blood were withdrawn at different time points (3-5,10, 30 and 60 min) and mixed with 50 µL of the 5% glucose solution. Blood half life of the FAD USPIO was determined by analysing the fluorescence (using TECAN microplate reader) in the blood at 530 nm for various time points.

References

[1.] S. Kunjachan, J. Jayapaul, M. Mertens E, G. Storm, F. Kiessling, T. Lammers, *Curr Pharm Biotechnol* **2011,** *Article in Press* .

[2.] R. Weissleder, *Nat.Rev.Cancer* **2002,** *2* 11-18.

[3.] R. Weissleder, M. J. Pittet, *Nature* **2008,** *452* 580-589.

[4.] C. J. Anderson, F. Dehdashti, P. D. Cutler, S. W. Schwarz, R. Laforest, L. A. Bass, J. S. Lewis, D. W. McCarthy, *J.Nucl.Med* **2001,** *42* 213-221.

[5.] P. Price, *Eur.J.Cancer* **2000,** *36* 691-693.

[6.] J. Drevs, I. Hofmann, H. Hugenschmidt, C. Wittig, H. Madjar, M. Müller, J. Wood, G. Martiny-Baron, C. Unger, D. Marme, *Cancer Res* **2000,** *60* 4819-4824.

[7.] B. G. Zagar, R. J. Fornaris, K. W. Ferrara, *Ultrasound Med Biol* **1998,** *24* 809-824.

[8.] K. W. Ferrara, C. R. Merritt, P. N. Burns, F. S. Foster, R. F. Mattrey, S. A. Wickline, *Acad Radiol* **2000,** *7* 824-839.

[9.] D. H. Turnbull, T. S. Bloomfield, H. S. Baldwin, F. S. Foster, A. L. Joyner, *Proc.Natl.Acad.Sci.U.S.A* **1995,** *92* 2239-2243.

[10.] J. P. Christiansen, J. R. Lindner, *Proceedings of the IEEE* **2005,** *93* 809-818.

[11.] G. M. Lanza, S. A. Wickline, *Prog Cardiovasc Dis* **2001,** *44* 13-31.

[12.] S. S. Gambhir, *Nat.Rev.Cancer* **2002,** *2* 683-693.

[13.] M. E. Phelps, A. Chatziioannou, S. Cherry, S. Gambhir, Molecular imaging of biological processes from microPET in mice to PET in patients *Molecular imaging of biological processes from microPET in mice to PET in patients*, pp. 1-9 .

[14.] D. M. Thomasson, A. Gharib, K. C. P. Li, *Acad Radiol* **2004,** *11* 1159-1170.

[15.] R. G. Pautler, S. E. Fraser, *Curr.Opin.Immunol* **2003,** *15* 385-392.

[16.] R. Weissleder, A. Moore, U. Mahmood, R. Bhorade, H. Benveniste, E. A. Chiocca, J. P. Basilion, *Nat.Med* **2000,** *6* 351-355.

[17.] E. A. Schellenberger, A. Bogdanov, D. Högemann, J. Tait, R. Weissleder, L. Josephson, *Mol Imaging* **2002,** *1* 102-107.

[18.] M. A. Funovics, B. Kapeller, C. Hoeller, H. S. Su, R. Kunstfeld, S. Puig, K. Macfelda, *Magn Reson Imaging* **2004,** *22* 843-850.

[19.] J. C. Frias, K. J. Williams, E. A. Fisher, Z. A. Fayad, *J.Am.Chem.Soc* **2004,** *126* 16316-16317.

[20.] V. Amirbekian, M. J. Lipinski, K. C. Briley-Saebo, S. Amirbekian, J. G. Aguinaldo, D. B. Weinreb, E. Vucic, J. C. Frias, F. Hyafil, V. Mani, E. A. Fisher, Z. A. Fayad, *Proc.Natl.Acad.Sci.U.S.A* **2007,** *104* 961-966.

[21.] B. A. Moffat, G. R. Reddy, P. McConville, D. E. Hall, T. L. Chenevert, R. R. Kopelman, M. Philbert, R. Weissleder, A. Rehemtulla, B. D. Ross, *Mol Imaging* **2003,** *2* 324-332.

[22.] A. Y. Louie, M. M. Hüber, E. T. Ahrens, U. Rothbächer, R. Moats, R. E. Jacobs, S. E. Fraser, T. J. Meade, *Nat.Biotechnol* **2000,** *18* 321-325.

[23.] R. Weissleder, *Science* **2006,** *312* 1168-1171.

[24.] B. N. G. Giepmans, S. R. Adams, M. H. Ellisman, R. Y. Tsien, *Science* **2006,** *312* 217-224.

[25.] H. R. Herschman, *Science* **2003,** *302* 605-608.

[26.] T. Jiang, E. S. Olson, Q. T. Nguyen, M. Roy, P. A. Jennings, R. Y. Tsien, *Proc.Natl.Acad.Sci.U.S.A* **2004,** *101* 17867-17872.

[27.] T. F. Massoud, S. S. Gambhir, *Genes Dev* **2003,** *17* 545-580.

[28.] M. Rudin, R. Weissleder, *Nat Rev Drug Discov* **2003,** *2* 123-131.

[29.] F. Stuker, C. Baltes, K. Dikaiou, D. Vats, L. Carrara, E. Charbon, J. Ripoll, M. Rudin, *IEEE Trans Med Imaging* **2011,** *30* 1265-1273.

[30.] G. A. F. van Tilborg, W. J. M. Mulder, N. Deckers, G. Storm, C. P. M. Reutelingsperger, G. J. Strijkers, K. Nicolay, *Bioconjug.Chem* **2006,** *17* 741-749.

[31.] E. Karathanasis, S. Suryanarayanan, S. R. Balusu, K. McNeeley, I. Sechopoulos, A. Karellas, A. V. Annapragada, R. V. Bellamkonda, *Radiology* **2009,** *250* 398-406.

[32.] R. Hardman, *Environ Health Perspect* **2006,** *114* 165-172.

[33.] H. Yang, Y. Zhuang, Y. Sun, A. Dai, X. Shi, D. Wu, F. Li, H. Hu, S. Yang, *Biomaterials* **2011,** *32* 4584-4593.

[34.] J. T. Bushberg, J. A. Seibert, E. M. Leidholdt Jr, J. M. Boone, *The essential physics of medical imaging*, second edition ed. Lippincott williams and wilkins, Philadelphia, USA, **2002**.

[35.] D. W. McRobbie, E. A. Moore, M. J. Graves, M. R. Prince, *MRI from picture to proton*, second edition ed. Cambridge University Press, UK, **2006**.

[36.] E. M. Haacke, R. W. Brown, M. R. Thompson, R. Venkatesan, *Magnetic Resonance Imaging: Physical Principles and Sequence Design*, Wiley, New York, **1999**.

[37.] Z. Liang, P. C. Lauterbur, *Principles of Magnetic Resonance Imaging: A Signal Processing Perspective*, IEEE Press, New York, **2000**.

[38.] R. G. Pautler, S. E. Fraser, *Curr.Opin.Immunol* **2003,** *15* 385-392.

[39.] D. E. Sosnovik, R. Weissleder, *Curr.Opin.Biotechnol* **2007,** *18* 4-10.

[40.] E. C. Cho, C. Glaus, J. Chen, M. J. Welch, Y. Xia, *Trends Mol Med* **2010,** *16* 561-573.

[41.] C. A. Haynes, W. Norde, *Colloids and Surfaces B: Biointerfaces* **1994,** *2* 517-566.

[42.] J. J. Gray, *Curr.Opin.Struct.Biol* **2004,** *14* 110-115.

[43.] G. B. Sigal, M. Mrksich, G. M. Whitesides, *J.Am.Chem.Soc* **1998,** *120* 3464-3473.

[44.] S. Vajda, Z. Weng, R. Rosenfeld, C. DeLisi, *Biochemistry* **1994,** *33* 13977-13988.

[45.] V. J. Hruby, F. al-Obeidi, W. Kazmierski, *Biochem.J* **1990,** *268* 249-262.

[46.] S. Laurent, D. Forge, M. Port, A. Roch, C. Robic, L. Vander Elst, R. N. Muller, *Chem.Rev* **2008,** *108* 2064-2110.

[47.] J. W. Bulte, T. Douglas, B. Witwer, S. C. Zhang, E. Strable, B. K. Lewis, H. Zywicke, B. Miller, P. van Gelderen, B. M. Moskowitz, I. D. Duncan, J. A. Frank, *Nat.Biotechnol* **2001,** *19* 1141-1147.

[48.] A. S. Arbab, G. T. Yocum, H. Kalish, E. K. Jordan, S. A. Anderson, A. Y. Khakoo, E. J. Read, J. A. Frank, *Blood* **2004,** *104* 1217-1223.

[49.] H. Kalish, A. S. Arbab, B. R. Miller, B. K. Lewis, H. A. Zywicke, J. W. M. Bulte, L. H. Bryant, J. A. Frank, *Magn Reson Med* **2003,** *50* 275-282.

[50.] E. Schulze, J. T. Ferrucci, K. Poss, L. Lapointe, A. Bogdanova, R. Weissleder, *Invest Radiol* **1995,** *30* 604-610.

[51.] A. Moore, E. Marecos, A. Bogdanov, R. Weissleder, *Radiology* **2000,** *214* 568-574.

[52.] J. C. Sipe, M. Filippi, G. Martino, R. Furlan, M. A. Rocca, M. Rovaris, A. Bergami, J. Zyroff, G. Scotti, G. Comi, *Magn Reson Imaging* **1999,** *17* 1521-1523.

[53.] M. Modo, M. Hoehn, J. W. M. Bulte, *Mol Imaging* **2005,** *4* 143-164.

[54.] B. Stella, S. Arpicco, M. T. Peracchia, D. Desmaele, J. Hoebeke, M. Renoir, J. D'Angelo, L. Cattel, P. Couvreur, *J Pharm Sci* **2000,** *89* 1452-1464.

[55.] Y. Zhang, N. Kohler, M. Zhang, *Biomaterials* **2002,** *23* 1553-1561.

[56.] J. W. M. Bulte, D. L. Kraitchman, *Curr Pharm Biotechnol* **2004,** *5* 567-584.

[57.] H. R. Herschman, *Science* **2003,** *302* 605-608.

[58.] S. A. Wickline, G. M. Lanza, *Circulation* **2003,** *107* 1092-1095.

[59.] S. Achilefu, *Chem.Rev* **2010,** *110* 2575-2578.

[60.] M. Zhao, D. A. Beauregard, L. Loizou, B. Davletov, K. M. Brindle, *Nat.Med* **2001,** *7* 1241-1244.

[61.] H. Poptani, A. M. Puumalainen, O. H. Gröhn, S. Loimas, R. Kainulainen, S. Ylä-Herttuala, R. A. Kauppinen, *Cancer Gene Ther* **1998,** *5* 101-109.

[62.] H. Hashizume, P. Baluk, S. Morikawa, J. W. McLean, G. Thurston, S. Roberge, R. K. Jain, D. M. McDonald, *Am.J.Pathol* **2000,** *156* 1363-1380.

[63.] J. Folkman, *Sci.Am* **1996,** *275* 150-154.

[64.] R. K. Jain, *Science* **2005,** *307* 58-62.

[65.] A. K. Iyer, G. Khaled, J. Fang, H. Maeda, *Drug Discov.Today* **2006,** *11* 812-818.

[66.] P. Ghosh, G. Han, M. De, C. K. Kim, V. M. Rotello, *Adv.Drug Deliv.Rev* **2008,** *60* 1307-1315.

[67.] F. Yuan, M. Dellian, D. Fukumura, M. Leunig, D. A. Berk, V. P. Torchilin, R. K. Jain, *Cancer Res* **1995,** *55* 3752-3756.

[68.] L. M. Hamberg, P. Boccalini, G. Stranjalis, G. J. Hunter, Z. Huang, E. Halpern, R. M. Weisskoff, M. A. Moskowitz, B. R. Rosen, *Magn Reson Med* **1996,** *35* 168-173.

[69.] C. G. Varallyay, L. L. Muldoon, S. Gahramanov, Y. J. Wu, J. A. Goodman, X. Li, M. M. Pike, E. A. Neuwelt, *J.Cereb.Blood Flow Metab* **2009,** *29* 853-860.

[70.] N. van Bruggen, E. Busch, J. T. Palmer, S. P. Williams, A. J. de Crespigny, *J.Cereb.Blood Flow Metab* **1998,** *18* 1178-1183.

[71.] J. B. M. Goense, A. C. Zappe, N. K. Logothetis, *Magn Reson Imaging* **2007,** *25* 740-747.

[72.] F. S. Villanueva, W. R. Wagner, *Nat Clin Pract Cardiovasc Med* **2008,** *5 Suppl 2* S26-S32.

[73.] S. A. Boutry, S. Laurent, L. V. Elst, R. N. Muller, *Contrast Media Mol Imaging* **2006,** *1* 15-22.

[74.] X. Montet, R. Weissleder, L. Josephson, *Bioconjug.Chem* **2006,** *17* 905-911.

[75.] X. Montet, K. Montet-Abou, F. Reynolds, R. Weissleder, L. Josephson, *Neoplasia* **2006,** *8* 214-222.

[76.] B. Chance, J. S. Leigh, H. Miyake, D. S. Smith, S. Nioka, R. Greenfeld, M. Finander, K. Kaufmann, W. Levy, M. Young, *Proc.Natl.Acad.Sci.U.S.A* **1988,** *85* 4971-4975.

[77.] M. A. Franceschini, K. T. Moesta, S. Fantini, G. Gaida, E. Gratton, H. Jess, W. W. Mantulin, M. Seeber, P. M. Schlag, M. Kaschke, *Proc.Natl.Acad.Sci.U.S.A* **1997,** *94* 6468-6473.

[78.] J. Wu, L. Perelman, R. R. Dasari, M. S. Feld, *Proc.Natl.Acad.Sci.U.S.A* **1997,** *94* 8783-8788.

[79.] R. Weissleder, V. Ntziachristos, *Nat.Med* **2003,** *9* 123-128.

[80.] A. Godavarty, A. B. Thompson, R. Roy, M. Gurfinkel, M. J. Eppstein, C. Zhang, E. M. Sevick-Muraca, *J Biomed Opt* **2004,** *9* 488-496.

[81.] E. Kuwana, E. M. Sevick-Muraca, *Biophys.J* **2002,** *83* 1165-1176.

[82.] R. Richards-Kortum, E. Sevick-Muraca, *Annu.Rev.Phys.Chem.* **1996,** *47* 555-606.

[83.] V. Ntziachristos, A. G. Yodh, M. Schnall, B. Chance, *Proc.Natl.Acad.Sci.U.S.A* **2000,** *97* 2767-2772.

[84.] S. V. Patwardhan, S. Bloch, S. Achilefu, J. P. Culver, *Conf Proc IEEE Eng Med Biol Soc* **2006,** *1* 2675-2678.

[85.] G. Zacharakis, H. Kambara, H. Shih, J. Ripoll, J. Grimm, Y. Saeki, R. Weissleder, V. Ntziachristos, *Proc.Natl.Acad.Sci.U.S.A* **2005,** *102* 18252-18257.

[86.] A. P. Demchenko, *Ultraviolet spectroscopy of proteins*, Springer-Verlag, New York, **1981**.

[87.] J. W. Longworth, *Luminescence of polypeptides and proteins. In Excited states of proteins and nucleic acids*, (Eds.: R. F. Steiner, I. Welnryb) Plenum, New York, **1971,** pp. 319-484.

[88.] E. A. Permyakov, *Luminescent spectroscopy of proteins*, CRC Press, London, **1993**.

[89.] A. J. W. G. Visser, *Photochem Photobiol* **1984,** *40* 703-706.

[90.] R. C. Benson, R. A. Meyer, M. E. Zaruba, G. M. McKhann, *Journal of Histochemistry & Cytochemistry* **1979,** *27* 44-48.

[91.] S. Huang, *Biophys.J* **2002,** *82* 2811-2825.

[92.] N. Abdullah, M. Balakumari, A. K. Sau, *Biophys.J* **2010,** *99* 2235-2244.

[93.] J. P. Knemeyer, N. Marme, M. Sauer, *Anal.Chem* **2000,** *72* 3717-3724.

[94.] N. G. Walter, J. M. Burke, *RNA* **1997,** *3* 392-404.

[95.] A. Kumar, V. Kumar, *Inorg Chem* **2009,** *48* 11032-11037.

[96.] K. Loo, N. Degtyareva, J. Park, B. Sengupta, M. Reddish, C. C. Rogers, A. Bryant, J. T. Petty, *J Phys Chem B* **2010,** *114* 4320-4326.

[97.] N. Ramanujam, *Neoplasia* **2000,** *2* 89-117.

[98.] N. M. Rageh, *Can J Anal Sci Spectrosc* **1997,** *42* 6.

[99.] D. Jannkaudakis, E. Thedoridou, A. Pekekoursla, *Chem Chron* **1972,** *1* 69.

[100.] H. Zollinger, *Color chemistry*, third ed. Wiley-VCH, Weinheim, **2003,** p. 544.

[101.] D. R. Williams, *Chem.Rev* **1972,** *72* 203-213.

[102.] G. Hallas, J. H. Choi, *Dyes and Pigments* **1999,** *40* 119-129.

[103.] S. Wang, S. Shen, H. Xu, *Dyes and Pigments* **2000,** *44* 195-198.

[104.] P. Mohan, S. Loya, O. Avidan, S. Verma, G. S. Dhindsa, M. F. Wong, P. P. Huang, M. Yashiro, M. Baba, A. Hizi, *J.Med.Chem* **1994,** *37* 2513-2519.

[105.] K. B. Lee, A. Al-Hakim, D. Loganathan, R. J. Linhardt, *Carbohydrate Research* **1991,** *214* 155-168.

[106.] K.-B. Lee, Y.-S. Kim, R. J. Linhardt, *ELECTROPHORESIS* **1991,** *12* 636-640.

[107.] S. Mahadevan, J. D. Erfle, F. D. Sauer, *J.Anim Sci.* **1979,** *48* 947-953.

[108.] N. Gao, *Methods* **2005,** *35* 323-327.

[109.] X. W. Bai, C. H. Song, J. M. You, Z. W. Sun, Y. Y. Fu, G. L. Li, *Chroma* **2010,** *71* 1125-1129.

[110.] P. L. Southwick, L. A. Ernst, E. W. Tauriello, S. R. Parker, R. B. Mujumdar, S. R. Mujumdar, H. A. Clever, A. S. Waggoner, *Cytometry* **1990,** *11* 418-430.

[111.] V. Buschmann, K. D. Weston, M. Sauer, *Bioconjug.Chem* **2003,** *14* 195-204.

[112.] Y. Lin, R. Weissleder, C. H. Tung, *Mol Imaging* **2003,** *2* 87-92.

[113.] T. Loevgren, K. Pettersson, *Time-resolved fluoroimmunoassay, advantages and limitations. In Luminescence immunoassay and molecular applications*, (Eds.: K. Vam Dyke, R. Van Dyke) CRC Press, Boca Raton, FL, **1990,** pp. 233-253.

[114.] I. Hemmila, *Progress in delayed fluorescence immunoassay. In Fluorescence spectroscopy, new methods and applications*, (Ed.: O. S. Wolfbeis) Springer-Verlag, New York, **1993,** pp. 259-266.

[115.] F. S. Richardson, *Chem.Rev* **1982,** *82* 541-552.

[116.] N. Sabbatini, M. Guardigli, J. M. Lehn, *Coordination Chemistry Reviews* **1993,** *123* 201-228.

[117.] V. Balzani, R. Ballardini, *Photochem Photobiol* **1990,** *52* 409-416.

[118.] M. Li, P. R. Selvin, *J.Am.Chem.Soc* **1995,** *117* 8132-8138.

[119.] U. Jeong, X. Teng, Y. Wang, H. Yang, Y. Xia, *Advanced Materials* **2007,** *19* 33-60.

[120.] J. Ripoll, V. Ntziachristos, C. Cannet, A. L. Babin, R. Kneuer, H. U. Gremlich, N. Beckmann, *Drugs R D* **2008,** *9* 277-306.

[121.] J. M. Perez, L. Josephson, T. O'Loughlin, D. Högemann, R. Weissleder, *Nat.Biotechnol* **2002,** *20* 816-820.

[122.] A. M. Morawski, G. A. Lanza, S. A. Wickline, *Curr.Opin.Biotechnol* **2005,** *16* 89-92.

[123.] K. Licha, *Topics in current chemistry* **2002,** *222* 1-29.

[124.] J. V. Frangioni, *Curr Opin Chem Biol* **2003,** *7* 626-634.

[125.] M. Doubrovin, I. Serganova, P. Mayer-Kuckuk, V. Ponomarev, R. G. Blasberg, *Bioconjug.Chem* **2004,** *15* 1376-1388.

[126.] M. F. Kircher, U. Mahmood, R. S. King, R. Weissleder, L. Josephson, *Cancer Res* **2003,** *63* 8122-8125.

[127.] E. E. Uzgiris, A. Sood, K. Bove, B. Grimmond, D. Lee, S. Lomnes, *Technol.Cancer Res.Treat* **2006,** *5* 301-309.

[128.] M. Niedre, V. Ntziachristos, *Proceedings of the IEEE* **2008,** *96* 382-396.

[129.] J. M. Cooperman, *Handbook of Vitamins*, (Ed.: J. Macklin) Marcel Dekker, New York **1991,** pp. 283-310.

[130.] P. R. Adiga, C. V. Murty, Vitamin carrier proteins during embryonic development in birds and mammals *Vitamin carrier proteins during embryonic development in birds and mammals*, pp. 111-136 .

[131.] P. Malhotra, A. A. Karande, T. K. Prasadan, P. R. Adiga, *Biochem.Int* **1991,** *23* 127-136.

[132.] D. B. Zheng, H. M. Lim, J. J. Pene, H. B. White, *J.Biol.Chem* **1988,** *263* 11126-11129.

[133.] H. L. Monaco, *EMBO J* **1997,** *16* 1475-1483.

[134.] S. N. Huang, P. W. Swaan, *J Pharmacol Exp Ther.* **2001,** *298* 264-271.

[135.] H. M. Said, A. Ortiz, M. P. Moyer, N. Yanagawa, *Am.J.Physiol., Cell Physiol* **2000,** *278* C270-C276.

[136.] J. Zempleni, D. M. Mock, *Proc.Soc.Exp.Biol.Med* **2000,** *225* 72-79.

[137.] C. K. Kumar, N. Yanagawa, A. Ortiz, H. M. Said, *Am.J.Physiol* **1998,** *274* F104-F110.

[138.] H. M. Said, T. Y. Ma, *Am.J.Physiol* **1994,** *266* G15-G21.

[139.] S. Mukherjee, R. N. Ghosh, F. R. Maxfield, *Physiol.Rev* **1997,** *77* 759-803.

[140.] S. N. Huang, M. A. Phelps, P. W. Swaan, *J Pharmacol Exp Ther.* **2003,** *306* 681-687.

[141.] L. M. Bareford, M. A. Phelps, A. B. Foraker, P. W. Swaan, *Mol.Pharmaceutics* **2008,** *5* 839-848.

[142.] A. B. Foraker, C. M. Khantwal, P. W. Swaan, *Adv.Drug Deliv.Rev* **2003,** *55* 1467-1483.

[143.] A. A. Karande, L. Sridhar, K. S. Gopinath, P. R. Adiga, *Int J Cancer* **2001,** *95* 277-281.

[144.] P. N. Rao, E. Levine, M. O. Myers, V. Prakash, J. Watson, A. Stolier, J. J. Kopicko, P. Kissinger, S. G. Raj, M. H. Raj, *Cancer Epidemiol.Biomarkers Prev* **1999,** *8* 985-990.

[145.] P. N. Rao, J. Crippin, E. Levine, J. Hunt, S. Baliga, L. Balart, L. Anthony, M. Mulekar, M. H. G. Raj, *Hepatol.Res* **2006,** *35* 83-87.

[146.] C. W. Mason, V. M. D'Souza, L. M. Bareford, M. A. Phelps, A. Ray, P. W. Swaan, *J Pharmacol Exp Ther.* **2006,** *317* 465-472.

[147.] S. R. Holladay, Z. Yang, M. D. Kennedy, C. P. Leamon, R. J. Lee, M. Jayamani, T. Mason, P. S. Low, *Biochim.Biophys.Acta* **1999,** *1426* 195-204.

[148.] T. P. Thomas, S. K. Choi, M. H. Li, A. Kotlyar, J. R. Baker, Jr., *Bioorg.Med.Chem.Lett* **2010,** *20* 5191-5194.

[149.] H. Y. Lee, S. H. Lee, C. Xu, J. Xie, J. H. Lee, B. Wu, et al, *Nanotechnology* **2008,** *19* 165101.

[150.] S. N. Huang, P. W. Swaan, *J Pharmacol Exp Ther.* **2000,** *294* 117-125.

[151.] C. W. Mason, V. M. D'Souza, L. M. Bareford, M. A. Phelps, A. Ray, P. W. Swaan, *J Pharmacol Exp Ther.* **2006,** *317* 465-472.

[152.] T. Johnson, A. Ouhtit, R. Gaur, A. Fernando, P. Schwarzenberger, J. Su, et al, *Front Biosci* **2009,** *Volume* 3634-3640.

[153.] A. A. Karande, L. Sridhar, K. S. Gopinath, P. R. Adiga, *Int J Cancer* **2001,** *95* 277-281.

[154.] C. S. Brock, S. R. Meikle, P. Price, *Eur J Nucl Med Mol Imaging* **1997,** *24* 691-705.

[155.] B. Paudyal, P. Paudyal, N. Oriuchi, Y. Tsushima, T. Nakajima, K. Endo, *Int J Oncol.* **2008,** *33* 1047-1054.

[156.] L. F. Pracchia, A. A. R. Chaves, J. J. Cerci, J. Soares Junior, J. C. Meneghetti, V. Buccheri, *Clinics* **2007,** *62* 121-126.

[157.] O. S. Wolfbeis, E. Urbano, *Journal of Heterocyclic Chemistry* **1982,** *19* 841-843.

[158.] P. F. Gordon, P. Gregory, *Organic chemistry in colour*, Berlin:Springer-Verlag, **1987,** pp. 96-104.

[159.] P. Skrabal, H. Zollinger, *Dyes and Pigments* **1988,** *9* 201-207.

[160.] R. Dembinski, *European Journal of Organic Chemistry* **2004,** *2004* 2763-2772.

[161.] S. Dandapani, D. P. Curran, *Chemistry* **2004,** *10* 3130-3138.

[162.] R. M. Moriarty, I. Prakash, R. Penrnasta, *Synthetic Communications: An International Journal for Rapid Communication of Synthetic Organic Chemistry* **1987,** *17* 409.

[163.] O. Mitsunobu, M. Eguchi, *Bulletin of the Chemical Society of Japan* **1971,** *44* 3427-3430.

[164.] J.J.Monaghan, M.Barber, R.S.Bordoli, R.D.Sedgwick, A.N.Tyler, *Org.Mass Spectrom.* **1982,** *17* 569.

[165.] A. B. Chin, I. I. Yaacob, *Journal of Materials Processing Technology* **2007,** *191* 235-237.

[166.] C. Albornoz, S. Jacobo, *Journal of Magnetism and Magnetic Materials* **2006,** *305* 12-15.

[167.] E. Hee Kim, H. Sook Lee, B. Kook Kwak, B. K. Kim, *Journal of Magnetism and Magnetic Materials* **2005,** *289* 328-330.

[168.] J. Wan, X. Chen, Z. Wang, X. Yang, Y. Qian, *Journal of Crystal Growth* **2005,** *276* 571-576.

[169.] M. Kimata, D. Nakagawa, M. Hasegawa, *Powder Technology* **2003,** *132* 112-118.

[170.] G. Salazar-Alvarez, M. Muhammed, A. A. Zagorodni, *Chemical Engineering Science* **2006,** *61* 4625-4633.

[171.] S. Basak, D. R. Chen, P. Biswas, *Chemical Engineering Science* **2007,** *62* 1263-1268.

[172.] R. Massart, *Magnetics, IEEE Transactions on* **1981,** *17* 1247-1248.

[173.] R. Massart, V. Cabuil, *Journal of chemical physics* **1987,** *84* 7.

[174.] J. P. Jolivet, P. Belleville, E. Tronc, J. Livage, *Clays and Clay Minerals* **1992,** *40* 531-539.

[175.] E. Tronc, P. Belleville, J. P. Jolivet, J. Livage, *Langmuir* **1992,** *8* 313-319.

[176.] A. K. Gupta, S. Wells, *NanoBioscience, IEEE Transactions on* **2004,** *3* 66-73.

[177.] D. K. Kim, Y. Zhang, W. Voit, K. V. Rao, M. Muhammed, *Journal of Magnetism and Magnetic Materials* **2001,** *225* 30-36.

[178.] A. Bumb, M. W. Brechbiel, P. L. Choyke, L. Fugger, A. Eggeman, D. Prabhakaran, et al, *Nanotechnology* **2008,** *19* 335601.

[179.] S. Lefebure, E. Dubois, V. Cabuil, S. Neveu, R. Massart, *Journal of Materials Research* **1998,** *13* 2975-2981.

[180.] X. Liang, X. Wang, J. Zhuang, Y. Chen, D. Wang, Y. Li, *Adv.Funct.Mater.* **2006,** *16* 1805-1813.

[181.] Z. Li, H. Chen, H. Bao, M. Gao, *Chemistry of Materials* **2004,** *16* 1391-1393.

[182.] Z. Li, Q. Sun, M. Gao, *Angew.Chem.Int.Ed.* **2005,** *44* 123-126.

[183.] N. Wu, L. Fu, M. Su, M. Aslam, K. C. Wong, V. P. Dravid, *Nano Letters* **2004,** *4* 383-386.

[184.] G. Kataby, M. Cojocaru, R. Prozorov, A. Gedanken, *Langmuir* **1999,** *15* 1703-1708.

[185.] Y. Ren, K. i. Iimura, T. Kato, *Langmuir* **2001,** *17* 2688-2693.

[186.] S. Sun, H. Zeng, D. B. Robinson, S. Raoux, P. M. Rice, S. X. Wang, G. Li, *J.Am.Chem.Soc* **2004,** *126* 273-279.

[187.] E. G. Moore, A. P. S. Samuel, K. N. Raymond, *Accounts of Chemical Research* **2009,** *42* 542-552.

[188.] M. Kawa, *Top Curr Chem* **2003,** *228* 193-204.

[189.] P. Drake, H. J. Cho, P. S. Shih, C. H. Kao, K. F. Lee, C. H. Kuo, X. Z. Lin, Y. J. Lin, *J.Mater.Chem.* **2007,** *17* 4914.

[190.] E. V. Groman, J. C. Bouchard, C. P. Reinhardt, D. E. Vaccaro, *Bioconjug.Chem* **2007,** *18* 1763-1771.

[191.] Y. Zhang, N. Kohler, M. Zhang, *Biomaterials* **2002,** *23* 1553-1561.

[192.] A. Ulman, *Chem.Rev* **1996,** *96* 1533-1554.

[193.] Q. Liu, Z. Xu, J. A. Finch, R. Egerton, *Chemistry of Materials* **1998,** *10* 3936-3940.

[194.] S. Mornet, J. Portier, E. Duguet, *Journal of Magnetism and Magnetic Materials* **2005,** *293* 127-134.

[195.] A. del Campo, T. Sen, J. P. Lellouche, I. J. Bruce, *Journal of Magnetism and Magnetic Materials* **2005,** *293* 33-40.

[196.] M. Yamaura, R. L. Camilo, L. C. Sampaio, M. A. Macado, M. Nakamura, H. E. Toma, *Journal of Magnetism and Magnetic Materials* **2004,** *279* 210-217.

[197.] W. Stöber, A. Fink, E. Bohn, *Journal of Colloid and Interface Science* **1968,** *26* 62-69.

[198.] A. P. Philipse, M. P. B. van Bruggen, C. Pathmamanoharan, *Langmuir* **1994,** *10* 92-99.

[199.] Y. Lu, Y. Yin, B. T. Mayers, Y. Xia, *Nano Letters* **2002,** *2* 183-186.

[200.] R. Lawaczeck, H. Bauer, T. Frenzel, M. Hasegawa, Y. Ito, K. Kito, N. Miwa, H. Tsutsui, H. Vogler, H. J. Weinmann, *Acta Radiologica* **1997,** *38* 584-597.

[201.] E. D. Smolensky, H.-Y. E. Park, T. S. Berquo, V. C. Pierre, *Contrast Media Mol Imaging* **2010**.

[202.] N. Lupu, *Nanowires Science and Technology*, (Ed.: N. Lupu) INTECH, Croatia, **2010,** p. 402.

[203.] S. G. Schulman, *Fluorescence and phosphorescence spectroscopy: physicochemical principles and practice*, Pergamon Press Ltd, England, UK **1977,** p. 95.

[204.] T. Htun, A. El-Rayyes, *Canadian Journal of Analytical Sciences and Spectroscopy* **2005,** *50* 159-166.

[205.] P. Reimer, T. Balzer, *Eur Radiol* **2003,** *13* 1266-1276.

[206.] M. Roming, H. Lunsdorf, K. E. J. Dittmar, C. Feldmann, *Angew.Chem.Int.Ed.* **2009,** 632-637.

[207.] S. J. H. Soenen, M. De Cuyper, *Contrast Media Mol Imaging* **2009,** *4* 207-219.

[208.] C. Zhang, M. Jugold, E. C. Woenne, T. Lammers, B. Morgenstern, M. M. Mueller, et al, *Cancer Res* **2007,** *67* 1555-1562.

[209.] F. Kiessling, J. Huppert, C. Zhang, J. Jayapaul, S. Zwick, E. C. Woenne, et al, *Radiology* **2009,** *253* 462-469.

[210.] C. Zhang, B. Waengler, B. Morgenstern, H. Zentgraf, M. Eisenhut, H. Untenecker, et al, *Langmuir* **2007,** *23* 1427-1434.

[211.] S. Kamila, J. F. Callan, R. C. Mulrooney, M. Middleton, *Tetrahedron Letters* **2007,** *48* 7756-7760.

[212.] Flanagan, S. H. Khan, S. Menchen, S. A. Soper, R. P. Hammer, *Bioconjug.Chem* **1997,** *8* 751-756.

[213.] D. H. Song, H. Y. Yoo, J. P. Kim, *Dyes and Pigments* **2007,** *75* 727-731.

[214.] D. H. Song, J. P. Kim, *Dyes and Pigments* **2009,** *80* 219-225.

[215.] L. C. Chan, B. G. Cox, *The Journal of Organic Chemistry* **2007,** *72* 8863-8869.

[216.] T. Y. S. But, P. H. Toy, *J.Am.Chem.Soc* **2006,** *128* 9636-9637.

[217.] P. Mohan, R. Singh, M. Baba, *J.Med.Chem* **1991,** *34* 212-217.

[218.] L. Zhang, R. He, H. C. Gu, *Applied Surface Science* **2006,** *253* 2611-2617.

[219.] A. B. Bourlinos, A. Bakandritsos, V. Georgakilas, V. Tzitzios, D. Petridis, *J Mater Sci* **2006,** *41* 5250-5256.

[220.] S. H. Im, T. Herricks, Y. T. Lee, Y. Xia, *Chemical Physics Letters* **2005,** *401* 19-23.

[221.] F. Y. Cheng, C. H. Su, Y. S. Yang, C. S. Yeh, C. Y. Tsai, C. L. Wu, M. T. Wu, D. B. Shieh, *Biomaterials* **2005,** *26* 729-738.

[222.] G. Jander, K. Jahr, *Massanalyse*, 17 ed. (Eds.: G. Schulze, J. Simon) **2009,** pp. 219-221.

[223.] Marczenko, *Spectrophotometric determination of elements*, John Wiley Verlag London, **1976,** p. 561.

[224.] J. H. YOE, A. L. JONES, *Industrial & Engineering Chemistry Analytical Edition* **1944,** *16* 111-115.

[225.] Y. P. He, S. Q. Wang, C. R. Li, Y. M. Miao, Z. Y. Wu, B. S. Zou, *J.Phys.D: Appl.Phys.* **2005,** *38* 1342-1350.

[226.] D. Portet, B. Denizot, E. Rump, J. J. Lejeune, P. Jallet, *J Colloid Interface Sci.* **2001,** *238* 37-42.

[227.] M. Hodenius, M. De Cuyper, L. Desender, D. Mueller-Schulte, A. Steigel, H. Lueken, *Chemistry and Physics of Lipids* **2002,** *120* 75-85.

[228.] V. E. Vaskovsky, E. Y. Kostetsky, I. M. Vasendin, *Journal of Chromatography A* **1975,** *114* 129-141.

[229.] G. T. Hermanson, *Bioconjugate Techniques*, Academic Press, an imprint of Elsevier, **1996,** pp. 305-307.

[230.] G. T. Hermanson, *Bioconjugate Techniques*, Academic Press, an imprint of Elsevier, **1996,** pp. 303-305.

[231.] G. T. Hermanson, *Bioconjugate Techniques*, Academic Press, an imprint of Elsevier, **1996,** pp. 317-320.

[232.] H. Lu, G. Yi, S. Zhao, D. Chen, L. H. Guo, J. Cheng, *J.Mater.Chem.* **2004,** *14* 1336.

[233.] K. J. Ryan, C. G. Ray, *Sherris Medical Microbiology*, fourth ed. (Eds.: K. J. Ryan, C. G. Ray) McGraw Hill, **2004,** pp. 409-412.

Appendices

Appendix 1: NMR spectra of different ligands

^{1}H NMR spectrum of compound 1 recorded in $CDCl_3$

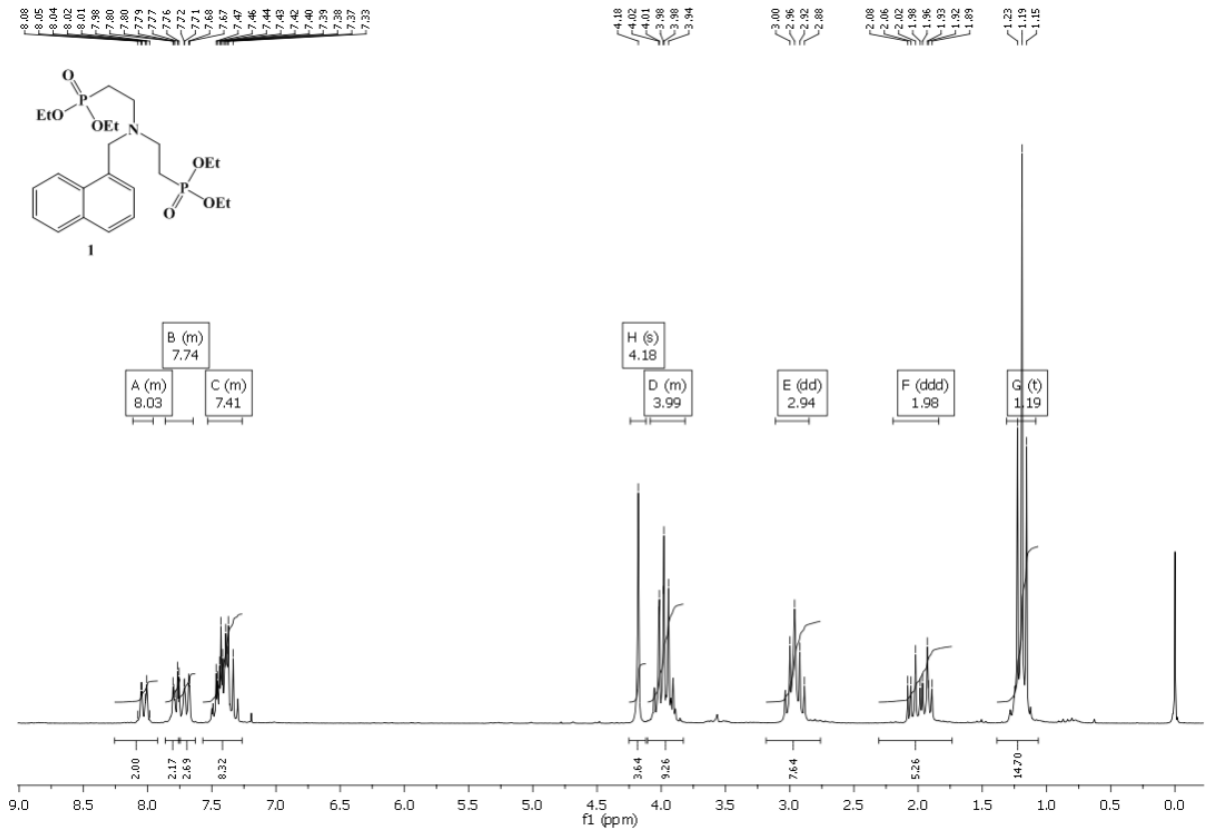

^{13}C NMR spectrum of compound1 recorded in $CDCl_3$

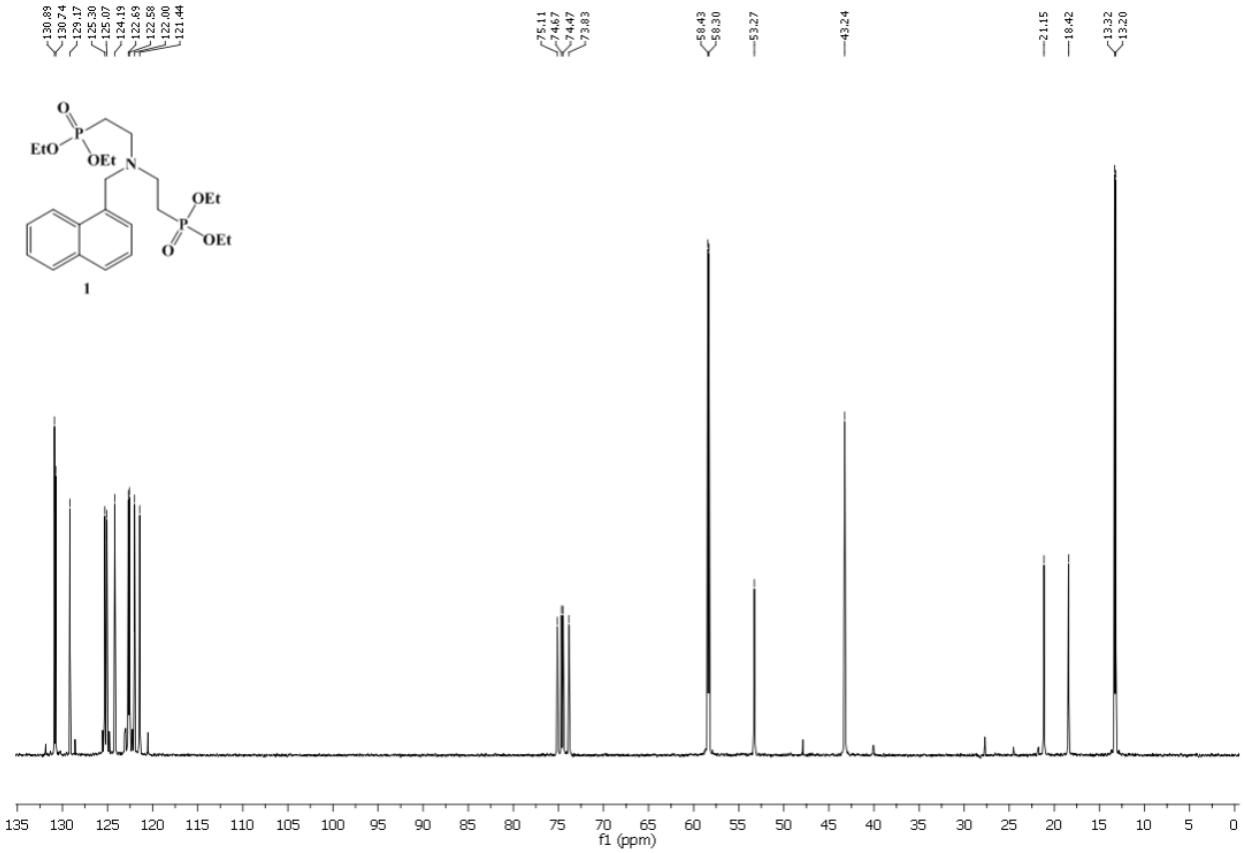

^{1}H NMR spectrum of compound 2 in CD_3OD

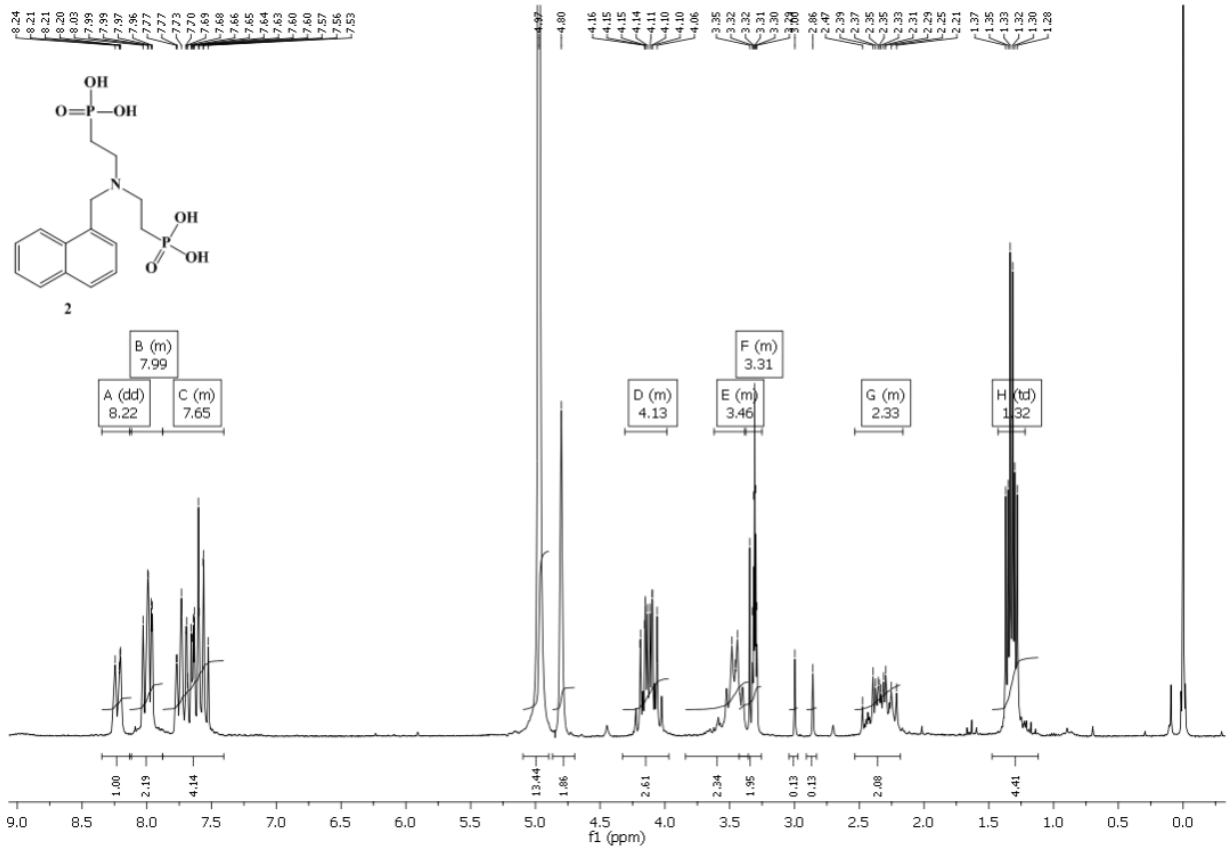

^{13}C NMR spectrum of compound 2 in CD_3OD

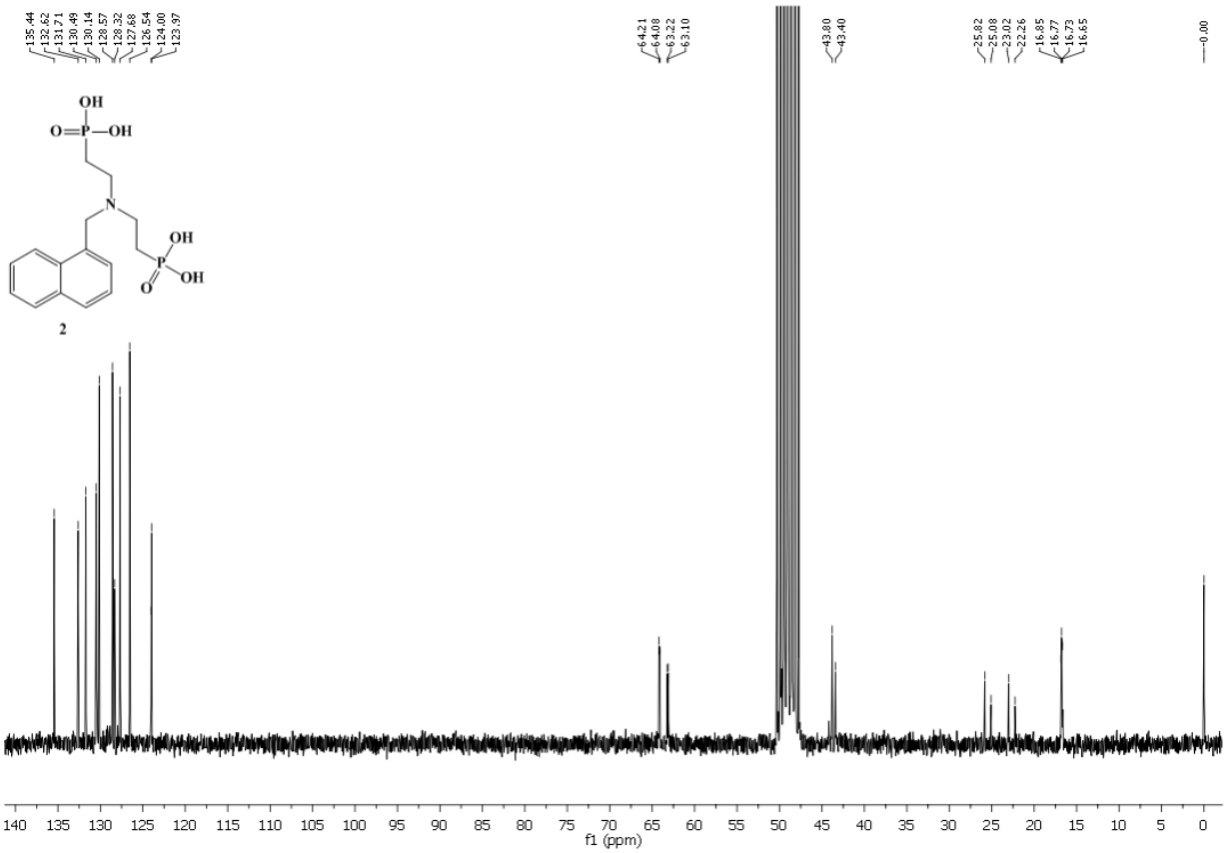

^{1}H NMR spectrum of compound 3 in DMSO d6

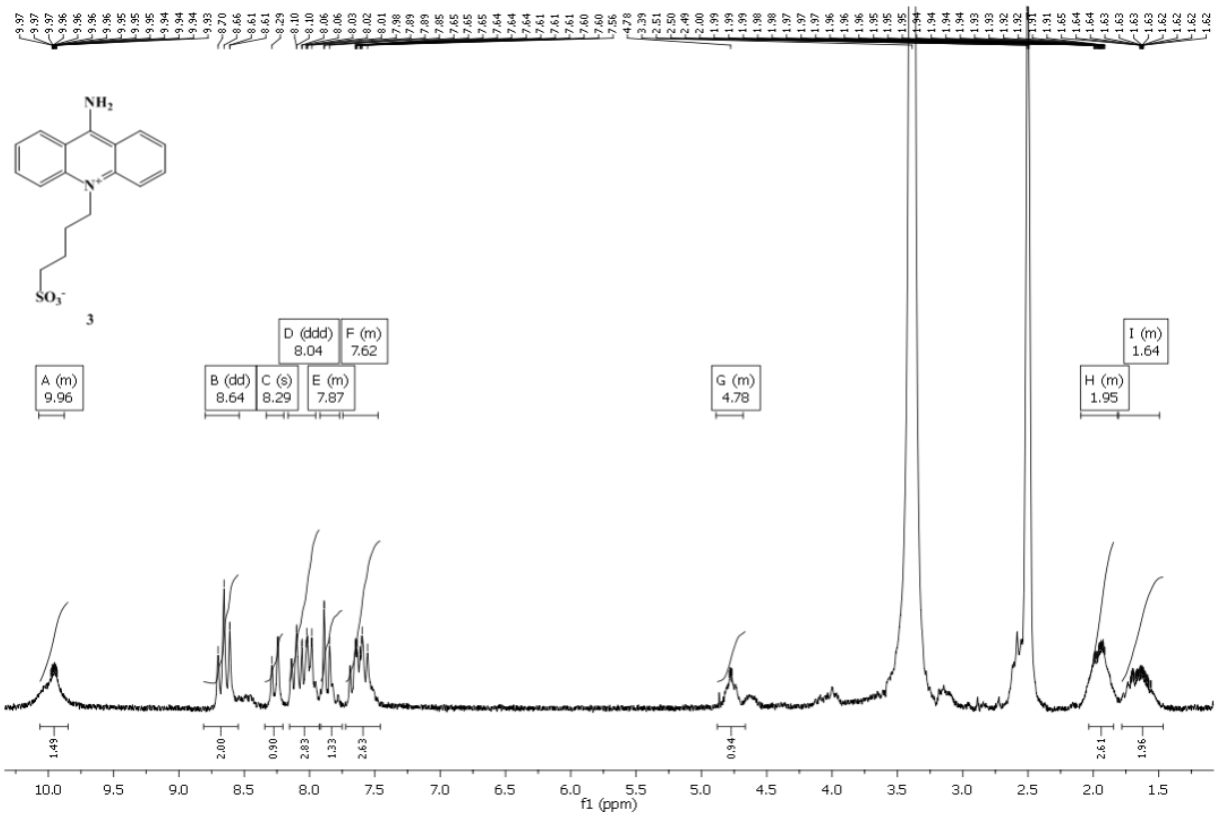

^{1}H NMR spectrum of compound 4 in D_2O

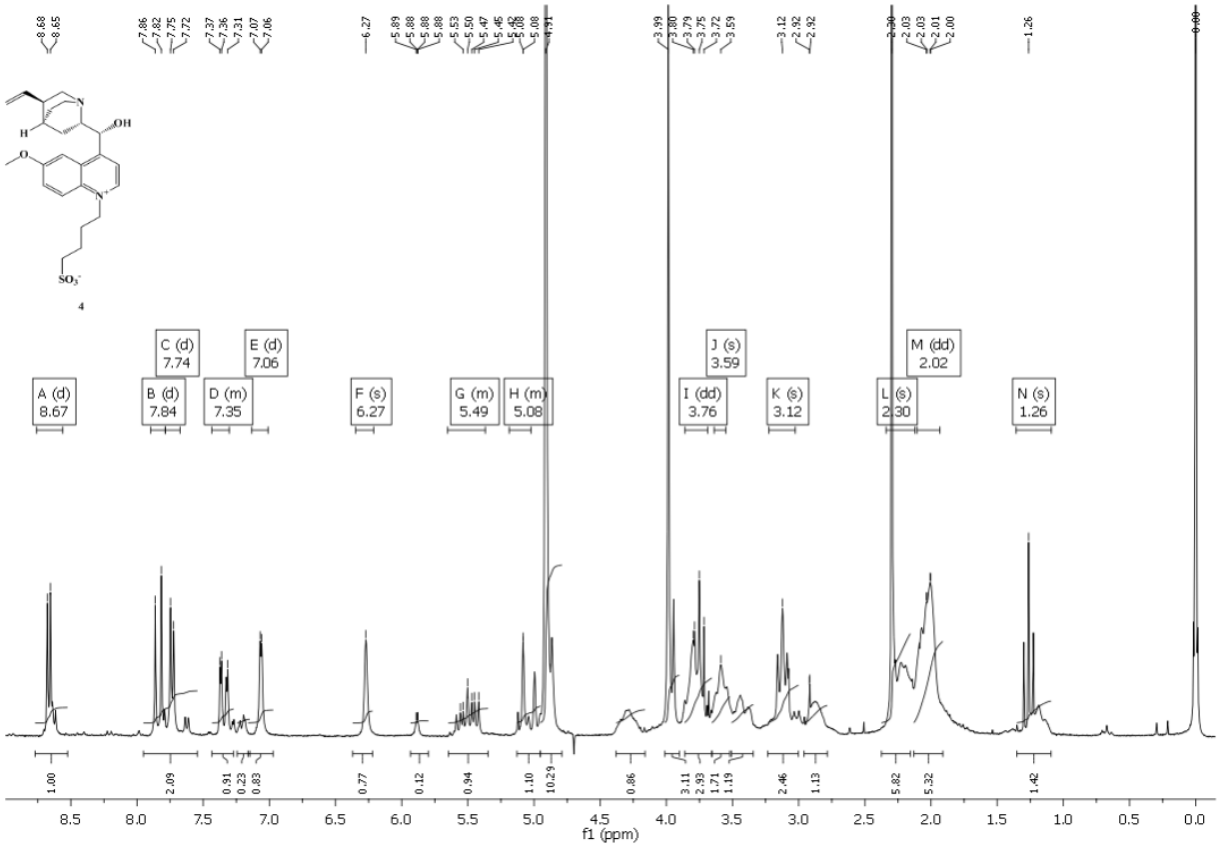

^{1}H NMR spectrum of compound 5 in D_2O

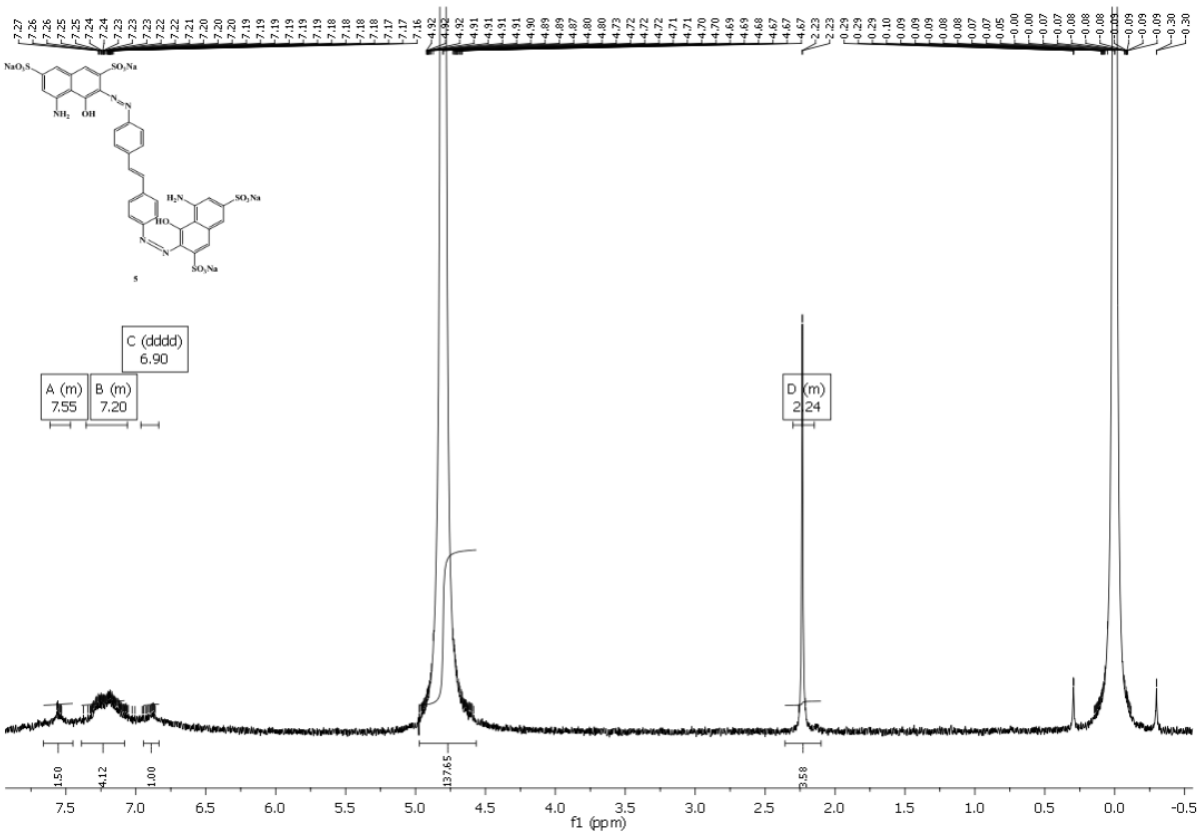

^{1}H NMR spectrum of compound 6 in D_2O

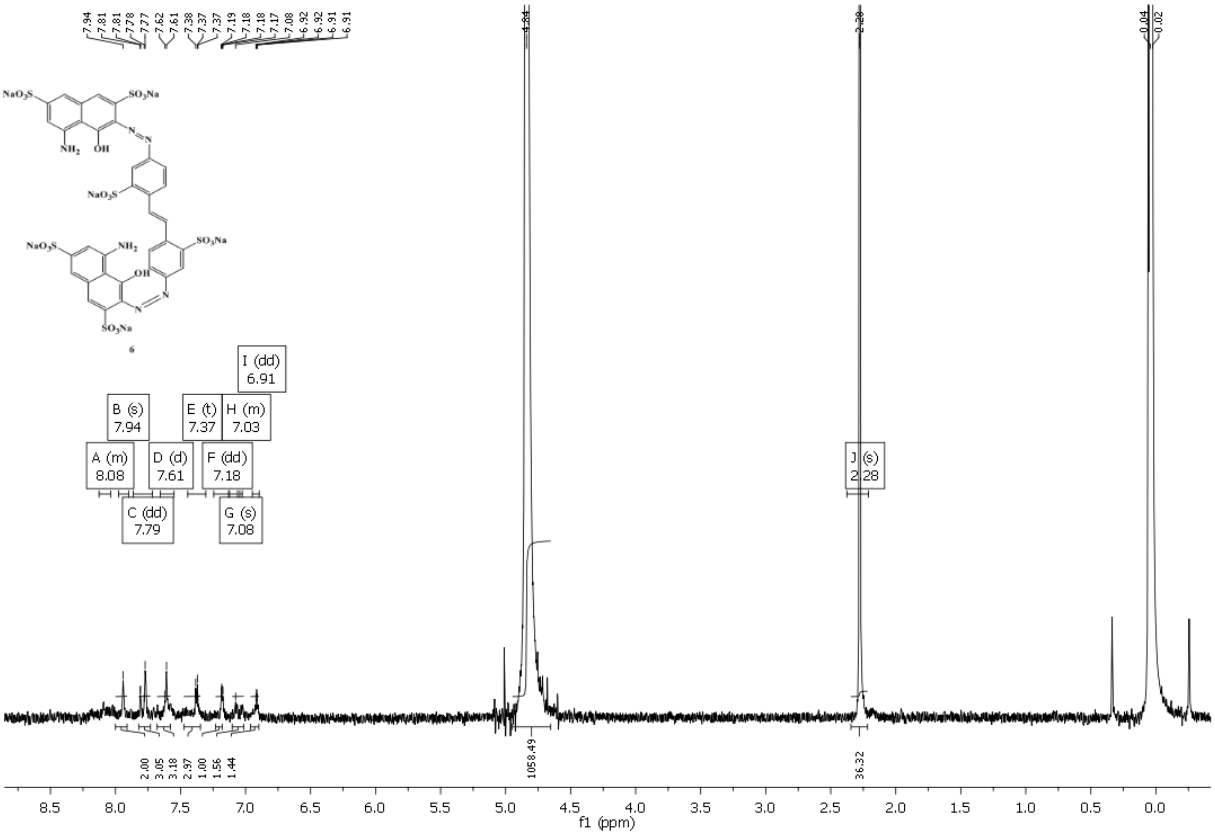

^{1}H NMR spectrum of compound 7 in CD_3OD

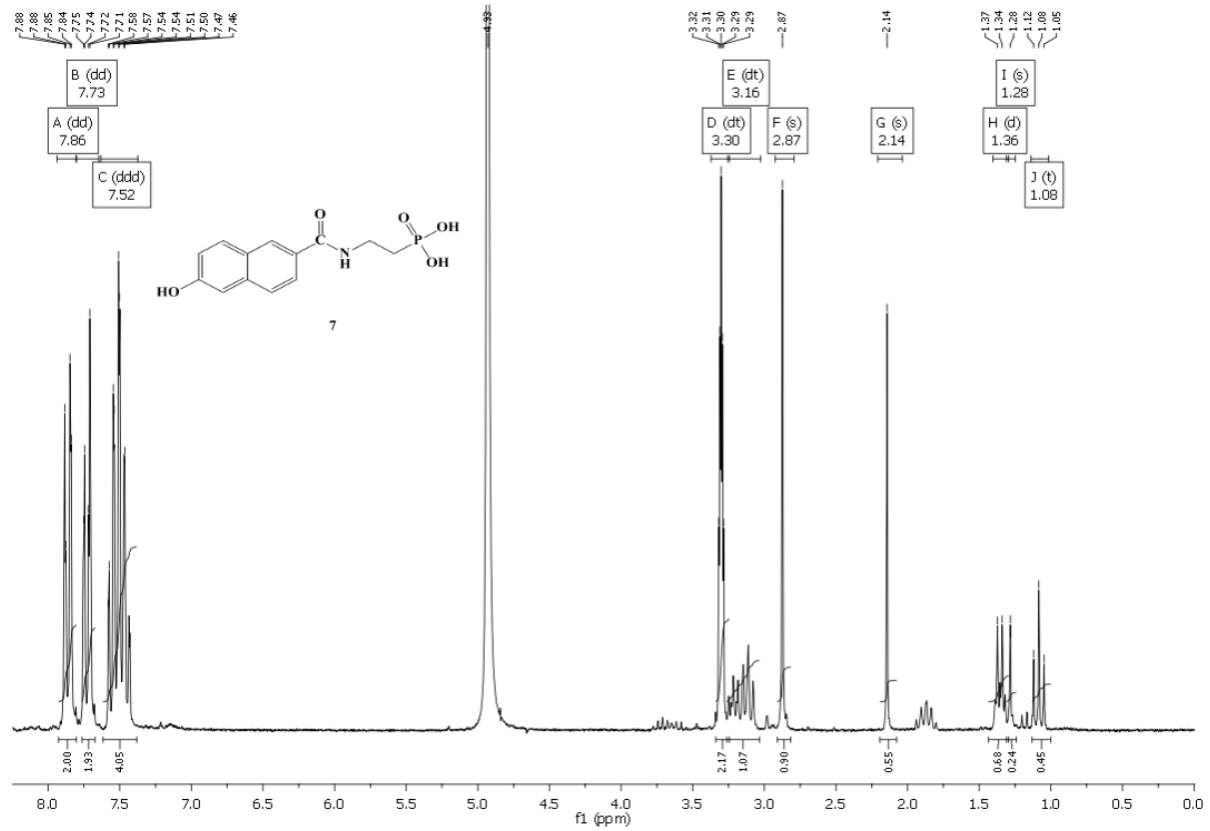

^{1}H NMR spectrum of compound 8 in D_2O

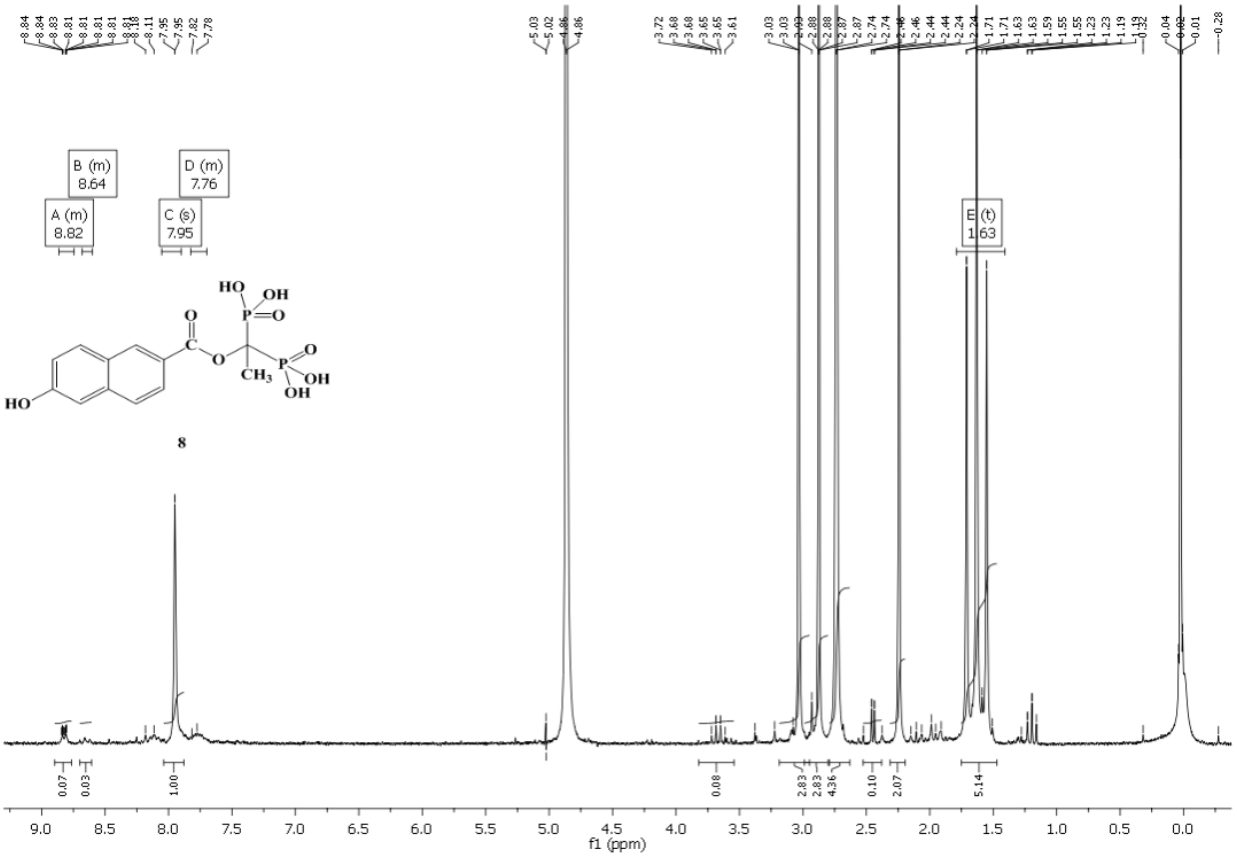

^{1}H NMR spectrum of compound 9 in D_2O

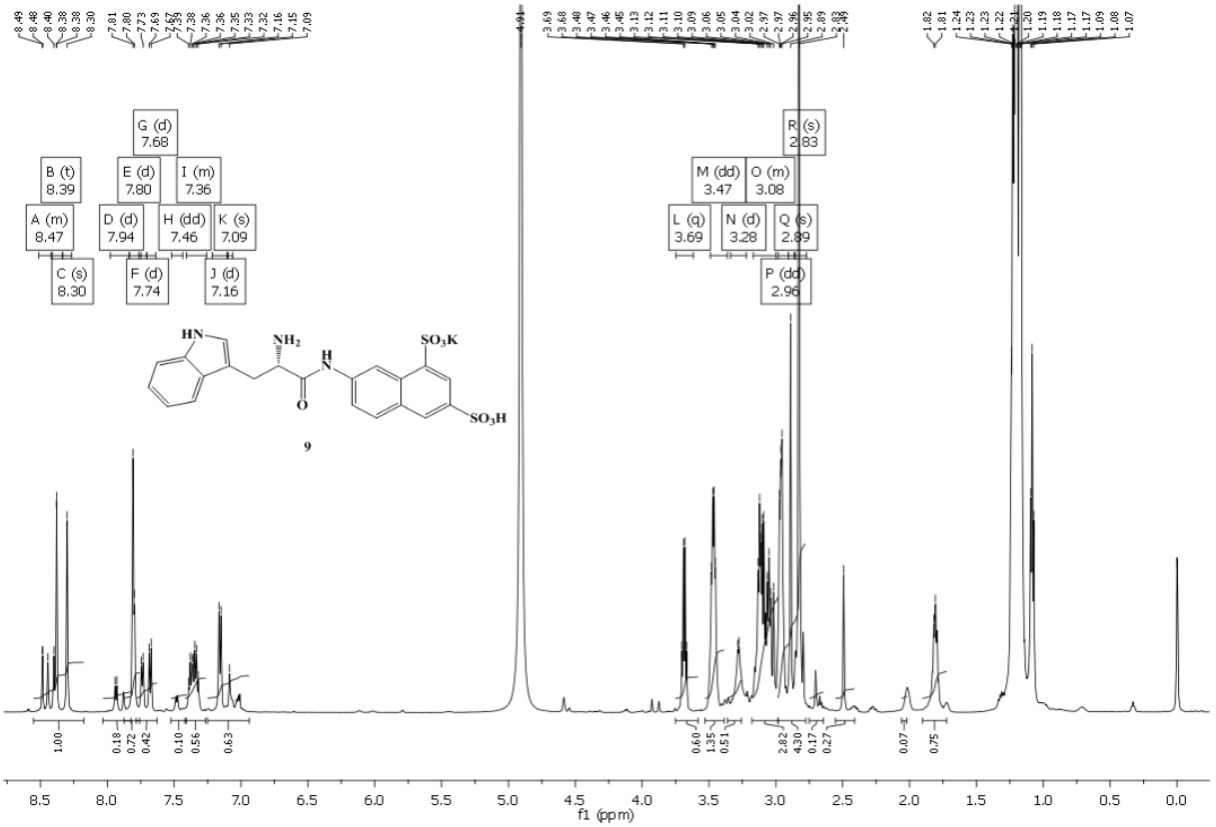

^{1}H NMR spectrum of compound 10 in D_2O

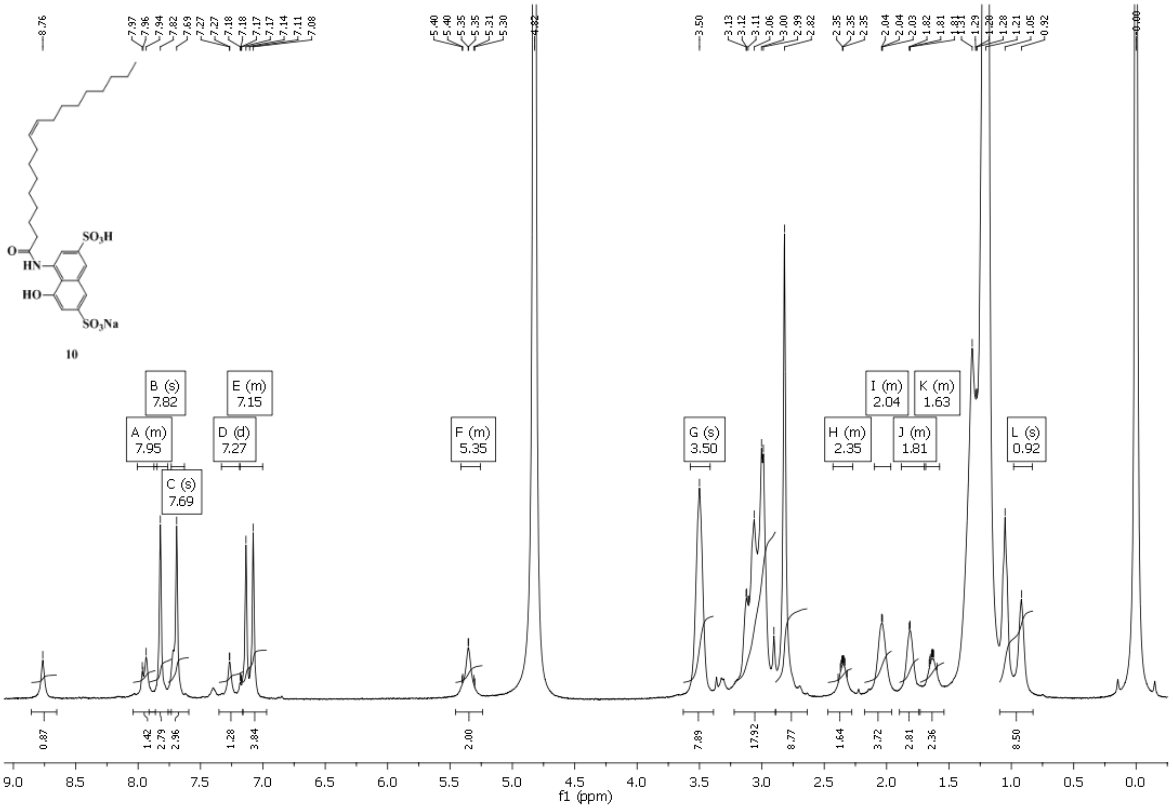

^{1}H-NMR spectrum of compound 11 in D_2O

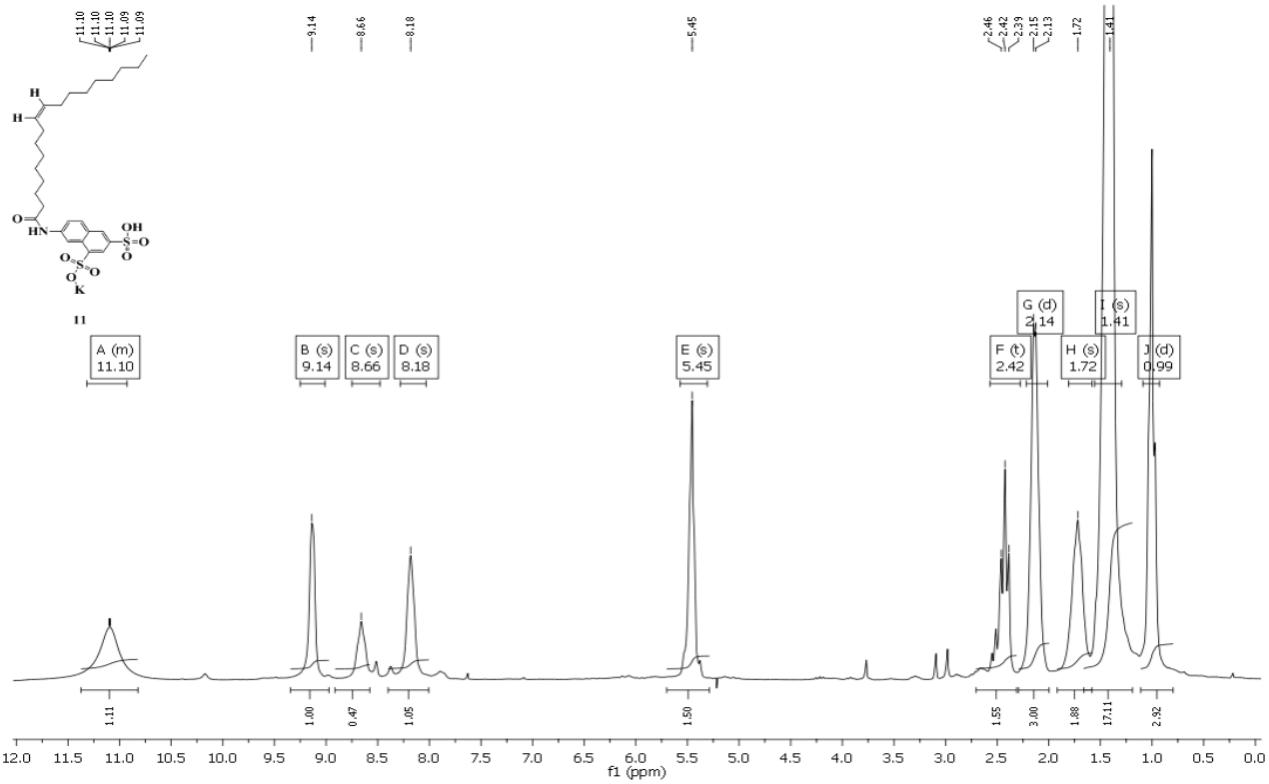

Appendix 2: Fluorescence microscopy of USPIO coated/conjugated with dye

Fluorescence microscopy of RITC and FITC conjugated/coated USPIO

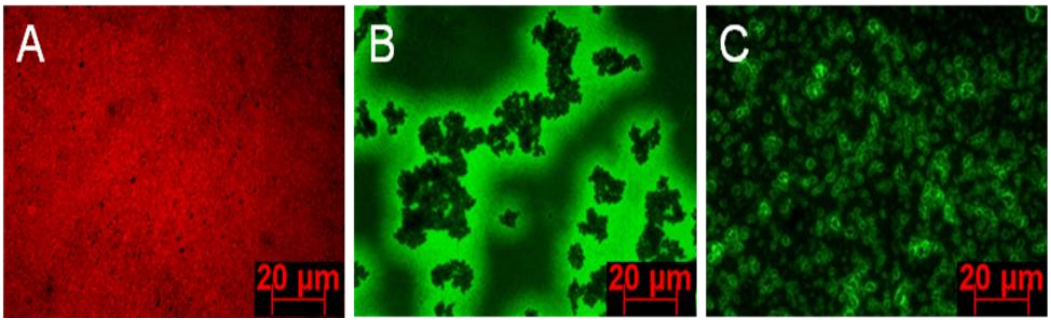

Figure A1. Fluorescence microscopy of dye conjugated USPIO. (A) RITC conjugated to APTMS-USPIO; (B) FITC conjugated to APTMS-USPIO and (C) FITC coated USPIO respectively.

Appendix 3: NUSPIO (Naphthalene USPIO) characterization results

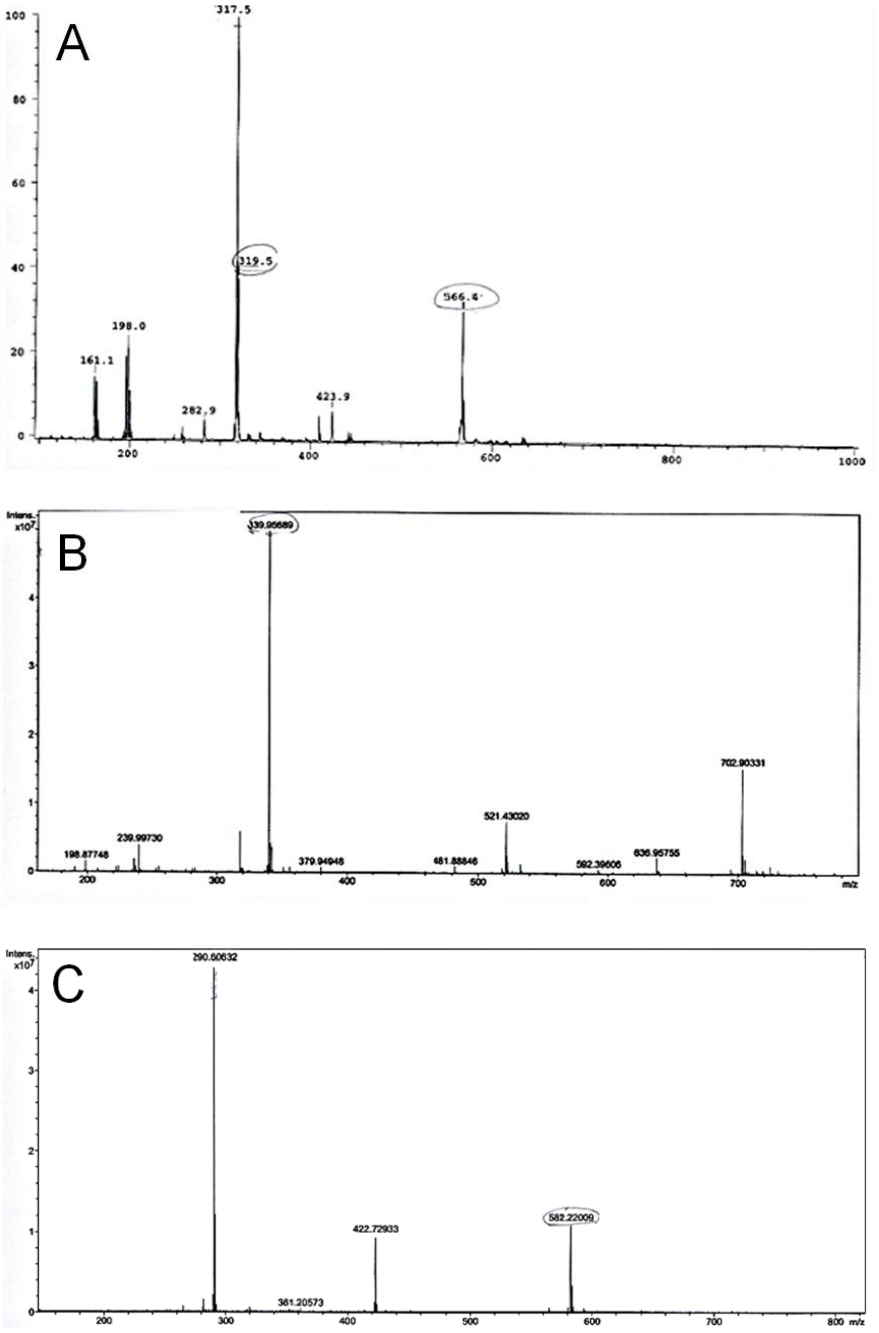

Figure A2. ESI mass spectra of (A) ANDS coupled to oleic acid in pyridine at high temperature (B) H-acid and (C) H-acid coupled to oleic acid respectively.

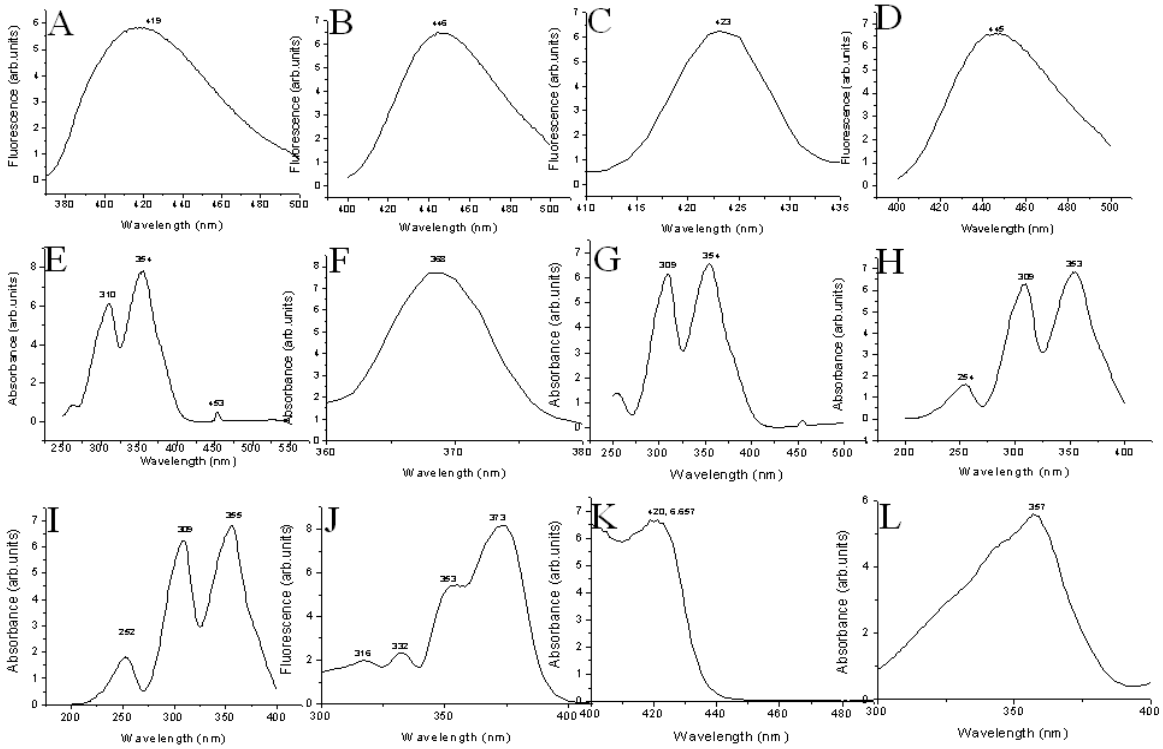

Figure A3. Fluorescence spectra recorded in water for (A) NUSPIO (H-acid) purified by dialysis against water and by exchange through basic resin, (B) NUSPIO (ANDS), (C) Napthol blue black and (D) ANDS were recorded in water. Absorption spectra recorded in water for (E) ANDS, (F) Napthol blue black, (G) NUSPIO (ANDS), (H) NUSPIO (H-acid, 40mmol/mL) purified by dialysis against water, (I) NUSPIO (H-acid, 40 mmol/mL) purified by resin exchange, (J) H-acid, (K) 4-(9-aminoacridinium-10-yl)butane-1-sulfonate and (L) NUSPIO (H-acid) purified by dialysis against water and PBS buffer respectively.

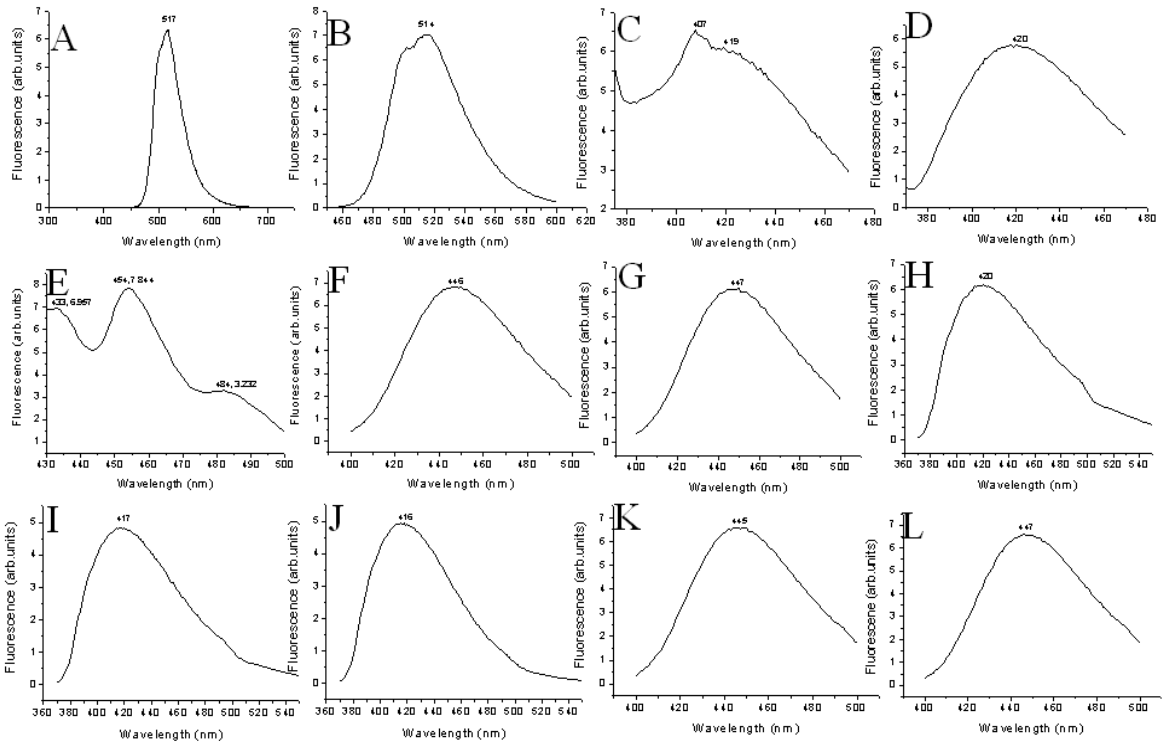

Figure A4. Fluorescence spectra recorded in water for (A) pyrene trisulfonic acid excited at 328 nm, (B) pyrene trisulfonic acid excited at 460 nm, (C) NUSPIO (H-acid) purified by dialysis against water and HEPES buffer, (D) NUSPIO (H-acid) purified by dialysis against water and PBS buffer, (E) 4-(9-aminoacridinium-10-yl) butane-1-sulfonate, (F) NUSPIO (H-acid) purified by dialysis against water and 0.15 M NaCl solution, (G) NUSPIO (H-acid) purified by dialysis against water and 0.15 M glucose solution, (H) H-acid excited at 300 nm, (I) H-acid excited at 340 nm, (J) H-acid excited at 360 nm, (K) NUSPIO (H-acid, 40 mmol/mL) purified by resin exchange method and (L) NUSPIO (H-acid, 40 mmol/mL) purified by dialysis against water respectively.

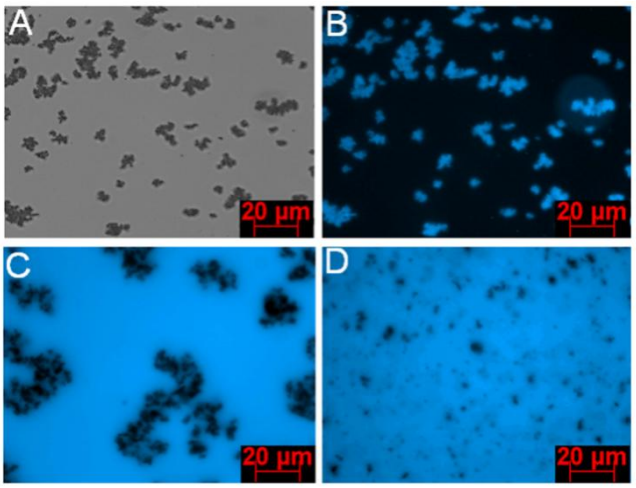

Figure A5. Bright field image of USPIO coated with ANDS (A); fluorescence image of USPIO coated with ANDS (B); fluorescence image of NUSPIO (H-acid) purified by dialysis against water and PBS buffer (C); fluorescence image of NUSPIO (H-acid) and dialysed against water and HEPES buffer respectively.

Appendix 4: FLUSPIO characterization results

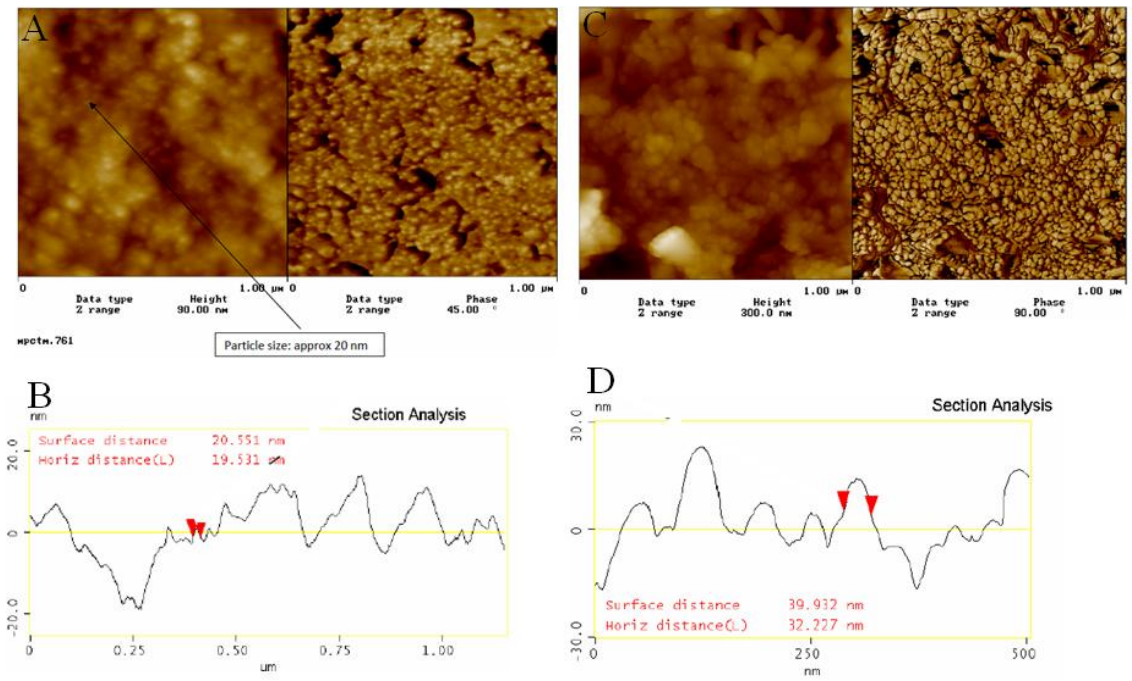

Figure A6. AFM images and size distribution of USPIO (A and B) and FLUSPIO (C and D). The size of the nanoparticles is close to the size of the AFM probe (near the resolution limit) which limits the accuracy of the size measurements of the individual nanoparticles. The particle size of USPIO is within the range 10-50 nm (B) and coincides well with TEM images. The particle size of FLUSPIO (with more defined particulate morphology) was approximately 20-40 nm respectively.

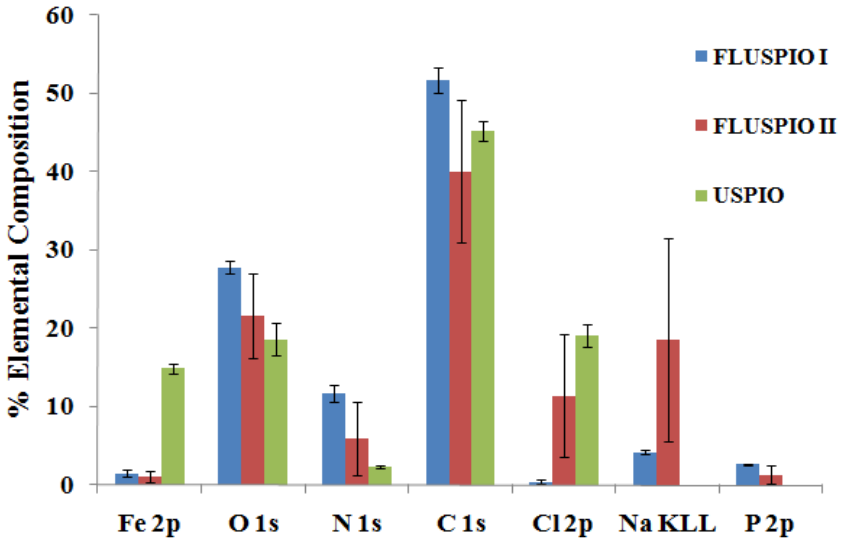

Figure A7. X-ray photoelectron spectroscopy (XPS) results of USPIO, FLUSPIO 1 (35 mM FMN) and FLUSPIO 2 (50 mM FMN). A higher percentage of iron was observed on uncoated sample (USPIO) and interestingly there is some iron still visible on the coated samples at about 1 atomic weight percentage for FLUSPIO. Carbon and chlorine are detected on uncoated samples respectively.

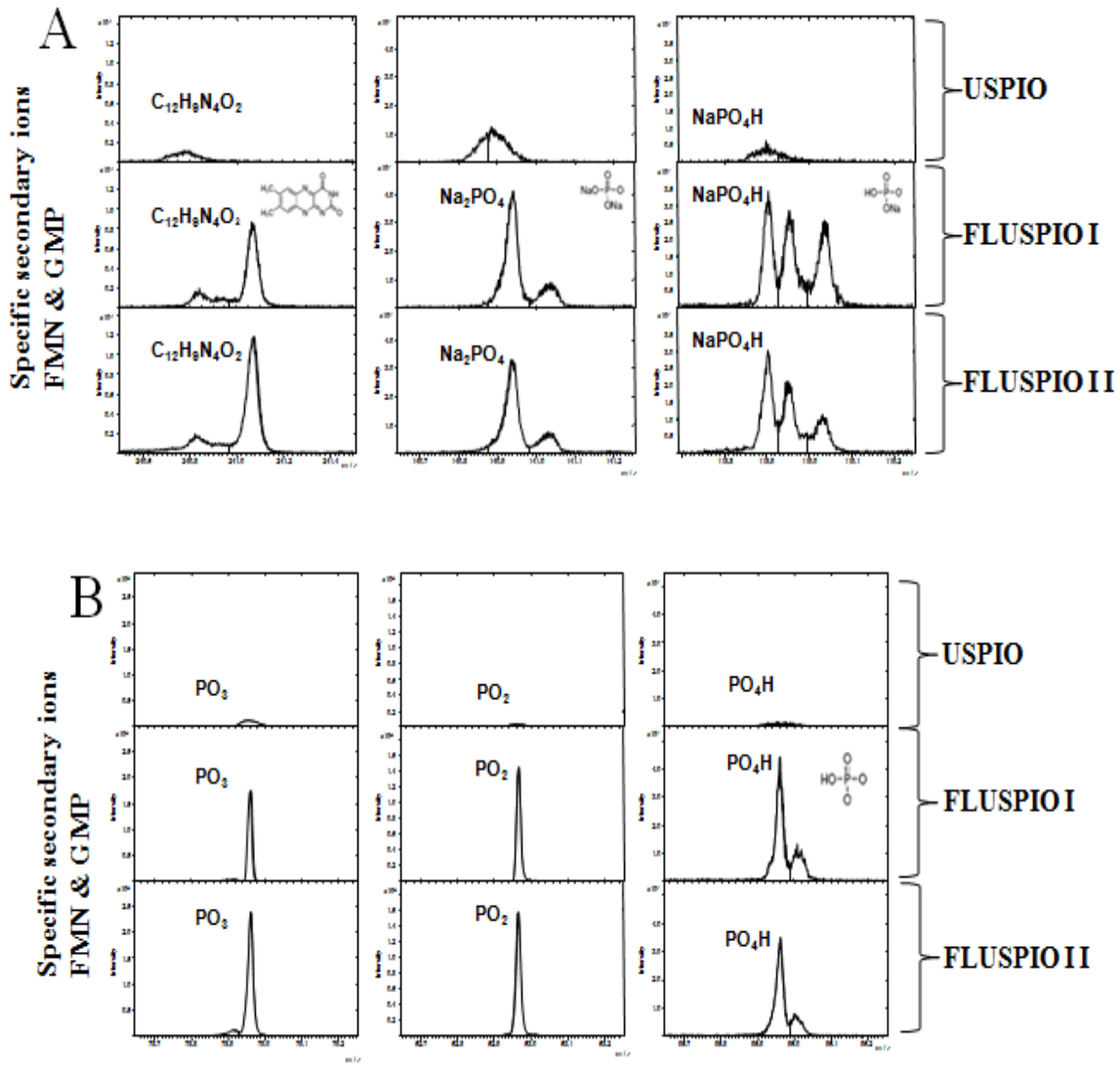

Figure A8. TOF-SIMS measurements displayed specific secondary ions for GMP and FMN from FLUSPIO (A and B) compared to the uncoated USPIO. Further, FLUSPIO displayed peaks for phosphate groups and some higher mass fragments appearing at slightly different strengths on two different coated samples (FLUSPIO I (35 mM FMN) and FLUSPIO II (50 mM FMN)). In close agreement with XPS, the uncoated USPIO showed a much stronger FeO peak respectively.

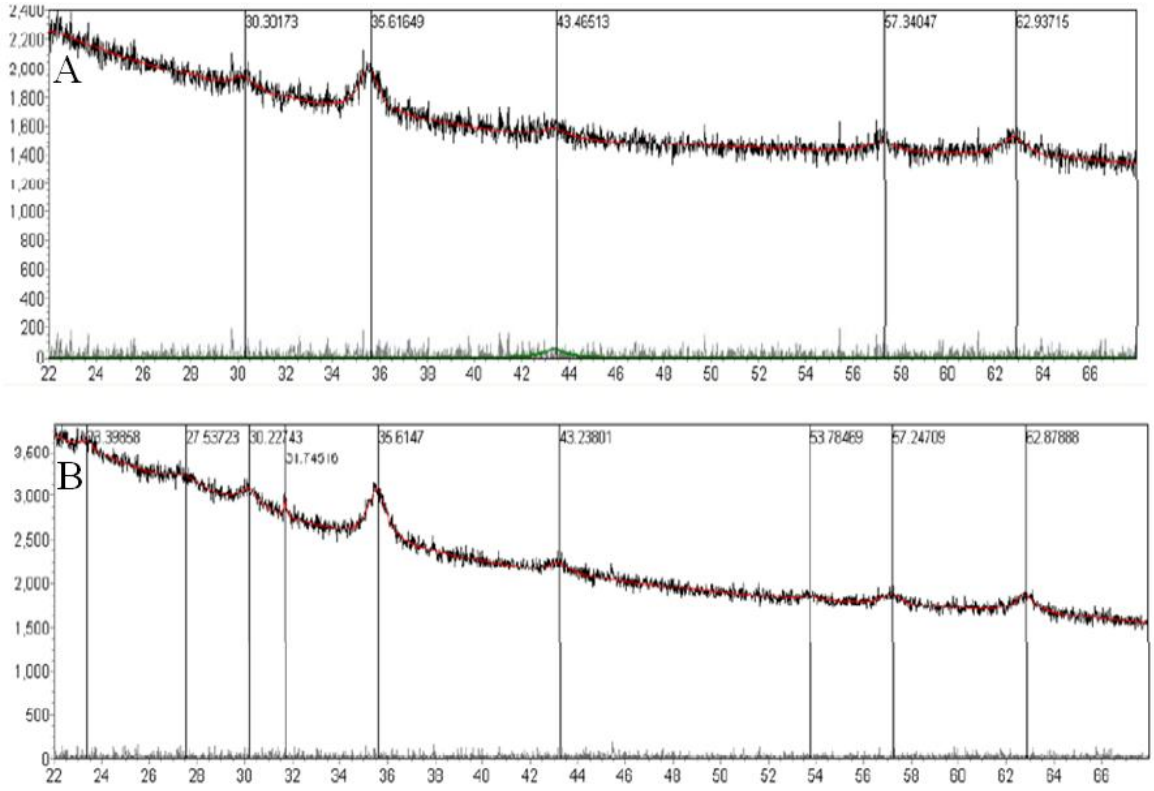

Figure A9. Experimental XRD patterns of USPIO (black, A) and FLUSPIO (black, B) with a calculated XRD of observed peaks (red) respectively.

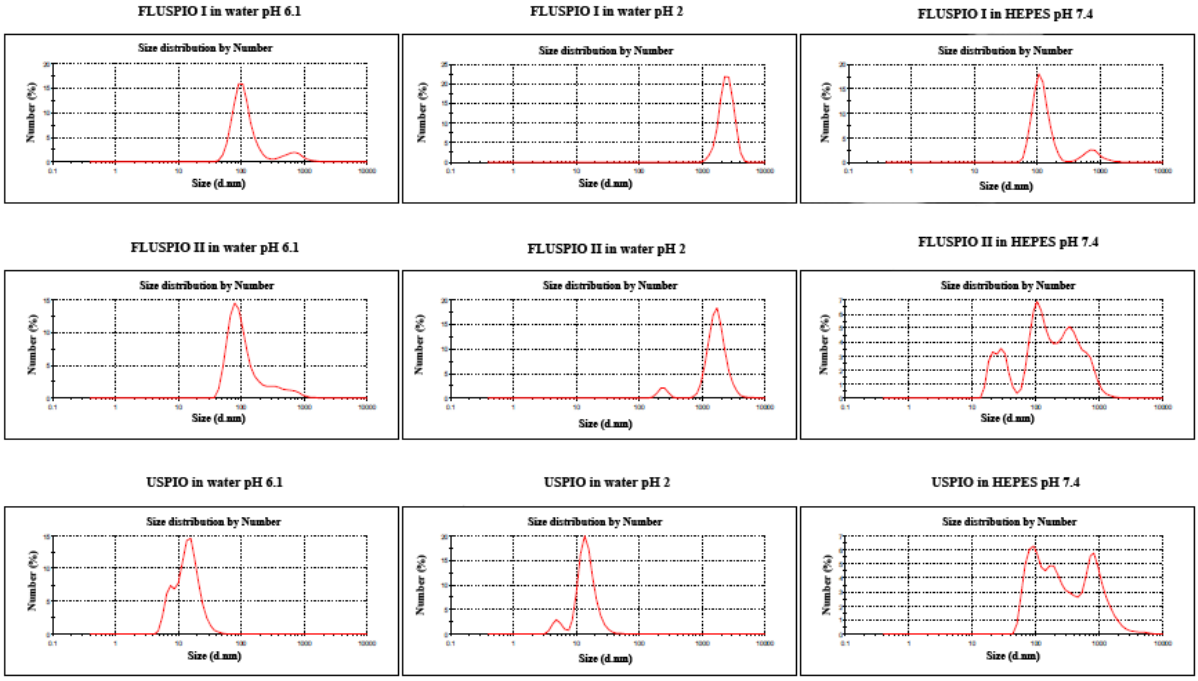

Figure A10. DLS size distribution by number for USPIO, FLUSPIO I (35 mM FMN), FLUSPIO II (50 mM FMN) at different pH (2.0, 6.1 and 7.4) respectively.

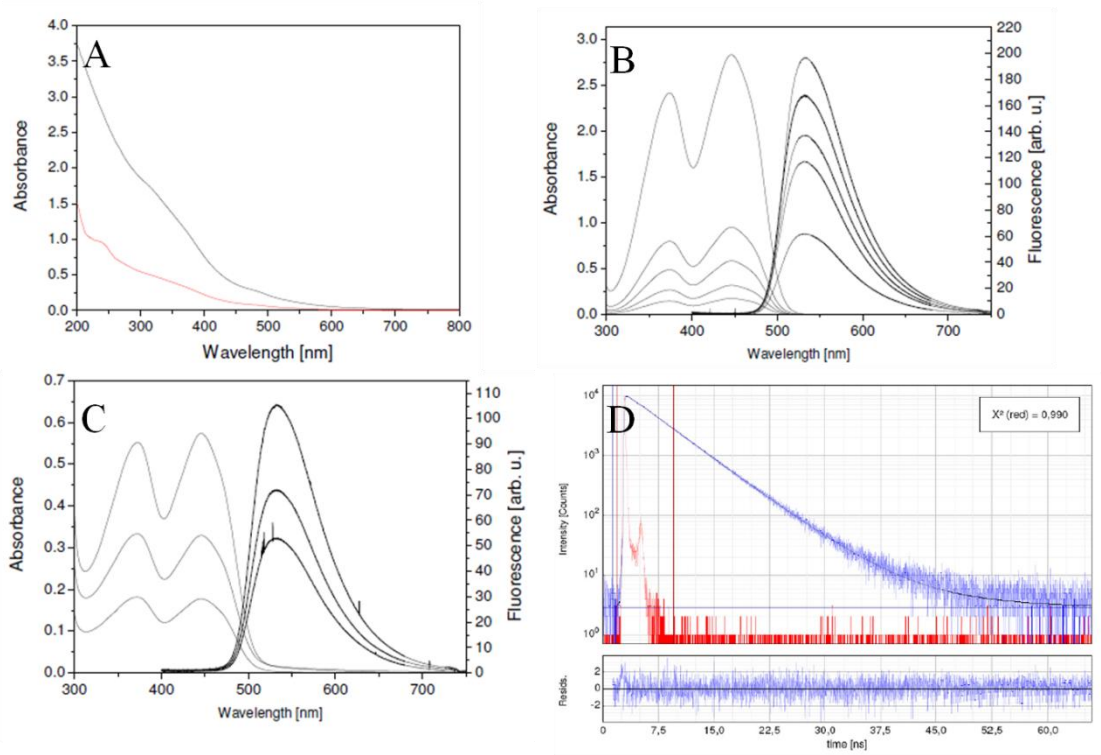

Figure A11. Absorption, fluorescence and fluorescence lifetime measurements of USPIO, FMN, FLUSPIO respectively. Absorbance of USPIO (A), absorbance and fluorescence of FMN (B), absorbance and fluorescence of FLUSPIO (C) and fluorescence lifetime measurements of FLUSPIO (D) respectively. The absolute quantum yield of free FMN and FMN on FLUSPIO is about 21% and the fluorescence lifetime of FMN and FMN on FLUSPIO is about 4.8 ns respectively.

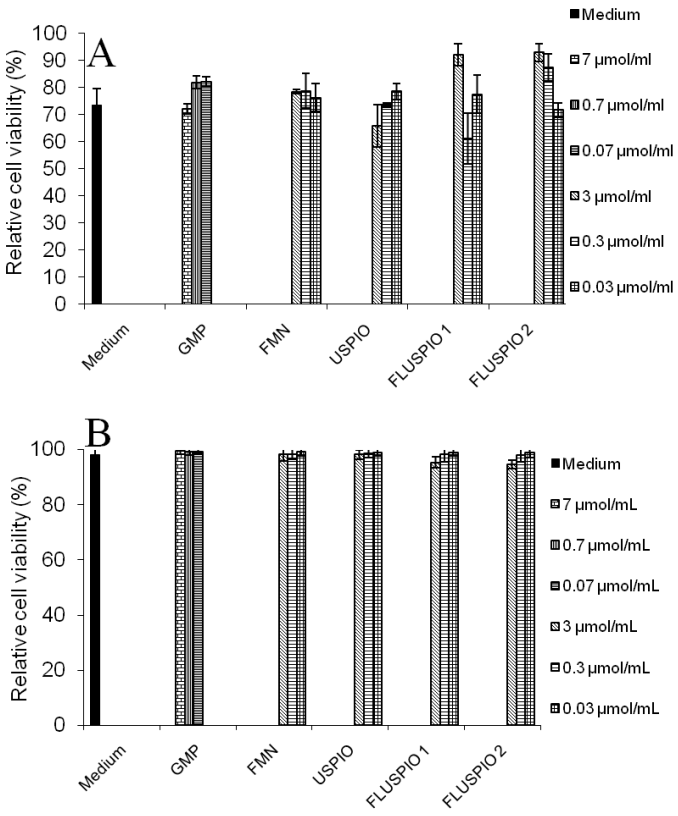

Figure A12. Trypan blue staining results for FLUSPIO 1 (35 mM FMN) and FLUSPIO 2 (50 mM FMN) incubated with HUVEC in two different time points respectively. Trypan blue staining did not show any relevant loss in cell viability after (A) 3 h incubation and (B) 24 h incubation with FLUSPIO at the respective cell labeling concentrations (0.3 µmol Fe/mL).

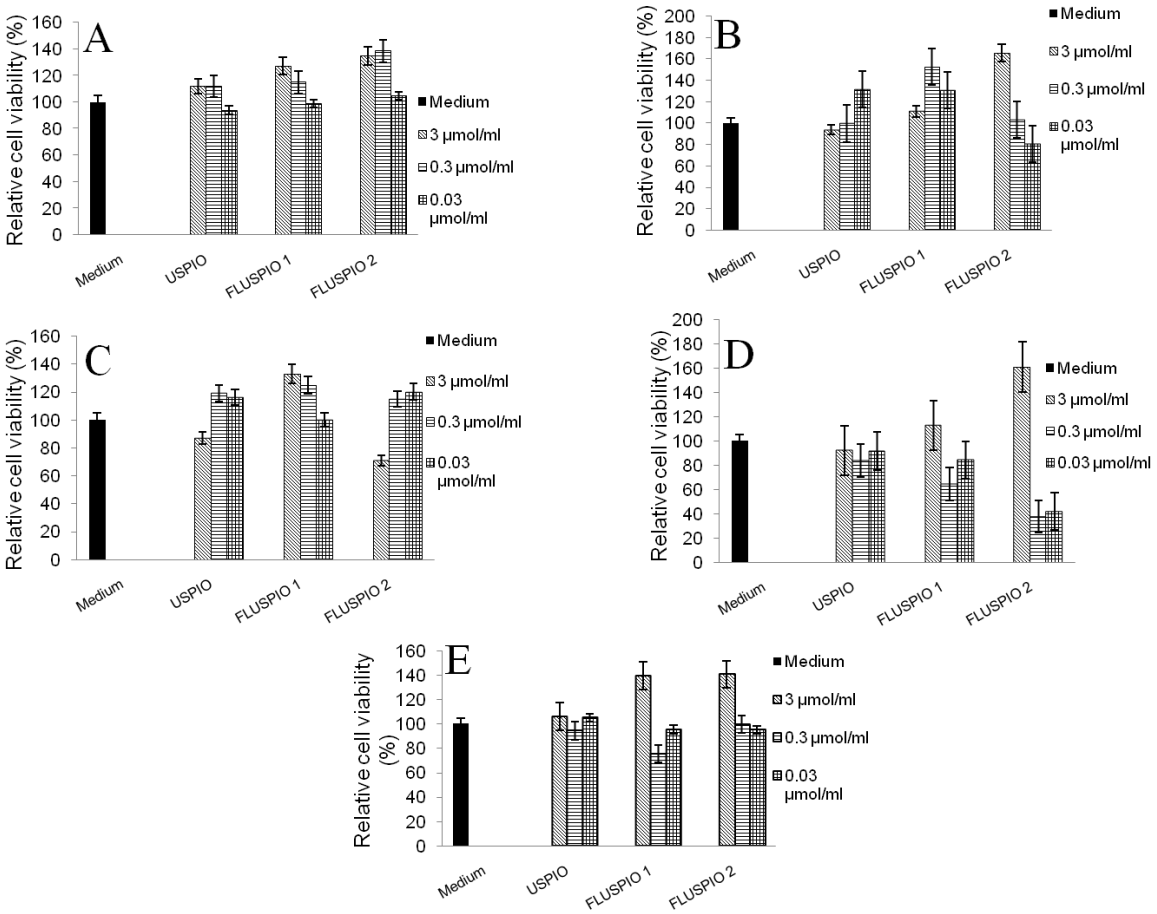

Figure A13. Results from direct cell viability counting experiments did not display any relevant loss in cell viability of PC-3 cells after incubation with FLUSPIO 1 (35 mM FMN) and FLUSPIO 2 (50 mM FMN) at different time points respectively. PC-3 cells (10^5 cells) were incubated for (A) 3 h (B) 12 h (C) 24 h (D) 48 h and (E) 72 h respectively with three different concentrations of FLUSPIO (3.0, 0.3. 0.03 µmol Fe/mL) respectively.

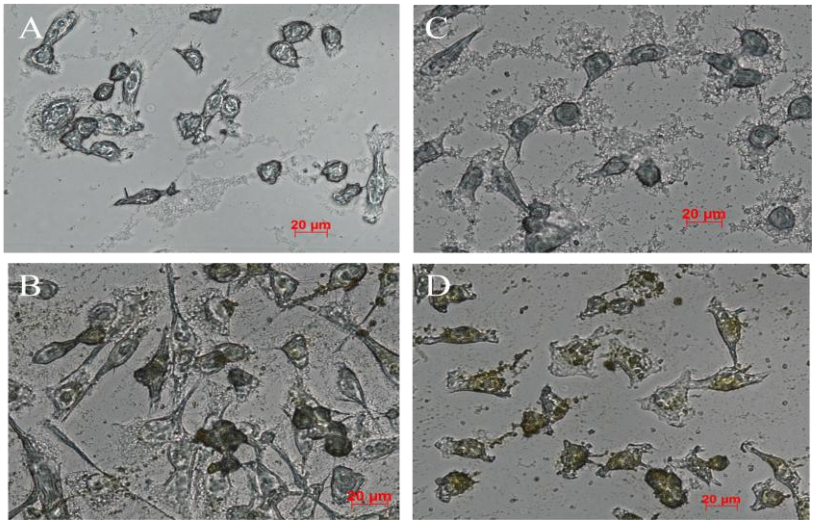

Figure A14. Bright field images of PC-3 and DU-145 incubated (3 h) with FLUSPIO (3.0 µmol Fe/mL) respectively. Bright field images of PC-3 incubated (A) growth medium (B) FLUSPIO. Bright field images of DU-145 incubated with (C) growth medium (D) FLUSPIO. The bright field images clearly show the high uptake of FLUSPIO in both prostate cancer cell types respectively.

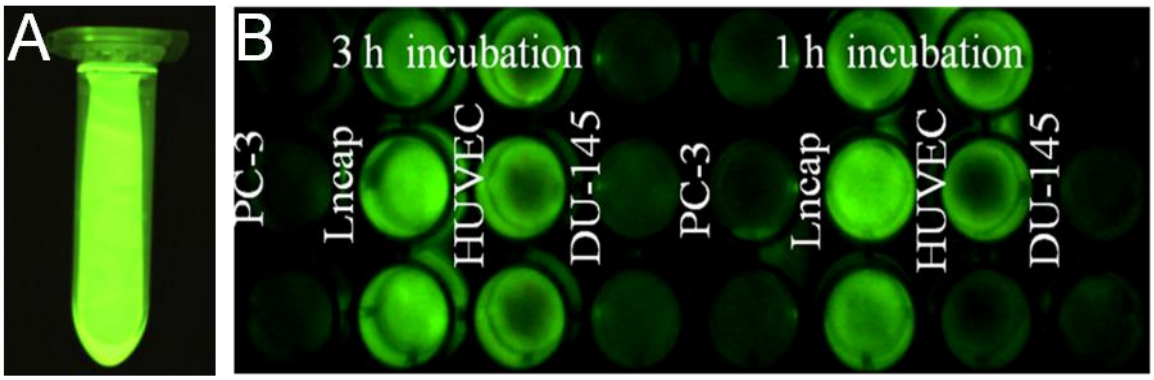

Figure A15. Fluorvivo Indec system (optical imaging) images of (A) FAD USPIO in 5% glucose solution and (B) FLUSPIO cellular uptake (incubated for 1 h and 3 h) in three different prostate cancer cells (PC-3, LnCap, DU-145) and activated endothelial cell line (HUVEC) suspended in 10% gelatin after MRI measurements respectively.

Erklärungen gemäß § 8 (3) b) und c) der Promotionsordnung:

a) ich erkläre hiermit, dass ich die vorgelegte Dissertation selbst verfasst und mich keiner anderen als der von mir ausdrücklich bezeichneten Quellen und Hilfen bedient habe
b) ich erkläre hiermit, dass ich an keiner anderen Stelle ein Prüfungsverfahren beantragt bzw. die Dissertation in dieser oder anderer Form bereits anderweititg als Prüfungsarbeit verwendet oder einer anderen Fakultät als Dissertation vorgelegt habe.

Heidelberg, 18. August 2011 ----------

(Jabadurai Jayapaul)

Biomaterials 32 (2011) 5863–5871

Contents lists available at ScienceDirect

Biomaterials

journal homepage: www.elsevier.com/locate/biomaterials

FMN-coated fluorescent iron oxide nanoparticles for RCP-mediated targeting and labeling of metabolically active cancer and endothelial cells

Jabadurai Jayapaul [a,c], Michael Hodenius [a], Susanne Arns [a], Wiltrud Lederle [a], Twan Lammers [a,b], Peter Comba [c], Fabian Kiessling [a,*], Jessica Gaetjens [a]

[a] Department of Experimental Molecular Imaging, RWTH Aachen University, Pauwelsstrasse 30, Aachen 52074, Germany
[b] Deparment of Pharmaceutics, Utrecht Institute for Pharmaceutical Sciences, Utrecht University, Sorbonnelaan 16, Utrecht 3584 CA, The Netherlands
[c] Anorganisch-Chemisches Institut,Universität Heidelberg, Im Neuenheimer Feld 270, Heidelberg 69120, Germany

ARTICLE INFO

Article history:
Received 1 March 2011
Accepted 22 April 2011
Available online 24 May 2011

Keywords:
Cell tracking
Flavin mononucleotide
Iron oxide nanoparticles
Magnetic resonance imaging
Molecular imaging
Riboflavin carrier protein

ABSTRACT

Riboflavin is an essential vitamin for cellular metabolism and is highly upregulated in metabolically active cells. Consequently, targeting the riboflavin carrier protein (RCP) may be a promising strategy for labeling cancer and activated endothelial cells. Therefore, Ultrasmall SuperParamagnetic Iron Oxide nanoparticles (USPIO) were adsorptively coated with the endogenous RCP ligand flavin mononucleotide (FMN), which renders them target-specific and fluorescent. The core diameter, surface morphology and surface coverage of the resulting FMN-coated USPIO (FLUSPIO) were evaluated using a variety of physicochemical characterization techniques (TEM, DLS, MRI and fluorescence spectroscopy). The biocompatibility of FLUSPIO was confirmed using three different cell viability assays (Trypan blue staining, 7-AAD staining and TUNEL). *In vitro* evaluation of FLUSPIO using MRI and fluorescence microscopy demonstrated high labeling efficiency of cancer cells (PC-3, DU-145, LnCap) and activated endothelial cells (HUVEC). Competition experiments (using MRI and ICP-MS) with a 10- and 100-fold excess of free FMN confirmed RCP-specific uptake of the FLUSPIO by PC-3 cells and HUVEC. Hence, RCP-targeting via FMN may be an elegant way to render nanoparticles fluorescent and to increase the labeling efficacy of cancer and activated endothelial cells. This was shown for FLUSPIO, which due to their high T_2-relaxivity, are favorably suited for MR cell tracking experiments and cancer detection *in vivo*.

1. Introduction

The vast majority of (pre-)clinically used MR contrast agents based on iron oxide nanoparticles are functionalized with (bio-) polymers like dextran, carboxydextran and polyethylene glycol. However, with few exceptions [1], polymeric coated magnetic nanoparticles are known to display relatively large hydrodynamic diameters and therefore display limitations in tissue penetration, diffusion, bio-distribution and metabolic clearance and might even induce side effects [2,3]. To overcome the afore-mentioned setbacks of polymer coatings, a thin layer of non-polymeric coating using organic biocompatible molecules was introduced in a simple, and straightforward synthetic method [4–6]. Based on the advantages of non-polymeric coatings, we here report for the first time fluorescent and non-polymeric flavin mononucleotide (FMN)-decorated iron oxide nanoparticles as versatile MR contrast agents. FMN and its precursor riboflavin (Rf) mediate various redox reactions that regulate the metabolism of carbohydrates, amino acids and lipids [7]. The cellular uptake of Rf is mediated by a membrane protein known as the riboflavin carrier protein (RCP), which strongly binds and transports Rf into the cell [8,9]. RCP is upregulated in cells with high metabolic activity like tumor cells [10,11] and activated endothelial cells. The current state of the art is that fluoro-2-deoxy-D-glucose (^{18}F-FDG) used for positron emission tomography (PET) imaging is the only clinically approved diagnostic agent for labeling cells with high metabolic activity [12–14]. On that basis, it was reasoned that besides ^{18}F-FDG-uptake, also the uptake of FMN-functionalized probes by RCP could serve as effective metabolic marker for diagnostic (and therapeutic) interventions using non-invasive imaging modalities.

Molecular imaging and cell tracking with magnetic resonance imaging (MRI) are frequently achieved using Ultrasmall Super-Paramagnetic Iron Oxide nanoparticles (USPIO) [15–25]. In this context, a fluorescent label incorporated into the nanoparticles is extremely helpful in detecting the labeled cells and tissues using optical imaging, as well as in histology [26–33]. The spectral

* Corresponding author. Tel.: +49 2418080116; fax: +49 241803380116.
E-mail address: fkiessling@ukaachen.de (F. Kiessling).

0142-9612/$ – see front matter © 2011 Elsevier Ltd. All rights reserved.
doi:10.1016/j.biomaterials.2011.04.056

characteristics of the FMN (display emission at 530 nm) are suboptimal for *in vivo* fluorescence imaging due to the green autofluorescence, high scattering and low penetration of photons into tissues that is prevalent in this spectral range. However, FMN conjugated USPIO could be evidently used for co-validation of the MR findings through histology. Therefore, the aim of this study was to develop a hybrid optical (for invasive clinical interventions) and MR probe targeting RCP, based on FMN-functionalized USPIO which specifically accumulates in cells with high metabolic activity.

To this end, USPIO cores were prepared by co-precipitation of iron salts in aqueous base at ambient temperature [34]. USPIO nanoparticles were adsorptively coated with non-polymeric fluorescent FMN in two steps, to yield FLUSPIO (Fluorescent Ultrasmall SuperParamagnetic Iron Oxides). FLUSPIO were purified by high-gradient magnetophoresis to generate a stable colloidal suspension which showed intense green fluorescence under ultraviolet irradiation. This versatile and simple synthetic strategy yields very stable magnetic nanoparticles with an intense fluorescence and does not require the use of colloidal stabilizers, such as citric acid, surfactants or polyethylene glycol (PEG). FLUSPIO were evaluated for their efficiency in MR cell labeling, and their specificity for RCP was studied in metabolically active cancer and endothelial cells by competitively blocking the upregulated RCP receptors.

2. Materials and methods

2.1. Materials

Ferric chloride ($FeCl_3$ >97 %), ferrous chloride tetrahydrate ($FeCl_2.4H_2O$ >99%), Riboflavin-5′-monophosphate sodium salt dihydrate (Flavin mononucleotide FMN, 73–79% (fluorimetric)), Trypan blue solution for microscopy, IDRANAL III standard solution ((EDTA-Na_2), reagent for metal titration, 0.1 M), 5-sulfo salicylic acid dehydrate (≥99% for metal titration), N-[Tris(hydroxymethyl)methyl]-2-aminoethanesulfonic acid sodium salt (TES, ≥99%), potassium bromide (KBr for IR spectroscopy) were purchased from Sigma Aldrich (Steinheim, Germany). Ammonia (NH_3 ≥25%), 4-(2-Hydroxyethyl)piperazine-1-ethanesulfonic acid, N-(2-Hydroxyethyl)piperazine-N′-(2-ethanesulfonic acid) (HEPES, ≥99.5 %), tris(hydroxymethyl) aminomethane (Tris HCl, ≥99.3%), hydrochloric acid (HCl, 37%) were purchased from Carl Roth (Karlsruhe, Germany). Guanosine-5′-monophosphate disodium salt hydrate (GMP, 98%) was purchased from AppliChem (Darmstadt, Germany). All chemicals were used without further purification.

2.2. Synthesis of iron oxide nanoparticles(Fe_3O_4)

Ultrasmall SuperParamagnetic Iron Oxide nanoparticles (USPIO) were synthesized by co-precipitation of ferrous (Fe^{2+}) and ferric (Fe^{3+}) salts in aqueous alkaline conditions. A modified one-pot synthesis protocol was followed [33]. We used a stoichiometric ratio of $2Fe^{3+}$:Fe^{2+}, 16 mmol (2.66 g) of $FeCl_3$ and 8 mmol (1.63 g) of $FeCl_2.4H_2O$ which was dissolved in 190 mL de-ionized water at RT by magnetic stirring for 10 min. Under vigorous stirring, 10 mL of 25% NH_3 were poured down the vortex of the iron solution. Immediately, magnetite formed a black precipitate. After stirring for 20 min, the particles were washed thrice with water and two times with 0.1 M HCl solution by magnetic separation using a rare-earth magnet. Magnetic fluids were dispersed in 100 mL of aqueous hydrochloric acid (0.1 M). The USPIO were sonicated for 20 min at RT. Subsequently, USPIO were centrifuged at 20,000 g for 15 min at RT in order to remove aggregates. Iron content of USPIO was determined by a titration method, in which magnetic particles were dissolved in 0.5 M HCl solution and oxidized using $(NH_4)S_2O_8$ to Fe^{3+}. The dissolved Fe^{3+} metal ions form a red complex with sulfo salicylic acid which is titrated with EDTA (Idranal III standard solution) to give yellow color as end point. The total iron concentration of USPIO determined by titrimetry [35] and colorimetry (tiron method) [36] was 161 mM. A colorimetric method was used to confirm the results from titrimetry.

2.3. Synthesis of FLUSPIO nanoparticles

Fluorescent Ultrasmall Superparamagnetic Iron Oxide nanoparticles (FLUSPIO) were synthesized by coating a thin layer of organic biocompatible molecules around the iron oxide core in a non-polymeric way [3]. We used flavin mononucleotide (FMN) as fluorescent and guanosine monophosphate (GMP) as non-polymeric coating molecules. Non-polymeric coating was performed by sonication (Ultrasonic cleaner, 30 W, VWR GmbH, Germany) of 143 mM USPIO with 35 mM FMN for 1 h at ambient temperature. Excess FMN was removed by high-gradient magnetophoresis. FMN modified particles were sonicated with 50 mM GMP for another 1 h at ambient temperature. Excess of GMP was removed by high-gradient magnetophoresis to yield the final fluorescent FLUSPIO nanoparticles.

2.4. General characterization - Transmission electron microscopy (TEM)

The morphology, size, and size distribution of the nanoparticles were characterized by TEM (EM 400 T (Philips, Eindhoven, The Netherlands). USPIO and FLUSPIO were embedded in 2% agarose, rinsed with distilled water and dehydrated with ethanol (30%, 50%, 70%, 90%,100%). Subsequently, they were embedded in Epon, polymerized 8 h at 37 °C, 56 h at 60 °C, and then cut into 70–100 nm thick slices. The particle size and size distributions were calculated using an image analysis program (iTEM software, Olympus, Germany) and by measuring the diameter of at least 100 particles.

2.4.1. Scanning electron microscopy (SEM)

The surface morphology of the nanoparticles was characterized by SEM [FEI (PHILIPS) ESEM XL 30 FEG; EDAX Falcon genesis]. USPIO and FLUSPIO in water were dried by dehydrating them with different percentages of ethanol (25%, 50%, 70–75%, 90–95%, 100%). Finally, trace amounts of water were removed by treating them with propylene oxide. Further, samples were dried and mounted on specimen stub with silver paste or graphite.

2.4.2. X-ray powder diffraction (XRD)

The crystal structures of the USPIO and FLUSPIO particles were characterized by using the Bruker D8 Advance x-ray powder diffractometer equipped with a monochromatic x-ray source (Cu$K\alpha_1$ 1.5406 Å) and calibrated against NIST1976 Corundum Standard Reference Material. Scans were recorded from 2 to 85° (2θ), with a 0.02° (2θ) step and a counting time of 0.5 s per step, and also from 22 to 68° (2θ), with a 0.02° (2θ) step and a counting time of 4 s per step.

2.4.3. SQUID magnetometry

The magnetic susceptibility of the fluorescent nanoparticles (FLUSPIO) was determined using SQUID magnetometry (Quantum Design MPMS-5XL) in the field range of $B = 5.0$ to -5.0 T and at $T = 290.0$ K. The data were corrected for the sample holder (Teflon capsules) and the diamagnetic contribution of the compound.

2.4.4. MR relaxometry

Nuclear MR relaxometry of FLUSPIO nanoparticles was performed in a clinical 3T whole-body MR scanner (PHILIPS Achieva, The Netherlands) using a knee coil (SENSE-flex-M, PHILIPS, The Netherlands) at RT. FLUSPIO were diluted in de-ionized water at concentrations ranging from 0.005 to 50 μg of Fe/0.3 mL. For MR measurements 0.3 mL/well of diluted FLUSPIO solution was filled in custom made phantoms (Greiner 96 well Flat Transparent Polystyrol microplate, Germany). Transverse relaxation times (T_2) were measured in 2 D scan mode using a multi-slice, multi shot spin echo sequences with 90° excitation pulse followed by a train of equally spaced 180° refocusing pulses [TR = 1500 ms, mTR = 1189 ms, TE = 8.1 ms (shortest), number of echoes = 20, inter-echo spacing = 8.1 ms, FOV = 130 × 162.5 mm, reconstruction matrix = 64 × 81, voxel size = 2 × 2, slice thickness = 3 mm, slice orientation = coronal, scan mode = multi shot (MS)]. Transverse relaxation times (T_2) were measured in 3 D scan mode using a multi-slice, multi shot spin echo sequences with 90° excitation pulse followed by a train of equally spaced 180° refocusing pulses [TR = 1500 ms, mTR = 716 ms, TE = 11.8 ms (shortest), number of echoes = 20, inter-echo spacing = 12 ms, FOV = 130 × 162.5 × 18 mm, reconstruction matrix = 64 × 81, voxel size = 2 × 2 × 3, slice orientation = coronal, scan mode = 3 D, TSE turbo direction = Y]. T2 relaxation times were calculated by a linear fit of logarithmic region of interest (ROI) signal amplitudes versus echo time (TE). Longitudinal relaxation times (T_1) were determined using a multi shot spin echo sequences with 10° excitation pulse without refocusing pulses [TR = 6.8 ms, TE = 3.3 ms (shortest), number of echoes = 1, FOV = 170 × 148.75 mm, reconstruction matrix = 152 × 130, voxel size = 1.12 × 1.11, slice thickness = 5 mm, slice orientation = coronal, scan mode = 2 D]. Relaxivities r1 and r2 were determined by a linear fit of the inverse relaxation times as a function of the iron concentrations.

2.5. Cell culture

PC-3 cells were cultured using McCoy's (Gibco, Invitrogen, Germany) cell culture medium supplemented with 10% fetal calf serum (Invitrogen, Germany) and 1% Pen/strep (10,000 U/mL penicillin; 10,000 μg/mL streptomycin, Invitrogen, Germany). LnCap cells were cultured using RPMI medium without glutamine (Gibco, Invitrogen, Germany), 10% fetal calf serum (Invitrogen, Germany), 1% non-essential amino acid (MEM), 0.5% sodium pyruvate and 1% Pen/strep (10,000 U/mL penicillin; 10,000 μg/mL streptomycin, Invitrogen, Germany). DU-145 cells were cultured using RPMI medium without glutamine (Gibco, Invitrogen, Germany), 10% fetal calf serum (Invitrogen, Germany) and 1% Pen/strep (10,000 U/mL penicillin; 10,000 μg/mL streptomycin, Invitrogen, Germany). HUVEC were cultured using human endothelial cell growth medium (Promocell, Germany) containing 2% growth supplements, 3% fetal calf serum (Invitrogen, Germany) and 1% Pen/Strep (10,000 U/mL penicillin; 10,000 μg/mL streptomycin, Invitrogen, Germany). Cells were cultured in T75 cell culture flasks (Cell star, Greiner, Germany) and incubated at 37 °C, 5% CO_2 and 95% relative humidity.

2.5.1. Trypan blue staining

The toxicity of the FLUSPIO on prostate cancer cells (PC-3) and HUVEC was investigated using trypan blue staining (trypan blue stain, Sigma–Aldrich, Steinheim, Germany). PC-3 cells and HUVEC (2×10^6 cells) were seeded in 6-well plates (BD Falcon, Germany). Medium was removed, and each well was washed with 2 mL PBS (phosphate buffered saline). Cells incubated with regular growth medium served as negative controls. The amount of free FMN and GMP, used as controls was determined according to their concentration in the FLUSPIO. FLUSPIO and USPIO were diluted in respective media, in order to have iron concentrations of 0.03, 0.3 μmol Fe/mL. 1 mL of medium containing nanoparticles, FMN or GMP was added to each well. 3 samples per condition were analyzed. Cells were incubated for 3, 12 and 24 h. After incubation, medium was removed and transferred to 15 mL falcon tubes. Cells were washed once with PBS and subsequently trypsinized. The cell suspension was centrifuged at 1000 rpm (Multifuge, Thermo scientific, Germany) for 5 min and the supernatant was removed. The cell pellet was dissolved in 0.5 mL of respective fresh cell medium. 50 μl of the cell suspension were mixed with 50 μl of the trypan blue staining solution (1:2). Trypan blue positive cells (dead cells) were counted using a Cedex XS (Innovatis AG, Germany) cell counter. The percentage of positive cells as a function of the total cell number was calculated.

2.5.2. TUNEL assay

Toxicity of the FLUSPIO on PC-3 cells and HUVEC was additionally evaluated using the In situ Cell Death Detection Kit, TMR red, (Roche Diagnostics GmbH, Mannheim, Germany). The cells ($1x10^5$ cells/mL) were grown on cover slips (12 mm, Carl Roth, Germany) inside 24 well plates (Cell star, Greiner bio-one, Germany). FLUSPIO diluted in cell culture medium (3.0, 0.3 μmol Fe/mL) were added to cells for 3 h. Duplicates were used. After incubation, medium was removed and cells were washed three times with PBS. Further, cells were fixed with 4% paraformaldehyde at RT for 15 min. Again, cells were washed three times with PBS. After fixation, cells were permeabilised for 2 min using the permeabilisation solution [(0.1% Triton X-100 (Sigma Aldrich, Steinheim, Germany) and 0.1% sodium citrate (Carl Roth, Germany)]. Cells were washed three times with PBS and then dried at RT. Negative control cells were treated only with 50 μL label solution (without active enzyme). Positive control cells were generated by incubation with recombinant DNase I for 10 min in order to induce DNA strand break. 50 μL of TUNEL reaction mixture (label solution + active enzyme solution) were added to the positive control cells and to the cells, which were previously treated with FMN, GMP, USPIO and FLUSPIO for 3 h. The TUNEL reaction mixture was incubated for 1 h at 37 °C in a humidified atmosphere in dark. After incubation, cells were washed three times with PBS for 10 min. Nuclei were counterstained with 4′,6′-diamino-2-phenylindole (DAPI, 5 μg/mL, Merck, Darmstadt, Germany). Viable and apoptotic cells were counted in five different fields of view/slide using a fluorescence microscope (AxioObserver Z1; Carl Zeiss GmbH, Germany). Images were acquired using a digital camera (AxioCam MRm; Carl Zeiss GmbH, Germany) with 10× magnification.

2.5.3. Flow cytometry analysis

7-amino actinomycin D (7-AAD) viability staining (eBioscience GmbH, Frankfurt, Germany) was used to determine the number of viable cells by flow cytometry (FACS Calibur, BD Bioscience). Both, PC-3 cells and HUVEC were grown in petridishes (200 X 20 mm; Greiner bio-one, Germany). Positive controls were generated by exposing the cells to a temperature of 60 °C for 18 min. We used $4x10^5$ cells (PC-3) and $2x10^5$ cells (HUVEC) in 300 μL for flow cytometry analysis. FLUSPIO were diluted in respective media of PC-3 and HUVEC with 3.0, 0.3, 0.03 μmol Fe/mL. After incubation, medium was removed and cells were washed three times with PBS. Cells were trypsinized as described above, and centrifuged. The cell pellet was suspended in 300 μL PBS with 2% fetal calf serum (Invitrogen, Germany). The cells were stained with 6 μL of 7-AAD viability staining solution by incubating them in dark at RT for 10 min before measurement.

2.6. Cellular uptake of FLUSPIO nanoparticles (MRI)

The intracellular uptake of FLUSPIO in prostate cancer cells (PC-3) and endothelial cells (HUVEC) was investigated using MRI. FLUSPIO and USPIO were diluted in the respective cell culture media, to have final iron concentration of 0.03, 0.3 and 3.0 μmol Fe/mL. FMN (0.03, 0.3, 3.0 μmol/mL) and GMP (0.07, 0.7, 7.0 μmol/mL) controls were also diluted in the respective cell culture media. The supernatant medium was removed when 80% confluency was reached and cells were washed once with PBS buffer. Subsequently, cells were labelled with 11 mL of medium with nanoparticles and controls. Three samples per condition were analyzed. Cells were incubated for 1 h at 37 °C, 5% CO_2 and 95% relative humidity. After incubation, cells were washed once with PBS and subsequently trypsinized using 4 mL of trypsin/EDTA (0.25%/0.5%). Trypsinization was stopped by adding cell culture medium and the cell suspension was centrifuged at 1000 rpm (Multifuge, Thermo scientific, Germany) for 5 min. The cell pellet was re-suspended in 50 mL of PBS buffer and washed three times by performing the centrifugation as described above. The total cell numbers in the suspension were counted and after washing the cell pellet with PBS, it was dissolved in 10% gelatin to have 2×10^6 cells/0.3 mL as final cell concentration. MR-relaxometry of cells was performed at 3 T using the MR-sequences described in section 2.4.4.

2.7. In vitro competition of FLUSPIO cellular uptake using excess FMN (MRI)

FMN competition experiments were performed in order to validate that the uptake of FLUSPIO is mediated by the riboflavin carrier protein (RCP). Cells were pre-incubated for 10 min with FMN in 10- and 100- fold excess (with respect to FMN on FLUSPIO) to block RCP. Subsequently, FLUSPIO were added (0.3 μmol Fe/mL) and cells were incubated for 30 and 60 min, respectively. After incubation, cells were trypsinized and prepared for MRI analysis as described above. Three samples per condition were analyzed.

2.8. Cellular uptake of FLUSPIO nanoparticles (TEM)

USPIO and FLUSPIO were diluted in PC-3 cell culture medium to 3 μmol Fe/mL. Cells were labelled using 11 mL of medium containing USPIO or FLUSPIO for 3 h and 6 h. After incubation, medium was removed and cells were washed thrice with PBS. Subsequently, cells were fixed in 3% glutaraldehyde (in 0.1 M Soerensen's phosphate buffer [pH 7.4; 13 mM NaH_2PO_4 .H_2O; 87 mM Na_2HPO_4 .$2H_2O$]) by incubation for 22 h, and subsequently washed with 0.1 M Soerensen's phosphate buffer. Fixed cells were embedded in 2% agarose, rinsed with distilled water and dehydrated with ethanol (80%–100%). Finally cells were processed for embedding in Epon, by polymerizing 8 h at 37 °C and 56 h at 60 °C, and then cut into 70–100 nm thick slices. After polymerization, cells were contrasted with uranyl acetate and lead citrate. The samples were analyzed with a PHILIPS EM 400 T microscope at 60 kV and micrographs were taken by an OLYMPUS CCD-Camera (MORADA).

2.9. Cellular uptake of FLUSPIO nanoparticles (ICP-MS)

Digestion of cells was performed in a closed vessel microwave reaction system (MLS ethos plus, MPV-100/HAT) after addition of 1.5 mL nitric acid (65%) to 1.5 mL hydrogen peroxide and 1 mL of internal standard (rhodium) using 1000 W for 45 min by raising the temperature from RT to 210 °C and left constant at 210 °C for another 15 min. Samples were diluted in 1:100 in water. The amount of intracellular iron was determined using a high-resolution sector field inductively coupled plasma mass spectrometer [ICP-MS (Elan-DRCII, Perkin–Elmer)] equipped with an injector (2.0 mm i.d. Quartz, Part No.: WE02-3916). Data were acquired at medium resolution using rhodium as an internal standard. A Quartz Cyclonic spray chamber (Part No.: WE02-52222) equipped with a Meinhard Type A quartz nebulizer was used for sample introduction. The instrument was tuned and calibrated via infusion of a 1 μg/mL rhodium standard solution. The iron content was expressed in picograms of iron per cell.

3. Results and discussion

3.1. FLUSPIO synthesis

USPIO nanoparticles prepared by co-precipitation were coated with non-polymeric fluorescent FMN, which strongly binds to the iron oxide cores via phosphate groups (Fig. 1a). The FMN coating was achieved in aqueous solutions of USPIO and FMN (at pH 4) under sonication at ambient temperature. The coating of USPIO with FMN alone did not lead to an efficient and stable coverage of the entire nanoparticle surface, which might be due to steric hindrance caused by the isoalloxazine ring of FMN. Consequently, by visual inspection nanoparticle sediments were found indicating particle agglomeration. In addition, the nanoparticle surface should not be covered entirely with FMN due to the quenching of green fluorescence that occurs at high concentrations. GMP is less bulky and contains a phosphate group (similar to that of FMN), which strongly chemisorbs to the iron oxide surface during the non-polymeric coating. Both, FMN and GMP are negatively charged molecules and their binding to USPIO results in a negative surface charge of FLUSPIO at pH 7.0, thus providing colloidal stabilization. Therefore, the addition of GMP was necessary to stabilize the colloidal suspension and to complete the surface coverage. Furthermore, GMP also allows for further functionalization with biomolecules (peptides, antibodies etc.,) using standard conjugation techniques via the amine group available in the guanine moiety.

3.2. FLUSPIO characterization

Transmission electron microscopy (TEM), dynamic light scattering (DLS) and scanning electron microscopy (SEM) were used to characterize the FLUSPIO. TEM analysis of USPIO, and FLUSPIO

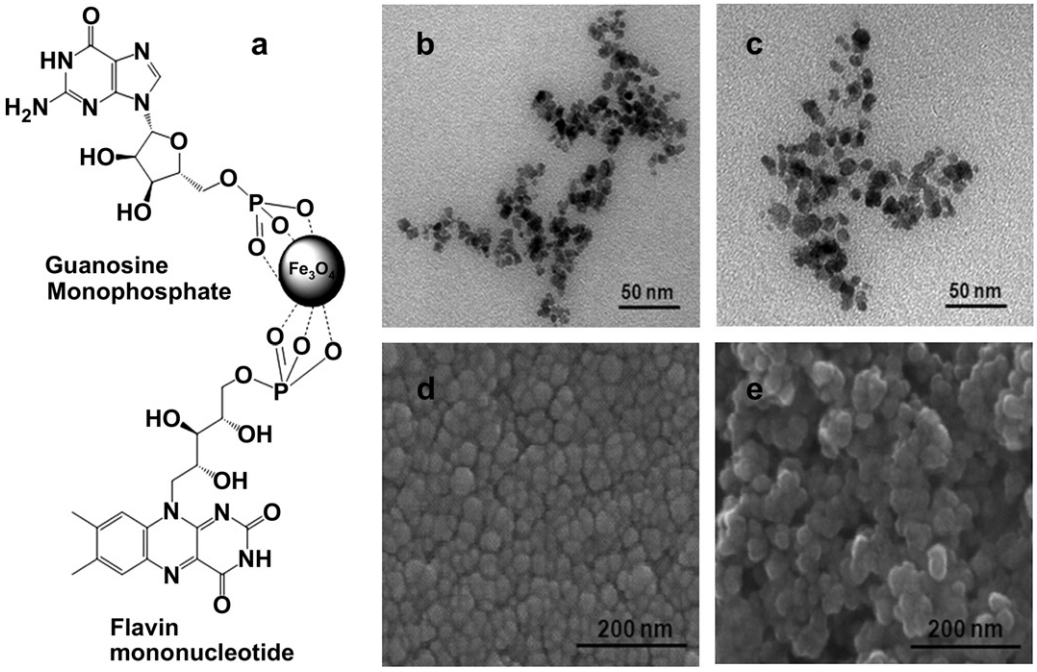

Fig. 1. Preparation of FLUSPIO. a: Schematic diagram showing the mode of binding of FMN and GMP to the iron oxide cores in FLUSPIO. b–c: TEM images of USPIO (b) and FLUSPIO (c). Quantitative analysis of the images reveals that both types of nanoparticles have a core diameter of 5 ± 1 nm and a narrow size distribution. d–e: SEM images of USPIO (d) and (e) FLUSPIO, displayed spherical morphology. Quantitative analysis indicated average sizes of 23 ± 4 nm (USPIO) and 27 ± 4 nm (FLUSPIO) respectively.

showed nanoparticles with an average iron core size of 5 ± 1 nm (see Table 1 and Fig. 1b,c). SEM was used to study the surface morphology of the nanoparticles. SEM images of USPIO and FLUSPIO confirmed the spherical surface morphology, with an average particle size of 23.19 ± 4.62 nm (USPIO) and 27.76 ± 4.76 nm (FLUSPIO) (see Fig. 1d,e). The increase in size observed in SEM could be attributed to clustering of the nanoparticles that occurs due to drying and/or to the conductive layer of sputtered gold on the nanoparticles surface. The thin layer of non-polymeric coating yields nanoparticles with a low hydrodynamic diameter which enhances the uptake of nanoparticles into tissues [3]. The hydrodynamic diameter (DLS) of the FLUSPIO in HEPES buffer showed an average hydrodynamic diameter of 97 ± 3 nm with a relatively low polydispersity index of 0.16. The broad average hydrodynamic diameter, which can be observed in Fig. 2a,b is an average of several runs, which displayed similar hydrodynamic diameter with comparable polydispersity index values. The increase in average hydrodynamic particle diameter of FLUSPIO in HEPES buffer may derive from the hydration shell and could be further increased by minor agglomeration which arises from the tendency of smaller iron cores to form clusters, which are not sterically stabilized by FMN and GMP. However, these DLS results of FLUSPIO are in line with the characteristics of clinically approved/used MR contrast agent Resovist (4 nm core size), which displayed hydrodynamic size distribution around ~60 nm. In comparison to FLUSPIO, USPIO, show stability only at pH 2 without any surface coverage with coating molecules, and displayed a large hydrodynamic diameter with a broad size distribution at pH 7 (252 ± 66 nm), due to aggregation between the iron cores at increasing pH (see Table 1 and Fig. 2a,b).

Zeta potential measurements were performed to determine the surface charge, electrophoretic mobility and colloidal stability of the USPIO and FLUSPIO particles at pH 2, 7 and 13 (Table 1). Under acidic conditions USPIO had a positive zeta potential due to their highly protonated surface hydroxyl and oxygen groups. USPIO agglomerated immediately in PBS buffer and saline solution (0.9% NaCl). A negative zeta potential was observed for FLUSPIO, which fosters for colloidal stability of the nanoparticles at neutral pH and usually leads to better pharmacokinetic properties. FLUSPIO were stable in physiological pH in water, HEPES buffer and in 5% glucose solution. However, after 15 min, aggregation was observed in PBS buffer and saline solution (0.9% NaCl) by visual inspection, likely because of the high ion concentrations and electrostatic interactions. No aggregation was found in cell culture medium, most probably due to colloidal stabilization of FLUSPIO by serum proteins (see Fig. S12 in the Supporting Information).

Table 1
Physico-chemical characterization of USPIO and FLUSPIO.

Sample	TEM diameter [nm]	Hydrodynamic diameter [nm]	Zeta potential in different pH solutions [mV]			MR Relaxivities at 3T in water	
		HEPES buffer (PDI)	pH 2	pH 7	pH 13	r2[$s^{-1}mM^{-1}$]	r1[$s^{-1}mM^{-1}$]
USPIO	5.5 ± 1.1	252 ± 66 (0.35)	32.83 ± 1.53	18.93 ± 2.46	−0.01 ± 0.03	n.d[c].	n.d[c].
FLUSPIO	5.6 ± 1.7	97 ± 3 (0.16)	4.59 ± 2.48	−31.13 ± 1.70	−31.70 ± 2.76	202.64 ± 0.48	2.13 ± 0.04
Resovist	4.2[a]	45.87 ± 0.09[b](0.30)	n.d.	−34.36 ± 2.30	n.d.	221.11 ± 0.61	5.21 ± 1.40

[a] Size of polycrystalline iron oxide with multiple single crystals and its reported relaxivity values [42].
[b] Hydrodynamic diameter of Resovist in water and its approximate zeta potential at pH 7.
[c] Relaxivity of USPIO at pH 7 could not be determined because of aggregation and susceptibility artefacts.

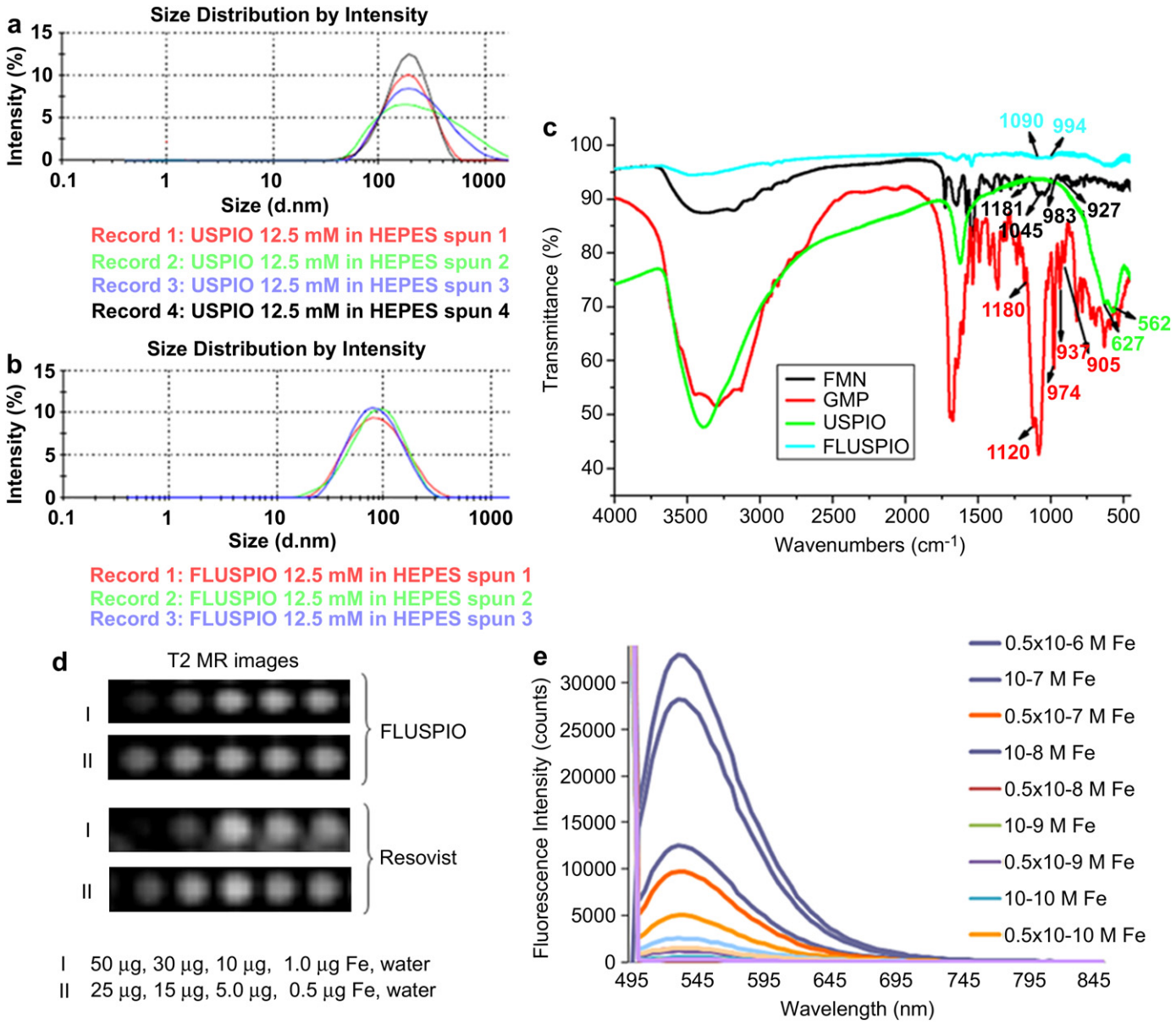

Fig. 2. Physico-chemical characterization of FLUSPIO. DLS analysis of (a) USPIO and (b) FLUSPIO. (c). FT-IR spectra of FLUSPIO with reference to free FMN, GMP and uncoated USPIO. (d). T_2-weighted MR images of FLUSPIO (50–0.005 µg) in comparison to Resovist in water. (e) Fluorescence emission spectrum of FLUSPIO at different concentration in water.

X-ray powder diffraction (XRD) analysis was used to determine the chemical composition and crystallinity of the FLUSPIO. The XRD patterns of FLUSPIO could be assigned to (220), (311), (400), (422), (511), and (440) reflections of the spinel structure of magnetite (JCPDS No. 19-0629) (see Fig. S1, in the Supporting Information). The observed diffraction peaks of USPIO are consistent with the expected diffraction peaks of Fe_3O_4. These peaks are also present in FLUSPIO, together with three other diffraction peaks. The additional peaks in FLUSPIO diffractogram at approximately 23.4 and 27.6° (2θ) are broad and are thus due to a material with low crystallite size, whereas the third additional peak at approximately 31.8° (2θ is sharp which is due to a material with larger crystallite size). The crystalline nature of their iron cores explains the high relaxivities of FLUSPIO found in MRI experiments. Fourier-transform infrared (FT-IR) spectroscopy confirmed the binding of FMN and GMP phosphate groups to nanoparticles, and this was validated by comparing the spectra of free FMN and GMP and unmodified USPIO (see Fig. 2c). The chemical composition of the surface (concentration of FMN, GMP) was analyzed by energy-dispersive X-ray spectroscopy (EDX), Vaskovsky phosphate determination, elemental analysis and thermogravimetry (TGA). As expected from the theoretically calculated ratio of phosphate to iron, the Fe:P ratio of the fluorescent nanoparticles determined by EDX was 1:0.231. This was further supported by the Vaskovsky phosphate determination (see Table S1 in the Supporting Information) and elemental analysis. TGA of the FLUSPIO showed a weight loss of 24% when heated to 600 °C (see Fig. S2, in the Supporting Information). This accounts for the decomposition of the surface coating (FMN and GMP), as well as for the dehydration of the inorganic matrix (theoretically calculated weight loss: 23%).

3.3. *Magnetic properties of FLUSPIO*

The superparamagnetic behavior of the FLUSPIO was studied by SQUID magnetometry, at a constant temperature of 290 K and a field of ±5 T. The magnetization vs field curve was compared to that of unmodified USPIO and showed the expected regular

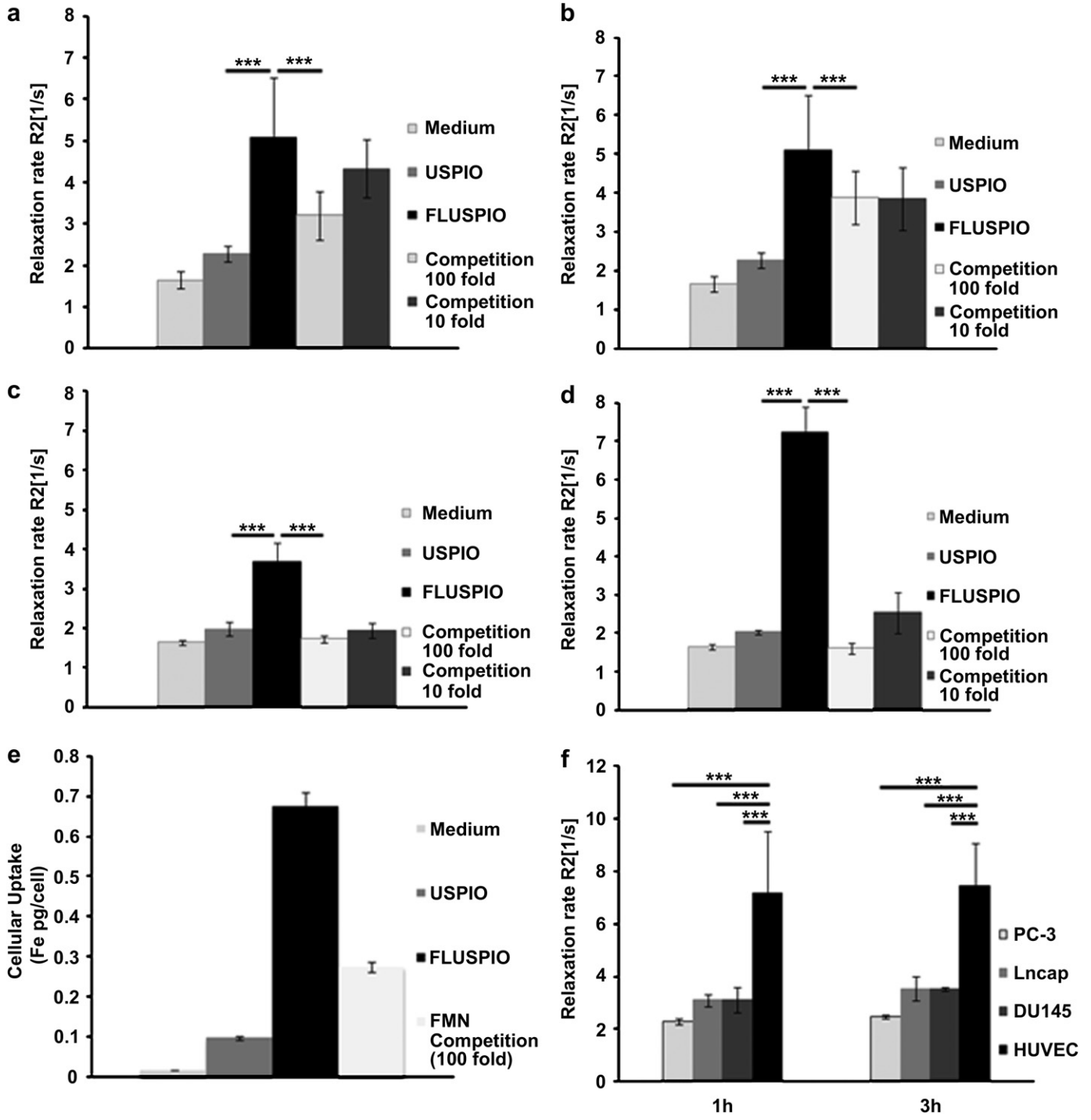

Fig. 3. FLUSPIO uptake analyzed by means of MR and ICP-MS. a: R2 relaxation rates of PC-3 cells in gelatin (9.0 x10^6 cells/0.3 mL) incubated with 0.3 μmol Fe/mL of USPIO, FLUSPIO and FLUSPIO plus free FMN (10- and 100-fold excess, for competition purposes) for different time intervals, i.e. 30 min (*a*) and 1 h (b). c: R2 relaxation rates of HUVEC in gelatin (1.0 x10^6 cells/0.3 mL) incubated with 0.3 μmol Fe/mL of USPIO, FLUSPIO and FLUSPIO plus free FMN (10- and 100-fold excess) for 30 min (*c*) and 1 h (d). e: ICP-MS determination of intracellular iron content in PC-3 cells after a 1 h incubation with USPIO, FLUSPIO and FLUSPIO in the presence of excess FMN (100-fold excess). (f). R2 relaxation rates of three different prostate cancer cell lines and HUVEC (2×10^6 cells/0.3 mL for each; in gelatin) incubated with 0.3 μmol Fe/mL of FLUSPIO for 1 h and 3 h. In all cases, two-sided student *t*-tests were performed to address statistical significance. ***: $p < 0.001$.

progression for superparamagnetic substances (see Fig. S3, in the Supporting Information) [33]. The MR relaxivity of the FLUSPIO in de-ionized water at RT at 3 T was found to be similar to that of the clinically used MR contrast agent Resovist (FLUSPIO: $r2 = 202.64 \pm 0.48\ s^{-1}mM^{-1}$, Resovist: $r2 = 221.11 \pm 0.61\ s^{-1}mM^{-1}$; see Table 1 and Fig. 2d), thereby confirming their contrast enhancement properties.

3.4. Fluorescence properties of FLUSPIO

Fluorescence spectroscopy and microscopy of the FLUSPIO revealed a high fluorescence intensity due to the photoluminescence of the FMN fluorophore associated with the nanoparticle surface [37]. The fluorescent nanoparticles can be excited in a wide wavelength range (250–500 nm), resulting in an intense

Table 2
Uptake of USPIO, FLUSPIO and FLUSPIO under competition with FMN in PC-3 cells (2×10^6 cells/0.3 mL) after 1 h incubation (ICP-MS).

ICP-MS iron content [pg Fe/cell]		
USPIO (0.3 μmol Fe/mL)	FLUSPIO (0.3 μmol Fe/mL)	FMN (100 fold)
0.097 ± 0.003	0.675 ± 0.31	0.274 ± 0.04

green emission at 530 nm with a moderate drop of about 40% in emission intensity after prolonged exposure to daylight (see Fig. 2e, Fig. S4 and Fig. S5, in the Supporting Information).

3.5. Cytotoxicity assay

The biocompatibility of the FLUSPIO was investigated using PC-3 cells (human prostate cancer cells) and HUVEC (as an example of activated endothelial cells). As shown in Fig. S6 and S7 (in the Supporting Information), neither trypan blue staining nor TUNEL staining (common assays used for determining the cytotoxicity of iron oxide nanoparticles) [38] indicated any significant change in cell viability at relevant cell labeling concentrations (i.e. up to 0.3 μmol Fe/mL). This observation was further confirmed by flow cytometry, in which 7-AAD (7-amino actinomycin D) was used to label dead cells, suggesting that the FLUSPIO are highly biocompatible (see Fig. S8, in the Supporting Information).

3.6. Cellular labeling and competition (MRI and ICP-MS)

Subsequently, the cellular labeling efficiency and the uptake of FLUSPIO were investigated by MRI (at 3 T). The cells were labeled with FLUSPIO, re-suspended in 10% gelatin (9×10^6 cells/0.3 mL; 0.3 μmol Fe/mL, 30 min and 1 h) and the R2 relaxation rates were determined. Three samples per condition were analyzed, and the cellular labeling and competition experiments were performed in triplicates. PC-3 cells in gelatin showed a significantly higher R2 relaxation rate after 1 h of incubation with FLUSPIO ($5.08 \pm 1.44\ s^{-1}$, $p < 0.001$) than with USPIO ($2.28 \pm 0.19\ s^{-1}$), indicating a higher cellular uptake of FLUSPIO (similar R2 values for FLUSPIO were obtained after 30 min incubation). Furthermore, the specificity of FLUSPIO uptake was investigated via competitive blocking of RCP with free FMN [39–41]. After the addition of free FMN to PC-3 cells and subsequent incubation with FLUSPIO for 30 min, the R2 relaxation rate was significantly reduced (10-fold FMN competition; $4.33 \pm 0.70\ s^{-1}$, $p < 0.05$; 100-fold FMN competition: $3.19 \pm 0.58\ s^{-1}$, $p < 0.001$; FLUSPIO incubation alone: $5.08 \pm 1.44\ s^{-1}$). Similar results were obtained when blocking RCP with free FMN for 1 h. In this case, the corresponding R2 relaxation rates were $3.84 \pm 0.81\ s^{-1}$ (10-fold FMN competition) and $3.87 \pm 0.69\ s^{-1}$ (100-fold FMN competition), respectively (Fig. 3a,b). The higher cellular uptake of FLUSPIO compared to USPIO and the capability of free FMN to block FLUSPIO internalization in PC-3 cells was confirmed by the quantification of the intracellular iron contents using inductively coupled plasma mass spectrometry (ICP-MS, Fig. 3e, Table 2).

In line with this, also HUVEC showed a significantly higher uptake of FLUSPIO (30 min: $3.69 \pm 0.45\ s^{-1}$, 1 h: $7.23 \pm 0.64\ s^{-1}$) than of USPIO (30 min: $1.98 \pm 0.17\ s^{-1}$, 1 h: $2.03 \pm 0.06\ s^{-1}$; see Fig. 3c,d). Competition experiments with free FMN confirmed the specificity of the RCP-mediated uptake of FLUSPIO in HUVEC. After RCP blocking by free FMN for 30 min, the R2 relaxation rate of HUVEC was decreased with respect to FLUSPIO alone (100-fold FMN competition: $1.73 \pm 0.07\ s^{-1}$; 10-fold FMN competition: $1.95 \pm 0.18\ s^{-1}$). Even after 1 h of FLUSPIO incubation, the uptake

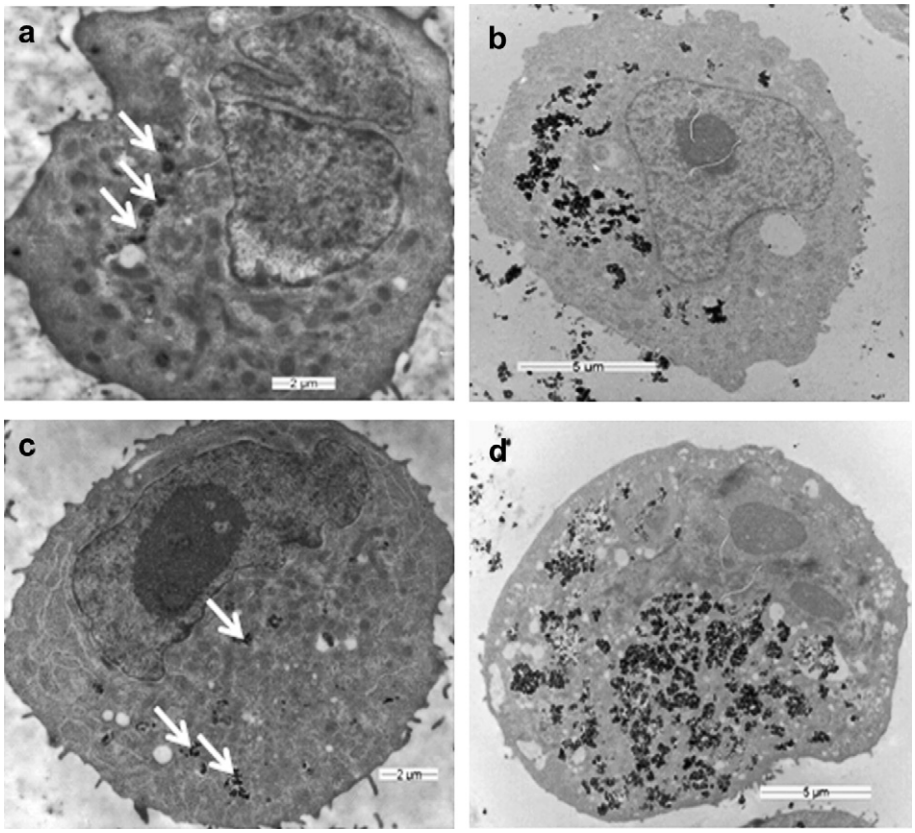

Fig. 4. FLUSPIO uptake analyzed by means of TEM. a–d: TEM images of PC-3 cells incubated with USPIO and FLUSPIO at an iron concentration of 3.0 μmol Fe/mL. After 3 h (a and b) and 6 h (c and d) of incubation, PC-3 cells have internalized only a small amount of uncoated USPIO (a and c; see arrows), while there is strong uptake for FLUSPIO (b and d).

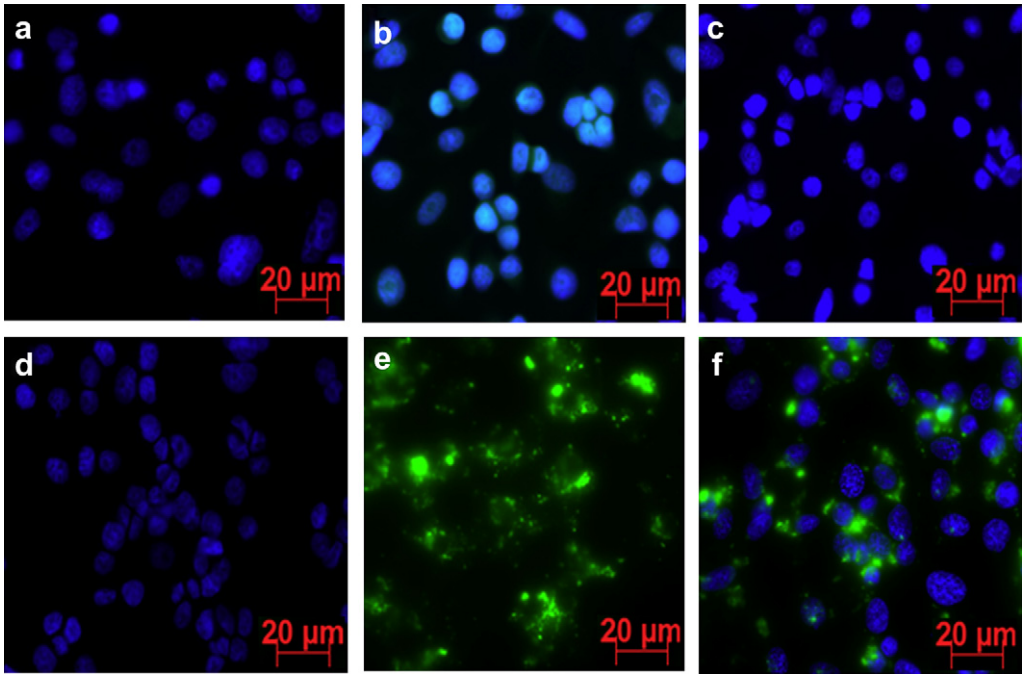

Fig. 5. FLUSPIO uptake analyzed by means of fluorescence microscopy. a–f: Fluorescence microscopy images of PC-3 cells incubated for 3 h with FLUSPIO (0.5 μmol Fe/mL). Nuclei are counterstained with DAPI. a: Blank medium. b: FMN. c: GMP. d: USPIO. e: FLUSPIO without DAPI. f: FLUSPIO plus DAPI. The images clearly show the vesicular (likely endosomal) localization of the FLUSPIO.

was still significantly lower in presence of 10- ($2.54 \pm 0.53\ s^{-1}$) and 100-fold excess ($1.60 \pm 0.12\ s^{-1}$) of free FMN (Fig. 3c,d). Together, these findings convincingly show that the RCP-mediated uptake of FLUSPIO by human prostate cancer cells (PC-3) and HUVEC is significantly higher than that of USPIO.

The less pronounced reduction of the relaxation rates (R2) by 10-fold FMN competition in PC-3 cells in comparison to HUVEC is most probably related to the higher unspecific particle uptake in these cells in comparison to RCP-mediated FLUSPIO internalization (see Fig. 3f). To the best of our knowledge, the regulation of RCP expression is still unclear. However, with increase in metabolic activity, cells are expected to have a higher demand for Rf. The Rf uptake in cells is facilitated by RCP. The increased uptake of Rf (FLUSPIO) by metabolically active cells points to an upregulation of RCP expression. Thus we hypothesize that the RCP expression level is linked to the metabolic activity of the cell. Unfortunately, the expression levels of RCP on the PC-3 and HUVEC cell surface could not be determined (and correlated to the MR findings) due to lack of a human RCP-binding antibody.

3.7. Fluorescence microscopy and TEM

In vitro experiments on PC-3 cells and HUVEC were also performed to evaluate the cellular labeling efficiency of FLUSPIO. The TEM images in Fig. 4a–d show that after 3 and 6 h, FLUSPIO strongly accumulated inside endosomes, while USPIO were not taken up effectively [39–41]. The high uptake of FLUSPIO by PC-3 cells was confirmed by fluorescence microscopy (Fig. 5a–f) and flow cytometry (see Fig. S9, in the Supporting Information). A strong green fluorescence of the cells was observed after FLUSPIO incubation (see Fig. 5a–f). The perinuclear fluorescence pattern strongly suggests endosomal localization of the FLUSPIO and supports the results from the TEM studies.

Furthermore, the dose- and time-dependency of nanoparticle uptake was investigated by incubating PC-3 and HUVEC cells with FLUSPIO of different iron concentrations (3.0, 0.3, 0.03 μmol Fe/mL) in the respective cell culture media for different incubation periods. As shown in Fig. S10 and S11 (in the Supporting Information), MR relaxometry of these cells showed increased R2 relaxation rates of FLUSPIO with increasing dose and incubation time. Interestingly, FLUSPIO were found to be taken up much more effectively by HUVEC than by PC-3 cells, which may be due to cell type-specific characteristics of activated endothelial cells. To investigate this interesting phenomenon in more detail, and to confirm FLUSPIO uptake in different cancer cells, a comparative MR relaxometry study was performed using PC-3, LnCap and DU-145 cells. All of these three prostate cancer cell lines are known to express RCP [10], and all three showed a high uptake of FLUSPIO. Remarkably however, in all cases, the R2 relaxation rate of HUVEC was found to be more than twice as high as that of the prostate cancer cell lines (Fig. 3f). Together, these findings suggest that FLUSPIO are highly suitable for targeting and labeling (angiogenic) endothelial cells [39–41].

In follow-up analyses, we aim to investigate the fluorescence and target specificity of USPIO with different core diameter by employing flavin and its derivatives (riboflavin, FMN, FAD) as an adsorptive, fluorescent and non-polymeric coating. In addition, we will investigate whether FLUSPIO also specifically accumulate in tumors and/or tumor endothelial cells after intravenous injection. We assume that *in vivo*, FLUSPIO will mostly target activated endothelial cells, thereby enabling molecular MR and optical imaging of tumor angiogenesis. Moreover, the concept of targeting RCP is not limited to USPIO, and FMN could serve as a versatile building block in generating contrast agents for other imaging modalities.

4. Conclusions

In summary, we here introduce RCP targeting as an effective way to specifically transport (iron oxide-based) nanomaterials into metabolically active tumor and endothelial cells. In this context, USPIO with an adsorptive fluorescent coating of FMN and GMP

(FLUSPIO) were synthesized, which are stable at physiological pH and show an intense fluorescence as well as high R2 relaxation rate in MRI. The high RCP-mediated uptake of FLUSPIO by activated endothelial and cancer cells suggest them as promising tools for molecular MRI and cell tracking experiments.

Acknowledgements

This work was supported by the DFG grant KI 1072/1-3 “Dual modal contrast agents for MRI and Optical Imaging techniques” by the InnoMeT grant z0909im008a “Entwicklung und Bildgebung patientenoptimierter Implantate” and by the EC (FP6: MediTrans). The authors would like to thank Mrs. Natascha Mertens for MRI measurements, Ms. Anne Rix for cell experiments, Dr. Matt Bunker (Molecular Profiles, Nottingham) for size determinations and for powder XRD measurements.

Appendix. Supplementary material

Supplementary data associated with this article can be found in the online version, at doi:10.1016/j.biomaterials.2011.04.056.

References

[1] Lee HY, Lee SH, Xu C, Xie J, Lee JH, Wu B, et al. Synthesis and characterization of PVP-coated large core iron oxide nanoparticles as an MRI contrast agent. Nanotechnology 2008;19:165101.
[2] Du L, Chen J, Qi Y, Li D, Yuan C, Lin MC, et al. Preparation and biomedical application of a non-polymer coated superparamagnetic nanoparticle. Int J Nanomedicine 2007;2:805–12.
[3] Zhang Y, Kohler N, Zhang M. Surface modification of superparamagnetic magnetite nanoparticles and their intracellular uptake. Biomaterials 2002;23:1553–61.
[4] Portet D, Denizot B, Rump E, Lejeune JJ, Jallet P. Nonpolymeric coatings of iron oxide colloids for biological use as magnetic resonance imaging contrast agents. J Colloid Interface Sci 2001;238:37–42.
[5] Mowat P, Franconi F, Chapon C, Lemaire L, Dorat J, Hindri F, et al. Evaluating SPIO-labelled cell MR efficiency by three-dimensional quantitative T2* MRI. NMR Biomed 2007;20:21–7.
[6] Cheng FY, Shieh DB, Yeh CS. Non-polymer coated Fe3O4 aqueous dispersion with NH3-surface modification as new magnetite nanoparticles and their biomedical applications. Proceedings of 2005 5th IEEE Conference on Nanotechnology Nagoya, Japan 2005.
[7] Huang SN, Swaan PW. Involvement of a receptor-mediated component in cellular translocation of riboflavin. J Pharmacol Exp Ther 2000;294:117–25.
[8] Mason CW, D'Souza VM, Bareford LM, Phelps MA, Ray A, Swaan PW. Recognition, cointernalization, and recycling of an avian riboflavin carrier protein in human placental trophoblasts. J Pharmacol Exp Ther 2006;317:465–72.
[9] Foraker AB, Khantwal CM, Swaan PW. Current perspectives on the cellular uptake and trafficking of riboflavin. Adv Drug Deliv Rev 2003;55:1467–83.
[10] Johnson T, Ouhtit A, Gaur R, Fernando A, Schwarzenberger P, Su J, et al. Biochemical characterization of riboflavin carrier protein (RCP) in prostate cancer. Front Biosci 2009;14:3634–40.
[11] Karande AA, Sridhar L, Gopinath KS, Adiga PR. Riboflavin carrier protein: a serum and tissue marker for breast carcinoma. Int J Cancer 2001;95:277–81.
[12] Brock CS, Meikle SR, Price P. Does fluorine-18 fluorodeoxyglucose metabolic imaging of tumours benefit oncology? Eur J Nucl Med Mol Imaging 1997;24:691–705.
[13] Paudyal B, Paudyal P, Oriuchi N, Tsushima Y, Nakajima T, Endo K. Clinical implication of glucose transport and metabolism evaluated by 18F-FDG PET in hepatocellular carcinoma. Int J Oncol 2008;33:1047–54.
[14] Pracchia LF, Chaves AAR, Cerci JJ, Soares Junior J, Meneghetti JC, Buccheri V. Metabolic test with fluorine-18-fluorodeoxyglucose in staging and detection of residual tumor or recurrence in Hodgkin lymphoma. Clinics 2007;62:121–6.
[15] Tong S, Hou S, Zheng Z, Zhou J, Bao G. Coating optimization of superparamagnetic iron oxide nanoparticles for high T2 relaxivity. Nano Lett 2010;10:4607–13.
[16] Schellenberger E, Schnorr JÃ, Reutelingsperger C, Ungethum L, Meyer W, Taupitz M, et al. Linking proteins with anionic nanoparticles via protamine: ultrasmall protein-coupled probes for magnetic resonance imaging of apoptosis. Small 2008;4:225–30.
[17] Golovko DM, Henning T, Bauer JS, Settles M, Frenzel T, Mayerhofer A, et al. Accelerated stem cell labeling with ferucarbotran and protamine. Eur Radiol 2010;20:640–8.
[18] Kluza E, van der Schaft DWJ, Hautvast PAI, Mulder WJM, Mayo KH, Griffioen AW, et al. Synergistic targeting of alphaVbeta3 integrin and galectin-1 with heteromultivalent paramagnetic liposomes for combined MR imaging and treatment of angiogenesis. Nano Lett 2010;10:52–8.
[19] Meier R, Henning TD, Boddington S, Tavri S, Arora S, Piontek G, et al. Breast cancers: MR imaging of folate-receptor expression with the folate-specific nanoparticle P11331. Radiology 2010;255:527–35.
[20] Henning TD, Wendland MF, Golovko D, Sutton EJ, Sennino B, Malek F, et al. Relaxation effects of ferucarbotran-labeled mesenchymal stem cells at 1.5T and 3T: discrimination of viable from lysed cells. Magn Reson Med 2009;62:325–32.
[21] Bulte JWM, Kraitchman DL. Iron oxide MR contrast agents for molecular and cellular imaging. NMR Biomed 2004;17:484–99.
[22] Frank JA, Miller BR, Arbab AS, Zywicke HA, Jordan EK, Lewis BK, et al. Clinically applicable labeling of mammalian and stem cells by combining superparamagnetic iron oxides and transfection agents. Radiology 2003;228:480–7.
[23] Bulte JWM, Kraitchman DL. Monitoring cell therapy using iron oxide MR contrast agents. Curr Pharm Biotechnol 2004;5:567–84.
[24] Bulte JWM, Kraitchman DL, Mackay AM, Pittenger MF, Arbab AS, Yocum GT, et al. Chondrogenic differentiation of mesenchymal stem cells is inhibited after magnetic labeling with ferumoxides. Blood 2004;104:3410–3.
[25] Santra S, Kaittanis C, Grimm J, Perez JM. Drug/dye-loaded, multifunctional iron oxide nanoparticles for combined targeted cancer therapy and dual optical/magnetic resonance imaging. Small 2009;5:1862–8.
[26] Kircher MF, Grimm J, Swirski FK, Libby P, Gerszten RE, Allport JR, et al. Noninvasive in vivo imaging of monocyte trafficking to atherosclerotic lesions. Circulation 2008;117:388–95.
[27] Veiseh O, Sun C, Gunn J, Kohler N, Gabikian P, Lee D, et al. Optical and MRI multifunctional nanoprobe for targeting gliomas. Nano Lett 2005;5:1003–8.
[28] Lu CW, Hung Y, Hsiao JK, Yao M, Chung TH, Lin YS, et al. Bifunctional magnetic silica nanoparticles for highly efficient human stem cell labeling. Nano Lett 2007;7:149–54.
[29] Sosnovik DE, Schellenberger EA, Nahrendorf M, Novikov MS, Matsui T, Dai G, et al. Magnetic resonance imaging of cardiomyocyte apoptosis with a novel magneto-optical nanoparticle. Magn Reson Med 2005;54:718–24.
[30] Aime S, Castelli DD, Crich SG, Gianolio E, Terreno E. Pushing the sensitivity envelope of lanthanide-based magnetic resonance imaging (MRI) contrast agents for molecular imaging applications. Acc Chem Res 2009;42:822–31.
[31] Xie J, Chen K, Huang J, Lee S, Wang J, Gao J, et al. PET/NIRF/MRI triple functional iron oxide nanoparticles. Biomaterials 2010;31:3016–22.
[32] Jarzyna PA, Skajaa T, Gianella A, Cormode DP, Samber DD, Dickson SD, et al. Iron oxide core oil-in-water emulsions as a multifunctional nanoparticle platform for tumor targeting and imaging. Biomaterials 2009;30:6947–54.
[33] Skajaa T, Cormode DP, Jarzyna PA, Delshad A, Blachford C, Barazza A, et al. The biological properties of iron oxide core high-density lipoprotein in experimental atherosclerosis. Biomaterials 2011;32:206–13.
[34] Bumb A, Brechbiel MW, Choyke PL, Fugger L, Eggeman A, Prabhakaran D, et al. Synthesis and characterization of ultra-small superparamagnetic iron oxide nanoparticles thinly coated with silica. Nanotechnology 2008;19:335601.
[35] Jander G, Jahr K. Massanalyse. 17 ed; 2009. 219–221.
[36] Bashir WA. Photometric determination of iron (III). Microchem J 1981;26:477–80.
[37] Roming M, Lunsdorf H, Dittmar KEJ, Feldmann C. ZrO(HPO4)1-x(FMN)x: Quick and easy synthesis of a nanoscale luminescent biomarker. Angew Chem Int Ed; 2009:632–7.
[38] Soenen SJH, De Cuyper M. Assessing cytotoxicity of (iron oxide-based) nanoparticles: an overview of different methods exemplified with cationic magnetoliposomes. Contrast Media Mol Imaging 2009;4:207–19.
[39] Zhang C, Jugold M, Woenne EC, Lammers T, Morgenstern B, Mueller MM, et al. Specific targeting of tumor angiogenesis by RGD-conjugated ultrasmall superparamagnetic iron oxide particles using a clinical 1.5-T magnetic resonance scanner. Cancer Res 2007;67:1555–62.
[40] Kiessling F, Huppert J, Zhang C, Jayapaul J, Zwick S, Woenne EC, et al. RGD-labeled USPIO inhibits adhesion and endocytotic activity of alpha v beta3-integrin-expressing glioma cells and only accumulates in the vascular tumor compartment. Radiology 2009;253:462–9.
[41] Zhang C, Waengler B, Morgenstern B, Zentgraf H, Eisenhut M, Untenecker H, et al. Silica- and alkoxysilane-coated ultrasmall superparamagnetic iron oxide particles: a promising tool to label cells for magnetic resonance imaging. Langmuir 2007;23:1427–34.
[42] Reimer P, Balzer T. Ferucarbotran (Resovist): a new clinically approved RES-specific contrast agent for contrast-enhanced MRI of the liver: properties, clinical development, and applications. Eur Radiol 2003;13:1266–76.

RGD-labeled USPIO Inhibits Adhesion and Endocytotic Activity of $\alpha_v\beta_3$-Integrin–expressing Glioma Cells and Only Accumulates in the Vascular Tumor Compartment[1]

Fabian Kiessling, MD
Jochen Huppert, PhD
Chunfu Zhang, PhD
Jabadurai Jayapaul, MS
Stefan Zwick, PhD
Eva C. Woenne, PhD
Margareta M. Mueller, PhD
Hanswalter Zentgraf, PhD
Michael Eisenhut, PhD
Yoseph Addadi, MD
Michal Neeman, PhD
Wolfhard Semmler, MD, PhD

Purpose: To investigate the biologic effect of arginine-glycine-aspartic acid (RGD)–labeled ultrasmall superparamagnetic iron oxide (USPIO) (referred to as RGD-USPIO) on human umbilical vein endothelial cells (HUVECs), ovarian carcinoma (MLS) cells, and glioblastoma (U87MG) cells and on U87MG xenografts in vivo.

Materials and Methods: All experiments were approved by the governmental review committee on animal care. USPIOs were coated with integrin-specific (RGD) or unspecific (arginine-alanine-aspartic acid [RAD]) peptides. USPIO uptake in HUVECs, MLS cells, and U87MG cells and in U87MG tumor xenografts was determined with T2 magnetic resonance (MR) relaxometry in 16 nude mice. Cells and tumors were characterized by using immunofluorescence microscopy. Trypan blue staining and lactate dehydrogenase assay were used to assess cytotoxicity. Statistical evaluation was performed by using a Mann-Whitney test or a linear mixed model with random intercept for the comparison of data from different experiments. Post hoc pairwise comparisons were adjusted according to a Tukey test.

Results: HUVECs and MLS cells internalized RGD-USPIOs significantly more than unspecific probes. Controversially, U87MG cells accumulated RGD-USPIOs to a lesser extent than USPIO. Furthermore, only in U87MG cells, free RGD and $\alpha_v\beta_3$ integrin–blocking antibodies strongly reduced endocytosis of nonspecific USPIOs. This was accompanied by a loss of cadherin-dependent intercellular contacts, which could not be attributed to cell damage. In U87MG tumors, RGD-USPIO accumulated exclusively at the neovasculature but not within tumor cells. The vascular accumulation of RGD-USPIO caused significantly higher changes of the R2 relaxation rate of tumors than observed for USPIO.

Conclusion: In glioma cells with unstable intercellular contacts, inhibition of $\alpha_v\beta_3$ integrins by antibodies and RGD and RGD-USPIO disintegrated intercellular contacts and reduced endocytotic activity, illustrating the risk of inducing biologic effects by using molecular MR probes.

Supplemental material: *http://radiology.rsna.org/lookup/suppl/doi:10.1148/radiol.2532081815/-/DC1*

[1] From the Department of Experimental Molecular Imaging, German Cancer Research Center, RWTH Aachen University, Pauwelsstrasse 20, 52074 Aachen, Germany (F.K., J.J.); Med-X Research Institute, Jiao Tong University, Shanghai, China (C.Z.); Department of Biological Regulation, Weizmann Institute, Rehovot, Israel (M.N., Y.A.); Department of Medical Physics in Radiology (F.K., J.H., J.J., S.Z., E.C.W., W.S.), Tumor and Microenvironment Group (M.M.M.), Department of Applied Tumor Virology (H.Z.), and Department of Radiopharmaceutical Chemistry (M.E.), German Cancer Research Center, Heidelberg, Germany. Received October 13, 2008; revision requested December 11; revision received February 11, 2009; accepted March 11; final version accepted May 11. Supported by the Deutsche Forschungsgemeinschaft (grant no. KI1072/1-3) and by the DKFZ-MOST cooperational program. **Address correspondence to** F.K. (e-mail: *fkiessling@ukaachen.de*).

Cell adhesion molecules such as $\alpha_v\beta_3$ integrin are overexpressed in activated endothelial cells and can be targeted with various ligands to visualize and inhibit tumor angiogenesis (1–6). Arginine-glycine-aspartic acid (RGD) peptides are one of the most popular ligands that target $\alpha_v\beta_3$ integrin. RGD peptides inhibit vessel sprouting and thus were initially used for antiangiogenic therapy (2,7,8). When conjugated to microbubbles (9,10), fluorescent markers (4,11), magnetic nanoparticles (5,12), or radiotracers (13–16), RGD allows the detection of angiogenesis. Tumor cells from gliomas (14,15), ovarian carcinomas (17,18), breast carcinomas (19), and other tumors (10–22) also express $\alpha_v\beta_3$ integrins. However, with the exception of RGD-coupled radiotracers (13–16), in most previous imaging studies, RGD was bound to signal molecules or particles that were too large to extravasate (10,23,24) and thus only $\alpha_v\beta_3$ integrins on the vascular lumen were targeted. If diagnostic $\alpha_v\beta_3$ integrin–targeting probes are capable of extravasation, there could be biologic effects on tumor cells. This holds particularly true for magnetic resonance (MR) imaging in which a high concentration of RGD-containing probes must accumulate to overcome the limited sensitivity for the detection of contrast media.

Thus, the purpose of this study was to evaluate the biologic effect of RGD-labeled ultrasmall superparamagnetic iron oxide (USPIO) (referred to as RGD-USPIO) on human umbilical vein endothelial cells (HUVECs), ovarian carcinoma (MLS) cells, and glioblastoma (U87MG) cells and on U87MG xenografts in vivo.

Advances in Knowledge

- Arginine-glycine-aspartic acid (RGD)–ultrasmall superparamagnetic iron oxides (USPIOs) accumulate in the microvasculature of U87MG gliomas but not in $\alpha_v\beta_3$ integrin–expressing tumor cells.
- In U87MG gioma cells, RGD-USPIOs inhibit adhesion and edycytotic activity.
- Different cell lines vary in their biologic response to RGD-USPIO.

Materials and Methods

All experiments were approved by the governmental review committee on animal care.

Study Flow Chart

The following experiments were performed in sequence:

1. Synthesis and characterization of USPIO, RGD-USPIO, and arginine-alanine—aspartic acid (RAD)–labeled USPIO (referred to as RAD-USPIO) (Appendix E1 [online]);
2. Characterization of $\alpha_v\beta_3$, α_v, and β_1 expression by HUVECs, U87MG cells, and MLS cells by using fluorescence-activated cell sorting (Appendix E1 [online]);
3. Use of MR relaxometry to investigate the cellular uptake of USPIO, RGD-USPIO, and RAD-USPIO (only HUVECs) and the ability of free RGD to block RGD-USPIO internalization (referred to as competition condition);
4. Investigation of USPIO and RGD-USPIO internalization by U87MG cells and by HUVECs by using transmission electron microscopy (Appendix E1 [online]);
5. Investigation of cell viability after USPIO and RGD-USPIO incubation by using trypan blue exclusion and lactate dehydrogenase assay (Appendix E1 [online]);
6. Assessment of RGD effects on unspecific USPIO uptake by HUVECs, U87MG cells, and MLS cells (MR relaxometry);
7. Incubation of U87MG cells with USPIO and monoclonal antibodies against $\alpha_v\beta_3$, α_v, and β_1 to further specify the effect of integrin blockade on USPIO endocytosis (MR relaxometry);
8. Immunofluorescence analysis of cadherin expression in HUVECs and U87MG cells incubated with USPIO and RGD-USPIO;
9. MR imaging and MR relaxometry in 16 nude mice bearing U87MG tumor xenografts before and after injection of USPIO and RGD-USPIO; and
10. Immunohistologic evaluation of U87MG tumor xenografts.

RGD-USPIO Uptake by Cells

HUVECs, U87MG cells, and MLS cells were incubated with RGD-labeled and unlabeled USPIO (0.03 μmol of iron per milliliter growth medium) for 1 hour (S.Z., 3 years of experience in MR physics; C.Z., 5 years of experience in nanoparticle chemistry; J.J., 1 year of experience in nanoparticle chemistry; Y.A., 3 years of experience in molecular biology). Competition experiments were performed by incubating HUVECs and MLS cells with RGD-USPIOs in the presence of 10 000-fold excess of RGD. One thousand–fold excess of RGD was used for U87MG cells because of distinct cell detachment in the presence of 10 000-fold excess of RGD.

To investigate whether RGD affects nonspecific phagocytosis, HUVECs and U87MG cells were incubated for 1 hour with unlabeled USPIOs (0.03 μmol of iron per milliliter) in the presence of 10 000-fold excess of RGD for HUVECs or 1000-fold excess of RGD for U87MG cells. The ex-

Published online before print
10.1148/radiol.2532081815

Radiology 2009; 253:462–469

Abbreviations:
HUVEC = human umbilical vein endothelial cell
RAD = arginine-alanine-aspartic acid
RGD = arginine-glycine-aspartic acid
ROI = region of interest
USPIO = ultrasmall superparamagnetic iron oxide

Author contributions:
Guarantors of integrity of entire study, F.K., S.Z., E.C.W., H.Z., W.S.; study concepts/study design or data acquisition or data analysis/interpretation, all authors; manuscript drafting or manuscript revision for important intellectual content, all authors; manuscript final version approval, all authors; literature research, F.K., J.H., C.Z., E.C.W., M.M.M., H.Z., M.E., M.N.; experimental studies, F.K., J.H., C.Z., J.J., S.Z., E.C.W., M.M.M., H.Z., M.E., Y.A.; statistical analysis, F.K., C.Z., J.J., E.C.W., H.Z., Y.A., M.N.; and manuscript editing, F.K., J.H., S.Z., E.C.W., M.M.M., H.Z., M.E., Y.A., M.N., W.S.

Authors stated no financial relationship to disclose.

periments described above were repeated three times.

U87MG cells were incubated with USPIO in the presence of monoclonal antibodies (Chemicon International, Temecula, Calif) selectively blocking $\alpha_v\beta_3$ (dilution, 1:40), α_v (dilution, 1:15), and β_1 (dilution, 1:50).

The particle uptake by cells was investigated with MR relaxometry (S.Z.) with a 1.5-T whole-body MR imager (Symphony; Siemens, Erlangen, Germany) in combination with a custom-made radiofrequency coil for excitation and signal reception. A total of 1×10^7 cells cultured within various conditions were dispersed into 300 μL of gelatin (10%). The gels were analyzed by using a Carr-Purcell-Meiboom-Gill sequence (repetition time msec/echo time msec, 1200/7–350; 32 echoes; field of view, 150 mm^2; matrix, 128 × 39; section thickness, 5 mm). T2 relaxation time was calculated by using a linear fit of the logarithmic region-of-interest (ROI) signal amplitudes versus echo time. The determined fit errors were in the same range for all probes and therefore were not considered in the statistical analysis. R2 was determined as 1/T2. In all MR relaxometry experiments, ROIs were defined randomly at five different positions of the gelatin gel in consensus by authors (S.Z. C.Z., J.J., and Y.A.). Means and measurement errors were calculated.

Effect on Cell Morphology and Adhesion

HUVECs and U87MG cells grown on glass slides were incubated for 1 hour with unlabeled USPIOs, RGD-USPIOs, and under competition conditions as described previously. Cell morphology was investigated by using a phase-contrast microscope (F.K., radiologist with 7 years of experience in molecular imaging; M.M.M., with 15 years of experience in molecular biology).

Cadherins were stained. Cadherins are major components of intercellular contacts like adherens junctions, fasciae adherents, and desmosomes. VE-cadherin was expressed in HUVECs, and N-cadherin was expressed in U87MG cells. Cells were seeded on glass slides and fixed in methanol and acetone. HUVECs were stained with primary rabbit anti–VE-cadherin (Alexis Biochemicals, San Diego, Calif), and U87MG cells were stained with mouse anti–N-cadherin (BD Transduction Laboratories, San Jose, Calif). Cy2-labeled antirabbit-IgG and antimouse-IgG secondary antibodies (Dianova, Hamburg, Germany) were used, respectively. Nuclear counterstaining was performed with 4′,6-diamidino-2-phenylindole (Pierce Biotechnology, Rockford, Ill) at a dilution of 1:100.

In Vivo Experiment in U87MG Tumor Xenografts

Tumors were induced with subcutaneous injection of U87MG human glioma cells (3×10^7) in the hind leg of 16 nude mice (C.Z., F.K., J.J.). Four weeks after tumor inoculation, eight mice received RGD-USPIOs, and eight received unlabeled USPIOs (dose: 900 μmol of iron per kilogram of body weight). Animals underwent MR imaging before and 6 hours after particle administration by using a T2*-weighted gradient-echo sequence (213/10.9; field of view, 130 × 56.9 mm; matrix, 256 × 256; section thickness, 1.5 mm; flip angle, 10°) and a Carr-Purcell-Meiboom-Gill sequence (1330/8.3–265.5; 32 echoes; number of signals acquired, five; field of view, 120 × 34.4 mm; matrix, 128 × 33; section thickness, 2 mm) for T2 relaxometry. R2 was determined for ROIs that covered the entire tumors at maximal extension. ROI definition was performed by authors (F.K., J.J., and C.Z.) in consensus. Mean ROI size was 0.42 $cm^2 \pm 0.22$.

Immunohistologic Staining of Tumors

Tumors were dissected, embedded in Tissue Tek (Sacura, Zoeterwoude, the Netherlands), and frozen in liquid nitrogen and cut (E.C.W., biologist with 4 years of experience; M.M.M.). Six-micrometer thin frozen slices were fixed in acetone and methanol and were air dried. Slices were stained with primary hamster antimouse CD61 and antihuman CD51/CD61 antibodies (BD Biosciences, San Jose, Calif) in combination with a Cy2-labeled antihamster-IgG secondary antibody. Counterstaining of endothelial cells was performed by using a rat antimouse CD31 antibody (BD Biosciences) in combination with a Cy5-labeled antirat immunoglobulin-G secondary antibody (Jackson ImmunoResearch Laboratory, West Grove, Pa). Nuclei were stained with 4′,6-diamidino-2-phenylindole. For Prussian blue staining, a standard protocol described in Appendix E1 (Appendix E1 [online]) was followed.

Statistical Analysis

To statistically compare the data on particle uptake by cells from different experiments, a linear mixed model with random intercept was used. Post hoc pairwise comparisons were adjusted according to a Tukey test. These figures (1,2) present data from one of three representative experiments. In this context, the marks indicating statistical significance are related to the statistical analysis described above. All quantitative data were expressed as mean ± measurement error.

R2 of U87MG tumors after administration of RGD-USPIO or USPIO and the data on particle toxicity were compared by using a Mann-Whitney test (two-tailed). Significant differences were assigned to P values less than .05.

Results

Endocytosis of USPIO and RGD-USPIO

In HUVEC and U87MG cell experiments, a significant ($P < .0001$) fixed effect was found for the uptake of USPIO and RGD-USPIO and under competition condition. In HUVECs, we found a higher uptake of RGD-USPIOs relative to RAD-USPIOs and USPIOs ($P < .001$) and a significant ($P < .001$) competitive inhibition of the uptake by the addition of free RGD.

U87MG glioma cells behaved differently (Fig 1). R2 increased to significantly higher levels after incubation with unlabeled USPIOs than after incubation with RGD-USPIOs ($P <$

.001). The lowest increase in R2 ($P <$ .001, compared with USPIO and RGD-USPIO incubation) was observed when the U87MG cells were maintained under competition condition.

MLS cells showed a particle uptake similar to that of HUVECs. After 1 hour, incubation R2 was significantly ($P <$ .01) higher in samples including MLS cells incubated with RGD-USPIOs than in those treated with unlabeled USPIOs and under competition condition.

Cytotoxicity Studies

Even after extended incubation times with unlabeled USPIOs, RGD-USPIOs, and free RGD, viability of HUVECs, U87MG cells, and MLS cells assessed with trypan blue staining and lactate dehydrogenase assay was not significantly different from cells incubated with regular growth medium (Fig E1 and Appendix E1 [online]).

Influence of Integrin Inhibition on Phagocytosis of USPIOs

MR relaxometry results indicated that, after addition of RGD, the uptake of plain USPIO was reduced in HUVECs (not significant) and U87MG cells ($P <$ .05), while almost no effect was found in MLS cells. In this context, the inhibition of particle uptake was much stronger in U87MG cells than in HUVECs (Fig 2). Inhibition of $\alpha_v\beta_3$, α_v, and β_1 by antibodies also inhibited the uptake of unspecific USPIO by U87MG cells. The effect was more pronounced when selectively blocking α_v compared with $\alpha_v\beta_3$ and β_1 (Fig E2 and Appendix E1 [online]).

Effect on Cell Morphology and Adhesion

By using phase-contrast microscopy, no changes in morphology and adhesion of HUVECs were visible after a 1-hour incubation with unlabeled USPIOs or with RGD-USPIOs or under competition condition. Similarly, incubation of U87MG cells for 1 hour at the same iron concentration with unlabeled USPIOs had no effect on cell morphology. However, U87MG cells incubated with RGD-USPIOs rounded off, separated from each other, and some even detached. This effect was even more pronounced when the cells were incu-

Figure 1

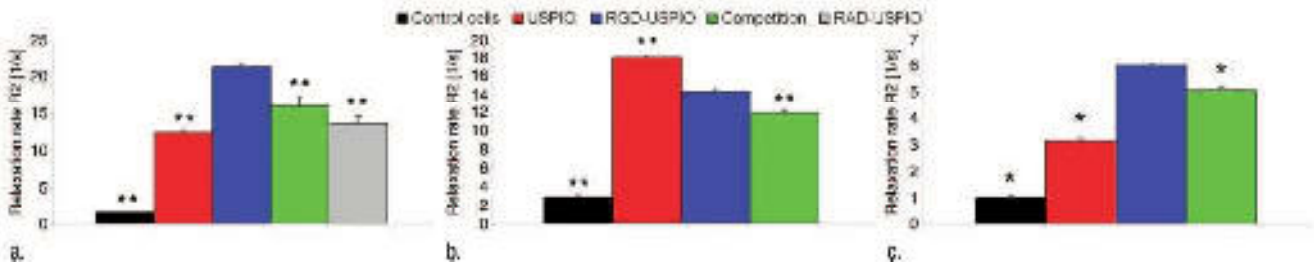

Figure 1: R2 relaxation rates of HUVECs, U87MG cells, and MLS cells suspended in gelatin and incubated for 1 hour with unlabeled USPIOs, with RGD-USPIOs, and under competition conditions. Means of five different ROIs per sample ± measurement errors are indicated. * = significant differences compared with RGD-USPIO incubated groups. **(a)** Compared with control cells (1.52 $sec^{-1} \pm 0.01$), R2 of HUVECs in gelatin was 12.35 $sec^{-1} \pm 0.24$ after incubation with unlabeled USPIOs and further increased to 21.39 $sec^{-1} \pm 0.47$ after incubation with RGD-USPIOs. Under competition condition, R2 only increased to 16.07 $sec^{-1} \pm 1.27$. R2 of RAD-USPIOs, which served as unspecific control in HUVECs, was 13.54 $sec^{-1} \pm 1.10$ and, hence, was in the same range as unlabeled particles. **(b)** In U87MG cells, RGD-USPIO uptake (R2 = 14.37 $sec^{-1} \pm 0.32$) was reduced compared with USPIO (R2 = 18.12 $sec^{-1} \pm 0.15$) and further decreased under competition condition (R2 = 11.97 $sec^{-1} \pm 0.29$). **(c)** R2 of MLS cells in gelatin increased more after RGD-USPIO (R2 = 6.05 $sec^{-1} \pm 0.06$) than USPIO (R2 = 3.13 $sec^{-1} \pm 0.10$) incubation. RGD-USPIO uptake was reduced under competition condition (R2 = 5.07 $sec^{-1} \pm 0.14$). * = $P <$ .05; ** = $P <$ .01.

Figure 2

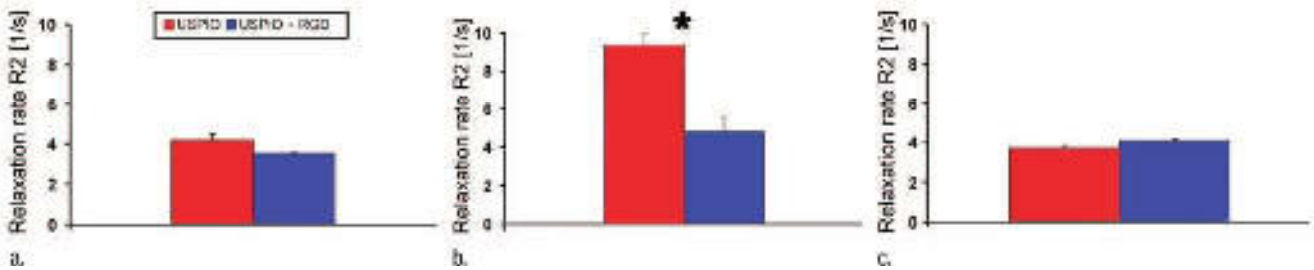

Figure 2: USPIO uptake in the presence of free RGD. **(a)** After 1-hour incubation with unlabeled USPIOs, R2 of HUVECs in gelatin was 4.19 $sec^{-1} \pm 0.30$ and decreased to 3.53 $sec^{-1} \pm 0.05$ when incubated with 10 000-fold excess of free RGD. **(b)** In U87MG cells, the inhibition of the uptake of unlabeled USPIOs by RGD was stronger than for the other cells. After 1-hour incubation, R2 was 9.40 $sec^{-1} \pm 0.64$ and decreased to 4.79 $sec^{-1} \pm 0.78$ in the presence of 1000-fold excess of free RGD. **(c)** In MLS cells, USPIO uptake is comparably high in presence and absence of RGD. After incubation with USPIO, R2 was 3.74 $sec^{-1} \pm 0.10$ and was 4.08 $sec^{-1} \pm 0.08$ when free RGD was added. * = significant differences ($P <$ .05) compared with RGD-USPIO incubated groups.

bated with RGD-USPIOs in the presence of 1000-fold excess of RGD.

Effect of RGD-USPIOs on Cadherin Expression

VE-cadherin was expressed at the lateral cell borders of HUVEC where the fasciae adherentes are localized, and there was no difference in staining intensity or localization when cells were incubated with medium or USPIOs. However, after incubation with RGD-USPIOs, an additional perinuclear staining of VE-cadherin occurred (Fig 3). A comparable result was obtained for MLS cells (not shown in Figure 3).

In contrast, the intercellular contacts of U87MG cells did not cover the entire lateral cell membranes and were more punctate. N-cadherin expression was also found at other plasma membrane compartments and in the perinuclear cytoplasm. There was no difference in cadherin distribution depending on incubation with unlabeled USPIO or medium. However, after incubation with RGD-USPIOs, membrane-associated cadherin staining was clearly reduced together with a strong enhancement of the cytoplasmic staining. At the same time, U87MG cells lost most of their intercellular contacts.

Incubation of U87MG cells with antibodies blocking $\alpha_v\beta_3$, α_v, and β_1 integrin also disintegrated cadherin-dependent intercellular contacts (Fig E3 and Appendix E1 [online]).

MR Imaging and Relaxometry of U87MG Tumor Xenografts in Nude Mice

Quantitative analysis of the changes in R2 relaxation rates ($\Delta R2$ = before injection − after injection) in tumors revealed significantly ($P < .05$) higher R2 after RGD-USPIO (2.4 $sec^{-1} \pm 1.5$) than after USPIO (0.3 $sec^{-1} \pm 0.2$) administration, indicating a higher uptake of RGD-USPIOs. Figure 4 shows the T2*-weighted appearances of these groups.

Histologic Evaluation of U87MG Tumor Xenografts

U87MG tumors showed a dense and homogeneous network of small vessels heterogeneously expressing $\alpha_v\beta_3$ integrins. $\alpha_v\beta_3$ integrin expression in U87MG tumor cells was also heterogeneous and occurred most strongly if the cells were localized near vascular networks (Fig 5).

Prussian blue staining revealed vascular and perivascular localization of RGD-USPIOs but no uptake by tumor cells (Fig 5), suggesting that preferential homing of RGD-USPIO to vascular structures is responsible for the change in R2. In control tumors, only a few unlabeled USPIOs were found in an unspecific distribution.

Figure 3

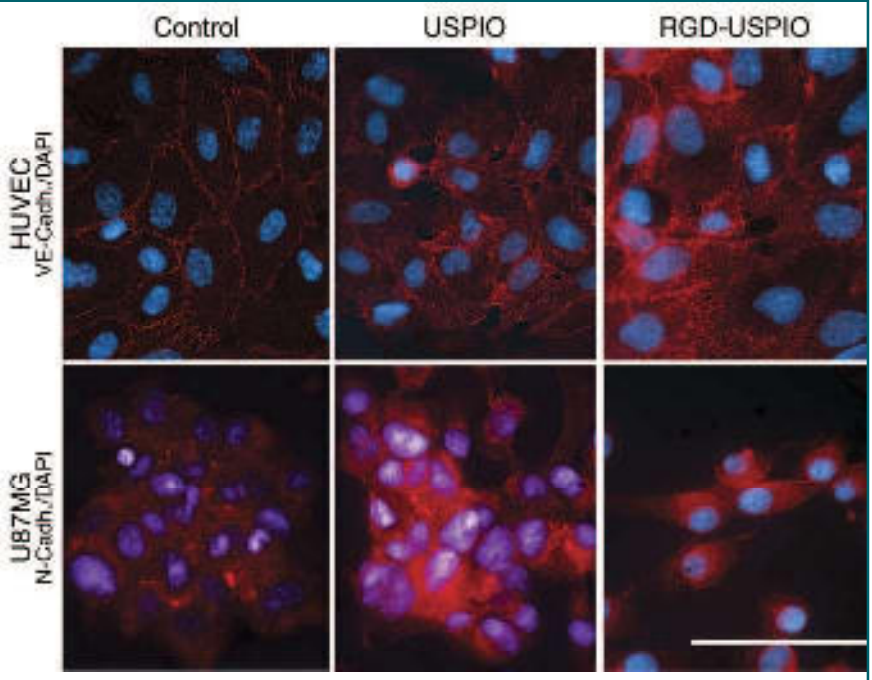

Figure 3: Immunofluorescence microscopy of HUVECs and U87MG cells. Staining (red) was performed against VE-cadherin *(VE-Cadh.)* (HUVEC) and N-cadherin *(N-Cadh.)* (U87MG) cells. Cell nuclei were stained with 4′,6-diamidino-2-phenylindole *(DAPI)* (blue). In HUVECs incubated with regular growth medium containing USPIO or not, VE-cadherin was located along the lateral cell membrane, which results in a netlike pattern of the cell monolayer at fluorescence microscopy. After RGD-USPIO incubation, this pattern is still present. However, an enhanced perinuclear staining also occurs. In U87MG cells incubated with regular growth medium in presence of USPIO or not, intercellular contacts are more punctual. While N-cadherin is most strongly expressed at intercellular contact zones, it can be located in other parts of the plasma membrane and perinuclearly. After incubation with RGD-USPIO, however, cells lose most of their intercellular contacts, round up, and separate from each other. Bar = 20 μm. (Original magnification, × 400.)

Discussion

RGD-coupled imaging compounds are frequently used to depict angiogenic tumor vessels and to label $\alpha_v\beta_3$ integrin–positive tumor cells (2,4,5,9–16,23,24). In nuclear medicine, radiolabeled diagnostic RGD compounds (13–16) are used in low doses (nanomolar scale) and thus relevant biologic effects were absent. MR imaging has a significantly lower sensitivity for RGD-labeled compounds than nuclear medicine. As a consequence, a high concentration of RGD-containing molecular MR probes must be accumulated in the target cell to induce a significant signal change in the tissue. Thus, biologic effects of RGD-labeled MR imaging probes in endothelial and tumor cells are of high interest.

As reported previously (5), HUVECs internalized RGD-USPIO more intensely than unlabeled and RAD-labeled USPIO, and RGD-USPIO uptake could be suppressed by compe-

tition with RGD. Controversially, U87MG cells accumulated USPIO more strongly than RGD-labeled ones, and the cyclic RDG-USPIO uptake further decreased under competition condition. Additionally, in U87MG tumor xenografts, RGD-USPIOs only accumulated in the vascular compartment but not in U87MG tumor cells. These results are in line with a recently published study by Xie and coworkers (25), who investigated the uptake of RGD-coupled iron oxide nanoparticles in U87MG tumors. Furthermore, in U87MG cells and HUVECs, the uptake of unspecific USPIO was reduced in the presence of RGD. Because we do not assume that unlabeled USPIO were internalized through an integrin-dependent pathway, RGD-USPIO and free RGD seemed to inhibit unspecific endocytosis in general. The latter assumption is supported by previous articles (26,27) on the inhibition of fibronectin-enhanced phagocytosis. Compared with U87MG cells, in HUVECs, the integrin-dependent inhibition of unspecific USPIO phagocytosis was less pronounced.

Both the unspecific and the receptor-mediated specific uptake contribute to the accumulation of RGD-USPIO in cells. In HUVECs, the significantly higher uptake of RGD-USPIO compared with USPIO most probably is because of a strong specific uptake but only a minor inhibition of the unspecific phagocytosis. In contrast, we assume that in U87MG cells the inhibition of unspecific accumulation was superior to the induction of a receptor-mediated RGD-USPIO uptake. In this case, internalized RGD-USPIO would mostly be attached to the integrin receptor, which should be validated in further experiments.

The question of why RGD-USPIOs block nonspecific endocytosis is raised. We excluded toxic effects of the particles on the cells because apoptotic cells have reduced biologic function. For U87MG and endothelial cells, it is known that long incubation with RGD peptide leads to cell death (28). This may be because blocking integrins causes a disruption of intercellular junctions (29), which leads to apoptosis if persisting during longer periods of time (30,31). However, our data suggest that incubation times chosen in our experiments were too short to increase cell death.

Intercellular junctions, including cadherins, are also known to be crucial for the maintenance of cell monolayer integrity, and their loss is important for malignant conversion of tumor cells (32,33). We demonstrated a loss of intercellular junctions in U87MG cells. It is assumed that integrin receptor-mediated signaling induces v-Src–mediated endocytosis of cadherins, presumably through phosphorylation of the cadherin complex (31). Integrins are able to regulate the intracellular calcium level, which has been shown to control adhesion and migration in a variety of cell types (34,35). We postulate that the initial loss of most intercellular contacts causes substantial cell stress to which the cells react with a reduction of phagocytotic activity and the synthesis of new cell contact proteins to reassemble monolayer integrity. This assumption is underlined by our findings that the pronounced loss of intercellular contacts coincided with reduced USPIO uptake.

The next question was why our

Figure 4

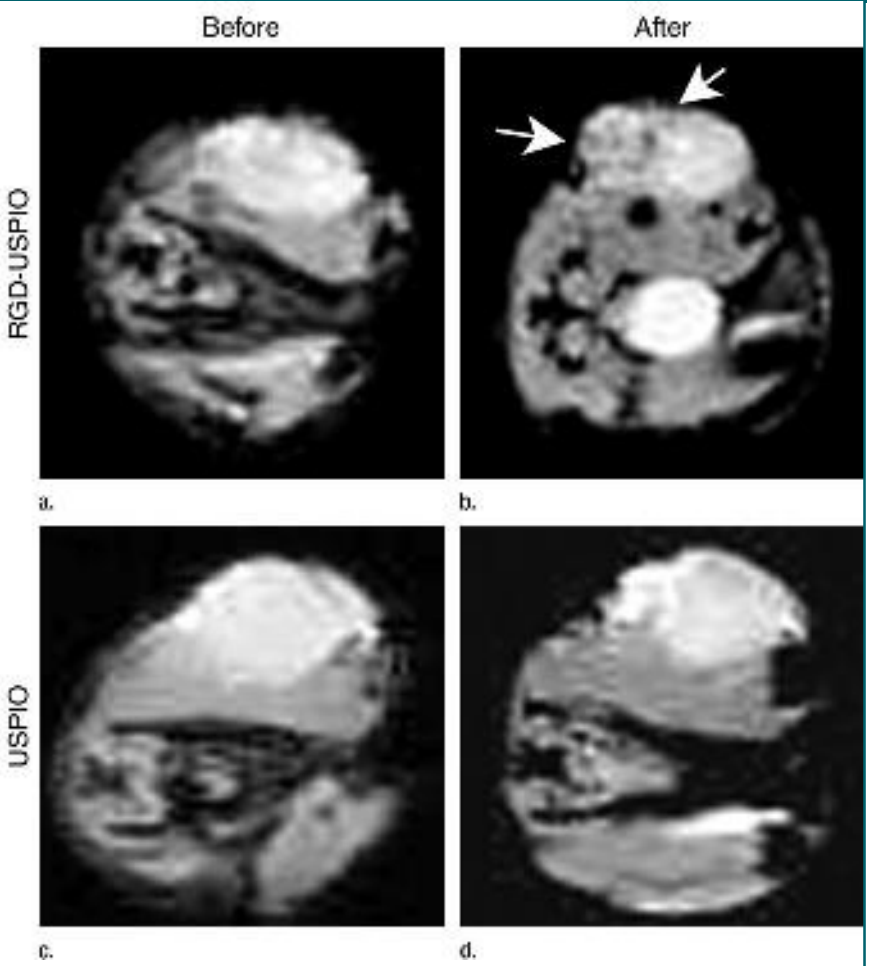

Figure 4: T2*-weighted MR images of tumors grown in mice that received RGD-USPIO **(a)** before injection and **(b)** 6 hours after injection and in mice that received unlabeled USPIO **(c)** before injection and **(d)** 6 hours after injection. Arrows = pronounced decrease in T2* signal intensity.

Figure 5

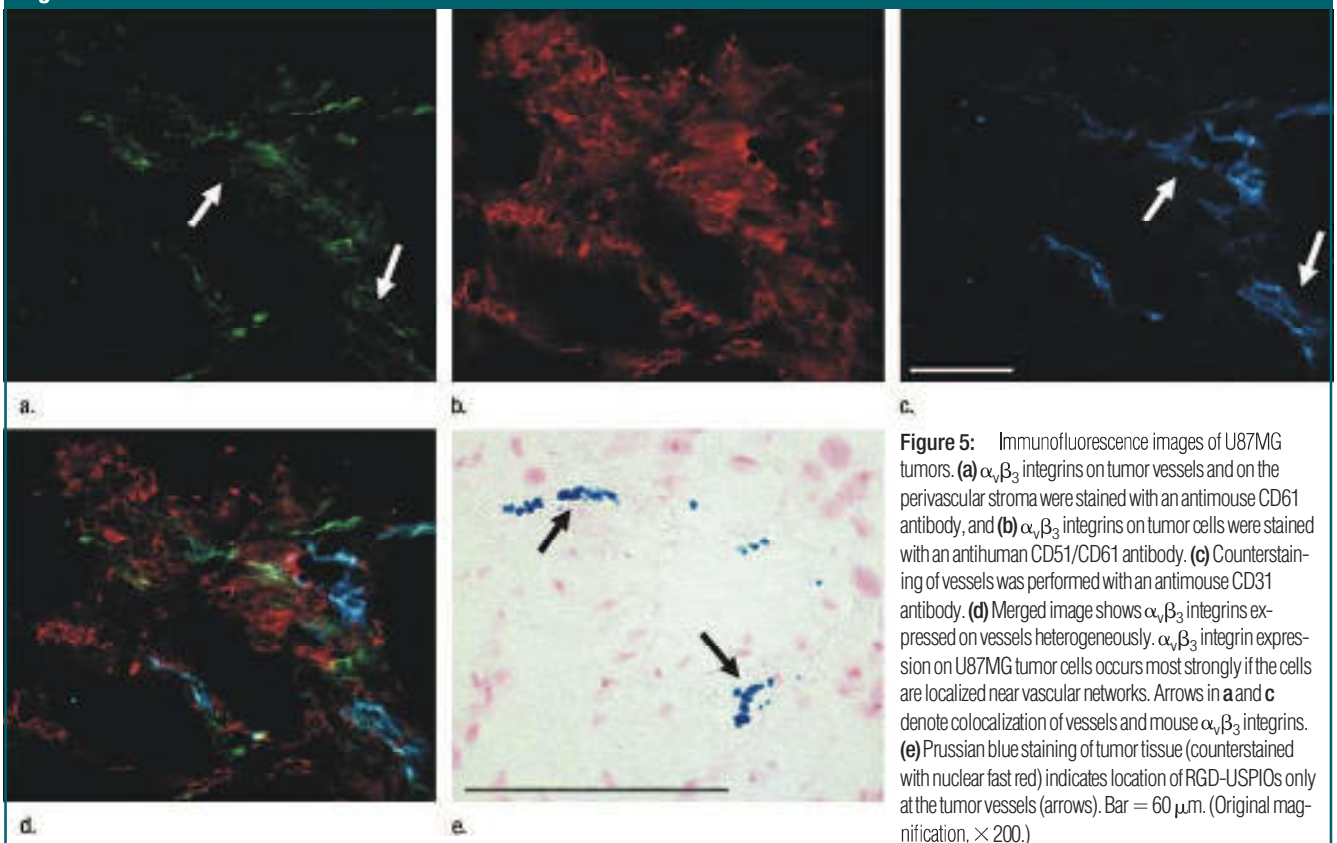

Figure 5: Immunofluorescence images of U87MG tumors. **(a)** $\alpha_v\beta_3$ integrins on tumor vessels and on the perivascular stroma were stained with an antimouse CD61 antibody, and **(b)** $\alpha_v\beta_3$ integrins on tumor cells were stained with an antihuman CD51/CD61 antibody. **(c)** Counterstaining of vessels was performed with an antimouse CD31 antibody. **(d)** Merged image shows $\alpha_v\beta_3$ integrins expressed on vessels heterogeneously. $\alpha_v\beta_3$ integrin expression on U87MG tumor cells occurs most strongly if the cells are localized near vascular networks. Arrows in **a** and **c** denote colocalization of vessels and mouse $\alpha_v\beta_3$ integrins. **(e)** Prussian blue staining of tumor tissue (counterstained with nuclear fast red) indicates location of RGD-USPIOs only at the tumor vessels (arrows). Bar = 60 μm. (Original magnification, × 200.)

three cell types reacted differently. One possible explanation for the much stronger reaction of U87MG to RGD compared with HUVECs and MLS cells is the lower quantity of differentiated intercellular contacts. In this context, particularly the MLS cells, which responded most weakly to RGD, are known to have substantial numbers of desmosomes, adherens junctions, and tight junctions (36,37). In HUVECs, monolayer integrity was not substantially affected by the blocking $\alpha_v\beta_3$ receptors with RGD-USPIO. In line with this assumption, immunofluorescence staining of cadherins continued to be prominent at the lateral cell borders after RGD administration, although perinuclear cadherin staining results point to integrin-dependent cadherin internalization (38,39). Another explanation for the differences between HUVECs, U87MG cells, and MLS cells can be the expressed integrin subtypes and their impact for cell adhesion.

Our study had limitations. We can only hypothesize about the molecular mechanism behind our findings, and future studies are needed to understand the interplay between integrin blockade, cadherin endocytosis, and decreased endocytotic activity. Our explanation of why some $\alpha_v\beta_3$ integrin–positive cells strongly respond to RGD and others do not needs further substantiation. Because integrins connect cells to interstitial components like fibronectin in vivo, further in vitro experiments should be performed on which the cells are grown on different matrices.

Another limitation of our in vivo approach was the high injected dose of RGD-USPIO. Our RGD-USPIOs underwent strong unspecific uptake by the reticuloendothelial system (5), which forced us to inject high doses to induce a sufficient signal change in tumors. Currently, we are trying to improve their pharmacokinetic properties by surface modifications. Nevertheless, this limitation weakened our conclusions because it was not intended to suggest our particles for clinical use and because more selectively accumulating RGD particles may not induce comparable biologic effects.

In conclusion, if molecular imaging is performed with high doses of diagnostic probes, biologic effects must be considered that can be highly divergent between different cells and may even include loss of cell adhesion and endocytotic activity.

Acknowledgments: We thank Renate Bangert and Birgit Hub for performing cell experiments and collecting immunohistochemistry data. An-

nette Kopp-Schneider, PhD, is acknowledged for performing the statistical analysis.

References

1. Sipkins DA, Cheresh DA, Kazemi MR, Nevin LM, Bednarski MD, Li KC. Detection of tumor angiogenesis in vivo by $\alpha_V\beta_3$-targeted magnetic resonance imaging. Nat Med 1998;4:623–626.
2. Temming K, Schiffelers RM, Molema G, Kok RJ. RGD-based strategies for selective delivery of therapeutics and imaging agents to the tumour vasculature. Drug Resist Updat 2005;8:381–402.
3. Cai W, Wu Y, Chen K, Cao Q, Tice DA, Chen X. In vitro and in vivo characterization of ^{64}Cu-labeled Abegrin, a humanized monoclonal antibody against integrin $\alpha_v\beta_3$. Cancer Res 2006;66:9673–9681.
4. Cai W, Shin DW, Chen K, et al. Peptide-labeled near-infrared quantum dots for imaging tumor vasculature in living subjects. Nano Lett 2006;6:669–676.
5. Zhang C, Jugold M, Woenne EC, et al. Specific targeting of tumor angiogenesis by RGD-conjugated ultrasmall superparamagnetic iron oxide particles using a clinical 1.5-T magnetic resonance scanner. Cancer Res 2007;67:1555–1562.
6. Carron CP, Meyer DM, Pegg JA, et al. A peptidomimetic antagonist of the integrin $\alpha_v\beta_3$ inhibits Leydig cell tumor growth and the development of hypercalcemia of malignancy. Cancer Res 1998;58:1930–1935.
7. Kerr JS, Wexler RS, Mousa SA, et al. Novel small molecule α_v integrin antagonists: comparative anti-cancer efficacy with known angiogenesis inhibitors. Anticancer Res 1999; 19:959–968.
8. Keenan RM, Miller WH, Kwon C, et al. Discovery of potent nonpeptide vitronectin receptor ($\alpha_v\beta_3$) antagonists. J Med Chem 1997;40:2289–2292.
9. Dayton PA, Pearson D, Clark J, et al. Ultrasonicanalysis of peptide- and antibody-targeted microbubble contrast agents for molecular imaging of $\alpha_v\beta_3$-expressing cells. Mol Imaging 2004;3:125–134.
10. Palmowski M, Huppert J, Kiessling F, et al. Molecular profiling of angiogenesis with targeted ultrasound imaging: early assessment of antiangiogenic therapy effects. Mol Cancer Ther 2008;7:101–109.
11. Hsu AR, Hou LC, Veeravagu A, et al. In vivo near-infrared fluorescence imaging of integrin $\alpha_v\beta_3$ in an orthotopic glioblastoma model. Mol Imaging Biol 2006;8:315–323.
12. Winter PM, Caruthers SD, Kassner A, et al. Molecular imaging of angiogenesis in nascent Vx-2 rabbit tumors using a novel $\alpha_v\beta_3$-targeted nanoparticle and 1.5 tesla magnetic resonance imaging. Cancer Res 2003;63:5838–5843.
13. Haubner R, Weber WA, Beer AJ, et al. Noninvasive visualization of the activated $\alpha_v\beta_3$ integrin in cancer patients by positron emission tomography and [18F]Galacto-RGD. PLoS Med 2005;2:e70.
14. Chen X, Hou Y, Tohme M, et al. Pegylated Arg-Gly-Asp peptide: ^{64}Cu labeling and PET imaging of brain tumor $\alpha_v\beta_3$-integrin expression. J Nucl Med 2004;45:1776–1783.
15. Jia B, Shi J, Yang Z, et al. ^{99m}Tc-labeled cyclic RGDfK dimmer: initial evaluation for SPECT imaging of glioma integrin $\alpha_v\beta_3$ expression. Bioconjug Chem 2006;17:1069–1076.
16. Li ZB, Wu Z, Chen K, Chin FT, Chen X. Click chemistry for (^{18})F-labeling of RGD peptides and microPET imaging of tumor integrin $\alpha_v\beta_3$ expression. Bioconjug Chem 2007;18:1987–1994.
17. Cruet S, Salamanca C, Mitchell GW, Auersperg N. $\alpha_v\beta_3$ and vibronectin expression by normal ovarian surface epithelial cells: role in cell adhesion and cell proliferation. Gynecol Oncol 1999;75:254–260.
18. Dijkgraaf I, Kruijtzer JA, Frielink C, et al. $\alpha_v\beta_3$ integrin-targeting of intraperitoneally growing tumors with a radiolabeled RGD peptide. Int J Cancer 2007;120:605–610.
19. Vellon L, Menendez JA, Lupu R. $\alpha_v\beta_3$ integrin regulates heregulin (HRG)-induced cell proliferation and survival in breast cancer. Oncogene 2005;24:3759–3773.
20. Huveneers S, van den Bout I, Sonneveld P, Sancho A, Sonnenberg A, Danen EH. Integrin $\alpha_v\beta_3$ controls activity and oncogenic potential of primed c-Src. Cancer Res 2007;67:2693–2700.
21. Beer AJ, Grosu AL, Carlsen J, et al. [^{18}F]galacto-RGD positron emission tomography for imaging of αvβ3 expression on the neovasculature in patients with squamous cell carcinoma of the head and neck. Clin Cancer Res 2007;13:6610–6616.
22. Li J, Tan H, Dong X, et al. Antisense integrin $\alpha_v\beta_3$ gene therapy suppresses subcutaneously implanted heptatocellular carcinomas. Dig Liver Dis 2007;39:557–565.
23. Kiessling F, Morgenstern B, Zhang C. Contrast agent and applications to assess tumor angiogenesis in vivo by magnetic resonance imaging. Curr Med Chem 2007;14:77–91.
24. Mulder WJ, Strijkers GJ, Habets JW, et al. MR imaging and fluorescence microscopy for identification of activated tumor endothelium using a bimodal lipidic nanoparticles. FASEB J 2005;19:2008–2010.
25. Xie J, Chen K, Lee HY, et al. Ultrasmall c(RGDyK)-coated Fe_3O_4 nanoparticles and their specific targeting to integrin $\alpha_v\beta_3$-rich tumor cells. J Am Chem Soc 2008;130: 7542–7543.
26. Wittwer D, Wiesner A. Peptide RGDS inhibits the fibronectin-enhanced phagocytosis of yeast cells by galleria mellonella hemocytes in vitro. J Invertebr Pathol 1996; 68:199–200.
27. Gresham HD, Adams SP, Brown EJ. Ligand binding specificity of the leukocyte response integrin expressed by human neutrophils. J Biol Chem 1992;267:13895–13902.
28. Chatterjee S, Matsumura A, Schradermeier J, Gillespie GY. Human malignant glioma therapy using anti-$\alpha_v\beta_3$ integrin agents. J Neurooncol 2000;46:135–144.
29. Guo W, Giancotti FG. Integrin signalling during tumor progression. Nat Rev Mol Cell Biol 2004;5:816–826.
30. Bates RC, Buret A, van Helden DF, Horton MA, Burns GF. Apoptosis induced by inhibition of intercellular contact. J Cell Biol 1994;125:403–415.
31. Erdreich-Epstein A, Tran LB, Cox OT, et al. Endothelial apoptosis induced by inhibition of integrins $\alpha_v\beta_3$ and $\alpha_v\beta_5$ involves ceramide metabolic pathways. Blood 2005; 105:4353–4361.
32. Vleminckx K, Vakaet L Jr, Mareel M, Fiers W, van Roy F. Genetic manipulation of E-cadherin expression by epithelial tumor cells reveals an invasion suppressor role. Cell 1991;66:107–119.
33. Perl AK, Wilgenbus P, Dahl U, Semb H, Christofori G. A causal role for E-cadherin in the transition from adenoma to carcinoma. Nature 1998;392:190–193.
34. Sjaastad MD, Nelson WJ. Integrin-mediated calcium signaling and regulation of cell adhesion by intracellular calcium. Bioessays 1997;19:47–55.
35. Schwartz MA, Denninghoff K. α_v integrins mediate the rise in intracellular calcium in endothelial cells on fibronectin even though they play a minor role in adhesion. J Biol Chem 1994;269:11133–11137.
36. Schiffenbauer YS, Meir G, Maoz M, Even-Ram SC, Bar-Shavit R, Neeman M. Gonadotropin stimulation of MLS human epithelial ovarian carcinoma cells augments cell adhesion mediated by CD44 and by α_v-integrin. Gynecol Oncol 2002;84:296–302.
37. Granot D, Addadi Y, Kalchenko V, Harmelin A, Kunz-Schughart LA, Neeman M. In vivo imaging of the systemic recruitment of fibroblasts to the angiogenic rim of ovarian carcinoma tumors. Cancer Res 2007;67: 9180–9189.
38. Bryant DM, Wylie FG, Stow JL. Regulation of endocytosis, nuclear translocation, and signalling of fibroblast growth factor receptor 1 by E-cadherin. Mol Biol Cell 2005;16: 14–23.
39. Balzac F, Avolio M, Degani S, et al. E-cadherin endocytosis regulates the activity of Rap1: a traffic light GTPase at the crossroads between cadherin and integrin function. J Cell Sci 2005;118:4765–4478.

Fluorescent magnetoliposomes as a platform technology for functional and molecular MR and optical imaging

Michael Hodenius[a,f,*], Christian Würth[b,*], Jabadurai Jayapaul[a], John Wong[d], Twan Lammers[a], Jessica Gätjens[a], Susanne Arns[a], Natascha Mertens[a], Ioana Slabu[e], Gergana Ivanova[e], Jörg Bornemann[g], Marcel De Cuyper[c,f], Ute Resch-Genger[b,**], Fabian Kiessling[a,**]

[a] Chair of Experimental Molecular Imaging, University of Aachen (RWTH), Aachen, Germany;
[b] Federal Institute for Materials Research and Testing, Berlin, Germany;
[c] Interdisciplinary Research Centre, K.U.Leuven-Campus Kortrijk, Kortrijk, Belgium;
[d] Chemical Process Engineering, University of Aachen (RWTH), Aachen, Germany;
[e] Applied Medical Engineering, Helmholtz-Institute, University of Aachen (RWTH), Germany;
[f] IMIR (In vivo Molecular Imaging Research group K.U.Leuven);
[g] Elektronenmikroskopische Einrichtung (EME), University of Aachen (RWTH), Aachen,
[*] Michael Hodenius and Christian Würth contributed equally to this manuscript.
[**] Corresponding authors: F. Kiessling, Chair of Experimental Molecular Imaging, University of Aachen (RWTH), Pauwelsstrasse 20, 52074 Aachen, Germany. (Tel): +49-241-8080116; (fax): +49 241 803380116; E-mail: fkiessling@ukaachen.de; U. Resch-Genger, Federal Institute for Materials Research and Testing, Richard-Willstätter-Straße 11, 12489 Berlin, Germany. (Tel): +49-30-8104-1134; (fax): +49-30-8104-1157; E-mail: Ute.Resch@bam.de.

1. INTRODUCTION

Numerous imaging modalities like magnetic resonance imaging (MRI), positron emission tomography (PET), computed X-ray tomography (CT), and optical imaging (OI) and their combinations such as PET-CT, PET-MRI and SPECT-CT have been developed to optimize the visualisation of pathologic conditions (1). For instance, in combining MRI and OI, a high spatial resolution, excellent soft tissue contrast and high anatomical detail provided by MRI can be combined with the high sensitivity of fluorescence imaging.

Frequently used MRI probes, such as the FDA approved Endorem and Resovist are superparamagnetic iron oxide nanoparticles (SPIO), which are routinely employed for the detection of malignant liver lesions (2). Ultrasmall SPIO (USPIO) with hydrodynamic diameters (D_h values) below 40 nm have an enhanced blood circulation time and are able to extravasate, which was proven to be promising for lymph node and bone marrow imaging (3,4). The comparatively few studies pursuing specific (U)SPIO accumulation in other malignant tumor tissues, include mainly dextran-coated USPIO, conjugated to e.g. human transferrin or tumor-specific monoclonal antibodies (5,6). However, dextran can desorb from the iron oxide surface, and may elicit allergic reactions (7,8).

Biocompatible magnetoliposomes (ML) are very attractive alternatives, which are built up of magnetite nanocores coated with a phospholipid bilayer. The inner layer phospholipids are tightly bound to the iron oxide surface by strong chemisorption forces (9), whereas the outer layer can be easily doped with fluorescent molecules and probes,

functionalised lipids, and differently charged amphiphiles enabling e.g. a finetuning of optical properties and the surface charge (10,11).

Although there is an increasing interest in fluorescent and magnetic materials, a systematic assessment of the influence of magnetic species like iron oxide on dye photophysics is rare. For example, a reduction in dye emission is been often reported for fluorescent magnetic particles for cell labelling and small animal imaging, yet not quantified (12-14).This motivated us to characterise the physicochemical of fluorescent ML containing dimyristoyl-*sn*-glycero-3-phosphoethanol-amine-*N*-(lissamine rhodamine B) (DMPE-L-R) in detail using steady state and time resolved fluorometry. In particular, the influence of the presence of superparamagnetic iron oxide cores, the number of DMPE-L-R molecules per particle, and the overall particle (DMPE-L-R) concentration, on the fluorescence properties of these materials were studied. Finally, the cytotoxicity and intracellular uptake of these new imaging reagents were investigated using human prostate cancer (PC-3) cells. The overall goal was here to underline the high potential of fluorescent ML as bimodal contrast agents for functional and molecular MR and optical imaging and to address the need for a better characterisation of the signal-relevant physico-chemical properties of such nanomaterials for future probe design and applications.

2. RESULTS AND DISCUSSION

2.1. Characterisation of classical and fluorescent ML and SUV

2.1.1. Core diameter, chemical composition, and D_h- and zeta values

Statistical analysis of the magnetite core diameter distribution by number as determined from transmission electron microscopy (TEM) images revealed average diameters of 9.9±3.2 nm, 9.7±3.1 nm, and 9.2±3.2 nm for the ML without DMPE-L-R (C-ML), and the fluorescent ML containing a low and a high molar DMPE-L-R fraction (FLU-ML 1 and 2, respectively). These values are very similar to the average core diameter of 9.4±2.8 nm for laurate (LA) coated magnetite particles acting here as the magnetic precursor cores for ML production (15).With FLU-ML 2, for instance, 76 % of the core diameters are between 6 and 12 nm (see SI). The almost uniform values for the phospholipid to Fe_3O_4 ratio ([PL]/Fe_3O_4 ratio) of the ML in the order of 0.39 - 0.47 M/kg, testify that in C-ML and both fluorescent ML the lipid content of the coating is not affected by including DMPE-L-R in the lipidic envelope. The hydrodynamic diameters (D_h values) measured for the final ML preparations were between 91.5 and 100.1 nm. Accordingly, the overall diameter of our fluorescent magnetoliposomes is about tenfold bigger than the single

magnetite core diameter and three- to fourfold bigger than the D_h values of the corresponding small unilamellar vesicles (SUV) (25.5 - 33.5 nm). The size of the D_h values suggest that the ML colloids exist as clusters of particles. Thus, the kinetic barrier for particle growth is apparently reached at D_h values of 90 - 100 nm (15). Although the various ML types are less negatively charged (zeta potential (ζ) values of -22.8 mV to -36.0 mV) compared to the LA-coated magnetite particles (ζ value: -47.3±1.4), the colloidal stability of the starting magnetic fluid is not hampered by substituting the LA molecules by phospholipids.

Concerning the chemical composition of the ML coat, it is remarkable that the molar DMPE-L-R fractions of 0.67 % and 1.97 % in FLU-ML 1 and 2, respectively, exceed that of the corresponding starting SUV (FLU-SUV 1: 0.31 % DMPE-L-R and FLU-SUV 2: 0.84 % DMPE-L-R) by a factor of about 2. This observation can be rationalised considering the difference in membrane curvature of the SUV (D_h = 25.5 - 33.5 nm) and that of the ML (D_h = 91.5 - 100.1 nm). In the case of differently sized liposomes, it is well known from the literature that lipid packing shows less defects in structures with a bigger radius as compared to liposomes with a small radius as in the case of SUV. Since DMPE-L-R contains two negative charges at the pH conditions used, it will be very prone to escape from the vesicles and, at equilibrium, it will preferentially reside in the larger ML. Also the idea of a stronger anchoring of lipophilic molecules, e.g. the cationic 1,2-distearyl-3-trimethylammonium propane in ML complexes as compared to liposomes was put forward by Soenen et al. (16). Similarly, Zhang et al. found a slower, more sustained release of the lipophilic anticancer agent paclitaxel from intraveneously applied ML compared to conventional liposomes in grafted tumors of BALB/C mice (17).

2.1.2. Fluorescence intensities of DMPE-L-R containing SUV and ML

The fluorescence spectra of SUV doped with DMPE-L-R show that the resulting emission intensities (rel. $FI_{em.}$) are proportional to particle concentration (see also SI, inset Figure S2A and S2B). Concentration-normalised emission intensities ($FI_{em.660}$, normalisation at an emission wavelength of 660 nm) were calculated and plotted vs. the DMPE-L-R concentration (Figure 1A and B). As follows from Figure 1A, for FLU-SUV 1 and 2, the $FI_{em.660}$ values decreased linearly by approximately 20 % with increasing DMPE-L-R concentration from 15 to 4500×10^{-9} M.

The corresponding emission spectra normalised at 626 nm at the vibronic shoulder do not reveal a red shift of the spectral position of the emission maximum and the blue wing of the emission band which are characteristic for inner filter effects. This is exemplary shown for FLU-SUV 2 in Figure 1C. The 20 to 26 % decrease of the $FI_{em.660}$ for FLU-SUV 2 compared to FLU-SUV 1 (Figure 1A) can be ascribed to the higher molar DMPE-L-R fraction of the

FLU-SUV 2 that increases the probability for the formation of non or barely fluorescent aggregates or other traps acting as energy sinks. The latter can involve fluorescence resonance energy transfer (FRET) from fluorescent monomers to non or only slightly emissive aggregates or FRET between chemically identical, yet spectroscopically different species differing in fluorescence quantum yield (18-20).

Also the fluorescent magnetoliposomes FLU-ML 1 and 2 (molar DMPE-L-R fractions of 0.67 and 1.97 %, respectively) revealed substantial fluorescence intensities at 15×10^{-9} M and higher DMPE-L-R concentrations (S2C and S2D in the SI). At low ML concentrations, the spectral shape of their $FI_{em.660}$ spectra match that of their magnetite-free counterparts (Figure 1D and SI (Figure S3)). However, the resulting $FI_{em.660}$ were much lower than those observed for the corresponding SUV within the whole DMPE-L-R concentration range studied (Figure 1A and B). Moreover, the drop of the $FI_{em.660}$ signal observed for FLU-ML 2 reached 63 % compared to only 20 % for FLU-SUV 2 upon increasing the DMPE-L-R concentration from 15 to 4500×10^{-9} M. These effects are attributed to the strong absorption of both excitation and emitted light by the magnetite core (inner filter effects). Also fluorescence quenching e.g. due to the heavy atom effect and superparamagnetism of iron oxide may contribute to the reduction in the measured emission intensities (21-23).

2.1.3. Absolute fluorescence quantum yields (Φ_f) *and fluorescence decay behaviour*

For a better understanding of the operative fluorescence quenching pathways, the Φ_f and the fluorescence decay behaviour of FLU-SUV were investigated for a DMPE-L-R content ranging from 0.31 to 4.81 mol %. For the measurements of Φ_f with the integrating sphere, re-absorption of emitted light due to the considerable spectral overlap of the absorption and emission band of FLU-SUV (see Figure 1C) was considered as previously described (24). For the extensively studied FLU-SUV 1 and 2 (DMPE-L-R fraction of 0.31 % and 0.84 %), the Φ_f were determined to 0.55±0.01 and 0.47±0.02, respectively. As shown in Figure 2 (right panel), the fluorescence quantum yield and the mean fluorescence lifetime τ_{int} are diminished with increasing DMPE-L-R concentration. This is consistent with earlier discussed FRET models in membranes (25,26).

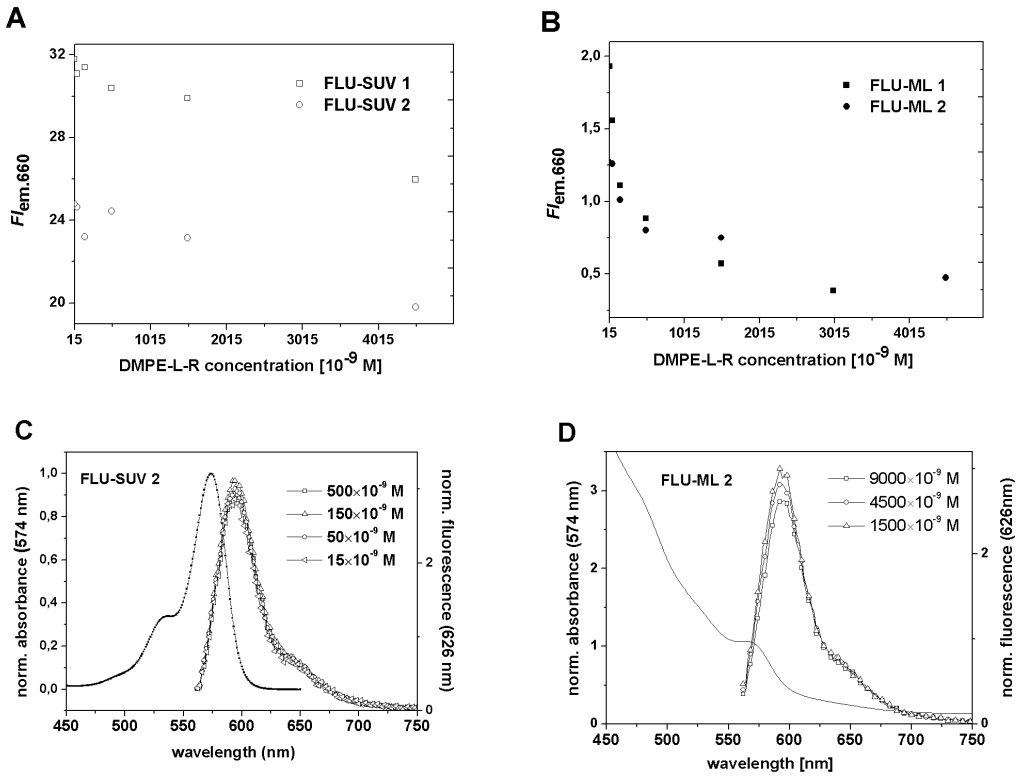

Figure 1

Figure 1. $FI_{em.660}$ as function of the particle (DMPE-L-R) concentration for both fluorescent SUV (**A**) and ML types (**B**). Normalised absorption spectrum (574 nm) and normalised uncorrected fluorescence spectra (626 nm) for varying DMPE-L-R concentrations for FLU-SUV 2 (**C**) and FLU-ML 2 (**D**). Excitation was at λ = 532 nm.

The straighforward determination of the Φ_f of FLU-ML was hampered by i) the strong absorption of the iron oxide nanoparticles at the excitation wavelength of 535 nm and ii) within the emission wavelength region of DMPE-L-R (*ca*. 550 nm to 750 nm) as well as by iii) self-absorption of the emitted photons by the fluorophore itself. The absorption of the iron core at the excitation wavelength was considered (see SI), whereas both the absorption of emitted photons by the magnetite core and DMPE-L-R-related re-absorption effects were neglected. Based on these assumptions, the Φ_f of FLU-ML 1 and 2 were determined to be 0.16±0.04 and 0.13±0.06, respectively. These values present lower limits of the actual fluorescence quantum yields of these materials.

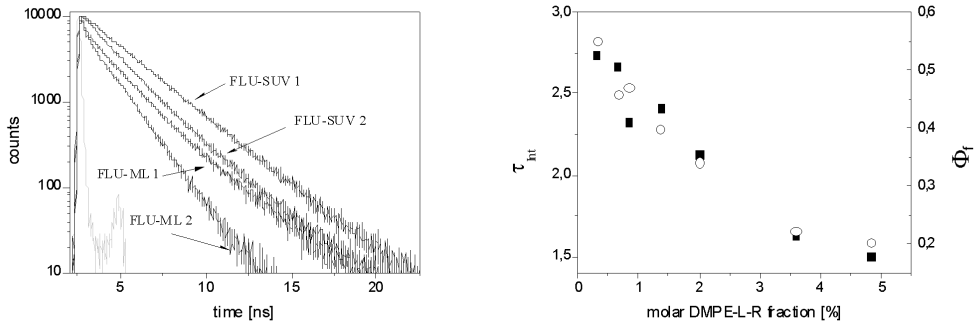

Figure 2

Figure 2. left panel: Fluorescence decay kinetics of FLU-SUV 1 and 2 and FLU-ML 1 and 2 in bi-distilled water and instrument response function (gray): right panel: Φ_f (○) and mean fluorescence lifetime τ_{int} (■) as function of molar DMPE-L-R fraction in FLU-SUV.

The considerably high measurement uncertainties found for FLU-ML 1 and 2 compared to those of the FLU-SUVs originate from the relatively high absorbance of the magnetite core at the excitation wavelength, compared to the absorbance of the fluorophore (see SI). The fluorescence decay kinetics of FLU-SUV 1 and 2 and FLU-ML 1 and 2 in bi-distilled water are summarised in Table 1 and Figure 2 (left panel). In all cases, double or tri-exponential decay kinetics are observed that display a clear influence of the DMPE-L-R content and the presence of superparamagnetic iron oxide nanoparticles on both the size and amplitude of the different decay components. Significantly, only the FLU-ML reveal a short-lived decay component with a lifetime τ_3 of 0.12 ns to 0.14 ns that is absent for the FLU-SUV.

Contrary, for FLU-ML 2 containing the highest molar DMPE-L-R fraction, the long lived decay component with a lifetime τ_1 of *ca*. 2.7 ns to 2.9 ns is absent. The influence of the fluorophore fraction and the presence of superparamagnetic iron oxide are similarly reflected by the average lifetimes of the samples (Table 1 and Figure 2).

The fluorescence lifetime τ_2 (1.32 ns to 1.78 ns) which is present for all samples lies very close to the fluorescence lifetime of 1.3 ns to 1.7 ns reported for rhodamine B dissolved in water (27,28).The lifetime $\tau_1$is comparable to the fluorescence lifetime of rhodamine B of 2.3 ns to 2.7 ns found in less polar ethanol (27). The most plausible explanation for the double exponential decay kinetics of FLU-SUV and the lifetimes τ_1 and τ_2 found for FLU-ML 1 seems to be two different surroundings of the rhodamine B molecules. The longer lifetime τ_1 is attributed to fluorophores in a less polar or more rigid environment that prevents or slows down TICT (twisted intramolecular

charge transfer) in rhodamine B (29). The absence of this lifetime in FLU-ML 2 may be ascribed to an enhanced FRET compared to FLU-ML 1 due to the higher fluorophore density.

Table 1. Fluorescence decay kinetics of FLU-SUV 1 and 2 and FLU-ML 1 and 2 in bi-distilled water. τ_i represent the lifetimes of the different decay components, $A(\tau_i$the fractional Intensities, τ_{int} the (intensity-weighted) mean lifetime and ♍ a parameter to judge the quality of the fits (see SI).

sample	molar DMPE-L-R fraction [%]	$A(\tau_1)$ [%]	τ_1 [ns]	$A(\tau_2)$ [%]	τ_2 [ns]	$A(\tau_3)$ [%]	τ_3 [ns]	τ_{Int} (eq. 3)	♍
FLU-SUV 1	0.31	83.0	2.89	17.0	1.78	-	-	2.74	0.98
FLU-SUV 2	0.84	71.8	2.69	28.2	1.40	-	-	2.33	0.97
FLU-ML 1	0.67	49.1	2.75	43.4	1.32	7.5	0.119	1.93	1.04
FLU-ML 2	1.97	-	-	88.5	1.48	11.5	0.142	1.33	1.13

The very short lifetimes τ_3 of 0.12 ns to 0.14 ns found exclusively for the FLU-ML (Table 1) can be ascribed to rhodamine B molecules located in the very close neighbourhood of the fluorescence quenching superparamagnetic iron oxide core, i.e., to DMPE-L-R molecules in the phospholipid leaflet directly attached to the magnetite nanoparticle surface. Possibly, these strongly quenched rhodamine B molecules act as acceptors and energy sinks for other fluorophores residing in the outer phospholipid layer in a distance sufficiently small for FRET. The reduction in average τ_{int} and Φ_f parallels the considerable decrease in fluorescence intensity of the FLU-ML compared to the FLU-SUV shown in Figure 1.

2.1.4. MR relaxivities.

Linear regression (least square method) of the blank-corrected transversal relaxation rates ($R2_{corr.}$ values) as function of iron concentration revealed T_2 relaxivities (r_2 values) of 465±9 $s^{-1}mM^{-1}$ and 440±4 $s^{-1}mM^{-1}$ for FLU-ML 1 and 2 as compared to the r_2 value of 554±11 $s^{-1}mM^{-1}$ found for C-ML (see Figure S5 in the SI). These values exceed the r_2 value of the LA-coated precursor particles (332±15 $s^{-1}mM^{-1}$) by a factor of *ca*. 1.5 and are even about twice as high as the r_2 value of 233±1 $s^{-1}mM^{-1}$ obtained for the commercial SPIO contrast agent Resovist, which is a FDA approved MRI contrast agent with a core diameter of 4.2 nm, and a D_h value of 60 nm ($R2_{corr.}$ values not shown in Figure S5). Since the ML particles form small clusters (D_h value: 91.5 - 100.1 nm), their extremely high r_2 values are in agreement with the data reported by Roch et al. (30) which report an increase in T_2 relaxation by proton diffusion, induced by magnetic field gradients around particle aggregates with enhanced magnetization.

In contrast to the T_2 relaxation, T_1 relaxation depends on a fast proton exchange between the bulk water phase with slow T_1 relaxation, and protons at the surface of magnetic particle aggregates, where T_1 relaxation is fast. Since the

residence time of protons (τ_D) is roughly proportional to the square of the particle size, this can explain the observed two- to threefold lower r_1 values of the ML of 3.59±0.13 $s^{-1}mM^{-1}$ (C-ML), 2.06±0.03 $s^{-1}mM^{-1}$ (FLU-ML 1), and 2.73±0.27 $s^{-1}mM^{-1}$ (FLU-ML 2), respectively, compared to Resovist (6.84 $s^{-1}mM^{-1}$).

2.2. In Vitro Studies on human PC-3 Cells

2.2.1. Viability of ML-incubated cells

In order to determine whether C-ML, FLU-ML 1, and FLU-ML 2 and the corresponding SUV show a potential dose- and time-dependent cytotoxicity on PC-3 cells, uptake studies with these materials were performed and the cells´ plasma membrane integrity and mitochondrial activity were evaluated by the trypan blue and MTT assay. The trypan blue assay revealed completely retained viabilities after 3 h incubation with all samples incubated at Fe concentrations of 0.03×10^{-3} M, 0.3×10^{-3} M and 3×10^{-3} M (data not shown). Incubation for 24 h reveals a viability decrease of 7 to14 % for the highest concentration of the ML (Figure 3A). Since under these conditions, no toxicity was noticed with the SUV-based structures (Figure 3B), the observed ML toxicity apparently originates from the magnetite cores. Incubation for 24 h with ML concentrations equaling 0.3×10^{-3} M and 3×10^{-3} M Fe, however, yielded apparent viabilities above 100 % with the MTT assay. This can be ascribed to a progressive accumulation of the magnetite particles in the lysosomes and subsequent formation of reactive oxygen species (ROS) (31,32). ROS species have been suggested to alter the cellular redox equilibrium state, and, as a result can enhance the reduction of the MTT salt used (16).

2.2.2. Visualisation of internalised ML in labelled PC-3 cells with TEM and fluorescence microscopy.

Detection of internalised fluorescent ML in PC-3 cells was done by TEM. After 3 hours of incubation with FLU-ML 2 (3×10^{-3} M Fe) and subsequent removal of excess ML, the images point to a moderate ML uptake, with the MLs mainly appearing as larger aggregates embedded in the endosomal and lysosomal vesicles as indicated by the arrows in Figure 4 (right).

Internalised fluorescent ML could be also visualised by fluorescence microscopy. PC-3 cells incubated with FLU-ML 2 and 1 (3×10^{-3} M Fe concentration) for 3 h are shown in Figure 5A and 5B (to localise the cells, the nuclei were stained with 4'-6-diamidino-2-phenylindole (DAPI)). Excitation at 557 nm yielded bright red emission from the

cytoplasm of the PC-3 cells treated with FLU-ML 2 and a less intense fluorescence with FLU-ML 1 under the same conditions. These observations are in line with the above described relative fluorescence intensity measurements of the aqueous ML samples, revealing a more than twofold higher fluorescence intensity for FLU-ML 2 compared to FLU-ML 1 at virtually the same particle concentration.

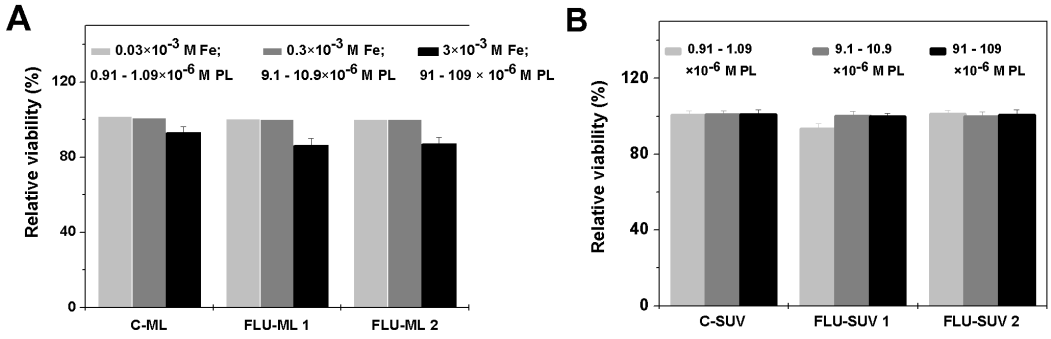

Figure 3

Figure 3. Relative viability measured by the trypan blue assay after 24 h incubation of PC-3 cells with 0.03, 0.3 and 3×10^{-3} M Fe concentrations of nonfluorescent and fluorescent ML (**A**) and the corresponding SUV (**B**). For the SUV preparations, the [PL] was carefully taken to be identical to those encountered in the corresponding ML systems. The viabilities are given relative to that of control cells not incubated with ML, but otherwise treated identically. The error bars indicate standard error of the mean (± SEM (n = 3)).

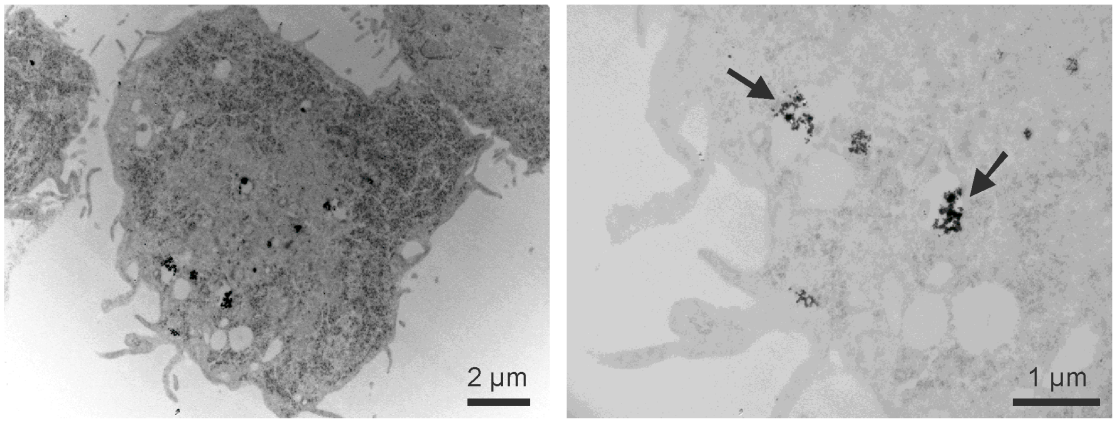

Figure 4

Figure 4. TEM images of PC-3 cells incubated with FLU-ML 2 for 3 h. The left TEM image shows an overview of a PC-3 cell slice. The right TEM image depicts the enlargement of the lower left part of the cell slice showing both magnetic particles lying free in the cytoplasm and clustered within endosomal and lysosomal vesicular structures (indicated by arrows).

To rule out unspecific background fluorescence, e.g. originating from proteins or other biomolecules in the cytoplasm, control experiments were performed with C-ML (Figure 5C) and cells incubated with ML-free medium for 3 h (Figure 5D). These images revealed no purple overlay spots, indicating the absence of ML in the nucleus.

2.2.3. T_2 and T_1 relaxation rates of incubated PC-3 cells in 10 % gelatine.

The traceability of incubated PC-3 cells in phantoms (10 % gelatine; 3.67×10^7 cells/mL) was controlled with MR relaxometry at 3 T after incubation for 3 h with LA-coated magnetite, C-ML or FLU-ML 2. For each particle type, the Fe concentrations were 0.03×10^{-3} M, 0.3×10^{-3} M, and 3×10^{-3} M, respectively. PC-3 cells incubated with C-SUV or FLU-SUV 2 at the same [PL] as used in the corresponding ML samples or with pure medium served as controls.

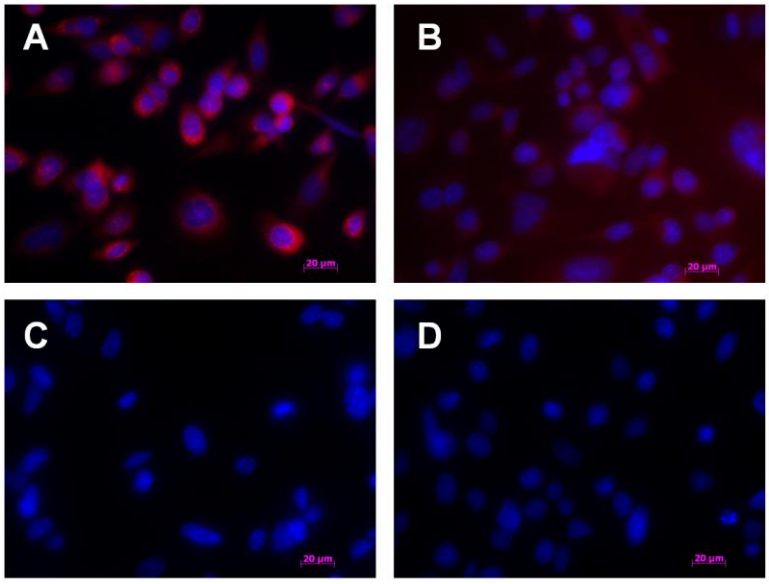

Figure 5

Figure 5. Fluorescence microscopy images of the DMPE-L-R and DAPI fluorescence of PC-3 cells incubated with (**A**) FLU-ML 2, (**B**) FLU-ML 1, and (**C**) C-ML for 3 h. The Fe concentration was adjusted to 3×10^{-3} M for all ML. An image of PC-3 cells incubated with ML-free medium for 3 h is shown as additional control (D). The nuclei were stained with DAPI.

As shown in Figure 6 , at the lowest iron concentration, the R2 value of 2.43±0.09 s^{-1} was slightly increased with LA-coated magnetite compared to PC-3 cells in pure medium (R2: 1.96±0.10 s^{-1}) For the ML, no changes were observed.

However, incubation at higher Fe concentrations (0.3×10^{-3} M and 3×10^{-3} M Fe) of LA-coated magnetite, C-ML and FLU-ML 2 led to increased R2 values of 3.01 - 3.69 s^{-1}, and even higher R2 values of 5.29 - 5.70 s^{-1}. To determine the r_2 value of ''internalised'' magnetite, we first subtracted the R2 value of 1.96±0.10 s^{-1} for PC-3 control cells in pure medium from the averaged R2 of 3.27±0.37 s^{-1} for incubated PC-3 cells (0.3×10^{-3} M Fe concentration of LA

coated magnetite, C-ML and FLU-ML 2) yielding a corrected, averaged R2 value of 1.39±0.23 s^{-1}. This value was divided by 1.43×10^{-5} M Fe, which is the corresponding Fe concentration of the PC-3 cell suspensions incubated with 0.3×10^{-3} M Fe after correction for the blank Fe concentration. This calculation yielded an averaged ''internalised r_2 relaxivity'' of 97.2±15.8 $s^{-1}mM^{-1}$ for the three magnetic colloids. Thus, the r_2 value of the magnetic particles was decreased by a factor 4.6±1.9 upon their internalisation, considering the averaged r_2 value of 450±112 $s^{-1}mM^{-1}$ for free particles in water.

Similarly, Bulte et al. found an approximately five-fold decreased r_2-value of internalised magnetodendrimers in human cervix carcinoma (HeLa) cells compared to magnetodendrimers in solution (33).We assume that the observed internalisation-induced decrease in r_2 relaxivity was the consequence of the predominant accumulation of the particles as larger clusters in endosomal and lysosomal compartments. This leads to a strong decrease of exchange velocities of bulk water phase molecules with the rapidly-relaxed protons residing at the magnetic structures and induces a strong increase of the τ_D to the ms scale of compartmentalised magnetic particles compared to free particles in water, which have a τ_D in the μs range (34).

Concerning longitudinal relaxation, no increased R1 were observed for the incubated PC-3 cell suspensions compared to control cell suspensions (data not shown). This is a consequence of the comparably low r_1 relaxivities of LA-coated magnetite, C-ML, and FLU-ML 2 in the range of 2.73 - 4.90 s^{-1} mM^{-1} in water.

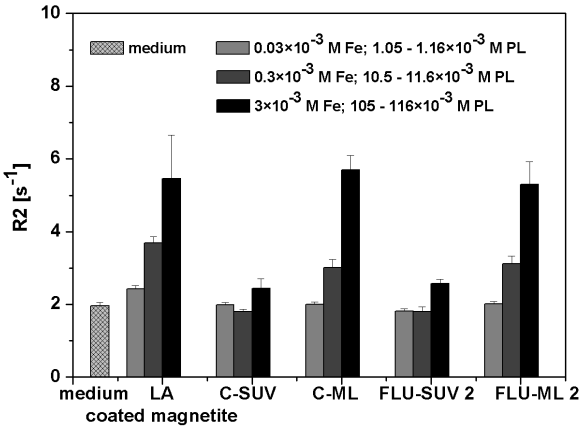

Figure 6

Figure 6. *T*2-relaxation rates (R2) of untreated PC-3 cells (medium), and PC-3 cells incubated with LA-coated magnetite, C-SUV, C-ML, FLU-SUV 2, and FLU-ML 2 for 3 h, respectively. Fe concentrations were 0.03, 0.3 and 3×10^{-3} M during incubation with magnetic colloids. During incubation with C-SUV and FLU-SUV 2, [PL] were 1.047×10^{-3} M, 10.47×10^{-3} M, and 104.7×10^{-3} M (C-SUV), and 1.155×10^{-3} M, 11.55×10^{-3} M, and 115.5×10^{-3} M (FLU-SUV 2). These [PL] correspond to the respective concentrations used for C-ML and FLU-ML 2.

3. CONCLUSIONS

Fluorescent magnetoliposomes are valuable diagnostic systems due to their excellent colloidal stability, low cytotoxicity and dose dependence of the MR signal.

In this context, the lower unspecific cellular uptake of these bimodal contrast agents as compared to most commercial USPIO will be a great advantage for all targeted MR and optical imaging approaches.

Although the fluorophore's normalised fluorescence, quantum yield and life time are

substantially reduced when increasing the number of fluorophore molecules per particle and upon attachment to superparamagnetic iron oxide cores, the FLU-ML internalised in PC-3 cells can still be visualised with fluorescence microscopy. Moreover, based on the results from our fluorescence studies, the quenching influence of the superparamagnetic iron oxide cores could be quantified. This underlines the potential of time-resolved fluorometry for the characterisation of such bimodal contrast agents. With this respect and for the design of bimodal probes with improved fluorescence properties, more systematic studies with systems where the fluorophore-iron oxide distance can be better controlled are of interest. Such studies should be extended to the use of fluorescence lifetime imaging thereby providing an extra parameter for probe and thus tumor location and possible the removal of undesired autofluorescence by time-gated emission.

4. EXPERIMENTAL

4.1. Materials

DMPC, DMPG, and DMPE-L-R ammonium salt were purchased from Avanti Polar Lipids Inc. (Birmingham, AL, USA). All other chemicals were from Sigma-Aldrich (Steinheim, Germany). Throughout this work a 5×10^{-3} M *N*-tris[hydroxymethyl] methyl-2-aminoethanesulfonic acid (TES) buffer (pH 7.0) was used. McCoy's medium (10 % FBS + 1% of penicillin/streptomycin) for cell culture was purchased from Invitrogen/GIBCO.

4.2. Production and characterisation of classical and fluorescent magnetoliposomes

4.2.1. Production of classical and fluorescent ML

ML were produced based on a method developed by De Cuyper et al. (11). In brief, classical SUV (C-SUV) composed of DMPC and DMPG (DMPC/DMPG molar ratio: 90/10) were prepared in TES buffer pH 7.0 by probe sonication (UP 200S titanium probe-tip sonicator; Hielscher). In a similar way, two fluorescent SUV (FLU-SUV) with initial molar DMPC/DMPG/DMPE-L-R ratios of 90/10/0.33 (FLU-SUV 1) and 90/10/1 (FLU-SUV 2) were synthesised. Each SUV type (total phospholipid content of 10 mg/mL) was then mixed with an aqueous ferrofluid (iron content of the ferrofluid stock solution of 179.4 mg/mL) consisting of superparamagnetic magnetite crystals (mean diameter of 10 nm) stabilised with a laurate (LA) coating (35). The phospholipid/iron weight ratio in the different liposome - iron oxide incubation mixtures was 6.9. The mixtures were subsequently dialysed. During this step, the fatty acids originally attached to the iron oxide surface were substituted by phospholipid molecules. Non-adsorbed lipids were removed by high gradient magnetophoresis as detailed in De Cuyper et al. yielding purified C-ML and FLU-ML 1 and 2 (36).

4.2.2. Physicochemical characterisation

Diameter size distribution of the ML magnetite cores, D_h values and values were determined by TEM, dynamic light scattering (DLS) and combined laser Doppler velocimetry and phase analysis light scattering, respectively.

4.2.3. Quantification of total phospholipid and iron concentration, and molar DMPE-L-R fraction

Total phospholipid ([PL]) and iron concentrations were determined spectrophotometrically as described in detail previously (36). DMPE-L-R molar fractions were obtained by lyophilising defined volumes of SUV and ML samples and extracting the phospholipids from the residues with 2.0 mL methanol. DMPE-L-R concentrations of the extracts were then determined by measuring the relative fluorescence at 600 nm (rel. $FI_{em.600}$) (excitation at 530 nm). The molar DMPE-L-R fraction was then calculated by dividing the DMPE-L-R concentration by [PL]. Details about the devices used and the exact protocol followed are described in the supporting information (SI).

4.2.4. Measurement of rel. $FI_{em.}$ spectra, fluorescence quantum yields (Φ_f) and fluorescence decay behavior

Uncorrected emission spectra ($FI_{em.}$ spectra) in the wavelength region of 560 to 850 nm (excitation at 532 nm) were taken for the various fluorescent SUV and ML types using a microfluorescence spectrometer (Infinite M200

microplate reader; TECAN Austria GmbH). The DMPE-L-R concentrations were selected between $(5 – 4500)\times10^{-9}$ M (FLU-SUV 1 and 2), $(5 – 3000)\times10^{-9}$ M (FLU-ML 1), and $(5 – 9000)\times10^{-9}$ M (FLU-ML 2), respectively. Rel. $FI_{em.}$ spectra of the diluted solutions of C-SUV and C-ML containing an identical [PL] as the fluorescent samples were measured under identical conditions and were taken as blanks. The absolute Φ_f of the FLU-SUV and FLU-ML, equaling the number of emitted photons (N_{em}) per absorbed photons (N_{abs}), were determined with a custom-designed integrating sphere setup at the Federal Institute for Materials Research and Testing (BAM). This setup enables spectrally resolved measurements of absolute fluorescence quantum yields in the wavelength region from *ca*. 400 nm to 950 nm (Würth, C.; Resch-Genger U. et al., own unpublished results). Fluorescence decay curves were measured by time-correlated single-photon counting (TCSPC) at 25 ° C using the FluoTime200 lifetime spectrometer of Picoquant GmbH equipped with a PMA182 detector, a PicoHarp300 TCSPC module, and a PDL800-B laser driver. The FLU-SUV and FLU-ML were excited at 532 nm, and the time-dependent fluorescence intensity profile was measured with the emission monochromator set to 590 nm. Details about the measurement conditions, software for analysing the fluorescence decay curves and equations for the calculation of fluorescence lifetimes are described in the SI.

4.2.5. MR relaxometry

Phantom measurements on all ML types used were performed by Nuclear MR relaxometry using a clinical 3.0 T whole body MR system (Philips Achieva, The Netherlands) in combination with a knee coil (sense-flex-M). ML particles were diluted in water in a concentration range between 3×10^{-7} to 2.5×10^{-3} M Fe and 300 µL of each dilution was filled in a well of a 96 well microtiter plate (flat bottom, transparent; Sigma-Aldrich). Transverse relaxation times (T_2) were measured in a 2 D scan mode using a multi-slice, multi shot spin echo sequence with a 90° excitation pulse followed by a train of equally spaced 180° refocusing pulses [TR = 1500 ms, mTR = 1189 ms, TE = 8.1 ms (shortest), number of echoes = 20, FOV = 130 x 162.5, reconstruction matrix = 64 x 81, voxel size = 2 x 2, slice thickness = 3 mm, slice orientation = coronal, scan mode = multishot]. T_2 relaxation times were calculated by a linear fit of the logarithmic region of interest (ROI) signal amplitudes versus echo time (TE). Longitudinal relaxation times (T_1) were determined using a multi shot spin echo sequence with a 10 ° excitation pulse without refocusing pulse [TR = 6.8 ms, TE = 3.3 ms (shortest), number of echoes = 1, FOV = 170 x 148.75 mm, reconstruction matrix = 152 x 130, voxel size = 1.12 x 1.11, slice thickness = 5 mm, slice orientation = coronal, scan mode = 2 D]. T_1 and T_2 relaxivities were calculated from the linear fit of the corrected relaxation rates, $R1_{corr.}$ and $R2_{corr.}$, as a function of the

iron concentration. $R1_{corr.}$ and $R2_{corr.}$ are the longitudinal and transversal relaxation rates of the ML containing samples corrected for the respective relaxation rates of water.

4.3. Cellular response to classical and fluorescent magnetoliposomes

4.3.1. Determination of dose dependence of uptake by PC-3 cells with MR relaxometry

Cellular ML uptake was tested with PC-3 cells cultured in McCoy's medium at 37 °C in a 5 % CO_2 atmosphere in a C150 incubator (Binder). 1.1×10^7 cells per flask (T75 cellstar tissue culture flask; Greiner, Sigma-Aldrich) were incubated for 3 h with 10 mL of C-ML, FLU-ML 2, LA-coated ferrofluid, C-SUV or FLU-SUV 2 in the growth medium or 10 mL pure growth medium. Iron concentrations in the growth medium were 3×10^{-5} M, 3×10^{-4} M, and 3×10^{-3} M Fe for C-ML, FLU-ML 2, and LA-coated ferrofluid, respectively. Each experiment was done in triplicate. Control experiments with C-SUV or FLU-SUV 2 containing the same [PL] as used for the corresponding experiments with C-ML and FLU-ML 2 were carried out. After incubation, cells were trypsinised and washed three times with 50 mL PBS. Then, the cells were suspended in 300 µL 10% gelatine and transferred into the wells of a 96 well microtiter plate (flat bottom, transparent; Greiner, Sigma-Aldrich). The uptake efficiency was determined by measuring the T_1 and T_2 MR relaxation times as described in the former section. Subsequently, the iron concentration of the gelatine cell suspensions was measured with inductively coupled plasma optical emission spectrometry (ICP-OES) as detailed in the SI.

4.3.2. Cell viability

The cell viability of the different ML and SUV samples was analysed using the trypan blue exclusion (trypan blue stain, Invitrogen Corp.) and the 3-(4,5-dimethylthiazol-2-yl)-2,5-diphenyl tetrazolium bromide (MTT) assay (37). Both viability tests were performed at iron concentrations of 3×10^{-5} M, 3×10^{-4} M, and 3×10^{-3} M Fe of the C-ML, FLU-ML 1 and FLU-ML 2 at incubation times of 3 h and 24 h, respectively. Control experiments were carried out with 1 mL of C-SUV and FLU-SUV 1 and 2 containing the same [PL] as the corresponding ML samples. Each experiment was performed in triplicate. For the trypan blue test, 2 mL suspensions of 1.6×10^6 trypsinised cells were incubated at 37 °C, 5 % CO_2 and 95 % air humidity for 24 h, washed once with 2 mL PBS buffer, and incubated with 1 mL of C-ML and FLU-ML 1 and 2 or medium free of particles for 3 h or 24 h. The cells were then washed once, trypsinised, and centrifuged at 1000 *g* (Heraeus Multifuge 1L) for 5 minutes. After resuspending with 0.5 mL medium, 50 µL of the cell suspensions were transferred into 1.5 mL Eppendorf tubes and mixed with 50 µL of

trypan blue stain solution. The amounts of living and dead PC-3 cells were counted with a Cedex XS cell counter (Roche Innovatis AG).

4.3.3. Fluorescence microscopy of internalised particles

For the detection of internalised fluorescent ML by fluorescence microscopy, 1 mL suspensions containing 5×10^5 cells were trypsinised and incubated as described above. Then, FLU-ML 1 or 2 (Fe concentration of 3×10^{-3} M) were added and the cells were incubated for 3 h. Similar experiments performed with 1 mL of C-ML (3×10^{-3} M Fe) or with the growth medium only, were taken as control. All experiments were done in triplicate. Then, the cells were washed three times with 2 mL of PBS buffer. Fixation of the cells on the coverslips was achieved by treatment with 0.5 mL pure ethanol. For nucleus staining, the cells were treated with 0.4 mL DAPI (5 µg/mL) for 30 minutes and the cells were rinsed with water. The internalised particles were viewed with an AxioObserver epifluorescence microscope (Carl Zeiss GmbH). The images were acquired with a digital AxioCam MRm camera and processed using the digital Axio Vision 4.7.2 software (both Carl Zeiss GmbH).

4.3.4. TEM of internalised particles.

1.1×10^7 cells were trypsinised and incubated in T75 cellstar flasks for 3 h as described above. 11 mL of FLU-ML 2 (3×10^{-3} M Fe) were added. The experiment was done in triplicate. Adherent cells were trypsinised and washed once with 50 mL PBS buffer. PC-3 cell pellets were fixed in 5 mL of 3 % glutaraldehyde (Agar Scientific) in 0.1 M Soerensen's phosphate buffer pH 7.4 (13×10^{-3} M $NaH_2PO_4 \times H_2O$ and 87×10^{-3} M $Na_2HPO_4 \times 2H_2O$) for 22 h, washed with 0.1 M Soerensen's phosphate buffer overnight, embedded in 2 % agarose, rinsed with bi-distilled water, and dehydrated with ethanol (30 % - 100 %). Finally, tissues were processed for embedding in Epon (Fluka), polymerised for 8 h at 37 °C and 56 h at 60 °C, cut into 70 - 100 nm thick slices, and stained with uranyl acetate and lead citrate (Ultrostain 1 and 2, Leica). The samples were analysed with a PHILIPS EM 400 T at 60 kV and micrographs were taken by a MORADA CCD-Camera (Olympus Soft Imaging Solutions GmbH).

Acknowledgments

The authors gratefully acknowledge Mariola Gschwendtner (Institut für Siedlungswasser-wirtschaft, RWTH Aachen University, Aachen, Germany) for technical support and other valuable assistance. Research supported in part by the Deutsche Forschungsgemeinschaft (DFG), Grant Number KI 1072/1-3, and Institute for the Promotion of Innovation through Science and Technology in Flanders (IWT—Vlaanderen) StrategischBasisOnderzoek (SBO), Project Nr. 80017 entitled "Integrated magnetic nanoparticle-enabled imaging of therapeutic cells"—"iMAGiNe".

REFERENCES

(1) Weissleder R, Pittet MJ. Imaging in the era of molecular oncology. Nature 2008; 452 (7187): 580-589; doi:10.1038/nature06917

(2) Kim MJ, Kim JH, Lim JS, Oh YT, Chung JJ, Choi JS, Lee WJ, Kim KW. Detection and characterization of focal hepatic lesions: mangafodipir vs. superparamagnetic iron oxide-enhanced magnetic resonance imaging. J. Magn. Reson. Imaging 2004; 20: 612-621; doi: 10.1002/jmri.20174

(3) Harisinghani MG, Barentsz J, Hahn PF, Deserno WM, Tabatabaei S, van de Kaa CH, de la Rosette J, Weissleder R. Noninvasive detection of clinically occult lymph-node metastases in prostate cancer. N. Engl. J. Med. 2003; 348: 2491-2499.

(4) Bulte JWM, De Cuyper M, Despres D, Frank, J. Short- vs. long-circulating magnetolipo-somes as bone marrow-seeking MR contrast agents. J. Mag. Reson. Imaging 1999; 9: 329-335; DOI: 10.1002/(SICI)1522-2586(199902)9:2<329::AID-JMRI27>3.0.CO;2-Z

(5) Kresse M, Wagner S, Pfefferer D, Lawaczeck R, Elste V, Semmler W. Targeting of ultrasmall superparamagnetic iron oxide (USPIO) particles to tumor cells in vivo by using transferrin receptor pathways. Magn. Reson. Med. 1998; 40: 236-242.

(6) Remsen LG, McCormick CI, Roman-Goldstein S, Nilaver G, Weissleder R, Bogdanov A, Hellstrom I, Kroll RA, Neuwelt EA. MR of carcinoma-specific monoclonal anti-body conjugated to monocrystalline iron oxide nanoparticles: the potential for noninvasive diagnosis. Am. J. Neuroradiol. 1996; 17: 411-418.

(7) Amstad E, Zurcher S, Mashaghi A, Wong JY, Textor M, Reimhult E. Surface functionalization of single superparamagnetic iron oxide nanoparticles for targeted magnetic resonance imaging. Small 2009; 5: 1334-1342; doi: 10.1002/smll.200801328

(8) Mornet S, Portier J, Duguet E. A method for synthesis and functionalization of ultrasmall superparamagnetic covalent carriers based on maghemite and dextran. J. Magn. Magn. Mater. 2005; 293: 127-134; doi:10.1016/j.jmmm.2005.01.053

(9) De Cuyper M, Noppe W. Extractability of the phospholipid envelope of magnetoliposomes by organic solvents. J. Colloid Interf. Sci. 1996; 182: 478-482; doi:10.1006/jcis.1996.0491

(10) Soenen SJH, Baert J, De Cuyper M. Optimal conditions for labelling of 3T3 fibroblasts with magnetoliposomes without affecting cellular viability. ChemBioChem. 2007; 8: 2067-2077; doi: 10.1002/cbic.200700327

(11) De Cuyper M, Müller P, Lueken H, Hodenius MAJ. Synthesis of magnetic Fe_3O_4 particles covered with a modifiable phospholipid coat. J. Phys.: Condens. Matter 2003; 15: S1425-1436; doi: 10.1088/0953-8984/15/15/308

(12) Bertorelle F, Wilhelm C, Roger J, Gazeau F, Ménager C, Cabuil V. Fluorescence-modified superparamagnetic nanoparticles: intracellular uptake and use in cellular imaging. Langmuir 2006; 22 (12): 5385-5391; doi: 10.1021/la052710u

(13) Corr SA, Rakovich YP, Gun'ko YK. Multifunctional magnetic-fluorescent nanocomposites for biomedical applications. Nanoscale Res. Lett. 2008; 3: 87-104; doi: 10.1007/s11671-008-9122-8

(14) Jańczewski D, Zhang Y, Das, GK, Yi DK, Padmanabhan P, Bhakoo KK, Tan TTY, Selvan ST. Bimodal magnetic–fluorescent probes for bioimaging. Microsc. Res. Tech. 2010; doi: 10.1002/jemt.20912

(15) Hodenius MAJ, Niendorf T, Krombach GA, Richtering W, Eckert T, Lueken H, Speldrich M, Günther RW, Baumann M, Soenen, SJH, De Cuyper M, Schmitz-Rode T. Synthesis, physicochemical characterization and MR relaxometry of aqueous ferrofluids. J. Nanosci. Nanotechnol. 2008, 8, 1-11. doi: 10.1166/jnn.2008.312

(16) Soenen SJH, Brisson AR, De Cuyper M. Addressing the problem of cationic lipid-mediated toxicity: the magnetoliposome model. Biomaterials 2009; 30: 3691-3701; doi:10.1016/j.biomaterials.2009.03.040

(17) Zhang JQ, Zhang ZR, Yang, H, Tan QY, Qin SR, Qiu XL. Lyophilized paclitaxel magnetoliposomes as a potential drug delivery system for breast carcinoma via parenteral administration: in vitro and in vivo studies Pharm. Res. 2005; 22: 573-583. doi: 10.1007/s11095-005-2496-8

(18) Johansson MK, Cook RM. Intramolecular dimers: a new design strategy for fluorescence-quenched probes. Chemistry-a European Journal 2003; 9 (15): 3466-3471; doi: 10.1002/chem.200304941

(19) Demchenko AP. Optimization of fluorescence response in the design of molecular biosensors. Anal. Biochem. 2005; 343: 1-22; doi:10.1016/j.ab.2004.11.041

(20) Resch-Genger U, Grabolle M, Cavaliere-Jaricot S, Nitschke R, Nann, T. Quantum dots versus organic dyes as fluorescent labels. Nature Methods 2008; 5 (9): 763-775; doi:10.1038/nmeth.1248

(21) Lakowicz JR. Principles of Fluorescence Spectroscopy. 3rd ed. ed.; Springer Science+Business Media, LLC: New York, 2006.

(22) Ye Y, Bloch S, Xu B, Achilefu S. Novel near-infrared fluorescent integrin-targeted DFO analogue. Bioconjugate Chemistry 2008; 19 (1): 225-234; doi: 10.1021/bc7003022

(23) Josephson L, Kircher MF, Mahmood U, Tang Y, Weissleder R. Near-infrared fluorescent nanoparticles as combined MR/Optical imaging probes. Bioconjugate Chem. 2002; 13: 554-560; doi: 10.1021/bc015555d

(24) Würth C, Lochmann C, Spieles M, Pauli J, Hoffmann K, Schuttrigkeit T, Franzl T, Resch-Genger U. Evaluation of a commercial integrating sphere setup for the determination of absolute photoluminescence quantum yields of dilute dye solutions. Appl. Spectrosc. 2010; 64 (7): 733-741; doi: 10.1366/000370210791666390

(25) Lantzsch G, Binder H, Heerklotz H. Membrane/water partition of oligo(ethylene oxide) dodecyl ethers and its relevance for solubilization. J. Fluoresc. 1994; 4 (4): 339-343; doi: 10.1007/BF01881452

(26) Loura LMS, de Almeida RFM, Prieto M. Detection and characterization of membrane microheterogeneity by Resonance Energy Transfer. J. Fluoresc. 2001; 11 (3): 197-209; doi: 10.1023/A:1012249117580

(27) Lopez Arbeloa I, Rohatgi-Mukherjee KK. Solvent effect on photophysics of the molecular forms of rhodamine B. Solvation models and spectroscopic parameters. Chem. Phys. Letters 1986; 129 (6): 607-614; doi:10.1016/0009-2614(86)80656-X

(28) Snare MJ, Treloar FE, Ghiggino KP, Thistlethwaite PJ. The photophysics of rhodamine B. J. Photochem. 1982; 18: 335-346; doi:10.1016/0047-2670(82)87023-8

(29) Grabowski, ZR, Rotkiewicz K, Rettig W. Structural changes accompanying intramolecular electron transfer: focus on twisted intramolecular charge-transfer states and structures. Chem. Rev. 2003; 103 (10): 3899-4031; doi: 10.1021/cr9407451

(30) Roch A, Gossuin Y, Muller RN, Gillis P. Superparamagnetic colloid suspensions: water magnetic relaxation and clustering. J. Magn. Magn. Mater. 2005; 293: 532-539; doi:10.1016/j.jmmm.2005.01.070

(31) Soenen SJH, De Cuyper M. Assessing cytotoxicity of (iron oxide-based) nanoparticles: an overview of different methods exemplified with cationic magnetoliposomes. Contrast Media Mol. Imaging 2009; 4: 207-219; doi: 10.1002/cmmi.282

(32) Bulte JWM, Arbab T, Frank JA. Preparation of magnetically labeled cells for cell tracking by magnetic resonance imaging. Methods Enzymol. 2004; 386: 2163-2169; doi:10.1016/S0076-6879(04)86013-0

(33) Bulte JWM, Douglas T, Witwer B, Zhang S.-C, Strable E, Lewis BK, Zywicke H, Miller B, van Gelderen P, Moskowitz BM, Duncan ID, Frank JA. Magnetodendrimers allow endosomal magnetic labeling and in vivo tracking of stem cells. Nat. Biotechnol. 2001; 19: 1141-1147; doi:10.1038/nbt1201-1141

(34) Billotey C, Wilhelm C, Devaud M, Bacri JC, Bittoun J, Gazeau F. Cell internalization of anionic maghemite nanoparticles: quantitative effect on magnetic resonance imaging. Magn. Reson. Med. 2003; 49: 646-654; doi: 10.1002/mrm.10418

(35) Khalafalla SE, Reimers GW. Preparation of dilution-stable aqueous magnetic fluids. IEEE Trans. Magn. 1980; 16: 178-183; doi: 10.1109/TMAG.1980.1060578

(36) De Cuyper M, Soenen SJH. Cationic magnetoliposomes. In Pharmaceutical Nanocarriers, Weissig, V. (ed). Springer: New York; 97-111, 2010.

(37) Mosmann T. Rapid colorimetric assay for cellular growth and survival: application to proliferation and cytotoxicity assays. J.Immunol.Methods 1983; 65: 55-63; doi:10.1016/0022-1759(83)90303-4